UNIVERSITY OF LONDON THESIS

Degree PhD Year 2007 Name of Author BENNETT Andrew James

The Characteristics of Hard Targets in SAR Imagery

PhD Thesis

Andrew J Bennett

August 2006

Department of Electronic & Electrical Engineering

University College London

ProQuest LLC
789 East Eisenhower Parkway
P.O. Box 1346
Ann Arbor, MI 48106-1346

Abstract

The exploitation of synthetic aperture radar (SAR) data for remote sensing and intelligence gathering purposes over complex terrains (such as urban areas) is a relatively immature subject. In this thesis, the detection and recognition of targets of military interest within urban areas is addressed. Such 'hard targets' may be vehicles or particular manmade structures within a scene (as opposed to geographical features or flora). Those techniques investigated can be divided into three areas; building height extraction, urban SAR exploitation and polarimetric assisted target recognition.

Theoretical performance limitations of interferometric SAR and shadow/layover analysis for building height extraction were derived and validated using example airborne data.

Techniques to assist analysts exploit SAR data over urban areas were developed and demonstrated. A post image formation matched filter enabled scatterers with non-uniform frequency and aspect angle responses to be categorised in wide bandwidth SAR imagery. Sub-aperture movies allowed the velocity of a moving target and the structure of a building's roof to be determined. The direction of multipath responses in squinted SAR was characterised. Additionally, modelling software enabled an assessment of the impact of radar shadowing on urban exploitation as a function of collection geometry, radar mode and terrain type.

Polarimetric features were shown to aid the task of target recognition and temporal and between class stabilities were quantified using example inverse SAR turntable imagery. To polarimetrically calibrate this data, a generalised distortion model was derived together with the development and demonstration of a Fourier method for the determination of calibration parameters using a rotating dihedral.

Table of Contents

Acronyms

ADAS	Airborne Data Acquisition System
AFV	Armoured Fighting Vehicle
APC	Antenna Phase Centre
APV	Armoured Personnel Vehicle
ATI	Along Track Interferometry
ATR	Assisted Target Recognition
CAD	Computer Aided Design
CC&D	Camouflage Concealment and Deception
CFAR	Constant False Alarm Rate
CONOPS	Concept of Operations
DEM	Digital Elevation Model
DFT	Discrete Fourier Transform
DSM	Digital Surface Model
DTM	Digital Terrain Model
ECM	Electromagnetic Counter Measures
EM	Electromagnetic
ESR	Enhanced Surveillance Radar
FFT	Fast Fourier Transform
FM	Frequency Modulated
FOPEN	Foliage Penetration
GPS	Global Positioning System
GRAPE	Generic Radar Processing Environment
GRP	Ground Reference Point
H	Horizontal
HH	Transmit H Receive H
HV	Transmit H Receive V
IA	Image Analyst
IMU	Inertial Measurement Unit
INS	Inertial Navigation System
InSAR	Interferometric SAR
ISAR	Inverse SAR
ISTAR	Intelligence, Surveillance, Target Acquisition, Reconnaissance
LIDAR	Light Detection and Ranging
MBT	Main Battle Tank
MIDAS	Mobile Instrumented Data Acquisition System
ML	Maximum Likelihood
MOCO	Motion Compensation
MoD	Ministry of Defence
MSTAR	Moving and Stationary Target Acquisition and Recognition
MTI	Moving Target Indication
NATO	North Atlantic Treaty Organisation
PolSAR	Polarimetric SAR
PRF	Pulse Repetition Frequency
PSD	Power Spectral Density
PWF	Polarimetric Whitening Filter
RADAR	Radio Detection and Ranging
RF	Radio Frequency
RMS	Root Mean Squared

RTW/RDE	Racal Thorn Wells/Racal Defence Electronics
SAR	Synthetic Aperture Radar
SIGINT	Signals Intelligence
SMARTbox	SAR Machine Aided Recognition Toolbox
SPTA	Salisbury Plain Training Area
UAV	Unmanned Air Vehicle
UHF	Ultra High Frequency
UK	United Kingdom
US	United States
V	Vertical
VH	Transmit V Receive H
VHF	Very High Frequency
VV	Transmit V Receive V

Symbols

	Description	Page	Figure
B_d	Doppler bandwidth	31	
B_e	effective bandwidth	28	
c	speed of light	27	
D	physical antenna length	29	
$\boldsymbol{E_r}$	received E-field	38, 154	
$\boldsymbol{E_s}$	scattered E-field	38, 154	
f_c	centre frequency	28	
f_d	Doppler frequency	30	
f_i	channel imbalances	155	
$g(x, y, z)$	complex reflectivity function	52	
$G(X, Y, Z)$	complex reflectivity function in Fourier space	59	
$G^j{}_i$	polarimetric channel gain	154	
$g^j{}_i$	polarimetric cross-talk	154	
h	height	30	1, 2
H	entropy	172	
h_1	minimum roof height above the ground	95	21
h_2	maximum roof height above the ground	95	21
L	synthetic aperture length	31	3
L	slant range swath (in tomographic image formation derivation)	54	9
$R(k, l)$	auto-correlation function	185	
R_0	range to target at mid-aperture	30	1, 2, 3, 4, 5
$\mathbf{R_0}$	mid-aperture range vector	34	4, 5, 45
R_t	range to target	26	1
$\mathbf{S}$	Sinclair scattering matrix	38, 154	
T	interpulse period	27	
T_e	effective pulse length	27	
T_{int}	integration time	31	
T_p	pulse width	27	
u	instantaneous slant range	52	9
v	platform velocity	30	
$\mathbf{v}$	velocity vector	34	4, 45
v_{los}	line of sight target velocity	131	
v_y	target velocity in range direction	132	
w	building width	94	19
W_a	azimuth swath width	48	
W_r	range swath width	47	
X	building range extent	94	19

	Description	Page	Figure
X_{3dB}	canonical match filter sinc width (units of Doppler bandwidth)	124	
X_s	Doppler sampling width	124	
Y	building shadow length	94	19
Y_0	region of support offset in Y direction	55, 122	11
Y_s	sampling frequency	124	
(X, Y)	frequency domain coordinates (slant plane)	55, 122	11
$(\hat{\mathbf{x}}, \hat{\mathbf{y}}, \hat{\mathbf{z}})$	slant plane	34	4
$\hat{\mathbf{x}}$	slant plane azimuth unit vector	34	4, 45
$\hat{\mathbf{y}}$	slant plane range unit vector	34	4, 45
$\hat{\mathbf{z}}$	slant plane unit normal	34	4, 45
$(\overline{\mathbf{x}}, \overline{\mathbf{y}}, \overline{\mathbf{z}})$	ground plane	34	4, 45
$\overline{\mathbf{x}}$	slant plane azimuth unit vector	34	4, 45
$\overline{\mathbf{y}}$	ground plane range unit vector	34	4, 45
$\overline{\mathbf{z}}$	ground plane unit normal	34	4, 45
α	$\pi\gamma$	52	
α	canonical scattering parameter {-1, -½, 0, ½, 1}	123	
α	alpha angle	173	
β_a	beam width	29	
$\Delta\theta$	angle in the slant plane over which the synthetic aperture is formed	36	3
Δt	transmit receive time delay	26	
$\Delta X \times \Delta Y$	frequency domain region of support widths (slant plane)	55, 122	11
ϕ	sensor aspect angle	95	19
ϕ	stereo angle	119	37
$\phi(t)$	phase (as a function of time)	30	
$\phi(\omega_k, \omega_l)$	power spectral density function	186	
$\phi(\omega_r)$	radial power spectral density function	186	
ϕ_b	bistatic angle	147	54
$\phi_{imaging}$	imaging bearing	143	50
ϕ_{leg}	imaging leg bearing	143	50
γ	frequency chirp rate	28	
γ^i_j	polarimetric cross-talk normalised to HH	154	
Γ^i_i	polarimetric channel gain normalised to HH	154	
η	angle between the slant plane and ground plane in x direction	59	12
φ	tilt angle	135	45
λ_c	centre wavelength	29	
θ	ground plane squint angle	35	4, 5
θ	dihedral seam angle	156	

	Description	Page	Figure
θ_s	slant plane squint angle	31	2
ρ_{az}	azimuth resolution	29	
ρ_r	range resolution	27	
σ_i	cross-talk elements	155	
τ_p	patch propagation time	54	
ω_0	$2\pi f_c$	52	
ψ	grazing angle	34	4, 5
ζ	slope angle	135	45

List of Figures

List of Tables

Dedication

This thesis is dedicated to Lucy Almgill and Gerald Bennett who supported me throughout with great patience and is in loving memory of Mary Bennett.

Acknowledgements

The writing of this thesis would not have been possible without the help and guidance of Dr David Blacknell, Dr Anthony Currie and Professor Hugh Griffiths.

The SAR imagery used was processed using software written by Alan Blake and Andy Horne and trials activities were ably assisted by the QinetiQ SAR trials ground team (in particular Mike Clarke and Andy Rhymer). SMARTbox was co-developed with Dave Blacknell, Dave Pedlar and David Carrington.

This work was carried out as part of UK MOD's ISTAR Research Programme.

1 Introduction

1.1 Research motivation

Synthetic Aperture Radar (SAR) image formation is a mature technology. However, in comparison, the exploitation of SAR data for remote sensing and intelligence gathering purposes, especially over complex terrains such as urban areas, is less well understood. From a military standpoint, the detection and recognition of targets within urban areas is of obvious significance. It is this objective that motivates this study.

Targets of interest may be vehicles or particular manmade structures within a scene. Herein we use the term 'hard targets' to differentiate these targets from other objects within the scene that are often of interest to civilian remote sensing applications, such as geographical features or flora.

SAR imagery, particularly from radar data collected over urban areas, often contains phenomena such as layover, shadowing, multipath and smearing, all of which are considered problematic in conventional image analysis. However, they can be utilised to provide information far beyond that available from optical imagery. Indeed, to fully exploit SAR data, one should consider methods that do not simply utilise the image product. Examples of such techniques include polarimetry, interferometry, stereography, canonical scattering analysis and sub-aperture imaging. These are some of the approaches taken by this study in examining the characteristics of hard targets in SAR imagery.

1.2 Research objectives and focus

This thesis is based upon work carried out as part of UK MOD's ISTAR Research Programme and hence its focus is the usage of SAR techniques to improve military capability in the area of Intelligence Surveillance Target Acquisition and Reconnaissance (ISTAR).

The intended concept of operations (CONOPS) under which the tools and techniques developed herein are to be deployed is described below:

> An image analyst is tasked with the extraction of intelligence information over multiple pre-specified urban areas (typically of sizes ~10km x 10km). A particular task may be concerned with the identification of a certain structure or vehicle within the area, the detailed modelling or mapping of an urban area or the monitoring of activities ('pattern of life') within the urban area.

Data supplied to support the task will be obtained by a radar onboard a military platform (such as an aircraft or UAV) operating in a SAR collection mode. The radar will be sufficiently specified such that it is able to produce SAR imagery with range and azimuth resolutions finer than 1m. Availability of the raw signal data is assumed.

The objective of this research is to develop and investigate tools and techniques that can assist the analyst to perform such tasks in an accurate and timely manner. Those techniques investigated in this study are all concerned with the analysis of hard targets in SAR imagery, generally employing both intensity and phase information and can be divided into three areas; building height extraction, urban SAR exploitation and polarimetric assisted target recognition.

1.3 Context of thesis

To extract information for intelligence or targeting requirements in urban areas it is often useful to provide image analysts with height measurements of a target building or group of buildings. Currently, many of the papers in the open literature (details of which are discussed in Chapter 3) utilise interferometric techniques to extract the heights of large flat roof buildings from relatively coarse resolution SAR data using image segmentation approaches. In this study, we look at very fine (<1m) resolution imagery and do not apply segmentation algorithms that often reduce information content and can be particularly unreliable over urban areas.

Both interferometric and shadow based height extraction techniques often assume target buildings are flat roofed and have very large footprints. Here, we do not make such assumptions and take a more fundamental approach by attempting to parameterise the conditions under which our techniques can be applied.

Aside from providing building height information, the ability to exploit SAR data of urban areas to aid the image analyst has not been widely studied. In particular, the ability to form squinted imagery (as described in section 2.1.7) is rarely fully utilised for urban SAR exploitation in published literature. In this thesis, we present examples of squinted urban imagery and investigate the how such a data collection strategy impacts upon phenomena such as glinting, multipath and shadowing. Using example imagery, we show how such features can be exploited for intelligence purposes.

SAR data from urban areas often exhibits behaviour that is not well described by traditional processing techniques where scatterers are assumed to be point like in the

radar and Doppler frequency bandwidth of interest. In order to exploit non-point-like scattering, frequency and azimuth filtering has been proposed in the open literature and a post-processing azimuth matched filter approach has been applied to FOPEN SAR (as we shall discuss further in section 3.2). A similar approach that also incorporates frequency filtering is developed and investigated here. Moreover, in this thesis the technique is applied to X-band SAR data and its ability to assist the analyst exploit urban imagery is assessed.

Many of the published papers that we shall discuss in Chapter 3 use polarimetry for land-use classification using coarse resolution SAR. Polarimetry has also been used for the detection of targets in rural areas at comparable resolutions. As achievable resolutions become finer, enabling the isolation of individual scatterers within a resolution cell, we propose that polarimetric decompositions techniques may be applicable to vehicle target identification. However, before such techniques can be used in ATR systems it is prudent to assess firstly whether polarimetric target signatures are stable. We attempt to address this task here.

1.4 Thesis roadmap

To enable this thesis to be read by a non-SAR specialist, Chapter 2 contains an introduction into the usage and basic principles of SAR data collection and processing. We follow the approaches of [1] and [2] to describe how the SAR imaging method can achieve both fine range and azimuth resolutions at long standoff ranges. The numerous SAR collection methods and associated system design considerations are discussed. Finally, we describe the tomographic image formation process first proposed in [3] to illustrate the Fourier relationship between the collected radar data and the processed SAR image.

In Chapter 3 we discuss relevant published work on building height extraction, urban SAR exploitation and polarimetric assisted target recognition (ATR) in order to illustrate more fully the context of this study as summarised in section 1.3.

In Chapter 4 we describe how shadow/layover analysis and interferometric SAR (InSAR) can be used to extract building heights from radar data. The conditions under which this approach can be applied are defined. Trials undertaken to demonstrate the application of these techniques using airborne SAR data are described and results are discussed. An investigation into the automation of the shadow/layover method is presented. Alternative methods for the extraction of building height information using stereography are also discussed.

Following the mensuration of building dimensions, Chapter 5 describes methods for further exploitation of SAR imagery of urban areas. The production of additional intelligence information from SAR data using techniques such as primitive scatterer analysis and sub-aperture SAR movies is investigated. The behaviour of multipath returns in squinted spotlight SAR is addressed theoretically, together with the production of simulation software to consider the impact of radar shadowing on urban SAR exploitation.

Our characterisation of hard targets also requires the examination of vehicle signatures in SAR imagery. In Chapter 6 we explore the potential benefits of polarimetry for ATR using data obtained by turntable inverse SAR (ISAR) experiments. To utilise this data fully, an efficient calibration procedure is required, hence we begin the chapter by developing a method to perform this task.

Finally, in Chapter 7 we draw upon techniques discussed in Chapters 5 and 6 to look at the problem of discriminating vehicle targets from buildings in urban areas. We discuss the results of applying post-processing algorithms to trials data obtained using a wide bandwidth polarimetric airborne SAR system. Overall conclusions and recommendations for further work are presented in Chapter 8.

1.5 List of key achievements

- A theoretical and experimental analysis of the use of InSAR over urban areas has resulted in the derivation of a set of conditions under which interferometry can be used to extract reliable building height information for both flat and apex roofed structures. InSAR techniques have been shown to allow battle damage assessment to be performed using airborne data.
- A methodology for the extraction of building height information using radar shadow and layover measurements has been developed and demonstrated upon airborne SAR imagery. Assisted detection and delineation algorithms have been optimised and utilised to allow the approach to be automated over urban areas.
- A post image formation match filter was developed and demonstrated to enable scatterers with non-uniform frequency and aspect angle responses to be categorised in wide bandwidth SAR imagery.
- Sub-aperture SAR movies have been exploited to extract intelligence information over urban areas. The velocity of a moving target and the structure of a building's roof are measured from sub-aperture movies.
- The direction of multipath responses in squinted spotlight SAR imagery has been modelled for the first time.
- The production of modelling software has enabled an assessment of the impact of radar shadowing on urban exploitation as a function of collection geometry, radar mode and terrain type for squinted spotlight SAR imagery.
- A generalised distortion model for the calibration of polarimetric SAR data has been derived together with the development of a Fourier method for the determination of polarimetric calibration parameters using a rotating dihedral.
- An assessment of the stability of polarimetric features for assisted target recognition has been performed using ISAR turntable imagery.

1.6 List of supporting publications

- A. J. Bennett, A. Currie, 'The Calibration and Characterisation of High Resolution Polarimetric SAR Target Signatures', Proceedings of IEE High Resolution Radar and Sonar Colloquium, 11 May 1999, pp5/1-5/7.
- W.E. Smith, D. Filiberti, A. J. Bennett, A. Currie, 'Calibration of Polarimetric SAR and Sensitivity to Calibration Error', Algorithms for Synthetic Aperture Radar Imagery VIII, Orlando, 16-19 April 2001, Proceedings of SPIE, Volume 4382, pp264-275, August 2001.
- A. J. Bennett, A. Currie, 'The Use of High Resolution Polarimetric SAR for Automatic Target Recognition', Algorithms for Synthetic Aperture Radar Imagery IX, Orlando, 1-3 April 2002, Proceedings of SPIE, Volume 4727, pp146-153, August 2002.
- A. J. Bennett, A. Currie, 'The Stability of Polarimetric Features for Target Classification from SAR Imagery', IEE Proceedings of Radar 2002', Edinburgh, 15-17 October 2002, pp395-399.
- A. J. Bennett, D. Blacknell, 'Infrastructure Analysis from High Resolution SAR and InSAR Imagery', Remote Sensing and Data Fusion Over Urban Areas, IEEE/ISPRS Joint Workshop, 22-23 May 2003, pp230-235.
- A. J. Bennett, D. Blacknell, 'The Extraction of Building Dimensions from High Resolution SAR Imagery', Proceedings of Radar 2003, Adelaide, 3-5 September 2003, pp182-187.
- A. J. Bennett, D. Blacknell, 'The Benefits and Detriments of Radar Shadowing in Urban SAR Imaging', Proceedings of EUSAR 2004, Ulm, 25-27 May 2004, pp419-422.
- A. J. Bennett, D. Blacknell, 'Exploiting the Intensity and Phase Characteristics of Airborne SAR Data Over Urban Areas', Algorithms for Synthetic Aperture Radar Imagery XII, Orlando, 28 March-1 April 2005, Proceedings of SPIE Volume 5808, May 2005, pp185-195.
- A. J. Bennett, 'Multipath in Squinted SAR Imagery', Proceedings of EUSAR 2006, Dresden, 16-18 May 2006.

2 SAR Fundamentals

2.1 SAR overview

In this section, we give an introduction into the utility of SAR, the various methods of data collection and define some of the commonly used SAR terminology.

2.1.1 SAR capabilities and usage

The Synthetic Aperture Radar (SAR) imaging process allows the collection of high resolution map-like imagery from airborne and spaceborne platforms. Illumination of the area of interest is provided either by the platform itself or by other sources of radio waves, enabling SAR systems to obtain data throughout day and night. Additionally, since at most frequencies of operation radio waves propagate through rain and clouds with little attenuation, SAR can also operate in all weather conditions. SAR's 24-hour, weather independent ability to provide geospatial mapping information, strategic and tactical intelligence from long stand-off ranges is crucial to its civilian and military utility.

Civilian systems are primarily concerned with remote sensing and terrain mapping applications. Some typical examples include [4]

- Cartography: map production and three-dimensional digital terrain models
- Vegetation assessment: deforestation monitoring, identification and estimation of crop growth
- Geology: measurement of landslides and erosion, identification of geological features
- Ocean surveillance: detection of waves, navigation channel surveillance and iceberg detection

Military deployments of SAR systems are numerous, including

- Intelligence gathering
- Surveillance
- Long range airborne reconnaissance
- Geolocation and precision targeting from strike aircraft
- Mapping

SAR is not the only sensor that, under certain conditions, can produce similar information. Competing sensors include

- Optical systems operating in the visible or infrared bands
- Active optical systems (laser radar)
- Non imaging radar

Optical imagery is often easier to interpret than SAR imagery however, unlike SAR, optical systems do not offer a 24-hour capability to collect data in all weathers.

2.1.2 Radar ranging

Radar is an acronym for radio detection and ranging. All radar systems transmit electromagnetic waves in the radio frequency band of the EM spectrum. This energy is directed at a target, which will absorb a fraction of this energy and scatter the remainder. The energy scattered in the direction of the radar receiver is converted into a voltage, termed the received signal.

The time between transmission and reception is determined by the path length between the transmitter and the target and the target and the receiver. Path length is not always the minimum straight-line distance between transmitter and target, and target and receiver. For example, where energy is first reflected by the ground or an atmospheric layer before scattering off a target, it can follow multiple paths (termed multipath scattering). Over the horizon radars use this effect by reflecting energy off charged particles in the ionosphere to increase the range of surveillance radars. Additionally, radar paths may be bent. The radar refractive index of the Earth's atmosphere decreases slightly with height. Therefore, a narrow beam of radar energy transmitted horizontally is bent towards the Earth allowing certain radars to see beyond the horizon [4].

Monostatic radar systems transmit and receive from the same spatial position such that the target range can be determined as half of the sum of the transmit and receive path lengths. Hence, given a time delay, Δt, the target range R_t is given by

$$R_t = \frac{c\Delta t}{2}, \tag{1}$$

where c is the velocity at which the EM wave propagates. Therefore, the accuracy to which the radar can measure Δt limits the accuracy to which target range can be determined.

2.1.3 Radar positioning

Most applications require measurement of the target's location, not merely its range. The line between the spatial positions of the radar and the target is the vector that

defines the target line of sight. Position of a target is defined by its range (the length of this vector) and the angle between the line of site and some reference unit vector such as north or the velocity vector of the platform onto which the target is mounted. Conventionally, this angle is decomposed into horizontal and vertical components, known as elevation and azimuth respectively.

Radar systems employ antennas to radiate and receive a beam of energy. Directional antennas produce a finite beam in a known direction. In conventional radar, a target's angular position cannot be determined to a greater accuracy than the width of this beam. Hence, azimuth resolution is determined by the radar's azimuth beam width. Narrow beam widths, which require large physical antennas (and/or high frequencies), are therefore preferable.

2.1.4 Range resolution and pulse compression

With pulsed radars, energy is transmitted over discrete time periods termed pulse widths, T_p. The time between the start of each successive pulse is the inter-pulse period, T, the reciprocal of which is the pulse repetition frequency (PRF). To avoid saturating receive channels, radars may not receive pulses during the transmit process. The period of time during which the radar accepts the received signal after transmission is called the range gate.

As stated previously, an accurate determination of target range relies upon an accurate measurement of the time delay, Δt. Hence, in conventional pulsed operation, Δt can only be calculated to an accuracy determined by the pulse width. In such cases the range resolution, ρ_r, is limited by

$$\rho_r = \frac{cT_e}{2}, \tag{2}$$

where T_e is the effective pulse length. For a pulse window function, $g(t)$, where the centre of the pulse occurs at the time, $t = 0$, the effective pulse length is given by

$$T_e = \frac{\int_{-\infty}^{\infty} g(t)dt}{g(0)}. \tag{3}$$

Correspondingly, the effective bandwidth of the pulse is

$$B_e = \frac{1}{2\pi} \frac{\int_{-\infty}^{\infty} G(\omega) d\omega}{G(0)}, \tag{4}$$

where $G(\omega)$ is the Fourier transform of the windowing function, $g(t)$. The pulse compression theorem leads to the result $T_e B_e = 1$ [1], and hence another representation of range resolution is

$$\rho_r = \frac{c}{2B_e}. \tag{5}$$

Note for rectangular pulses where

$$g(t) = \begin{cases} 1 & |t| \le T_p/2 \\ 0 & |t| > T_p/2 \end{cases}, \tag{6}$$

$T_e = T_p$ and $B_e = 1/T_p$.

Therefore, range resolution is optimised by choosing as short a pulse as possible (or as wide as bandwidth as possible). However, for a radar of any given power, the energy incident upon a target and subsequently scattered and received is proportional to the pulse width. Thus, reducing the pulse width decreases the energy received by the radar, which in turn limits its maximum operating range.

One method of overcoming this problem is through use of pulse compression. Such techniques use pulses that are modulated in some way such that their average power remains sufficiently high (enabling long range operation) but that also allows them to be compressed upon reception so that their compressed pulse width is much narrower and hence the achievable range resolution is much finer.

For SAR systems (and indeed most other radars), the most common form of pulse compression coding is the Linear Frequency Modulated (FM) chirp. Such systems transmit pulses whose frequencies are ramped linearly in time. During the transmission of a rectangle pulse over a time, T_p, the frequency as a function of time can be described by

$$f(t) = \begin{cases} f_c + \gamma t & |t| \le T_p/2 \\ 0 & |t| > T_p/2 \end{cases}, \tag{7}$$

where f_c is the centre frequency of the pulse (at $t = 0$) and γ is defined as the chirp rate. The chirp rate is the rate at which the frequency varies over time. It can be shown that

pulse compression of such a signal (which is commonly achieved in spotlight SAR by de-ramp processing) produces an effective bandwidth [1]

$$B_e = \gamma T_p . \tag{8}$$

Hence, such systems can achieve a range resolution of

$$\rho_r = \frac{c}{2B_e} = \frac{c}{2\gamma T_p} . \tag{9}$$

Crucially, if the chirp rate is sufficiently high, this allows long pulses to be transmitted (hence producing a high average power) whilst still maintaining fine range resolutions, thus allowing the operation of fine range resolution SAR systems at long ranges.

The requirement for fine range resolution with long pulse lengths drives the need for larger bandwidths. Obviously, the theoretical maximum bandwidth of any Linear FM system is equal to $2f_c$ and therefore low frequency radars will be limited in their finest achievable range resolution. However, in most cases, particularly at higher frequencies, the expense of producing hardware with large operating bandwidths and the frequency allocation issues associated with such transmissions, provide practical limitations on range resolution.

2.1.5 Azimuth resolution using SAR

As stated earlier, for convention real beam radar systems, azimuth resolution is determined by the radar's azimuth beam width. An unweighted antenna of length, D, transmitting with a centre wavelength of λ_c will provide a 3dB azimuth beam width,

$$\beta_a = 0.89\frac{\lambda_c}{D}, \tag{10}$$

and hence a target at a range, R_t, is resolvable to a spatial distance of

$$\rho_a \approx 0.89\frac{R_t\lambda_c}{D}. \tag{11}$$

For most target recognition purposes, radar resolution of <1m is required. In order to achieve this with an X-band (3cm wavelength) airborne system operating at a range of 100km, the length of antenna required would be greater than 2.6km. Such an antenna is obviously impractical.

One method of achieving a finer azimuth resolution is to use the along track motion of an imaging platform to synthesise a long, side-looking antenna. Essentially, as a pulse is

transmitted, the platform position moves further down its flight path and the received pulse is stored by the radar system. This process is repeated in order to form what is termed a synthetic aperture. This can be thought of as a large phased array, but instead of each element of the array simultaneously receiving each pulse, only one element receives each pulse as it moves along the extent of the synthetic aperture (the technique was developed from ideas pioneered by Carl Wiley in the early 1950s, whilst working for the Goodyear Aircraft Corporation [6]).

Consider a platform moving in the direction of the x-axis at a height h, imaging a point target at a range R_t (our definition of a point target stipulates that its scattering properties are independent of imaging geometry and remain constant over the transmitted frequency bandwidth). If, at the point where the platform is perpendicular to the target, its range is R_0 (corresponding to $x=0$), then the y-axis is defined along the ground range vector as shown in Figure 1. Then given that, $R_0 >> x$,

$$\begin{aligned} R_t^2 &= x^2 + y^2 + h^2 \\ R_t &= (R_0^2 + x^2)^{1/2} \\ &= R_0 (1 + \frac{x^2}{R_0^2})^{1/2}, \\ &\approx R_0 + \frac{x^2}{2R_0}. \end{aligned} \tag{12}$$

Assuming a perfectly straight and level flight path, the two-way phase, as a function of x, can be written as

$$\phi(x) = -2\pi \frac{2R_t}{\lambda} = \phi_0 - \frac{2\pi x^2}{R_0 \lambda}, \tag{13}$$

where $\phi_0 = \frac{4\pi R_0}{\lambda}$. Note that phase is a quadratic function of x. Or, given a platform velocity, v,

$$\phi(t) = \phi_0 - \frac{2\pi (vt)^2}{R_0 \lambda}, \tag{14}$$

the phase can also be expressed as a quadratic function of time, t (with $t=0$ *when* $x=0$).

This change in phase produces a Doppler frequency,

$$f_d = \frac{1}{2\pi} \frac{d\phi(t)}{dt} = -\frac{2v^2 t}{R_0 \lambda}. \tag{15}$$

Therefore, analogously to our discussion of range resolution for linear FM pulse compression, the frequency (in this case Doppler frequency) is a linear function of time with a chirp rate, $\gamma_d = \frac{2v^2}{R_0\lambda}$. This analogy leads to the usage of the term 'azimuth compression' when referring to this method of achieving high azimuth resolution by combining pulses. Note that the comparison with range compression is only valid over the time during which the pulse is transmitted, this time is often referred to as fast time.

For an integration time, T_{int}, (which is analogous to the pulse width T_p in fast time) the Doppler bandwidth of the single point scatterer is thus

$$B_d = \frac{2v^2 T_{\text{int}}}{R_0\lambda} = \frac{2vL}{R_0\lambda}, \tag{16}$$

where L is the length of the synthetic aperture. The azimuth resolution, ρ_{az}, which can be achieved by Doppler compression, is

$$\rho_{az} = \frac{v}{B_d} = \frac{R_0\lambda}{2L}. \tag{17}$$

Note that the above derivation has been performed for a broadside imaging collection, such that the centre of the aperture coincides with the position where the platform to target vector, R_0, is perpendicular to the platform track as shown in Figure 1. For cases where the centre of the aperture is squinted as in Figure 2, then for a squint angle of θ_s in the slant plane (see Figure 2), and where $R_0 = \sqrt{x_0^{\,2} + y_0^{\,2} + h^2}$ is the range to aperture centre, the target range is given by

$$\begin{aligned}
R_t^{\,2} &= (x_0 - vt)^2 + y_0^{\,2} + h^2 \\
&= R_0^{\,2} - 2x_0 vt + v^2 t^2 \\
&= R_0^{\,2} - 2R_0 vt\sin\theta_s + v^2 t^2 \\
R_t &= R_0\sqrt{1 - \frac{2vt}{R_0}\sin\theta_s + \frac{v^2 t^2}{R_0^{\,2}}} \\
&\approx R_0\left[1 - \frac{2vt}{R_0}\sin\theta_s + \frac{v^2 t^2}{2R_0^{\,2}} - \frac{v^2 t^2}{2R_0^{\,2}}\sin^2\theta_s\right] \\
&= R_0\left[1 - \frac{2vt}{R_0}\sin\theta_s + \frac{v^2 t^2}{2R_0^{\,2}}\cos^2\theta_s\right],
\end{aligned} \tag{18}$$

to second order, the condition, $R_0 >> vt$ .The phase is then given by

$$\phi(t) = -\frac{4\pi R_0}{\lambda} + \frac{4\pi v t}{\lambda}\sin\theta_s - \frac{2\pi v^2 t^2}{R_0\lambda}\cos^2\theta_s, \tag{19}$$

such that the Doppler frequency is then

$$f_d = \frac{2v}{\lambda}\sin\theta_s - \frac{2v^2 t}{R_0\lambda}\cos^2\theta_s. \tag{20}$$

The first term is term is constant with both range and time and represents the central Doppler frequency. For a synthetic aperture, L, the second term provides a Doppler bandwidth of

$$B_d = \frac{2vL}{R_0\lambda}\cos^2\theta_s. \tag{21}$$

From inspection of Figure 3, resolution in the azimuth direction is given by

$$\rho_{az} = \frac{v}{B_d}\cos\theta_s = \frac{R_0\lambda}{2L\cos\theta_s}. \tag{22}$$

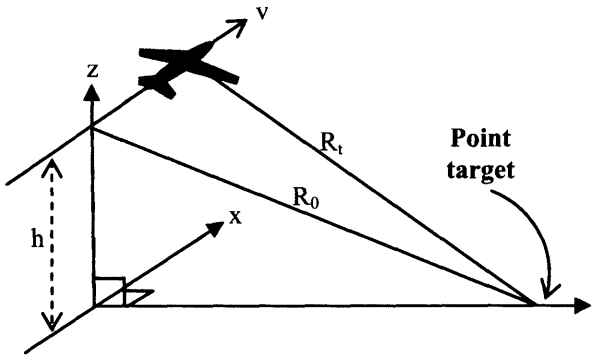

Figure 1: Broadside SAR collection geometry

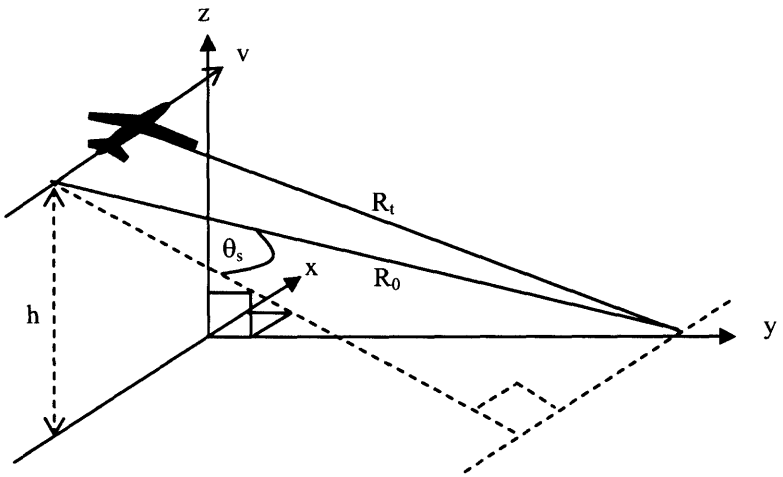

Figure 2: Squinted SAR collection geometry

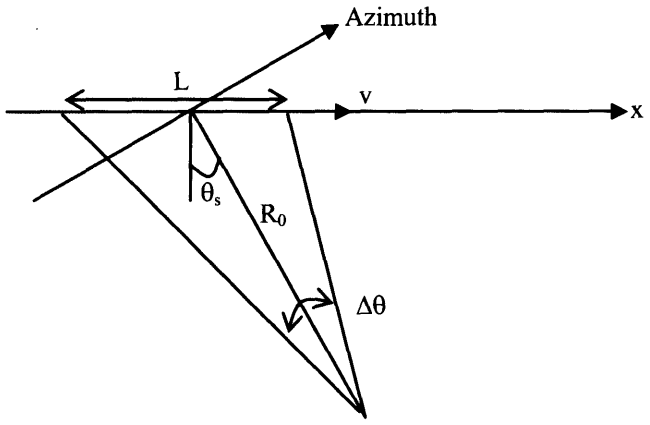

Figure 3: Squinted SAR collection geometry in slant plane

2.1.6 SAR collection geometrical definitions

Two planes, the slant plane and the focus plane, and two positions, the sensor location at aperture centre and the scene centre (or the ground reference point (GRP)) describe the SAR collection geometry (see Figure 4) [2].

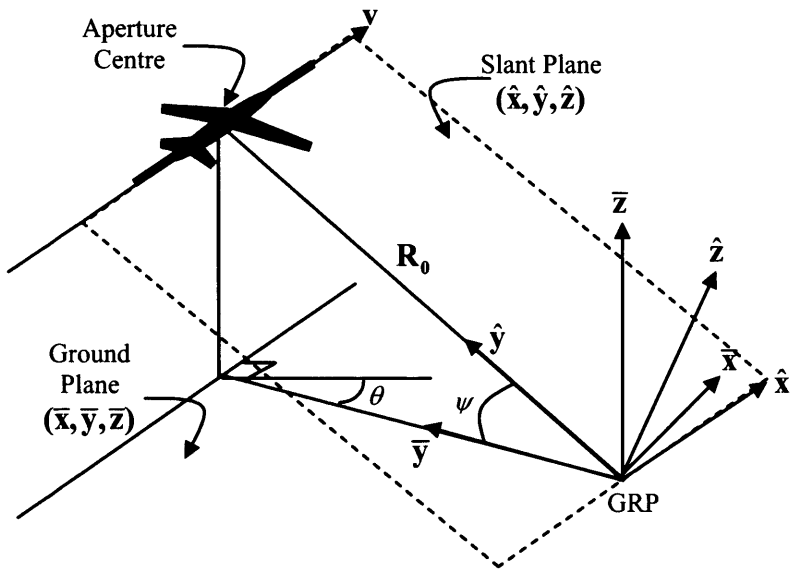

Figure 4: Definitions of slant and ground planes and angles θ and ψ [2]

The line from the sensor at aperture centre to the GRP is defined as the slant range and defines the mid-aperture range vector, $\mathbf{R_0}$, with magnitude, R_0. The slant plane, $(\hat{\mathbf{x}},\hat{\mathbf{y}},\hat{\mathbf{z}})$, may be defined in several ways but, if we assume the collection platform has a constant velocity vector, $\mathbf{v}$, then its normal is

$$\hat{\mathbf{z}} = \frac{\mathbf{R}_0}{R_0} \times \frac{\mathbf{v}}{|\mathbf{v}|}. \tag{23}$$

The projection of $\mathbf{R_0}$ onto the ground plane, $(\bar{\mathbf{x}},\bar{\mathbf{y}},\bar{\mathbf{z}})$, is known as the ground or standoff range (Figure 5) and the angle formed by the intersection of these two lines at the GRP is defined as the grazing angle, ψ. The direction perpendicular to the ground range is termed the azimuth direction (the $\bar{\mathbf{x}}$ axis in Figure 4).

The operating range of SAR systems is commonly quoted as their ground or standoff range. By their nature, airborne, long standoff systems operate with small grazing angles. Shallow grazing angles reduce layover distortions and offer the finest range resolution, however the radar shadows cast by objects such as trees or buildings can obscure areas of interest at very small grazing angles. Spaceborne sensors can operate with both shallow and steep grazing angles, as can sensors that can operate near to

target areas (such as UAVs). Very steep grazing angles reduce ground range resolution and the resultant layover effects can make image exploitation difficult. The height of the imaging sensor above the ground plane is its altitude.

The radar's squint angle is commonly defined as the angle between the ground range direction and the broadside direction in the ground plane (perpendicular to the sensor track), shown as, θ, in Figure 4. Hence a system operating with a 0° squint angle is imaging at broadside. Positive squints are defined as occurring when the sensor is looking forwards and negative squints when the sensor is looking backwards. Note that the ground plane squint angle, θ, is not generally equal to squint angle in the slant plane, θ_s as defined previously (Figure 2).

The extent of the area on the ground, in the range direction, over which the SAR system can collect and process data, is known as the ground range swath (Figure 5). This quantity is dependent upon grazing angle, but is often quoted as a maximum swath (occurring when the sensor collects from its shallowest grazing angle). The corresponding extent in the azimuth direction is less widely quoted. This quantity is a function of radar beam width and is dependent upon operating range and collection mode.

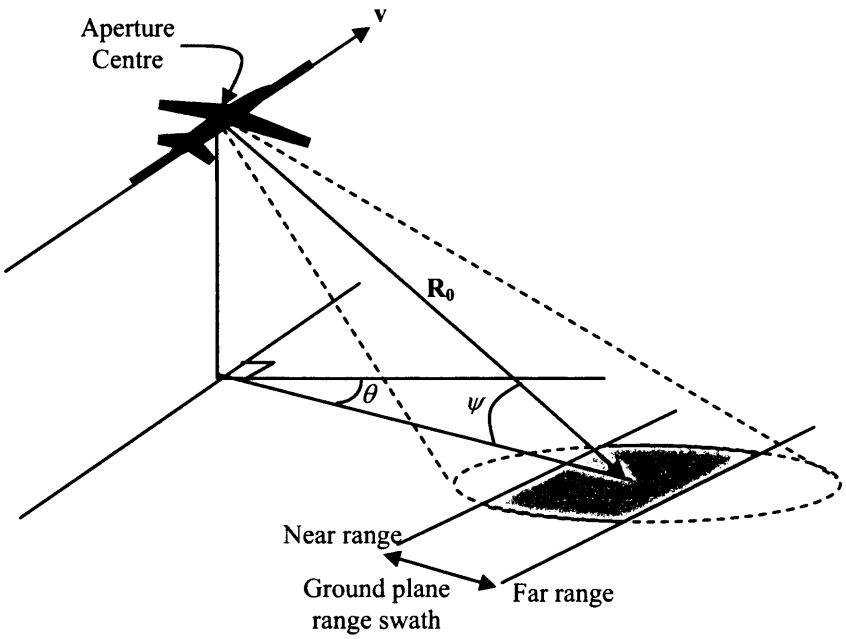

Figure 5: Definitions of ground range, near range, far range and range swath. The collection mode illustrated is spotlight.

2.1.7 SAR data collection methods

Stripmap

SAR was first developed as a sideways (or broadside) imaging sensor. In this mode, the radar illuminates a patch on the ground perpendicular to the direction of platform motion. As the platform moves, so too does the illuminated area, sweeping out a strip at constant range on the ground (Figure 6). This method of SAR data collection is now referred to as stripmap collection [1, 2]. In such a case, the time during which a point scatterer is illuminated by the swept beam determines its maximum Doppler bandwidth. A scatterer is illuminated by the radar whilst it remains within its beam width, β_a. This in turn constrains the length of the synthetic aperture to $R_0\beta_a$ which, from equations (17) and (10), limits the finest achievable resolution to

$$\rho_{az} = \frac{\lambda}{2\beta_a} = \frac{D}{1.78}. \tag{24}$$

Stripmap collection is best suited to remote sensing applications and wide areas surveillance tasks that require large coverage rates but not high azimuth resolutions.

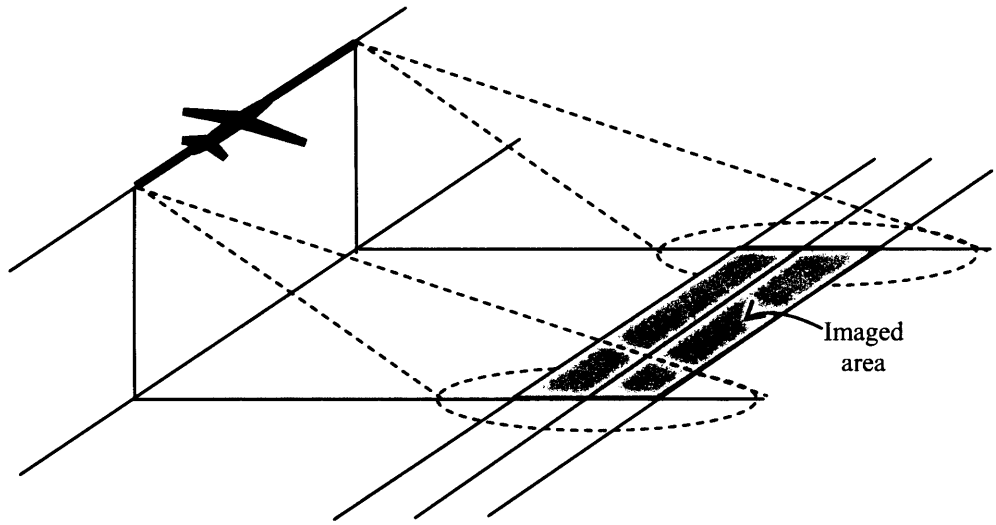

Figure 6: Broadside stripmap collection mode

Spotlight Mode

If an application requires finer azimuth resolution then, from the above argument, the obvious solution is to use a collection method which ensures the scatterer is illuminated for the maximum time possible, thus allowing the longest possible synthetic aperture to be produced. This is achieved if the antenna dwells upon a particular area on the Earth's surface (Figure 5). Such a collection is termed spotlight mode imaging [1, 2]. For broadside spotlight imaging ($\theta = 0°$), the length of aperture is $\sim R_0\Delta\theta$, where $\Delta\theta$ is the

angle in the slant plane over which the synthetic aperture is formed, so from equation (17), the azimuth resolution is given by

$$\rho_{az} = \frac{\lambda}{2\Delta\theta}. \tag{25}$$

Hence to achieve an azimuth resolution of 1m at X-band, data over an angle of 0.86° is required.

For squinted spotlight operation, from Figure 3, the length of the synthetic aperture is

$$L \approx \frac{R_0 \Delta\theta}{\cos\theta_s}, \tag{26}$$

such that the azimuth resolution is (again)

$$\rho_{az} = \frac{\lambda}{2\Delta\theta}. \tag{27}$$

Note that for both spotlight and stripmap SAR processing, the achievable azimuth resolution is independent of the platform to target range. This enables high fidelity imagery to be produced from long stand-off ranges making SAR very useful for surveillance, intelligence and remote sensing applications.

Also noteworthy, if data is collected over an angle, $\Delta\theta$, in either broadside or squinted spotlight modes the resultant SAR image has the same azimuth resolution, independent of squint angle. However, from equation (26), the greater the squint angle the longer the required synthetic aperture.

Fundamental limits on the finest achievable resolution for any given wavelength are calculable ($\rho_{az} > \lambda/4$) [2], however in practice azimuth resolution is often limited by motion compensation (MOCO) effectiveness and weighting factors designed to reduce imaging artefacts such as sidelobes.

Spotlight collection is utilised if high resolution imagery is required over specific regions, such applications include targeting and intelligence tasks. Often SAR systems will initially produce coarser resolution stripmap imagery that is subsequently analysed in order to cue a spotlight image collection over particular areas of interest.

Hybrid Mode

As its name suggests, hybrid mode is a combination of stripmap and spotlight collection modes. Essentially, the spotlight GRP is moved over the ground to provide a longer

dwell time and hence a resolution that is finer than that achievable by using the stripmap collection mode alone [7]. Certain SAR systems offer this mode yet its use it not commonplace.

Squinted SAR

Both stripmap and spotlight collection can be performed from imaging angles other then broadside (Figure 3). These, so-called, squinted collections greatly increase the utility and flexibility of SAR systems. However, as the radar is squinted further away from the broadside position, azimuth resolution is reduced [1, 2].

Multiple squinted images can be obtained from a single straight track enabling one to view the target from a range of different aspect angles. This capability is potentially very useful when imaging buildings or vehicles whose radar responses vary considerably with aspect angle (see sections 5.2.2 and 6.3). Hence, for accurate image interpretation and aided target recognition (ATR) imaging a target over a range of aspect angles is highly desirable [8]. Furthermore, where airspace restrictions are in force, the ability to squint allows a far greater coverage area than conventional broadside imaging.

Polarimetric SAR

Polarimetric radar systems are able to transmit and receive radiation in two orthogonal polarisation states. Most commonly used are linearly polarised systems, which emit and receive either horizontal, H, or vertical, V, polarisations. Hence four channels of transmit and receive combinations are formed; two co-polar channels, *HH* and *VV*, and two cross-polar channels, *HV* and *VH*. Where, for example, *HV* denotes the case when horizontally polarised radiation is transmitted and vertically polarised is received. Circularly polarised systems, which transmit and receive right and left-handed circular polarisations are also used, albeit less widely [9, 10].

Unlike conventional single channel SAR, fully polarimetric systems allow a more detailed description of the scattering behaviour of the imaged area to be obtained. For each in scene pixel one may calculate a scattering matrix, **S**, which may be used to characterise a target's response for any given transmit/receive basis.

$$\mathbf{E}^R = \begin{bmatrix} E_H^R \\ E_V^R \end{bmatrix} = \mathbf{S}\mathbf{E}^T = ce^{i\phi} \begin{bmatrix} S_{HH} & S_{VH} \\ S_{HV} & S_{VV} \end{bmatrix} \begin{bmatrix} E_H^T \\ E_V^T \end{bmatrix}, \tag{28}$$

where c is a constant amplitude for fixed range and radar cross section and ϕ a constant phase for fixed range [9, 10]. Appropriate analysis of polarimetric scattering matrices formed from the four polarimetric channels can allow the extraction of a more detailed description of the scattering behaviour and physical structure of the imaged area than by using conventional single channel SAR alone [11, 12].

Polarimetry has two main drawbacks; a fourfold increase in data storage and transfer requirements and a heavy reliance on calibration (for monostatic radars reciprocity allows $HV=VH$ resulting in a threefold increase). In order to fully exploit polarimetric radar data it is essential that an accurate polarimetric calibration be performed. In addition to magnitude, it is vital that the relative phase of each channel may be accurately calibrated, in practice this is far from trivial (see sections 3.3.1 and 6.2).

Cross-track Interferometry (InSAR)

In addition to range and azimuth information, cross-track interferometric, or 3D SAR provides a means of extracting the height of an imaged scene and, at high resolutions, height profiles of targets of interest. The process requires two images of a scene to be obtained from sensors separated by a small difference in altitude. This can be achieved in two ways. One method is to fly two separate imaging legs at slightly different altitudes (dual-pass interferometry). Alternatively, one may have a single platform with one transmit antenna and two vertically separated receive antennas, the data may then be collected simultaneously (single-pass interferometry). The two images are then co-registered and pixel height may be calculated as a function of their difference in phase [13, 14]. The resultant product is known as a digital elevation map (DEM).

Stereo SAR

Stereography is another technique for the production of DEMs. As we shall show later, areas above the focus plane of a SAR image (usually the ground plane) appear to be laid over in a direction perpendicular to the track of the imaging platform. For broadside (non-squinted) data collections, the layover is always in the range direction towards the sensor [1]. The extent of the layover is proportional to the height of the object above the focus plane.

The stereo process involves the production of two images, obtained from geometries such that the layover is different in each image. This difference is then measured, allowing an estimate of height to be made and the production of a DEM. Stereo

collection geometries are numerous [15]. Examples include; same side parallel pass, opposite side, single pass curved track and cross-track coherent stereo [16, 17].

Bistatic and Multi-static SAR

As opposed to mono-static systems which transmit and receive on the same platform, bistatic radars are able to transmit on one platform and receive on another [18, 19 and 20]. Bistatic systems are often advantageous in cases where countermeasures such as jamming or stealth technology are deployed. In the case of directional jamming, passive receive antennas cannot readily be detected and jammed. Hence, if the radar illuminating the scene is jammed, SAR imagery can still be produced. Certain stealthy targets are designed to scatter incident energy away from the radar providing the illumination, thus reducing the energy of the returned signal (for mono-static radars). Bistatic systems are therefore able to counter this problem since the receive antenna need not be collocated with the transmit antenna. In addition, it may also be possible to perform bistatic interferometry using two vertically displaced platforms.

Multi-static SAR systems, as their name suggests, are able to transmit and receive on multiple platforms. They can be operated individually such that transmission and reception occurs on the same platform or in modes that allow the reception of energy from several sources. A network of UAVs or a constellation of satellites operating multistatically offers an increased anti-stealth and counter-ECM capability together with the potential to image a target from a multitude of look angles. Such systems are therefore potentially beneficial to surveillance and targeting tasks [21].

Low Frequency SAR

Operating SAR systems at low frequencies (e.g. UHF) enables foliage penetration (FOPEN). At such frequencies, the transmitted and received radar energy is subject to far less attenuation from foliage than at shorter wavelengths such as X-band [22]. Hence even if a target is obscured by forest or jungle canopies, it may still be detectable [23, 24].

Interleaved SAR

It is also possible to produce and operate radar systems that transmit low frequency pulses that are interleaved with pulses of a different frequency, such as X-band. In this way one can produce FOPEN imagery and high resolution imagery simultaneously [25, 26].

Multiple-Beam Radars

Certain radar systems are able to radiate multiple beams. Such systems are beneficial as they allow greater collection flexibility and often a larger area coverage rate. The multiple beams may be arranged in the azimuth direction or the range direction, or both [4].

Along-track Interferometry

Along-track interferometry (ATI) is an interferometric SAR technique that can be used to measure the velocities of slow ground moving targets. The technique was developed to map ocean currents however methods have now been developed to detect discrete, moving targets in areas of interest. Two separate antennas (or phase centres) are mounted on the same platform, displaced along the direction of platform motion. The phase difference between the SAR images formed from each antenna allows an estimate of velocity to be made [27].

Table 1 summarises the advantages and disadvantages of the SAR modes discussed.

Mode	Advantages	Disadvantages	Applications
Stripmap	Wide area coverage	Coarser azimuth resolution	Mapping, wide area surveillance, target detection
Spotlight	Finest achievable azimuth resolution	Smaller ground coverage, fine MOCO requirements	Intelligence gathering, target recognition
Hybrid	Combination of fine azimuth resolution and wide area coverage	Coarser resolution than spotlight and less coverage than stripmap	Mapping, wide area surveillance
Squinted	Tasking and collection flexibility. Multiple data collects during one platform track	Some loss of azimuth resolution	Targeting, imaging within regions of denial of airspace
Polarimetric	Additional target information	Calibration often problematic. Increased no. of channels requiring more comms bandwidth	Terrain classification, target identification
Cross-track Interferometric	Height extraction (DEMs)	Constrained imaging geometries, poor performance over urban areas, computationally intensive	Mapping, intelligence gathering, height measurement for geolocation
Stereo	Height extraction (DEMs)	Constrained imaging geometries, computationally intensive	Mapping, intelligence gathering, height measurement for geolocation
Bistatic	Counter stealth, less vulnerable to jamming	Immature technology, hardware expensive	Protection of high value long standoff assets
Multi-static	Counter stealth, less vulnerable to jamming. Flexibility of tasking and collection.	Unproven technology, hardware expense	Netted systems, UAV technologies
Low frequency	Foliage penetration, counter CC&D	Often poor resolution, target recognition limited, large antenna size required, often subject to RF interference effects	Mapping earth's surface in forested areas. Detection of 'hidden targets'
Interleaved	Foliage penetration and high resolution imagery	Increased data rate requirements	Mapping earth's surface in forested areas. Detection of 'hidden targets'
Multi-beam	Increased collection flexibility	Hardware expense, reduced image size	Surveillance and real time targeting tasks
Along-track Interferometric	Measurement of slow moving targets	Requirement for two antennas, processing intensive	Mapping of ice sheets and oceanography, some MTI applications

Table 1: Summary of SAR collection modes

2.2 SAR system design considerations

Herein we present a brief discussion on the methodology behind SAR system design and how the chosen radar parameters affect potential applications.

2.2.1 Centre frequency

The choice of centre frequency for SAR systems is a critical design consideration, dependent on factors such as physical antenna size, transmitted power, antenna beam width and atmospheric attenuation. As with many radar parameters, the chosen frequency is often a compromise to meet between multiple operational requirements.

Band designation

Frequencies band designation is confused by the use of two systems. During the Second World War, the letters L, S, C, X, and K were used to define the frequency bands and this system is still used by the US IEEE. However, there also exists the NATO designation system that uses the letters A-M proposed in the 1970s. Unfortunately, the bands do not coincide and both are often used. Within the radar community the US IEEE bands remain the most commonly used, however the NATO bands are often used for electronic countermeasures purposes. Both designations are shown in Table 2.

US IEEE	Frequency/GHz	NATO Equivalent	NATO Band	Frequency/GHz	US IEEE
VHF	0.03-0.3	A, B	A	0.03-0.25	VHF
UHF/P	0.3-1	B, C	B	0.25-0.5	VHF,UHF/P
L	1-2	D	C	0.5-1	UHF/P
S	2-4	E, F	D	1-2	L
C	4-8	G, H	E	2-3	S
X	8-12	I, J	F	3-4	S
Ku	12-18	J	G	4-6	C
K	18-27	J, K	H	6-8	C
Ka	27-40	K	I	8-10	X
			J	10-20	X, Ku, K
			K	20-40	K, Ka

Table 2: Radar band designations. P-Band is 0.216-0.450GHz [28].

Antenna size

In general, the physical size of a SAR's real antenna is proportional to wavelength, hence at lower centre frequencies hardware is often large and heavy and unsuitable for platforms such as fighter aircraft and small UAVs [4].

Transmitted power

The transmit power of a SAR system dictates is maximum operating range, and therefore in many cases, for example long standoff assets such as airborne surveillance radars, high power outputs are desirable. Larger and heavier SAR systems, operating at longer wavelength, are able to generate more average power than smaller, high frequency systems [4].

Resolution

As we have shown previously in equation (24), for SAR stripmap operation the best achievable azimuth resolution is proportion to the physical length of the antenna [4]. Therefore smaller (often higher frequency) antennas are able to achieve finer azimuth resolutions. However for a spotlight collection this limitation is not present and the angle over which the aperture must be formed for a given azimuth resolution is proportional to the radars wavelength as shown in equation (25). Hence for low frequency SAR systems very large apertures must be flown. This can be problematic in terms of motion compensation and in areas with restricted airspace.

Moreover, equation (5) shows that the range resolution of a SAR is proportional to its bandwidth, which cannot be greater twice its centre frequency. Therefore in some cases, such as low frequency FOPEN SAR systems, range resolution can be limited by choice of centre frequency.

Beam width

For spotlight SAR operation, wide beam widths allow a greater ground coverage area (Figure 7). Therefore, since antenna beam width is directly proportional to the ratio of the wavelength to the width of the antenna (see equation (10)), for a given size of antenna, the lower the operating frequency the wider the ground swath. Note that in considering equation (25), unlike conventional real beam radar, a wider beam does not mean a coarser angular resolution.

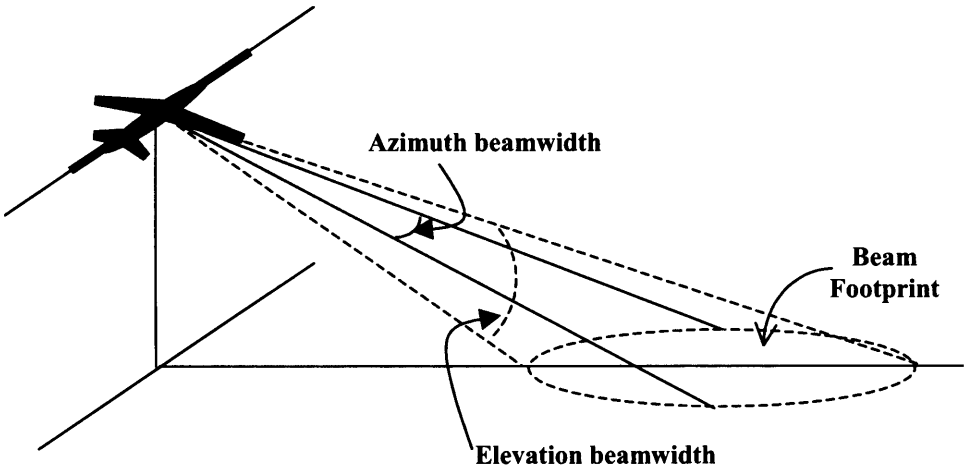

Figure 7: Diagram showing the azimuth and elevation beam widths. Also illustrating the definition of the radar's beam footprint.

Attenuation

In passing through media other than a vacuum, radio waves may be attenuated by two basic mechanisms: absorption and scattering. Both these processes are dependent on the frequency at which SAR systems are operated. Absorption is generally due to oxygen and water vapour present in the atmosphere. At X-band and below this effect is largely negligible, but above this frequency, radar performance is increasingly degraded by absorption. Scattering effects can also increase attenuation, for example at L-band and above, scattering from tree canopies and foliage is considerable. However, SARs operated with lower centre frequencies are attenuated far less and are able to penetrate such obstructions (FOPEN) [22, 23, 24].

Interference effects

The presence of electrical interference from sources external to the SAR system is also dependent on the frequency of operation. Low frequency UHF radars operate in the same frequency band as many communications and broadcasting sources and therefore experience interference as a result. Such signals can be removed from the received return, by creating 'notches' in the received frequency spectrum. However, this reduces the RF bandwidth and hence coarsens range resolution [23, 25].

Image interpretability

Choice of frequency also effects how readily SAR imagery may be interpreted. In general, the higher the centre frequency the more SAR imagery appears similar to optical imagery and is thus easier to interpret for analysts other than those trained specifically for SAR exploitation. Lower frequency imagery often contains artefacts

caused by diffraction effects and other complex mechanisms and is very difficult to interpret, even for those from a radar background.

Common SAR centre frequencies

Most SAR systems operate at X-band since atmospheric attenuation is low (though not negligible), antennas can be made relatively small (small enough even to fit in the nosecone of fighter aircraft) and finally due to the wide availability of microwave components for 10GHz radars.

2.2.2 Other SAR design considerations

As we have seen above, one radar parameter, such as centre frequency can have a large effect on the collection and operating characteristics of a SAR sensor. Similarly, the choice of additional radar system parameters, such as bandwidth and transmit power, often depends upon one or more of the other system parameters.

In the following section we describe how the choices made in the design stage of a SAR system affect its tasking capabilities and imaging performance.

Platform

The platform on which the sensor is mounted has a huge effect on its performance and potential tasking applications. SAR systems are most commonly operated from spaceborne, manned airborne and UAV (unmanned air vehicle) platforms. Table 3 summarises the relative merits of the three different platforms.

Platform	Advantages	Disadvantages	Applications	Examples
Spaceborne	Extremely long standoff. Wide area coverage. Predictable orbit: few MOCO issues and controlled imaging geometries (allowing interferometry and change detection).	Very expensive. High transmit power required. Limited retasking opportunities Constrained revisit periods. Additional communications and data transfer requirements.	Remote Sensing and mapping. Intelligence.	Radarsat-1,2 SRTM
Airborne	Long standoff. Timeliness. Retasking capability. Relatively cheap.	MOCO often problematic (especially whilst under manoeuvres). Hardware size limited for smaller aircraft.	Remote Sensing and mapping. Wide area surveillance. Air to ground targeting.	GeoSAR Ramses U2 ASTOR JSTARS F-16 PodSAR
UAVs	No humans are at risk, therefore can operate at short range. (low power). Relatively cheap.	MOCO issues. Limited ground coverage. Hardware size limitations. Often difficult to fly remotely.	Surveillance. Tactical support.	Global Hawk. Predator.

Table 3: Summary of relative merits of SAR platform type

PRF

The choice of pulse repetition frequency (PRF) for a SAR system is a compromise between a value low enough to avoid range ambiguities and high enough to avoid Doppler ambiguities. If the PRF is too high then returns from scatterers at far ranges may be received simultaneously with subsequent pulses scattered at nearer ranges. It is then not possible for the radar to discriminate between these returns and they are range ambiguous. The PRF must be low enough to prevent this happening and hence the scene width in range, W_r, is limited by

$$W_r = \frac{cT_p}{2}\cos\psi \,. \tag{29}$$

Conversely, if the PRF is lower then the Doppler bandwidth between two targets on the ground (equation (16)), then the targets are Doppler ambiguous. Stationary targets on the ground with the most positive and negative Doppler shifts occur at the leading and trailing edges of the real antenna mainlobe. Hence to prevent this, a high PRF must be chosen such that it is wider than the extent of this Doppler spread, thus constraining the azimuth scene size to

$$W_{az} = \frac{R_0 \lambda \cos^2 \theta_s}{2v} PRF . \quad (30)$$

Bandwidth and Pulse width

From equation (5), the wider the bandwidth of the transmitted pulse the finer the range resolution. For mapping applications, relatively narrow bandwidth systems (10-250MHz) may be sufficient. However for target recognition and intelligence tasks, which require fine resolution, wide bandwidths of the order of GHzs may be required.

Wide bandwidth systems do have certain disadvantages. Most problematic are hardware costs that are often prohibitively expensive. Additionally, the requirement to transmit over a wide range of frequencies means that frequency allocation can be an issue and interference effects (from both surrounding emitters and hostile ECM systems) are more likely.

If the chirp rate, γ, is constrained, then the bandwidth is dependent on the length of the transmitted pulse. In such cases, longer pulse lengths, which produce wider bandwidths, are often required to satisfy resolution specifications.

Furthermore, for radars with limited transmitted peak powers, long pulse lengths provide larger range swaths increased energy for target illumination and hence and longer maximum operating ranges. Pulse lengths are however limited by the choice of PRF, in that the pulse length can obviously not be greater than the interpulse period ($1/PRF$).

Transmit power

To allow data collection from long stand off ranges requires large transmit power. Radars with large transmit peak powers are larger and heavier then lower power systems, hence are not practical for smaller platforms such as fighter aircraft and UAVs. Although, in general high power systems are often preferable, their presence is obviously easier to detect by SIGINT equipment.

Polarisation

Most target and clutter signatures in SAR imagery are dependent on transmit polarisation, therefore the choice of operating polarisation can affect system performance. Linearly polarised systems are most commonly used, with the choice of either horizontal or vertical polarisation made dependent on specific collection requirements. Additionally, fully polarimetric systems that can transmit and receive two

orthogonal polarisations are used to obtain polarimetric data for land use classification and target recognition tasks.

Scan Type

Radars can be either mechanically scanned or E-scanned. E-scan (electronically scanned) radars use arrays which steer beams using transmit/receive elements that are phase or intensity modulated, whereas mechanically scanned radars (sometimes called M-scan) steer the beam by physically moving the direction of the radar antenna. In some systems a combination of these two approaches is used.

E-scan radars have the ability to beam steer far more quickly than conventional mechanically scanned radars and also allow the production of additional phase centres and arrays that can split to perform numerous tasks simultaneously. Mechanically scanned radars have the advantage that they are often considerable cheaper than E-scan antennas and may be swept over greater angles.

2.3 Image formation

Following the system design and the subsequent collection of the SAR data, formation of the SAR image is next stage in the SAR exploitation chain. The Fourier relationship between the collected data and the SAR image is crucial to the understanding of SAR phenomenology and will form the basis of much of this study. As such, in this section we use the tomographic approach described in [2, 3] to illustrate this relationship.

The formulation utilises the projection slice theorem, which is described as follows.

2.3.1 Projection slice theorem

Consider a 3-D complex valued function, *g(x, y, z)*, and its Fourier transform, *G(X, Y, Z)*, defined as

$$G(X,Y,Z) = \int_{-\infty}^{\infty}\int_{-\infty}^{\infty}\int_{-\infty}^{\infty} g(x,y,z)e^{-j(xX+yY+zZ)}dxdydz. \tag{31}$$

The function *g(x, y, z)* may be projected onto the *x*-axis in the *(x, y, z)* space by integrating over the *(y, z)* plane along this axis. Its 1-D projection function is thus given by

$$p_1(x) = \int_{-\infty}^{\infty}\int_{-\infty}^{\infty} g(x,y,z)dydz. \tag{32}$$

the Fourier transform of which is then

$$P_1(X) = \int_{-\infty}^{\infty} p_1(x)e^{-jxX}dx = G(X,0,0), \tag{33}$$

which is the 1-D projection of the Fourier transform of *g(x, y, z)* along the corresponding axis, *X*, in the Fourier space *(X, Y, Z)*.

The projection slice theorem is the generalisation of this result where *g(x, y, z)* is projected onto the line, *u*, where *u* is part of the rotated coordinate system *(u, v, w)* defined by the rotation angles θ and ψ (see Figure 8) [2].The projection of *g(x, y, z)* onto *u* is then given by integrating over the *(v, w)* plane along *u* such that

$$p_{\theta,\psi}(u) = \int_{-\infty}^{\infty}\int_{-\infty}^{\infty} g[x(u,v,w), y(u,v,w), z(u,v,w)]dvdw, \tag{34}$$

with the corresponding Fourier transform

$$P_{\theta,\psi}(U) = \int_{-\infty}^{\infty} p_{\theta,\psi}(u) e^{-juU}\, du = G(U). \tag{35}$$

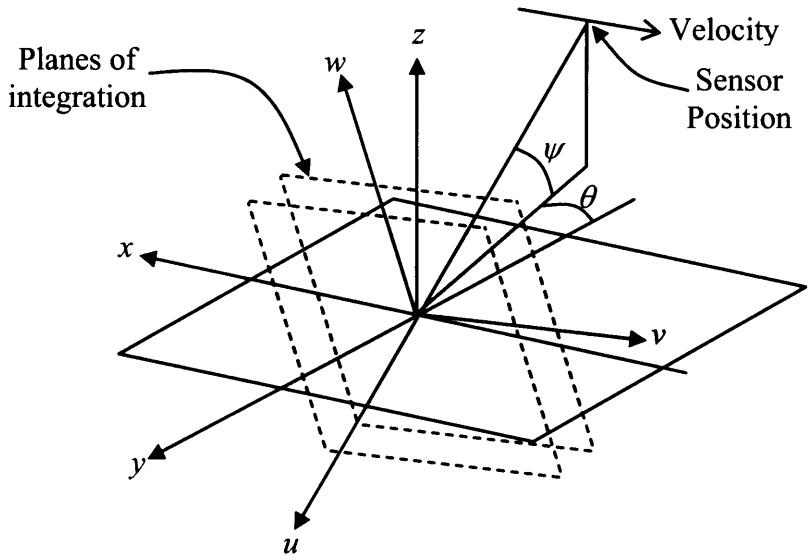

Figure 8: Diagram defining imaging geometry and ground and integration planes [2]

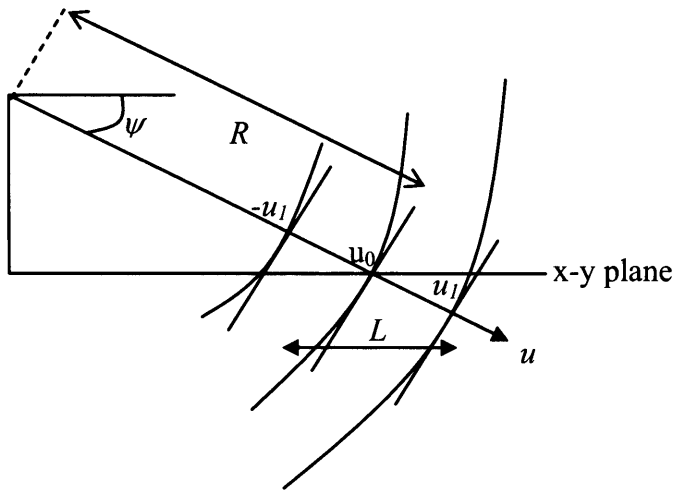

Figure 9: Diagram defining R and u_0 [2].

2.3.2 Narrowband reconstruction of scene reflectivity

For the spotlight SAR imaging process, we define *g(x, y, z)* as the 3-D complex radar reflectivity function of the imaged scene. The form of *g(x, y, z)* is constrained by the following conditions [2]:

- *g(x, y, z)* = 0 except on the finite surface that is being illuminated by spotlight radar collection
- *g(x, y, z)* = 0 in regions of radar shadow
- *g(x, y, z)* is constant over the range of aspect angles and chirped frequencies used to form the image (we shall investigate later how the validity of this assumption can be investigated).

The angles θ and ψ are the azimuth and grazing angles associated with the spotlight collection geometry shown in Figure 5. The radar transmits and receives a pulse along the u-axis where the set of coordinates *(u, v, w)* are obtained by a rotation of (θ, ψ) of the *(x, y, z)* axis as shown in Figure 8. The range to scene centre is *R* and the illuminated slant range swath along *u* covers the region $-u_1$ to u_1 as shown in Figure 9.

Following the previous discussion regarding range resolution, a transmitted pulse with an FM chirp may be described as $\mathrm{Re}\{s(t)\}$ where (from equation (7))

$$s(t) = \begin{cases} e^{j\left[2\pi f_c t + \pi\gamma t^2\right]} & |t| \le T_p/2 \\ 0 & |t| > T_p/2 \end{cases}. \tag{36}$$

Defining $\omega_0 = 2\pi f_c$ and $\alpha = \pi\gamma$ we can rewrite (36) as

$$s(t) = \begin{cases} e^{j\left[\omega_0 t + \alpha t^2\right]} & |t| \le T_p/2 \\ 0 & |t| > T_p/2 \end{cases}. \tag{37}$$

If the standoff range, is sufficiently large so that, $R >> u_1$, then the planar wavefront approximation is valid [3] and we can assume that the return from a differential region along the *u*-axis, u_0, is equal to sum of all the contributions of *g(x, y, z,)* on the *v*-*w* plane with $u = u_0$. Therefore, the returned signal received at (θ, ψ) is given by

$$r0_{\theta,\psi}(t) = A\,\mathrm{Re}\left\{ p_{\theta,\psi}(u_0)\, s\left(t - \frac{2(R+u_0)}{c} \right) \right\} du, \tag{38}$$

where $p_{\theta,\psi}(u_0)$ is defined as in equation (34) and A is a scale factor accounting for propagation and other effects. If A is considered constant then by superposition, the return from the illuminated patch is given by the integral

$$r_{\theta,\psi}(t) = A\,\mathrm{Re}\left\{\int_{-u_1}^{u_1} p_{\theta,\psi}(u_0)\, s\left(t - \frac{2(R+u)}{c}\right) du\right\}, \tag{39}$$

where

$$\frac{-T_p}{2} + \frac{2(R + L\cos\psi)}{c} \le t \le \frac{T_p}{2} + \frac{2(R - L\cos\psi)}{c}. \tag{40}$$

The first stage of SAR processing is the demodulation of the received pulse. Here we use the de-chirp approach which begins with the mixing (or multiplication) of the received signal with a reference signal which replicates the signal that is received by a point scatterer at the scene centre. This reference signal is

$$r_{ref}(t) = \mathrm{Re}\{s(t - \tau_0)\}, \tag{41}$$

where $\tau_0 = \dfrac{2R}{c}$. Thus the result of the mixing process is

$$\bar{r}_{\theta,\psi}(t) = \frac{A}{2}\mathrm{Re}\left\{\int_{-u_1}^{u_1} p_{\theta,\psi}(u)\left[e^{\left\{j\left[\omega_0\left(2t-\frac{2u}{c}-\tau_0\right)+\alpha\left((t-\tau_0)^2+\left(t-\tau_0-\frac{2u}{c}\right)^2\right)\right]\right\}} + e^{\left\{j\left[\frac{4\alpha u^2}{c^2}-\frac{2u}{c}(\omega_0+2\alpha(t-\tau_0))\right]\right\}}\right] du\right\} \tag{42}$$

where we have used equations (39) and (41) and the trigonometric identity $\cos a\cos b = \dfrac{1}{2}[\cos(a-b)+\cos(a-b)]$. The first term is centred on twice the carrier frequency, whereas the second is centred on baseband. We may low pass filter to remove the first term such that

$$\hat{r}_{\theta,\psi}(t) = \frac{A}{2}\mathrm{Re}\left\{\int_{-u_1}^{u_1} p_{\theta,\psi}(u)\left[e^{\left\{j\left[\frac{4\alpha u^2}{c^2}-\frac{2u}{c}(\omega_0+2\alpha(t-\tau_0))\right]\right\}}\right] du\right\}. \tag{43}$$

If we mix $r_{\theta,\psi}(t)$ with $\mathrm{Im}\{s(t-\tau_0)\}$, low pass filter and use $\cos a\sin b = \dfrac{1}{2}[\sin(a-b)+\sin(a-b)]$ we obtain the quadrature component

$$\tilde{r}_{\theta,\psi}(t) = \frac{A}{2}\mathrm{Im}\left\{\int_{-u_1}^{u_1} p_{\theta,\psi}(u)\left[e^{\left\{j\left[\frac{4\alpha u^2}{c^2}-\frac{2u}{c}(\omega_0+2\alpha(t-\tau_0))\right]\right\}}\right]du\right\}. \tag{44}$$

The I and Q components are then combined to form

$$\bar{r}_{\theta,\psi}(t) = \hat{r}_{\theta,\psi}(t) + \tilde{r}_{\theta,\psi}(t) = \frac{A}{2}\left\{\int_{-u_1}^{u_1} p_{\theta,\psi}(u)\left[e^{\left\{j\left[\frac{4\alpha u^2}{c^2}-\frac{2u}{c}(\omega_0+2\alpha(t-\tau_0))\right]\right\}}\right]du\right\}, \tag{45}$$

which, when the residual video phase (RVP) term, $\frac{4\alpha u^2}{c^2}$, (which is small for most SAR systems) is neglected [1] we then obtain

$$\bar{r}_{\theta,\psi}(t) \approx \frac{A}{2}\left\{P_{\theta,\psi}\left[\frac{2}{c}(\omega_0 + 2\alpha(t-\tau_0)\right]\right\}, \tag{46}$$

where $P_{\theta,\psi}(U)$ is given by equation (35). Since t is bounded as described in (40) then the bounds of U (also known as the region of support) are then

$$\frac{2}{c}\left(\omega_0 - \alpha T_p + \frac{4\alpha L\cos\psi}{c}\right) \le U \le \frac{2}{c}\left(\omega_0 + \alpha T_p - \frac{4\alpha L\cos\psi}{c}\right). \tag{47}$$

The Fourier domain in which U is defined is often termed the spatial frequency domain.

From Figure 9 the patch propagation time is the two way time delay between target at $-u_1$ and u_1 and is equal to

$$\tau_p = \frac{4L\cos\psi}{c}, \tag{48}$$

such that (46) and (47) become

$$\bar{r}_{\theta,\psi}(t) \approx \frac{A}{2}\left\{P_{\theta,\psi}(U)\right\}, \tag{49}$$

where

$$\frac{2}{c}\left(\omega_0 - \alpha(T_p - \tau_p)\right) \le U \le \frac{2}{c}\left(\omega_0 - \alpha(T_p + \tau_p)\right). \tag{50}$$

Therefore, the deramped received signal, $\bar{r}_{\theta,\psi}(t)$, represents a projection of the ground reflectivity function's Fourier transform, *G(X, Y, Z)*, along the line described by the angles θ and ψ. This is a key result, which states that the Fourier transform of

$\bar{r}_{\theta,\psi}(t)$ will produce a narrow band reconstruction of the ground reflectivity function *g(x, y, z)* along the same line in real space.

Note that most SAR sytems operate with a pulse length $T_p >> \tau_p$ such that the region of support can be approximated by

$$\frac{2}{c}(\omega_0 - \alpha T_p) \leq U \leq \frac{2}{c}(\omega_0 + \alpha T_p). \tag{51}$$

Or alternatively,

$$\frac{4\pi}{\lambda} - \frac{2}{c}(2\pi B_e) \leq U \leq \frac{4\pi}{\lambda} + \frac{2}{c}(2\pi B_e), \tag{52}$$

where B_e is the effective chirp bandwidth described in (4).

2.3.3 Tomographic spotlight SAR characteristics

To this point we have only considered collection of a single line described by the angles θ and ψ. However, if the sensor is moving and dwells upon a point on the *x, y*-plane (spotlight mode), then each pulse will describe a line in the spatial frequency domain which in turn will describe a collection surface. If the sensor follows a straight line path then the collection surface will be planar, this is the slant plane as defined in (23). Defining the axis, Y', as the centre pulse line, the orthogonal axis X' describes the slant plane

(X', Y'). If the sensor collects data over an angular region, $\Delta\theta$, then the collected data forms an annulus as shown in Figure 10 and Figure 11. The annulus is offset from the origin by an amount, $Y_0' = \frac{4\pi}{\lambda}$.

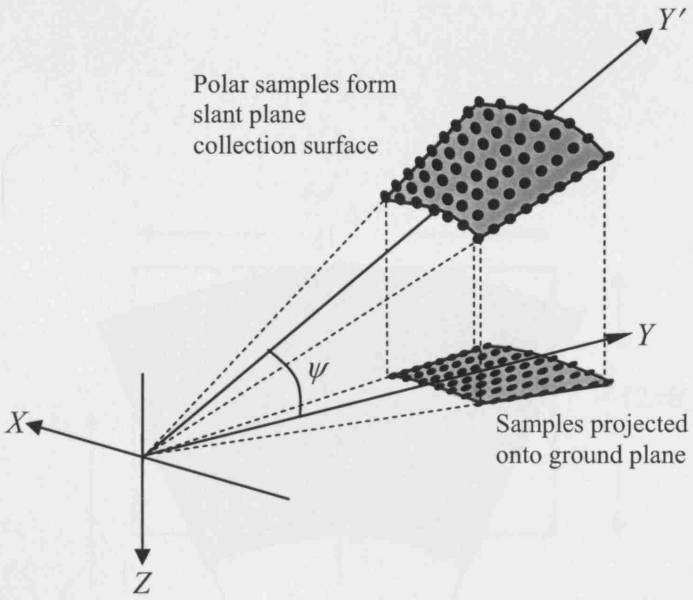

Figure 10: Straight line sensor track with polar samples forms a slant plane collection surface which can be projected onto the ground plane [2]

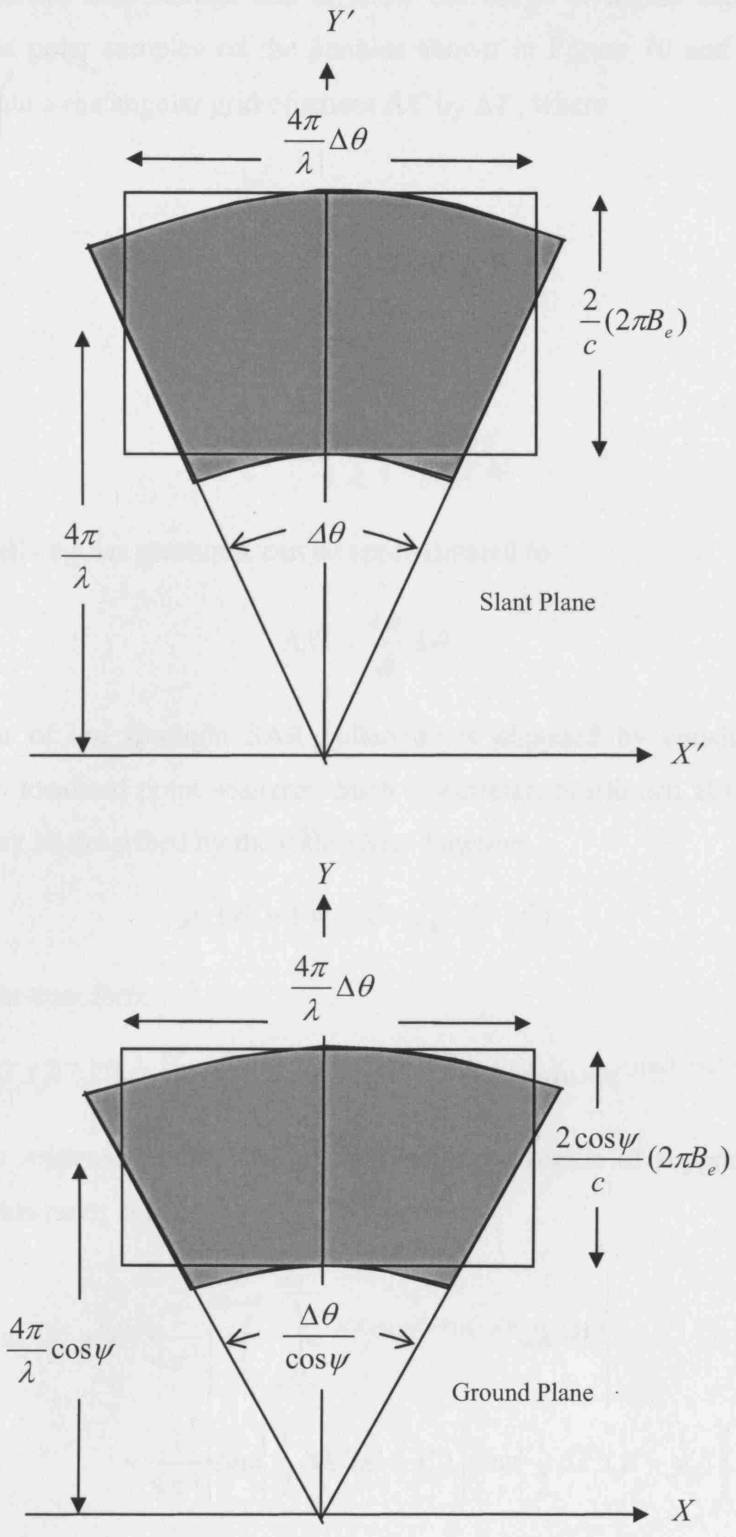

Figure 11: Slant plane support and result of projection onto the ground plane [2]

To enable efficient data storage and to allow the usage of digital signal processing techniques, the polar samples on the annulus shown in Figure 10 and Figure 11 are interpolated onto a rectangular grid of extent $\Delta X'$ by $\Delta Y'$, where

from (52),

$$\Delta Y' = \frac{2}{c}(2\pi B_e), \tag{53}$$

and

$$\Delta X' = 2\left(\frac{4\pi}{\lambda}\right)\sin(\Delta\theta/2), \tag{54}$$

which, for small angular apertures, can be approximated to

$$\Delta X' = \frac{4\pi}{\lambda}\Delta\theta. \tag{55}$$

The resolution of the spotlight SAR collection is obtained by consideration of its response to an idealised point scatterer. Such a scatterer, positioned at (x_0', y_0') on the slant plane, may be described by the reflectivity function

$$g_p(x', y') = \delta(x' - x_0', y' - y_0'), \tag{56}$$

with the Fourier transform

$$G_p(X', Y') = \iint \delta(x' - x_0', y' - y_0') e^{-j(x'X' + y'Y')} dxdy = e^{-j(x_0'X' + y_0'Y')}. \tag{57}$$

The amplitude response of the SAR system (with the region of support described in Figure 11) to this point is then

$$\begin{aligned} g_p(x', y') &= \frac{1}{4\pi^2}\left|\int_{Y_0'}^{Y_0'+\Delta Y'}\int_{-\frac{\Delta X'}{2}}^{\frac{\Delta X'}{2}} e^{-j(X'(x_0'-x')+Y(y_0'-y'))} dX'dY'\right| \\ &= \frac{1}{4\pi^2}\left|\operatorname{sinc}\left[\frac{1}{2}\Delta X'(x' - x_0')\right]\operatorname{sinc}\left[\frac{1}{2}\Delta Y'(y' - y_0')\right]\right| \end{aligned} \tag{58}$$

If we use the zero crossing points of the sinc (which occur at $x' - x_0' = 2\pi / \Delta X'$ and $y' - y_0' = 2\pi / \Delta Y'$) as estimates for the system resolution then we obtain

$$\rho_{x'} = \frac{2\pi}{\Delta X'} = \frac{\lambda}{2\Delta\theta}$$
$$\rho_{y'} = \frac{2\pi}{\Delta Y'} = \frac{c}{2B_e} \quad , \tag{59}$$

which is consistent with our previous approach (equations (9) and (25)).

2.3.4 Spotlight SAR reconstruction of an imaged surface

Recalling our definition of the complex reflectivity function *g(x, y, z)*, which is taken to be zero except on the finite surface that is being illuminated by spotlight radar collection, we can use the model [2]

$$g(x,y,z) = r(x,y)\delta(z - h(x,y)), \tag{60}$$

where *r(x, y)* is a surface reflectivity density with ground co-ordinates *(x, y)*, *h(x, y)* is the terrain height at the same point and δ is the Dirac delta function. Using (31) the Fourier transform of *g(x, y, z)* is then

$$\begin{aligned} G(X,Y,Z) &= \iiint r(x,y)\delta(z - h(x,y))e^{-j(xX+yY+zZ)}dxdydz \\ &= \iint r(x,y)e^{-jZh(x,y)}e^{-j(xX+yY)}dxdy \end{aligned} \quad . \tag{61}$$

If our slant plane passes through the origin of *(X, Y, Z)* it may be described by the equation

$$Z = \alpha X + \beta Y \, , \tag{62}$$

where α and β are defined by the collection angles θ and ψ (as in Figure 8), which are given by

$$\begin{aligned} \alpha &= \tan\theta\tan\psi = \tan\eta \\ \beta &= \tan\psi \end{aligned} \quad , \tag{63}$$

and we introduce the angle, η, which is the angle between the slant plane and ground plane in the direction of *x*-axis (Figure 12). Note that following the approach in [2], we have redefined the direction of the *y*-axis to be from the GRP to the sensor. Equation (61) then becomes

$$G_0(X,Y) = \iint r(x,y)e^{-j(\alpha X+\beta Y)h(x,y)}e^{-j(xX+yY)}dxdy \, . \tag{64}$$

$G_0(X, Y)$ is then the Fourier reconstruction of the surface reflectivity function in terms of the ground plane spatial frequencies *X* and *Y*. As discussed earlier, the region of support as shown in Figure 11, is defined by the angle over which the data is collected, $\Delta\theta$, the

grazing angle, ψ, and the radar's bandwidth and centre frequency. This region of support is offset from the origin of (X, Y) in the Y direction by $Y_0 = \frac{4\pi}{\lambda}\cos\psi$. Spotlight SAR processing takes place using this offset data, $G_1(X, Y)$, where

$$\begin{aligned} G_1(X,Y) = G_0(X,Y+Y_0) &= \iint r(x,y)e^{-j(\alpha X+\beta(Y+Y_0))h(x,y)}e^{-j(xX+y(Y+Y_0))}dxdy \\ &= \iint r_1(x,y)e^{-j(\alpha X+\beta Y)h(x,y)}e^{-j(xX+yY)}dxdy \end{aligned} \quad (65)$$

where we have defined

$$r_1(x,y) = r(x,y)e^{-j\beta Y_0 h(x,y)}e^{-jyY_0}. \quad (66)$$

The inverse Fourier transform of $G_1(X, Y)$ is the reconstructed image

$$\begin{aligned} g_1(x,y) &= \iint G_1(X,Y)e^{j(xX+yY)}dXdY \\ &= \iint_A \left\{\iint r_1(\tilde{x},\tilde{y})e^{-j(\alpha X+\beta Y)h(\tilde{x},\tilde{y})}e^{-j(\tilde{x}X+\tilde{y}Y)}d\tilde{x}d\tilde{y}\right\}e^{j(xX+yY)}dXdY \\ &= \iint\left[\iint_A e^{j[X(-\alpha h(\tilde{x},\tilde{y})-\tilde{x}+x)+Y(-\beta h(\tilde{x},\tilde{y})-\tilde{y}+y)]}dXdY\right]r_1(\tilde{x},\tilde{y})d\tilde{x}d\tilde{y} \end{aligned} \quad (67)$$

where the inverse Fourier transform integral is performed over the area A which is $G_1(X, Y)$'s region of support interpolated onto a rectangle of size ΔX by ΔY (as shown in Figure 11) where

$$\begin{aligned} \Delta X &= \frac{4\pi}{\lambda}\Delta\theta \\ \Delta Y &= \frac{2}{c}\cos\psi(2\pi B_e) \end{aligned} \quad (68)$$

The innermost double integral in (68) evaluated over A is the sinc function, $s_A(x, y)$, such that

$$g_1(x,y) = \iint s_A(-\alpha h(\tilde{x},\tilde{y}) - \tilde{x} + x, -\beta h(\tilde{x},\tilde{y}) - \tilde{y} + y)r_1(\tilde{x},\tilde{y})d\tilde{x}d\tilde{y} \quad (69)$$

with the sinc function

$$s_A = \Delta X\Delta Y \operatorname{sinc}\left(\frac{x\Delta X}{2\pi}\right)\operatorname{sinc}\left(\frac{y\Delta Y}{2\pi}\right). \quad (70)$$

If terrain height, $h(x, y)$, is a slowly varying function within the area illuminated then (70) may be thought of as the convolution

$$
\begin{aligned}
g_1(x+\alpha h(x,y), y+\beta h(x,y)) &= \iint s_A(x-\tilde{x}, y-\tilde{y}) r_1(\tilde{x},\tilde{y}) d\tilde{x} d\tilde{y} \\
&= s_A(x,y) \otimes r_1(x,y) \\
&= s_A(x,y) \otimes \left[r(x,y) e^{-j\beta Y_0 h(x,y)} e^{-jyY_0} \right]
\end{aligned}
\quad . \tag{71}
$$

The role of terrain height, $h(x, y)$, in Equation (71) will be important for later chapters. Imaging a flat scene with $h(x, y) = 0$ will result in a convolution of the reflectivity function $r(x, y)$ with the sinc function $s_A(x, y)$. Essentially the image $g_1(x, y)$, will then be a narrowband reconstruction of the reflectivity function $r(x, y)$ using the region of support A.

However, for non-planar surfaces there will be an additional phase term $\beta Y_0 h(x,y)$, which is exploited in interferometry as we will discuss later. Furthermore, a scatterer in the scene at a point (x, y) will appear in the reconstructed image at a point $(x+\alpha h(x,y), y+\beta h(x,y)) \equiv (x+\Delta x, y+\Delta y))$ where

$$
\begin{aligned}
\Delta x &= \alpha h(x,y) = \tan\eta h(x,y) = \tan\psi \tan\theta h(x,y) \\
\Delta y &= \beta h(x,y) \mathrm{s} = \tan\psi h(x,y)
\end{aligned}
\quad . \tag{72}
$$

The quantities Δx and Δy describe the translational shift due to the layover effect [16, 17] and are exploited in stereography as we will see later. Figure 12 shows the extent and direction of layover for an object of height h. The direction of this layover is always perpendicular to the sensor's velocity vector.

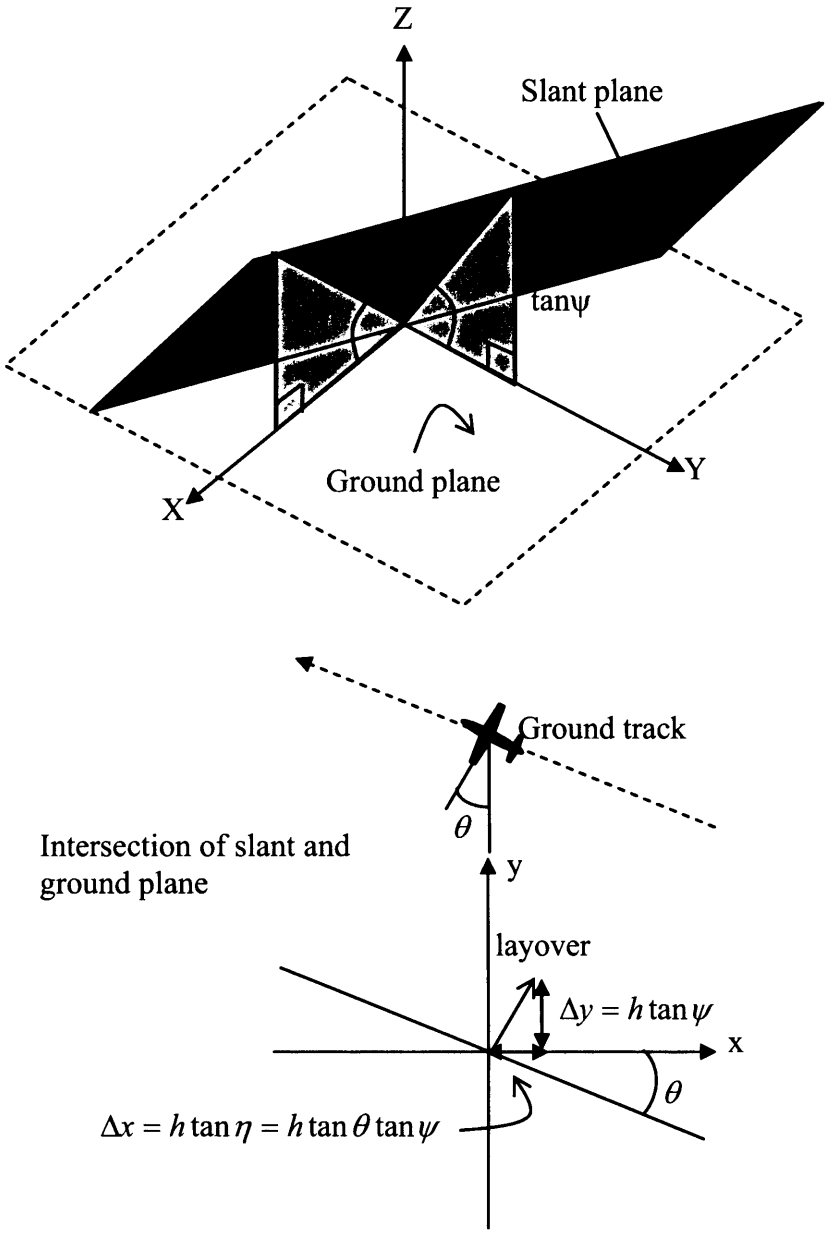

Figure 12: Geometry of slant plane defining ψ and η and associated layover for an object at the origin with height h [16].

2.3.5 Motion compensation (MOCO)

The previous description of the SAR imaging process assumed that the motion of the platform was perfectly straight and level and at a constant speed. However, particularly for airborne SAR systems, this is unachievable and systems must either correct for motion changes in flight, or accurately measure and record the position of the sensor's Antenna Phase Centre (APC) to enable motion compensation to be performed post data collection.

As the SAR process is sensitive to small errors in phase, MOCO systems must account for very small perturbations from the desired platform track and potential vibrational effects [1]. Additionally, such errors must be overcome during very long synthetic apertures for high resolution and low frequency systems. For example the X-band example stated earlier would require an effective MOCO solution over an aperture length of 1500m and a 10° error in phase would equate to APC positional errors as small as only ~1mm. Any uncompensated errors will manifest themselves as increased sidelobe levels and degraded image resolution.

Most airborne SAR MOCO systems have both an inertial measurement unit (IMU) and a global positioning system (GPS). Additional inertial navigation systems (INS) are used primarily for aircraft navigation, however, in some cases are used to assist in the flying of the desired flight path, setting the correct range gate and antenna pointing. The IMU, which is comprised of accelerometers or gyros, is usually rigidly connected to the APC. The GPS is often positioned elsewhere. The position of the APC is recorded by measuring the position of the platform using the GPS and measuring the vector between the GPS and the IMU thus accounting for the pitch, roll and yaw of the aircraft.

The MOCO system allows adjustments to the beam steering, range gate timings and the reference signal (used in the range compression process). After the motion compensation many SAR systems use autofocus techniques which use properties of the returned signal to further improve the MOCO solution and can often account for drift within the GPS and IMU measurements.

Note that spaceborne SAR satellites have more deterministic orbits and suffer less from vibrational effects and hence do not generally require MOCO.

3 Review of relevant research

The aim of this section is to describe and discuss relevant previous research and hence set a benchmark for the tasks considered in this thesis; building height extraction, urban SAR exploitation and polarimetric assisted target recognition. Below we review previous and current research on these three topics.

3.1 Building heights from SAR imagery

SAR imaging of urban areas has recently taken on increased significance for both military and civilian applications. From a military standpoint, effective mapping and modelling of urban environments is a crucial component of mission planning. To aid the identification of structures within the area of interest or to enable an accurate model of the urban area to be produced, the extraction of the heights of buildings within the scene is of obvious benefit.

The use of radar to obtain topological height data for wide area, low resolution terrain mapping applications is well understood [4, 14]. Previously, much research into height extraction from SAR imagery has been focused on the study of rural scenes. However, the extraction of high resolution terrain information over urban areas is more problematic. In this section, we describe and discuss previous research on this subject. Additionally, we describe work on the use of stereo techniques for terrain extraction that are potentially useful for imaging urban areas.

3.1.1 Building heights from InSAR data

Historically, the extraction of height information for remote sensing applications has been performed using interferometric SAR. Although originally developed for the production of coarse resolution models over low relief terrain, many recent research initiatives have attempted to apply the technique to extract height information over urban areas.

For example, in [29] Gamba and Houshmand attempt to find the height of building roofs by using interferometric SAR data obtained from the NASA/JPL AIRSAR (TOPSAR) system. Their approach is to apply machine vision segmentation algorithms to interferometric data in order to find the planes that are assumed to represent the roofs of each building. Rather than using a pixel-to-pixel segmentation algorithm, to reduce computational cost the algorithm works on scan lines (a function associated with the surface along a particular line of the image). Segments with the same scan line function (subject to a noise defined threshold) are grouped as belonging to the same surface. In

[29] only planar surfaces are considered, so the functional form of the scan lines is linear. A region growing stage is then performed which assesses whether segments belong to a single plane by comparing the slopes and intercept of neighbouring segments. Without supporting arguments, in [29] the approach then approximates each plane with a horizontal plane. In this step a large amount of information is lost and the analysis is thus restricted to structures with flat roofs only.

A limited number of experimental results from large, flat roofed, high-rise buildings are presented. From such results, a mean height error of 2.2m is calculated by comparison with ground truth. However, measurements of the area of each building are very inaccurate, with results greatly underestimating the actual area. Little explanation is given for this discrepancy in [29]. Additionally, it is suggested that the algorithm is not well suited for use over wide areas.

The approach rather blindly uses an image segmentation algorithm upon elevation data without much appreciation of the characteristics of both the data and the system used to produce it. The differences between elevation data produced by SAR interferometry, LIDAR and photogrammetry are numerous and as a result, subsequent analysis is required to account for such differences.

In addition to the exploitation of the AIRSAR system, which in the trial described above was operated at C-band (but may also be operated at L and P-band), Gamba and Houshmand have also applied interferometric techniques to X-band data. In [30] the interferometric SAR performance of the C-band AIRSAR and X-band Intermap Star-3i systems are compared over the same urban area in Los Angeles. AIRSAR is able to produce digital elevation models (DEM) with height accuracies of up to 2.5m with 5m post-spacing, whereas the Intermap system can produce DEMs with height accuracies of up to 1.5m with 2.5m post-spacing.

In this study the objective is to calculate the underlying bald Earth height information (termed here as the digital terrain model, DTM) and the heights of the buildings above this surface (described as the digital surface model, DSM). The first stage of the process is the generation of the DTM from the DEM produced by the interferometric data. Three approaches are described in [30]; low pass filtering of the DEM (essentially discarding height changes above a certain threshold), morphological filtering (an erosion and dilation technique commonly used with LIDAR data) and a combination of two (first applying the morphological filtering and then the low pass filtering). The low-pass filtering is shown to 'over smooth' the DTM and results in an over-estimation of

the underlying terrain height. The morphological filtering produces a more accurate but noisier DTM and hence the third method is seen as good combination of the two methods. The building height estimation is performed by firstly applying the segmentation technique to the DEM described in [29] and then subtracting the DTM to leave the DSM.

Using both the C- and X-band systems the UCLA campus was imaged and results of the three approaches are compared with CAD model data accurate to the order of centimetres. Unfortunately, as the two collections were from different geometries, it is difficult to compare the performance of the two operating systems. The problem of phase discontinuities resulting from the phase unwrapping process is briefly discussed in [29], however evidence of such an effect was not found in the data sets in question (this was potentially due to the coarseness of the post-spacing used). Analysis of the DTMs produced showed that the combination technique produced the best results for both the C- and X-band data. Building extraction from the resulting DSMs was performed by photo-interpretation (this requires additional imagery and a degree of *a priori* knowledge and is therefore not the ideal approach). Perhaps surprisingly (given the resolution differences between the two bands) the building height information of the C- and X-band derived DSMs were broadly comparable. However, the shape and extent of the buildings were more accurately reproduced by the X-band system.

In both [29] and [30] only InSAR data is used to generate height information. In areas where the correlation between the two InSAR channels is poor (for example in shadow regions) phase noise will introduce errors into the height measurements. Phase smoothing can be used to reduce noise levels, unfortunately resulting in the loss of important height information at building edges. In [31] Soergel et al investigate the use of interferometric data in combination with the intensity SAR image in an attempt to improve the accuracy of building height information. Soergel's approach is to use the segmented intensity image to weight the phase derived height information over urban areas.

Firstly, a pre-processing stage involving a de-speckle filter is applied to the intensity image. This is followed by the segmentation stage, which uses an adaptive region growing algorithm. Segments with average intensity levels below a given threshold are masked. In the next step, height is smoothed by taking an intensity weighted mean over each segment. A post-processing stage is then applied which accounts for segments

containing shadow regions (this occurs in segments where two closed areas of height data can be formed).

The technique is applied to data obtained at X-band with an effective interferometric baseline of 1m, and a ground resolution of 1m in range and azimuth. The area imaged was Frankfurt airport. Several tie points with known height information were identified in the intensity image and it was found that the interferometrically derived DEM contained an offset (due to inaccurate navigation data) of 8m. After the appropriate correction, the height information of the largest buildings was found to be correct to an accuracy of around 2m. However, other smaller buildings were only accurate to approximately 5m.

The concept behind the smoothing technique is not clearly explained in [31]. It appears to render the resultant 3D model more visually appealing yet its effect on the accuracy of the height information is not discussed. Additionally, the technique is limited to flat roofed buildings.

In [32] Stilla et al again utilise phase and intensity information of interferometric SAR data as described above but coherence is also used in the segmentation process. Buildings are assumed to be flat roofed and to appear as right-angled structures in the SAR imagery. The procedure is the same as in [31], but in this case, the height information is weighted by coherency rather than intensity therefore allowing height information from areas with low coherency (such as roads and shadows) to be disregarded as unreliable. The technique is applied to data collected over Frankfurt airport with the AER-II FGAN SAR sensor. Imagery and building height models are shown, but accuracies are not discussed. It is noted that the level of detail of the building height model is not comparable with that obtained by LIDAR techniques.

A brief discussion regarding the limitations of building reconstruction with InSAR is presented. It is shown that if the height of the building, $h = w\tan(90-\psi)$, where, w, is its width and, ψ, the collection grazing angle, then no radar returns are available from the building roof alone and hence InSAR height measurements over such regions are unreliable. The optimal imaging geometries would therefore be shallow grazing angle collections, were it not the case that such geometries would give rise to large areas of occultation due to radar shadowing, particular in dense urban areas. Using LIDAR data of an urban area in Karlsruhe, these areas of layover are predicted.

The analysis of the limitations of urban InSAR techniques is very useful. However, the approach is limited to flat root buildings and (although it is not explicitly stated in [32]) only valid for broadside (non-squinted) SAR collections.

In [33] Tison et al approach the problem of building height measurement in a similar manner to Gamba and Soergel, in that a 3D model is generated based upon the output of a classification algorithm. The inputs to the algorithm are the amplitude, interferogram and the coherence data sets obtained from an InSAR sensor. The technique aims to jointly retrieve height information and class information using a Markovian fusion scheme. Six inputs to the Markovian framework are derived from three pattern recognition operators (classification, filtering and structure extraction). Unfortunately, [33] does not explain the characteristics of these individual operators and their classification performance in detail. Interpretation of these results is therefore difficult. It appears that the scheme requires a degree of manual parameter optimisation before it yields satisfactory results.

The fusion scheme is applied to data from the ONERA RAMSES X-band sensor operating over Dunkirk. The results show a visual improvement of the 3D building models. The limited availability of ground truth enabled an RMS height error of around 2.5m to be estimated for the largest buildings within the scene. The RAMSES system's spatial resolution and interferometric height accuracy were too coarse to enable the extraction of smaller residential buildings.

In all the research described above the scene of interest is imaged from only one aspect angle. In [34] Bolter and Leberl investigate the potential increase in performance that can be obtained by the processing of multiple view interferometric SAR data. Bolter and Leberl use interferometric data obtained from the Sandia Spotlight SAR System to generate 3D models of buildings. The test site used was the McKenna MOUT site, Ft. Benning, GA and interferometric data was obtained from four cardinal viewing angles.

The method firstly involves separation of buildings from other objects within the scene. The effects of shadowing and layover are minimised by taking the maximum height from each of the four data collections for each pixel within the scene (presumably some image registration was performed in order to ensure that the pixel's spatial position is common in each image). This technique allows even small buildings to be measured. Noise on the height measurements is then reduced by application of a 3x3 pixel median filter. The resultant image is then used to distinguish between objects above the terrain surface and bare earth to produce a binary mask containing areas of interest. These areas

are then restored to the original resolution. The next step involves the use of texture measures to differentiate between buildings and other objects within the scene (when compared to areas of vegetation, buildings generally have a higher mean coherency and a lower height standard deviation). The final stage is the fitting of the height data to either a flat roofed rectangular building model or a gabled roof rectangular building model.

The results show that height extraction of buildings is relatively successfully (RMS errors ±2.18m) but extraction of area coverage is less accurate due to problems segmenting the imagery. The discrimination between flat roof and gabled roof buildings was only incorrect in the case of one building in the sample set of 15. The technique of using more than one imaging angle is of obvious benefit. However the automated extraction, particularly the segmentation stage, is not currently robust.

3.1.2 Building heights from shadow analysis

Due to problems with phase noise in regions of shadow, InSAR techniques can yield unreliable height information over urban areas. However, shadows can be exploited in order to infer information about the object that has cast them. One such approach is detailed in [35]. Here Bolter uses analysis of shadowing effects in order to generate building models directly from SAR imagery, referring to algorithms that produce 3D models by utilising shadow and layover information as phenomenological based approaches. Bolter firstly describes how simulated SAR imagery is produced in an attempt to reconstruct a single building using such an approach. The simulation is based upon ray optics and is dependent only on the input imaging geometry and digital elevation model, the object being to simulate shadowing and layover effects rather than a high fidelity SAR image.

Using the simulated image, a process designed to reconstruct the building structure is described. The method begins with the segmentation of the shadow region from which the height of certain walls can be estimated (dependent on illumination angle). The process is repeated using simulated imagery from four cardinal look angles and the building structure is then reconstructed. The process is then applied to a building in four real SAR images collected with the Sandia Spotlight Sensor and processed to a resolution of 0.3m. In contrast to the simulated images, which do not contain speckle, the segmentation stage is more problematic and height information is therefore considerably noisier. Nevertheless, when viewed in comparison with building reconstruction using InSAR, the reconstruction of the building is very successful. This technique however is dependent on the full shadow being visible in all four images and the underlying terrain being perfectly horizontal in the shadow region.

Shadow height extraction need not be utilised in isolation if InSAR data is also available. In [36] Tison et al use a combination of InSAR and shadow estimation techniques in order to estimate building heights. The height measurement is modelled as an energy minimisation problem. For each shadow, several position estimates are made and evaluated dependent on both amplitude and interferometric information.

Simple layover and shadows models are used, implicitly assuming certain collection constraints and building properties (dimensions and roof type). The automated process attempts to find the near and far range roof positions and the shadow length. Shadow detection is made using the Markovian classification scheme discussed earlier. Searching for building positions is performed on a line-by-line basis, with no

restrictions on building shape. Building edges are regularised by comparison with values of surrounding lines. The energy function is dependent on the amplitude and interferometric image with an arbitrary weighting between them and minimised accordingly.

The algorithm is tested on data obtained over Dunkirk by the RAMSES sensor. Against visual extraction of buildings, it is shown to be successful for bright tall buildings, but less effective at modelling smaller buildings. The stage that introduces most errors is the shadow detection. A criticism of this technique is the numerous parameters that need to be chosen (three Fisher distribution parameters for segmentation, a roof height variation parameter, the building separation distance, maximum and minimum building lengths, an energy weighting parameter, a layover disregard distance and the regularisation length's upper and lower bounds). The choice of these parameters will have great impact on performance and any optimisation would take considerable effort. It is likely that such parameters would also be dependent upon imaging geometry and on the type of scene imaged.

Additionally, it is stated that the approach is independent of the underlying terrain. The length and shape of a radar shadow is dependent on terrain onto which it is cast. Here the shadow is used to estimate building dimensions and hence the previous statement is incorrect. Even if the underlying terrain is found by interferometric methods, it cannot be found in these shadow regions without imaging from different look angles.

3.1.3 Terrain extraction from stereo SAR

Another technique for the extraction of height information from SAR data is stereography. In [15] Desai presents a clear and thorough examination into the feasibility of extracting 3D information from spotlight SAR stereo imaging techniques. This is also the first work discussed in this section to consider the effect of squint angle on layover.

Similarly to repeat pass interferometry, stereo SAR requires that multiple imaging paths are flown to extract target height information. However, from an operational perspective the stereo collection process does not require flight paths to be identical (in fact relatively large differences in flight paths can produce improved height accuracies). The stereo process uses the differential layover between two SAR images formed with two distinct slant planes to extract target height information.

An analysis of how height information can be collected from curved, two-sided and same side parallel flight paths is provided in [15]. Additionally, it is shown that stereo cannot be used to extract height information from constant altitude straight-line flight paths. The effect on height accuracy of image resolution and crossing angle is quantified and a discussion on the importance and issues associated with the registration process is presented. The most problematic aspect of the technique is the correspondence problem, which is the identification and localisation of scatterers in the two images that form the stereo pair. This is complicated by the finite persistence of scatterers in SAR imagery.

The stereographic technique has been extended further by Jakowatz [37] et al who have developed a novel and potentially powerful technique for the extraction of 3D information from spotlight SAR images. [37] describes how, for ground plane imagery, the direction of layover is always normal to the line of intersection between the ground and slant planes. Hence, for straight and level flight the layover direction is always perpendicular to the line of the aircraft's ground track. For broadside collections the layover is therefore always in the range direction, however for squinted collections this is no longer true (this effect is not widely appreciated in the literature).

Jakowatz et al then describe two imaging collections (one squinted forwards and one backwards) that image the same scene but with flight paths that cross at a point at the centre of both synthetic apertures. As such, the layover in the range direction is the same in both images but is in opposite directions on the azimuth axis. Measurement of the azimuth layover difference allows height information to be obtained. In addition,

because the two images are coherent, the necessary registration step can be done in the complex domain thus enabling improved height measurement accuracy.

A DEM produced from imagery obtained by the Sandia Twin Otter airborne SAR system is shown. The system was operated at 15GHz to produced imagery at 0.3m resolution and the stereo pair was collected with a crossing angle of 20°. The resultant DEM was accurate in height to approximately 0.3m (RMS) such that buildings 4m tall and even fence posts were accurately rendered with a post spacing of ~1.5m.

In [16] Yocky et al extend the coherent cross track stereo technique to non-symmetrical collections and summarise other non-coherent stereo approaches. The image registration process and analysis of data obtained by the Sandia Twin Otter airborne SAR operating at 16.7GHz (Ku-band) are discussed in more detail. The resultant DEMs are compared with those obtained by the Rapid Terrain Visualisation Advanced Concept Demonstrator (RTV-ACD), which has a three-phase centre interferometric SAR operated on board a deHavilland DHC-7 airframe. The InSAR and cross-track SAR produced DEMs were both accurate in height to ~0.8m (RMS). Their application to data obtained over urban areas is not addressed, but is of interest to this study. It is suspected that, since InSAR encounters problems with phase unwrapping in urban areas, the cross-track coherent stereo technique would produce the most accurate and robust DEMs. Unfortunately, this technique was not available for consideration within the timescale of our study.

3.2 Urban SAR exploitation

The nature of urban environments presents specific problems for radar surveillance and intelligence analysts. Phenomena such as layover, shadowing and multi-path are commonplace and make image analysis of urban scenes a challenging problem. In addition, scatterers in such images often differ from the idealised point targets assumed in traditional SAR processing. Here we look at the published techniques that attempt to investigate and exploit all theses characteristics.

3.2.1 Urban simulation techniques

In [38] Soergel et al describe and quantify the effect of shadow and layover on SAR imagery of urban areas by using a LIDAR derived DEM as an input to a non-coherent SAR simulator. The focus of the study is the visibility of roads and buildings within the scene.

Layover and shadowing effects are described and characterised together with the dihedral type returns commonly found in SAR images of urban areas. The use of layover and shadow lengths to find building elevations is described subject to certain conditions. The dependence of shadow length on position within the range swath is discussed, however it is not stated that this effect is often negligible for long standoff sensors (where range>> swath).

The simulation uses LIDAR and SAR data of a college campus in Karlsruhe, Germany. The real SAR scene used as comparison was produced using the FGAN AER II system and processed to a resolution of 1m from a grazing angle of 55°. The DEM is produced by the first pulse LIDAR data that, unlike the last pulse derived DEM, contains scattering from foliage and hence best represents the X-band SAR data. In addition to modelling shadows and layover from buildings, the simulation also considers the effect of natural objects, such as trees. Analysis of the simulated scene involves a computation of the percentage areas that are shadow, layover, mixed and reliable for building and road detection. 72 aspect angles where considered at 5° intervals at 9 grazing angles ranging from 30° to 70° (producing a total of 648 simulated images). Using the percentage visible area for roofs and buildings as a quality measure, the optimal viewing angles for one, two, three and four image sets were calculated. In [38] it was shown that using 4 images 85% of the roofs are visible (note that the text in section III contains an error) but only 62% of the roads are visible.

In [39] Franceschetti et al go one step further and attempt to simulate raw signal SAR data over urban areas in order to optimise sensor configuration and operating modes for the collection of data over a particular urban scene.

Required inputs to the model are topological and dielectric data for the imaged area and buildings within it and a description of the SAR sensor and imaging configuration. The simulator uses both physical optics and geometrical optics and is valid under the condition that bandwidth is much smaller than the radar centre frequency (hence this approach is not applicable to low frequency and very fine resolution, <0.5m, X-band SAR systems). Buildings are modelled as prisms made from lossy dielectric materials with dimensions much larger than the wavelength of the illuminating radiation and surface roughness is characterised by Gaussian statistics. The simulation is based upon the Kirkhoff approach; modelling first order contributions (elementary scattering from roofs, walls, terrain etc), second order contributions (such as ground-wall or wall-ground interactions) and third order contributions (e.g. ground-wall-ground scattering).

The imaged scene is approximated by rectangular planar facets, which are smaller than a resolution cell but much larger then the radar's wavelength. A ground to slant range projection is used to account for layover and foreshortening effects and ray tracing algorithms are used to identify shadowed facets. Double and treble bounce scattering is modelled by additional contributions to the surface reflectivity function and the application of appropriate range offsets.

Outputs of the SAR simulator are presented in [39], but unfortunately, no real data is used as comparison and hence it is difficult to evaluate its performance.

3.2.2 Urban multipath analysis

Although multipath is commonplace in urban SAR imagery, little research has been published addressing this issue. One technique that has been developed to identify multipath effects in urban imagery is described in [40]. In this study, Garren at al investigate a processing technique that separates such scattering events from direct scattering echoes. The software developed is called the Image Reconstruction Algorithm for Multipath Scattering (IRAMS).

Conventional SAR image formation assumes that all scattering events are due to direct path events and hence for areas containing multipath, such processors will produce imperfect reconstructions of the imaged area. The IRAMS approach uses the fact that ideal responses in SAR magnitude images remain stationary with respect to aspect angle

changes, whereas multipath returns drift predominately in the cross-range direction. The extent of the drift (to first order in aspect angle) is directly proportional to the delay introduced by the increased path length. N SAR images are produced over a range of aspect angles and separated into $N/2$ pairs of adjacent images. Comparing each image pair allows an estimation of the relative contributions from direct and multipath scattering events with delays greater than a particular threshold. Direct and multipath images are then produced. This process is repeated M times with $N/4$, $N/8$...etc pairs (where $M=log_2N$) which have increasingly smaller delay thresholds until the final pair is processed. This allows many images to be produced with varying degrees of multipath delays.

The approach could be potentially very useful for urban SAR exploitation, both to remove multipath artefacts and to identify regions of multipath scattering in order to further exploit such behaviour. However, it should be noted that laid over scatterers will also drift with aspect angle hence the two effects may be confused. Unfortunately, the IRAMS was only tested upon simulated data, so only limited conclusions regarding its utility are made in [40]. The analysis of multipath in SAR imagery is not widely found in the open literature and the effect is still to be satisfactorily characterised.

3.2.3 Urban feature extraction

Scatterers common in urban scenes are often not well described by the point scattering model assumed in conventional SAR processing. Techniques have been developed in [41], [42] and [43] that utilise the non-point-like behaviour of certain targets to aid target recognition. Although not specifically developed for the exploitation of urban SAR imagery, it is feasible that these techniques could be useful for such tasks.

Both [41] and [42] describe an algorithm for the extraction of features from complex SAR imagery. SAR images are processed to generate a list of physical characteristics of the scattering objects that comprise the target.

The scattering model used is based upon the General Theory of Diffraction which states that if the wavelength of radiation is small compared to the size of object, a scattering response can be modelled as consisting of a number of isolated scattering centres. The scattering responses are categorised according to their frequency and aspect angle dependencies which allows information regarding an objects location, amplitude, shape and orientation to be estimated. Responses are characterised as either localised (trihedrals, points, top hats and spheres) or distributed (dihedrals, flat plates, and broad side edge returns).

Parameter estimation is described using two methods; an approximate maximum likelihood method (ML), which is shown to be the most robust technique, and a variation on the initial step of the ML approach which reduces computational load at the expense of classification performance. Frequency domain algorithms are inherently slow as the number of scattering centres is often very large and parameter estimation does not decouple as it does in the image domain (however operation in the image domain is only possible if the bandwidth is small compared to the centre frequency). In [41] a compromise is made; the method is applied in the image domain but data is reconstructed in the frequency domain. The algorithm begins by segmenting the complex SAR image using a watershed approach that isolates regions of high energy. This is repeated recursively in the ML algorithm with the reconstructed model subtracted from the SAR image and an additional non-linear optimisation technique is used to obtain approximate maximum likelihood estimates of parameters with an assumed additive Gaussian noise model. The fast algorithm only does this stage once, extracting the features from each of the initial segments. [42] also includes a description of how the estimated parameters can be normalised such that they are independent of resolution, frequency and bandwidth.

The technique is applied to both simulated data and a target image chip from the MSTAR dataset. Results on the simulated data shows that parameter extraction is heavily dependent on noise levels and conclusions from the MSTAR set are only qualitative assessments.

Another area where these techniques have been widely used is foliage penetration. In [43] Allen et al present a similar approach that characterises targets by *a priori* knowledge of their scattering response variation with aspect angle and frequency. This research however is concerned with the wide area detection of man-made objects under tree canopies using foliage penetration (FOPEN) VHF/UHF SAR. Such approaches are particularly suited for FOPEN SAR, since in many cases such systems have large fractional bandwidths and require spotlight collections over very wide angles and hence target responses are more likely to exhibit frequency and angular variations. Additionally, at such long wavelengths, often only large canonical objects contribute to the radar return.

Most problematic for FOPEN SAR systems is the discrimination between bright returns due to trees and man-made targets. At low frequencies, scattering from tree trunks can be modelled by 'top hats' (cylinders on a reflective ground plane). Their response with

respect to azimuth angle is essentially uniform and varies roughly linearly with frequency. In comparison, scattering from man-made structures appears similar to long, side on dihedrals formed by the intersection between object and ground plane. Such objects have narrow azimuth responses and quadratic variations with frequency. [43] considers only the difference in azimuth response and uses a matched filter detection approach to attempt to differentiate the two classes. Results using imagery obtained with the 200-400MHz SRI radar show a 1000 times reduction in tree trunk false alarm rate using the matched filter approach.

Although not applied to X-band imagery of urban scenes here, a similar matched filtering approach may be useful in distinguishing the complex returns found in urban imagery.

3.3 Polarimetric ATR

In addition to intensity and phase information, the use of polarimetry may be potentially useful in the assisted recognition of manmade hard targets. Over recent years, there has been considerable interest in the use of polarimetric SAR imaging techniques for both geoscience and military applications. As a result, the number of publications addressing the subject is considerable. A subsection of relevant research areas of interest are discussed which fall into three main categories; calibration, target decomposition and ATR.

3.3.1 Calibration

The main polarimetric calibration method that is investigated in this thesis utilises a rotating dihedral calibration target. One of the first studies to employ such a technique was developed by Schimpf and is presented in [44] where the requirement for a robust calibration procedure is correctly emphasised. The advantages of using only one calibration target are described together with the problem of boresighting errors. The standard model of two normalised 2x2 distortion matrices for transmit and receive is employed, hence it is implicitly assumed that (for example) the receive distortions on *HH* are identical to those on *VH*. The calibration parameters are calculated by solving a system of non-linear equations. When imaging a rotating dihedral the benefit of having a continuum of orthogonal polarisation states is demonstrated, however in [44] it seems only the minima and maxima are used in the determination of the calibration parameters, the whole rotation only being used as a guide to the alignment of the reflector. The accuracies to which the distortion parameters are measured are given. Although boresighting errors are mentioned their effects, and any other possible errors, are not estimated. How the rotation angle of the dihedral is measured is also not explained.

Another study to address the use of a rotating dihedral was undertaken by Muth and is described in [45]. Muth addresses the issues of absolute calibration and polarimetric calibration of monostatic radar measurements. A detailed discussion into the associated error analysis is also included. Absolute calibration is achieved by imaging engineered metal cylinders, a procedure is proposed and an error analysis is presented. The polarimetric calibration, which is our current concern, is achieved again through the imaging of a rotating dihedral. The standard model of two normalised 2x2 distortion matrices for transmit and receive is again used. In order to solve for the calibration parameters, Muth assumes that the errors on receive are identical to those on transmit,

hence rendering the model unsuitable for radars which have separate transmit and receive paths. By using Fourier analysis, full exploitation of the dihedrals full rotation is achieved and using the invariance of matrix's determinant, an estimate of calibration errors is obtained. Again however, little experimental procedure is included in [45] and the measurement of the dihedrals seam angle is not discussed.

Polarimetric calibration methods that make assumptions about the statistical properties of collected clutter data in order to perform polarimetric calibration are numerous and are widely used in the remote sensing community. In [46] Cordey reviews and evaluates the van Zyl method which uses clutter statistics to calibrate for the crosstalk errors of a SAR system. Two 2x2 distortion matrices on transmit and receive are used. The channel imbalances are taken as unity assuming a perfect channel imbalance calibration process has been performed. Reciprocity between the transmit and receive crosstalk is also assumed. Van Zyl relies on the assumption that, in a perfect system, the correlation of the co and the cross channels is zero over a region of randomly distributed clutter. Cordey outlines theoretical arguments for the validity of this assumption but substantial experimental evidence is not provided.

The two co to cross correlations are expanded to first order in crosstalk and an iterative process is used to estimate the two required crosstalk parameters by using observed values of the co-polar correlations and an iterative estimate of the cross-channel power. Estimation of the errors in the measured crosstalk powers using this process are quantified. For an error of less than 0.1dB in crosstalk power, the co to cross correlation must be no greater than –10dB. One obvious shortcoming, which is recognised in [46], is that performing this technique on regions with non-zero co to cross correlation effectively nullifies this correlation. In order to test the zero correlation assumption, one requires calibrated imagery but the only calibration method that the author employs is the van Zyl method, which suppresses any such correlations.

Methods using calibration targets and clutter statistics can be combined to enable a more thorough polarimetric calibration to be performed. In [47] Sheen et al describe a method that concentrates primarily on the relative polarimetric phase calibration for two airborne SARs (NADC/ERIM P-3 SAR and NASA/JPL DC-8 SAR). Simplified circuit diagrams of both systems are discussed with reference to their effects on calibration. The standard model of two 2x2 distortion matrices is applied together with an additional noise term. The P-3 system is shown to operate in a similar way to certain modes of the MIDAS system, whose calibration is addressed later in this study. Four pulses are

attenuated separately and hence four independent paths within the radar are generated. Sheen recognises that this means the standard model is no longer valid but no additional model is suggested. Unlike similar studies it is accepted that one must phase calibrate not only between the two co-polar channels but also between the co and cross-polar channels. However, no technique to perform this calibration is presented.

The method of imaging trihedral reflectors is shown to be effective only in finding the phase difference between the two co-channels if the cross-talk (or in Sheen's terminology, channel coupling) is neglected. The use of in scene clutter areas to perform phase calibration is also addressed. However, this is only possible if one assumes negligible cross-talk and one also assumes there to be zero correlation between the co and cross channels over the selected region of clutter. These assumptions are supported by analysis of the P-3 data. The clutter technique does have advantages in that it can be used to calibrate each scene individually and, unlike the deployment of calibration targets, can be used over a wide area. However, in [47] analysis of the DC-8 data showed that the assumptions on which the clutter technique is based do not hold for all types of clutter. The author is aware of these limitations and advises that the procedure be implemented cautiously.

[47] also provides details of an investigation into the range dependency of the co-channel phase calibration. The origin of this effect is a spatial difference between the H and V receive phase centres. Along-track errors are assumed negligible in those strip-map images analysed. Analysis shows, as expected, no range dependency in cross-channel phase difference and co-channel dependence is shown to be consistent with theory.

3.3.2 Decomposition techniques

Polarimetric decompositions are simply combinations of the four transmit receive channels. Most commonly, they are designed to combine the four channels statistically independently or in a manner that highlights the underlying scattering processes. Such techniques fall into three main categories; those based on Stokes vectors, those based on Eigen analysis of coherency or covariance matrices and those which employ a coherent decomposition of a target's scattering matrix.

Examples of decompositions based on Stokes matrices include Huynen's original approach of assuming a single target with an additional noise term [11]. Eigenvector based decompositions produce three (or four for bistatic scattering) statistically independent images that may also be modified for speckle reduction. This approach was first used by Cloude and contains a subset of related techniques such as entropy analysis and the H, α, β decomposition [11, 48, 49].

Coherent decompositions are variations on the decomposition of the scattering matrix into the four Pauli spin matrices. Examples include the odd-even bounce decomposition [50], Krogager's sphere, diplane, helix decomposition [51] (which itself is a further decomposition of the odd-even bounce decomposition) and the related Cameron decomposition [52]. These approaches require *a priori* information and, since the technique is coherent, speckle and other noise sources are not removed.

In [11] Cloude and Pottier present a review of the formulation and equivalence of various forms of decomposition techniques together with a discussion of their relative merits. The authors provide a concise revision of the definitions and conventions of commonly used scattering matrix representations. Three categories of decompositions are discussed; those based on Stokes vectors, those based on Eigen analysis of coherency or covariance matrices and those which employ a coherent decomposition of a targets scattering matrix.

Decompositions which model partially polarised targets as target scattering and target fluctuations are presented, including Huynen's approach. These techniques are based upon analysis of a targets Mueller matrix and determination of the noise term can reduce speckle in some cases. Eigenvector based decompositions are also analysed. This approach was first used by Cloude and contains a subset of related techniques. One such technique is model-based decompositions, in which simplifying assumptions as to the form of the target's scattering matrix are made, for example Freedman's decomposition into random, rough surface and dihedral scattering. This is made as a

consequence of assuming that the scatterers have reflective symmetry about the radar's line of sight and as a result, entropy is zero and only five independent scattering parameters remain. This assumption also results in the van Zyl decomposition where one scattering mechanism is dominant and can be characterised by the eigenvector angle α.

Coherent decompositions (such as Krogager's sphere, diplane, helix decomposition and Cameron's decomposition) are criticised in [11] due to their requirement for *a priori* information and, since the technique is coherent, speckle and other noise sources are not removed. However, it is rightly stated that for high resolution data, such as that used for our study, the technique is valid since individual scatterers can be resolved and entropy is generally low.

Some of the literature concerned with each of the most commonly used decompositions is discussed below.

Sphere, deplane, helix decomposition

The sphere, diplane, helix decomposition has been a widely used tool for analysing polarimetric data for some time. In [51] Krogager considers several properties of this decomposition and relates them to other such target parameters. Although optical and radar images are often decomposed incoherently into Stokes vectors, coherent decomposition of radar imagery is becoming more commonplace. Krogager attempts to formulate a coherent decomposition technique in which the polarimetric channels map to well-defined physical target types and contrasts this approach with approaches such as the Pauli spin matrix decomposition, which mix different scattering mechanisms.

In the sphere, diplane and helix decomposition the three polarimetric channels are decomposed into returns arising from scattering from sphere or single bounce type scatterers, double bounce scattering from diplane structures and helix scatterers that return only circularly polarised radiation. Previously the decomposition was dependent on antenna orientation but co-author Czyz produces a more general roll-invariant form, which decomposes into diplanes and helices of determinable orientation angles. This more general roll-invariant technique is far more powerful both because antenna alignment is not required and because orientation angles of the dihedral and helix type scatters may be extracted. However [51] notes that one must be cautious in interpreting this orientation angle since diplane type scattering can result from helix-helix and diplane-helix coupling.

One disadvantage of the technique is that the decomposed basis is not orthogonal. While sphere and diplane are mutually orthogonal the diplane and the helix components are not. One has to comprise the requirement for an orthogonal basis in order to generate a basis that separates into such elementary scatterers. Orthogonality can be achieved but only through a basis consisting of a sphere and two helix type scatterers. Unfortunately, [51] contains no experimental evidence to validate the decomposition model. No attempt to apply the method to calibration targets is made; this would provide an indication of the robustness of the classification of elementary scatterers. Nevertheless, this technique does appear to be of possible use in the analysis of hard target signatures, where the identification of individual scattering types may aid target recognition.

Cameron decomposition

In [52] Cameron and Leung introduce a physical based decomposition model. An orthogonal basis is presented decomposing polarimetric imagery into non-reciprocal, maximum symmetric and minimal symmetric scattering mechanisms. Scattering matrices are first separated into those that correspond to reciprocal and non-reciprocal scatterers. Reciprocal scatters are then decomposed further into two non-orthogonal components containing symmetric and non-symmetric scatterers. Matrices from helix type scatterers are distinguished since they have a stronger degree of asymmetry than other elementary scatterers, these scatterers form a minimal symmetric component. Other remaining scatterer types belong to the maximum symmetric component and can be identified by the rotation angle that diagonalises the symmetric component of their scattering matrices.

The author also shows that the three components; non-reciprocal, maximum symmetric and minimal symmetric are mutually orthogonal. Although the three components are based on physical properties, their derivations are somewhat involved and hence their physical significance is unclear. However when this basis is decomposed further, individual scattering types are identified and their relationships to objects within the image is much more obvious. In addition, orientations certain scattering targets may be obtained with this technique. The decomposition technique is applied to ISAR and SAR data. From ISAR imagery of a calibration reflector array, four reflectors from a total of five are correctly identified following the application of the author's sidelobe reduction algorithm. ISAR imagery of a soft skinned vehicle is also decomposed into scattering types. Using SAR imagery, three reflectors are correctly identified together

with their respective orientations. This technique looks promising. The ability to both identify and orientate differing scattering types may prove a useful aid to an operator driven, or an automatic, target recognition system. Unlike other articles of the same genre, Cameron's work benefits from presenting results of applying the decomposition to real data.

H/A/α decomposition

Although primarily concerned with land classification, Pottier and Cloude's entropy, anisotropy and alpha parameter decomposition may well be applicable to hard target signature analysis [48]. The technique is a statistical approach that is based on Eigen analysis of a target's average coherency matrix. The coherency rather than correlation matrix is used in [48] as it renders general target properties more visible. Although (as the two matrices are related by a unitary transform), the Eigen analysis is equally applicable to the more readily calculable correlation matrix. The average coherency matrix is found over a certain spatial region but the size of which is not clearly defined in [48].

The entropy is a defined as a logarithmic sum of the normalised eigenvalues. When this sum is small the region of interest contains one dominating scattering mechanism, when entropy tends to one the region contains more polarimetric variation. In the case where entropy equals unity the region contains no polarimetric information, such as a return from a completely random noise process. Also introduced in [48] is the alpha parameter, which is a weighted mean of the eigenvectors rotation angles. Alpha is an angle of between 0° and 90° and can be used to identify scattering types. For example, 0° corresponds to sphere type scattering and 90° diplane type scattering. The final parameter is the anisotropy, which characterises the polarimetric information contained within the second and third eigenvalues. In [48] it is shown that all three parameters are roll invariant, an important property of any decomposition basis.

Pottier and Cloude then apply the decomposition to NASA/JPL AirSAR data, using multiples of the three parameters to identify stable features of certain scattering types over areas of differing terrain. The notion of identifying polarimetrically stable regions may be a useful tool for interpreting target vehicle signatures and coupled with the alpha and anisotropy parameters could be of use in identifying scattering types within a vehicle's target signature which may aid exploitation.

Degree of polarisation decomposition

Touzi et al have investigated the use of polarimetric features generated by partially polarising scatterers. In [53] the authors present a method for optimising the degree of polarisation of a partially polarised wave. This generates maximum and minimum values for the degree of polarisation and the total scattered intensity. Combinations of these four indices are used in an attempt to classify land use within NASA/JPL imagery. Four base feature combinations are also formed. These include the dynamic range of the degree of polarisation and the normalised dynamic range of the scattered intensity together with more commonly used features such as the span and the fractional polarisation. The relative classification performance between these measures is explored. The extrema of degree of polarisation and total intensity are found to best characterise different areas of land-use.

This technique attempts to use classical wave analysis descriptors as features. The motivation behind the use of these particular set of features is not explained in [53] and their physical significance is not well understood. Touzi et al hope that looking empirically at the differences between features on known areas of the scene will give clues to the physical processes that produce them. One feels that although there may be useful aspects of this approach, a rigorous theoretical understanding as to the origin of these features is vital to their full utilisation.

Odd/even bounce decomposition

Jackson et al present results of the use of polarimetric detection and classification techniques based upon the odd/even decomposition scheme in order to find downed aircraft. In [50] the authors first apply Novak's polarimetric whitening filter (which will be described in the following section) in order to detect possible targets and then use this new basis of polarimetric channels to help distinguish targets from false alarms. It is well understood that when using the PWF, unlike traditional intensity methods, detection does not require a bright target but a target whose polarimetric signature is unlike that of the assumed clutter statistics.

Recognition is based upon the somewhat simplified assumption that man made targets, such as an aircraft's tail, will appear as dihedral type scattering centres and natural clutter is assumed to produce mainly single bounce type scattering. The three polarimetric images are thus decomposed into odd and even bounce images. The classification performances of the odd, even and odd/even bounce ratio features are examined. In [50] results are compared according to the number of false alarms

obtained by applying each discriminator on both the whitened and original images. When two aircraft were imaged within a clutter scene the odd/even bounce ratio proved to be the most successful classifier but when debris from an actual site was imaged the odd discriminator was most successful. Jackson et al postulate that the difference arises from the lack of double bounce scattering in the debris imagery that is prominent from the tail sections of the aircraft in the aircraft imagery. One unexpected result is that classification performances are degraded for the whitened image. This could be a result of the clutter within the image not being well described by the assumed K-distribution, although this seems unlikely from related published results. Alternatively the transformation to the new PWF basis may change the nature of the decomposition such that the calculated components no longer correspond to odd or even type scattering. This is not addressed in [50].

3.3.3 Polarimetric automatic target recognition

Polarimetry is increasingly used in the detection stages of ATR systems. The most commonly used post-processing filters and detection techniques have been developed by Novak and are described in [54] and [55].

In [54] Novak et al present their widely-used polarimetric whitening filter (PWF) technique for the reduction of speckle in polarimetric SAR imagery. The PWF transforms to a new uncorrelated basis that minimises the ratio of the standard deviation to the mean. This optimal basis is calculated by using the assumption that the clutter can be modelled by a K-distribution. Unlike rival techniques, the speckle reduction is achieved without the degradation of resolution. The process is well proven to improve target detection performance. Our study will however be mainly concerned with later states in an ATR system namely, discrimination and classification.

In [55] a methodology and results from a polarimetric automatic target recognition scheme is presented. The process consists of three stages; pre-screening or detection, discrimination and classification. The pre-screening consists of running a CFAR over PWF data. Discrimination uses 2-D matched filtering to extract potential targets and target orientation. Natural clutter is then discriminated using textural features such as fractal dimension, standard deviation and rank fill ratio. Classification is achieved through the use of 2-D pattern matching algorithms. As only three discrimination features are used, performance is somewhat limited but [55] provides a useful introduction into the development of a polarimetric ATR system.

4 Building Height Extraction from Urban SAR Imagery

4.1 Foreword

4.1.1 Scope

To extract information for intelligence or targeting tasks it is often useful to provide image analysts with height measurements of a target building or group of buildings. In section 3.1 we discussed techniques that utilise SAR for the extraction of building dimensions and in particular building heights. Many of the approaches applied segmentation to coarse resolution (>1m) imagery and made assumptions about the structure of those buildings imaged. Here we utilise fine resolution (<1m) imagery and do not apply segmentation methods that often introduce errors and losses of information, particular over urban areas. We develop and demonstrate techniques based upon layover/shadows signatures and interferometry and take care to define under what conditions these approaches are be valid.

Additionally, we present methods and examples of how digital elevation models (DEMs) can be produced over urban areas using SAR and some of their inherent limitations. The work involves both theoretical analysis and experimental results using airborne SAR imagery. Example imagery is presented and discussed.

4.2 Terminology

4.2.1 Shadowing

Radar shadowing occurs when part of the target to radar transmit and receive path is obscured. The resulting SAR image has a downrange region of low backscatter consisting only of system noise or sidelobes from nearby scatterers. In urban areas, particularly at shallow grazing angles, tall buildings can cast large radar shadows. When a target is within such a region then no scattering information can be obtained from it, this effect is sometimes termed occultation (Figure 13(i)). If part of an object is obscured by its own shadow then self-shadowing (Figure 13(iii)) occurs. Shadowing, although often problematic, can also be used to aid exploitation since the size and shape of radar shadow can give valuable information about the object from which it is cast.

4.2.2 Multipath

Multipath effects are also common in SAR images of urban areas. This effect occurs when either the transmitted or received radar signal is scattered from more than one object or surface (Figure 13(ii)). If a radar signal is scattered directly from an object

then this return always appears at a nearer range than any multipath interactions. This occurs since the multipath path length is always longer than the direct line of sight (LOS) path. We shall investigate multipath effects in later chapters.

4.2.3 Layover

Layover, as shown in Figure 13(iv), occurs when scattering centres with heights above the ground plane appear at a nearer range than scatterers at ground level. As we showed previously, as a result of the image formation process, the direction of layover is always perpendicular to the velocity vector of the sensor (therefore is in the range direction for broadside imaging). The layover effect is particularly pronounced at high imaging grazing angles.

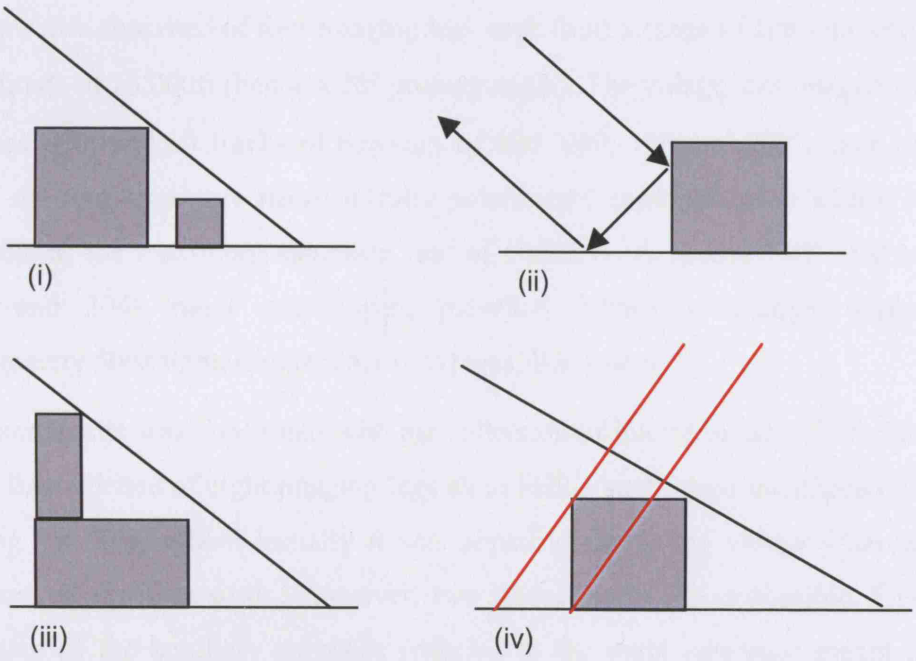

Figure 13: Diagram showing radar phenomenology common to urban scenes: (i) Radar shadowing causing occultation of the smaller building, (ii) Multipath between the building wall and the near range ground plane, (iii) Self shadowing and (iv) layover where returns from the roof appear nearer in range than those from the base of the building.

4.3 Data Collection

The data used in this chapter was obtained using QinetiQ's Enhanced Surveillance Radar (ESR). The radar was flown on two sorties, once in November 2001 [56] and again in May. The urban area imaged was a village in Salisbury Plain Training Area (SPTA). The planning, management and co-ordination of all aspects of the trial, ground truthing and processing activities were the author's work. However, the SAR and interferometric SAR image formation algorithms used were written by others (see acknowledgements).

4.3.1 ESR

The Enhanced Surveillance Radar (ESR) is mounted on a BAC 1-11 aircraft. It may operate with a frequency bandwidth of up to 450MHz at a nominal centre frequency of 9.69GHz and at sampling rates of up to 500MHz. The radar is fully programmable and is able to operate fully polarimetrically in modes including stripmap, spotlight and squinted SAR. Additionally, ESR is able to collect single pass interferometric (3D) data at single polarisations.

4.3.2 Imaging sorties

The objective of the first sortie was to collect high resolution fully polarimetric spotlight data of the village from a range of aspect angles.

The first sortie consisted of four imaging legs each from a range of approximately 18km at an altitude of 28 000ft (hence a 28° grazing angle). The village was imaged from four directions with aircraft tracks of bearings of 000, 090, 180 and 270°, each of length 7.2Nm. All four legs were flown in fully polarimetric spotlight mode with a 450MHz bandwidth at the maximum sampling rate of 500MHz. A spatial PRF of 0.15m was chosen and 2048 range gates were recorded. Hence a spotlight footprint of approximately 500x400m (range x azimuth) was illuminated.

The second sortie was concerned with the collection of interferometric (3D) data of the village. It comprised of eight imaging legs all in ESR's single pass interferometric mode receiving *VV* polarisation. Initially it was hoped to image the village from the same geometries as the first sortie. However, two issues made this impossible. Firstly, the lower gain of the auxiliary antennas (relative to the main antennas) meant that, for acceptable signal to noise levels, imaging was only possible from a shorter range. Secondly, at this shorter range strict air traffic restrictions around the congested airspace over SPTA only permitted imaging from the south of the village. Consequently, the imaging legs were flown with an aircraft bearing of 270°. Legs were flown at 28, 20 and 15° grazing angles at ranges of between 5 and 8km. Stripmap data was collected over a bandwidth of 225MHz with spatial PRFs of 0.15m and 1kHz temporal PRFs

4.3.3 Data processing

All the spotlight data was processed using QinetiQ's Third Generation SAR Processor [57]. The processor enabled the production of high resolution imagery over a range of squint angles. Information from ESR's INS (Inertial Navigation System) and IMU (Inertial Measurement Unit) is decoded and the aircraft's trajectory can be extracted.

This is then used to form an accurate motion compensation solution that enables the focusing of SAR imagery at high resolutions. The processor also allowed an autofocus correction to be performed [57]. However, for this data set it was found that its application was not required due to the fidelity of the MOCO solution. Spotlight imagery was produced at a resolution of 0.4m with a pixel spacing of 0.3m in both range and azimuth directions. The lengths of each of the four legs enabled squint angles of approximately +/- 20° from the boresight position to be processed.

The 3-d imagery discussed in this study is single pass stripmap 3d imagery. Stripmap imagery was produced by the QinetiQ's GRAPE (Generic Radar Processing Environment [58]) processor and then underwent further processing (image registration, roll correction, phase unwrapping and geometric corrections) until the final height image was produced. At the time of processing, no digital elevation map (DEM) was available and hence all building height maps were produced using the approximation that, over the small area of interest, the terrain is approximately planar.

4.3.4 Polarimetric calibration

Polarimetric calibration of the spotlight imagery was performed as described in [59]. SAR data of dihedral and trihedral calibration targets was collected prior to the village imaging. From analysis of the calibration data, we were able to extract ESR's polarimetric complex channel imbalances and apply the appropriate phase corrections to the village imagery. Calibration errors due to cross-talk between polarimetric channels were neglected following previous studies that showed cross polar isolation to be better than 30dB.

4.3.5 Ground truth

Ground truth of the village has been obtained in a number of forms. Architectural maps of the buildings within the village and their relative positions have been used to support the study. These were supplemented by two ground truthing collections in June 2001 and November 2002, during which GPS data and digital photography were recorded. An example of the digital photography obtained is shown in Figure 14. In addition, airborne photography of several areas of the village were also obtained, one example is shown in Figure 15.

Figure 14: Example of digital photography.

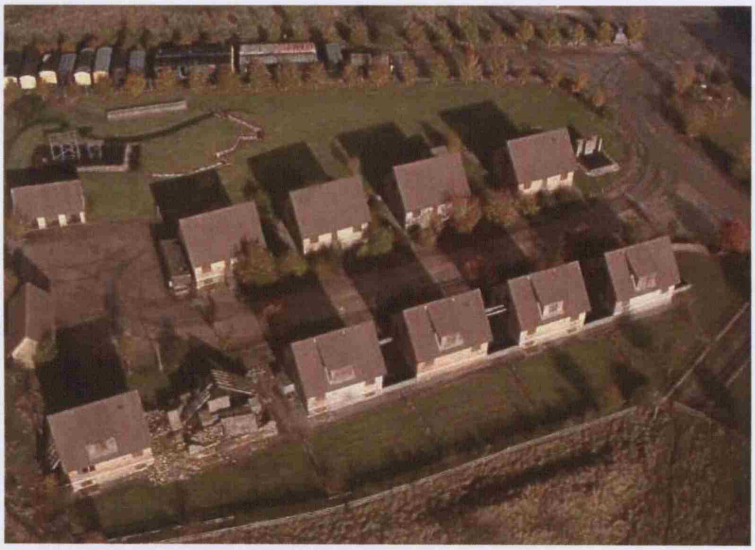

Figure 15: Example of aerial photography (Middlebarn Close).

4.4 Building height estimation from radar shadowing and layover

The shadowing and layover effects described in the previous section may be used to help interpret SAR imagery of urban areas. In this section, we attempt to use such information to provide estimates of building heights and widths. These dimensions may then be used to either discriminate or classify buildings within SAR imagery. In all cases, we assume that the imaging squint angle is small so the layover direction can be assumed to be in the range direction. The squint range of +/- 20° means that the ratio of cross-range to range layover, from (72) and Figure 12, is $\tan\theta$. The mean error is then

$$\frac{1}{40}\int_{-20}^{20}\left|\tan\theta\right|d\theta = \frac{1}{20}\int_{0}^{20}\tan\theta d\theta = \frac{1}{20}\left[-\ln\cos\theta\right]_{0}^{20} \approx 0.003. \tag{73}$$

We begin by considering flat roofed buildings and extend our approach to apex, or gabled roofed structures. The procedure and its fundamental limitations are described in detail together with examples of analysis performed upon real SAR imagery.

4.4.1 Flat roofs

Assuming the full extent of a building's structure and radar shadow are unobscured one can obtain the height and width of a flat roofed building as shown in Figure 19. The building's orientation with respect to the sensor's aspect angle, ϕ, range extent, X, and length of shadow, Y, are all measurable quantities. Then, given that the sensor's grazing angle, ψ, the height, h, and width, w, are (Figure 19)

$$h = Y\sin\psi. \tag{74}$$

$$w = \frac{X}{\cos\psi}\cos\phi. \tag{75}$$

Note that we have nominally defined the width dependent on the building's orientation with respect to the radar. The additional dimension, nominally length, may be calculated from the extent of the building return perpendicular to this width. Here also, we have assumed that the range of the radar, R, is large compared to building's dimensions and the far field approximation is valid (i.e. $R>>h$ and $R>>w$).

In this case the width of the building return, X, is bounded by the extent of the return from the roof. However, this is only true if $\psi < \tan^{-1}\left(w/h\right)$. At larger grazing angles this inequality is no longer satisfied and the far range building return now comes from the

ground plane-building interaction as shown in Figure 20. Since the only measurable quantities are, X, Y and ϕ, we then may calculate

$$h = \frac{X}{\sin\psi}. \tag{76}$$

$$w = \left(\frac{Y}{\cos\psi} - \frac{h}{\tan\psi}\right)\cos\phi. \tag{77}$$

Hence, for flat roofed structures, we have identified two distinct cases; case I, where $\psi < \tan^{-1}\left(w/h\right)$ and case II, where $\psi > \tan^{-1}\left(w/h\right)$.

4.4.2 Apex roofs

Applying a similar analysis to buildings with sloping roofs one finds four distinct cases [60]. For such structures we are now concerned with two heights, both the height of the lowest point of the roof above the ground, h_1, and the building's maximum, h_2. The four cases are thus defined in terms of h_1, h_2, w, and ψ and are depicted in Figure 21 to Figure 24. Case I, shown in Figure 21, occurs when the building return, X, is bounded by the leading edge of the building roof and its apex. Case II, shown in Figure 22, has the far range building return resulting from scattering between the ground plane and the building's wall. Cases III and IV (Figure 23 and Figure 24) both occur when the radar's grazing angle is greater than the angle of the slope of the roof. At these geometries Cases III and IV are directly analogous to the flat roof cases I and II if $h=h_1$. Essentially the width of the building extent and the length of the shadow are independent of the roof structure. However, this is only true if the ratio of the building's two heights, $\frac{h_2}{h_1} > 1.5$. In the case where, $\frac{h_2}{h_1} = 1.5$, cases II and III merge and when, $\frac{h_2}{h_1} < 1.5$, the order of the two cases (with respect to increasing grazing angle) reverses.

The boundaries and resulting equations for h_1, h_2 and w are summarised in Table 1. In all cases the imaging direction is assumed to be perpendicular to the building's leading edge (i.e. the $\cos\phi$ term is omitted for calculations of width). We also take, $\frac{h_2}{h_1} > 1.5$.

Note that, using this method alone, it is not possible to simultaneously estimate both h_1 and h_2 at one particular grazing angle. Also, estimates of width are not possible without prior knowledge of either h_1 or h_2 for cases I and II.

4.4.3 Class distinction

From the previous two sections, we see that before estimates of a building's height and width can be made one must first establish which class a building belongs to. Whether we are in case I or II depends upon h and w, the very quantities we are trying to find. Take for example a flat roofed building, applying the case I solution to a case II imaging scenario we introduce errors of

$$\Delta h = w\sin\psi\cos\psi - h\sin^2\psi\,. \tag{78}$$

$$\Delta w = h\tan\psi - w. \tag{79}$$

Conversely, applying the case II equation to case I will produce errors of

$$\Delta h = \frac{w}{\tan\psi} - h\,. \tag{80}$$

$$\Delta w = h\tan\psi - w. \tag{81}$$

Hence applying the case I solution to a high rise flat with h = 60m and w = 20m from a grazing angle of 30°, from (78) and (79) we will introduce errors of –6.3m and 14.6m for h and w respectively. Similarly, imaging a small house with h = 8m and w = 8m at the same grazing angle and applying the case II solution will produce errors of 5.9m and -3.4m.

For an accurate measurement of height, it is therefore vital to choose the imaging geometry such that the buildings of interest all fall into a known case. In order to employ this technique a certain degree of *a priori* knowledge of building size is required. This information could come from the use of additional imaging geometries or interferometry in the case of building heights. Figure 25 and Figure 26 show the boundaries between cases for flat and apex roofed buildings.

From the first figure we see that at airborne long standoff geometries (~5°) aside from very tall narrow buildings (where, h~10w) we can confidently assume that the case I equations are valid. However as we approach short range UAV or spaceborne geometries (>30°) we can only apply these equations to buildings where, h<2w.

Figure 26 shows a similar plot for apex roofed buildings. In this particular case, for illustration, we have chosen buildings which have h_2/h_1 =1.6. Here, at airborne type geometries, we again fall predominately into the case I category for buildings for h_2

$<5w$. However at the higher grazing angles (>30°) buildings that have $h_2<w$ fall into either the II, III or IV cases.

4.4.4 Results

The following section presents a worked example of how the technique discussed previously can be used to find heights and widths of buildings from the SAR imagery.

The four polarimetric channels were combined to form a span image ($|HH|^2+|HV|^2+|VH|^2+|VV|^2$). For illustrative purposes, we consider two buildings within this spotlight scene. Figure 16(a) shows an extracted image chip with a large barn at its centre. Figure 16(b) shows an image of a small residential house. Both these buildings are shown in the photograph of the area, Figure 16(c). Range profiles from cross-sections through the two buildings are shown in Figure 17 and Figure 18.

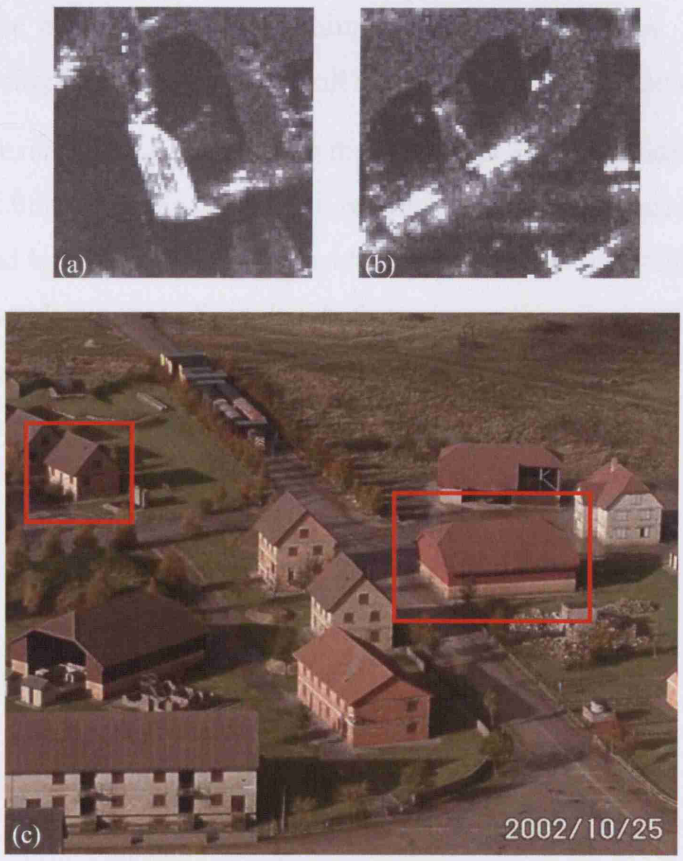

Figure 16 (a): Extract of Spotlight SAR image showing barn, (b) small house, (c) photograph of area, showing the small house (top left) and the barn (right).

From the range profile of the barn, Figure 17, we can measure the extent of the building return, X = 13.5m, and the length of the shadow, Y = 19.5m. From the SAR image in Figure 16(a) we may also estimate the orientation of the barn with respect to the radar, ϕ= 15°. At our current grazing angle, the barn falls in the flat roof case I (although the roof is gabled, the roof has constant height in range). From (74) the height, h = 9.2m. The width of the barn from (75) is, w = 14.8m. Given the actual height of the barn is 9.5m one observes that the height has been calculated to within ~0.3m. The correct width of the barn is 18.9m and was thus underestimated by~4m.

The small house, which at a grazing angle of 28° is in the apex roof case II, has a measured orientation, ϕ=31°. From the SAR image, aerial photograph, and corresponding range profile we see that between range cells 0-8m, scattering is from the trees in front of the building. The extent of the building return and the length of the shadow are then, X = 2.7m, and Y = 18.8m. Hence from Table I we calculate, h_1 = 5.8m, and given that, h_2 = 8.8m (from architectural drawings), we calculate the width, w = 8.1m. The actual height and width of the small building is, h_1 = 4.5m and w = 7.6m. Thus, we have overestimated both dimensions, possibly due to errors when

discriminating the returns from the building and the nearby trees. Additionally, the width of the building return, *X*, is very small in terms of the resolution of the image.

From these two examples we see that for the larger flat roofed building we are able to estimate the building's dimensions with a reasonable degree of success. However, for small apex roofed buildings, height and width information is difficult to extract at this resolution. The small number of pixels which comprise the target make the estimation of height from the building return alone inaccurate.

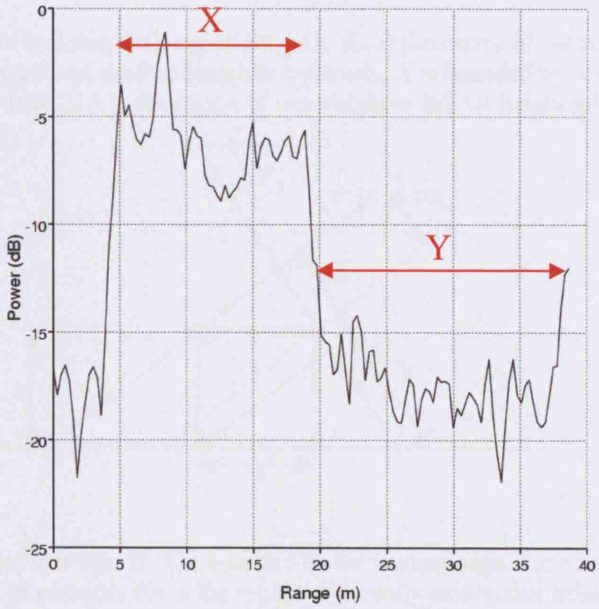

Figure 17: Range profile of a cross-section through the barn (absolute power is uncalibrated).

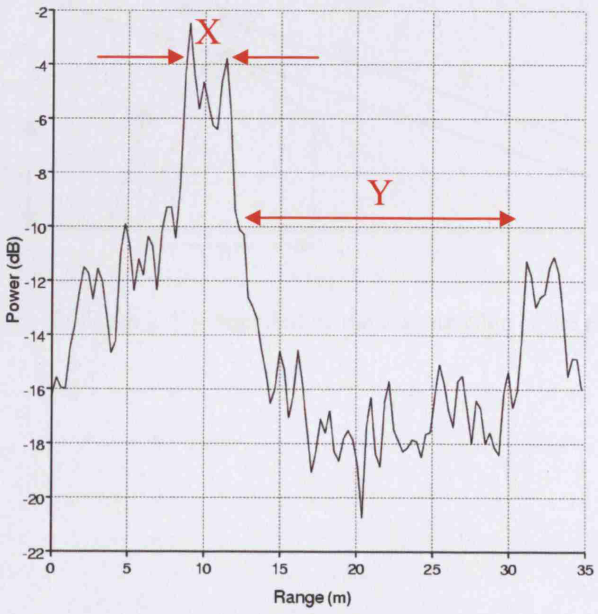

Figure 18: Range profile of a cross-section through the small house (absolute power is uncalibrated).

4.4.5 Diagrams and tables

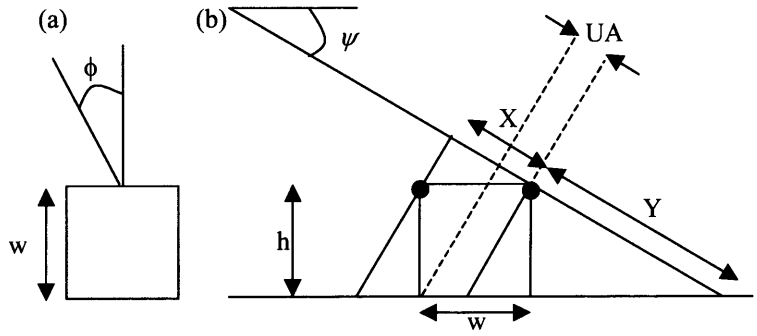

Figure 19: (a) Plan view of building defining orientation, ϕ, (b) Geometry of flat roof case I, X and Y are the measured building extent and shadow length respectively. X is bounded by scattering from the two corners of the roof. UA is the region of unambiguous InSAR height information.

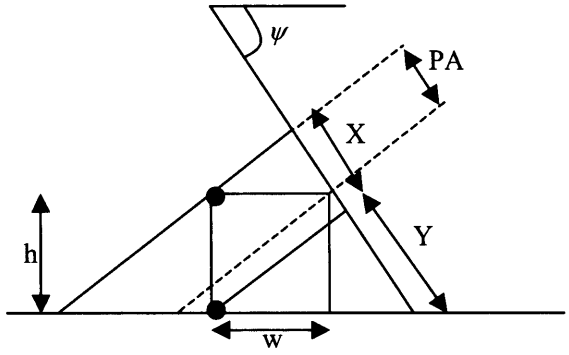

Figure 20: Geometry of flat roof case II. X is bounded by the leading edge of the roof and the return from the ground plane-building interaction. PA is the region of partially ambiguous InSAR height information.

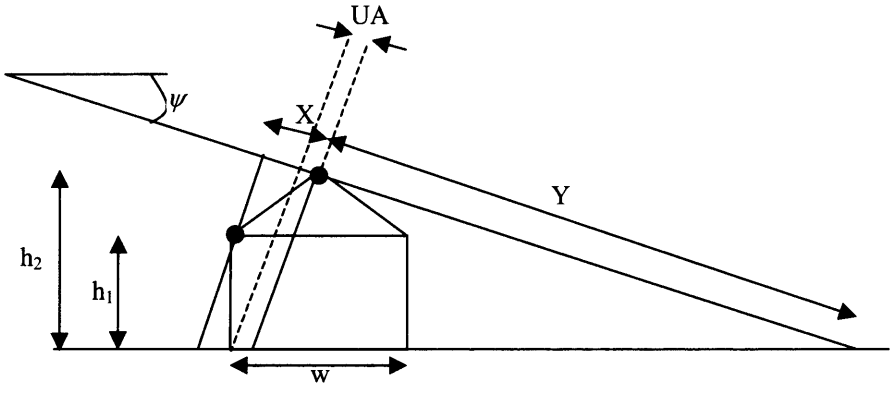

Figure 21: Geometry of apex roof case I. X is bounded by the leading edge of the roof and the roof apex.

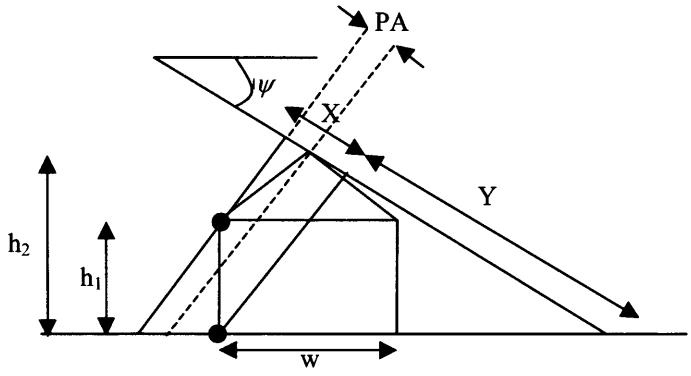

Figure 22: Geometry of apex roof case II. *X* is bounded by the leading edge of the roof and the return from the ground plane-building interaction.

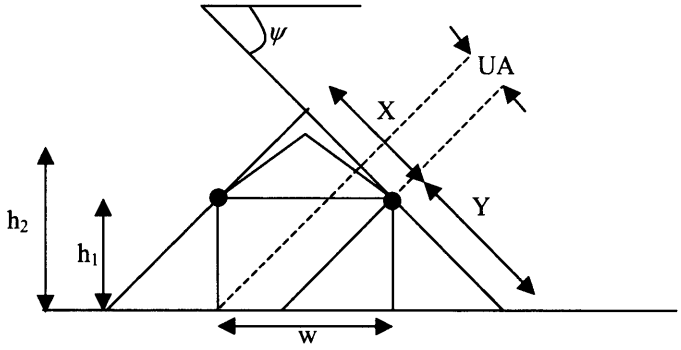

Figure 23: Geometry of apex roof case III. *X* is bounded by the near and far range edges of the roof.

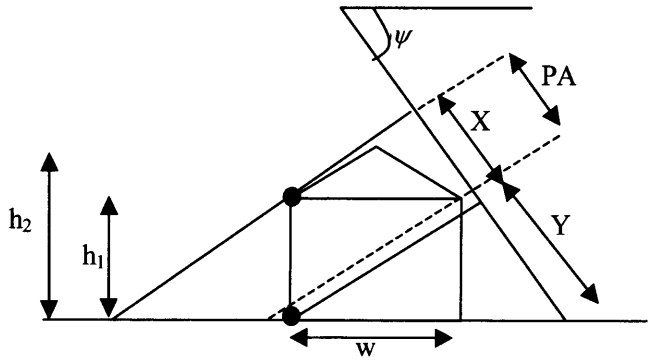

Figure 24: Geometry of apex roof case VI. *X* is bounded by the leading edge of the roof and the return from the ground plane-building interaction.

Case	Boundaries	h_1	h_2	W
I	$\psi < \tan^{-1}\left(\frac{w}{2h_2}\right)$	-	$Y \sin\psi$	$2\left[\frac{X}{\cos\psi} + (h_2 - h_1)\tan\psi\right]$
II	$\tan^{-1}\left(\frac{w}{2h_2}\right) < \psi < \tan^{-1}\left(\frac{w}{2(h_2 - h_1)}\right)$	$\frac{X}{\sin\psi}$	-	$\frac{2Y}{\cos\psi} - \frac{2h_2}{\tan\psi}$
III	$\tan^{-1}\left(\frac{w}{2(h_2 - h_1)}\right) < \psi < \tan^{-1}\left(\frac{w}{h_1}\right)$	$Y \sin\psi$	-	$\frac{X}{\cos\psi}$
IV	$\psi > \tan^{-1}\left(\frac{w}{h_1}\right)$	$\frac{X}{\sin\psi}$	-	$\frac{Y}{\cos\psi} - \frac{h_1}{\tan\psi}$

Table 4: Boundaries between cases for apex roofed buildings and calculations of heights h_1 and h_2, and width, w.

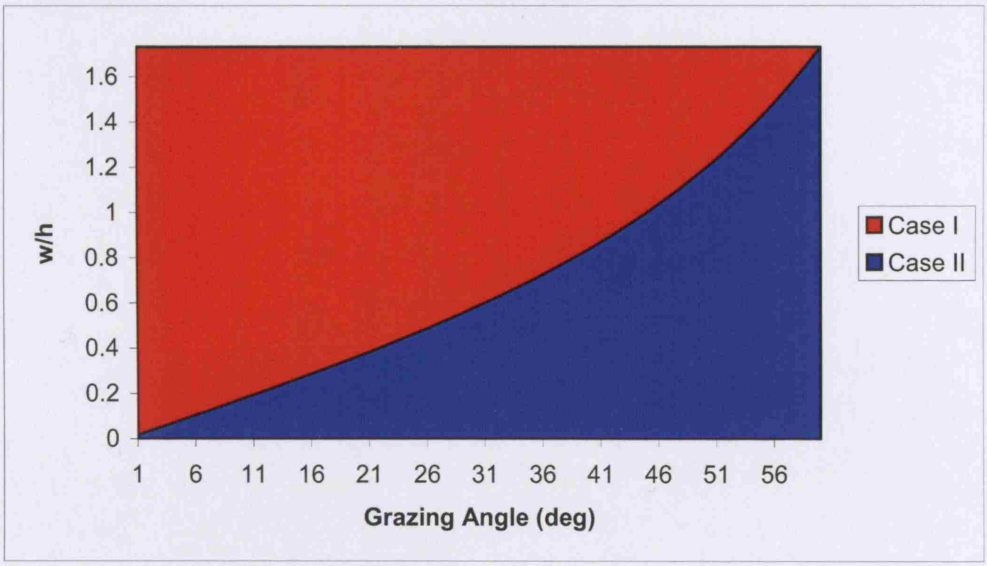

Figure 25: Graph showing the division between classes with respect to grazing angle for flat roofed building. The *y*-axis is *w/h* in the current terminology.

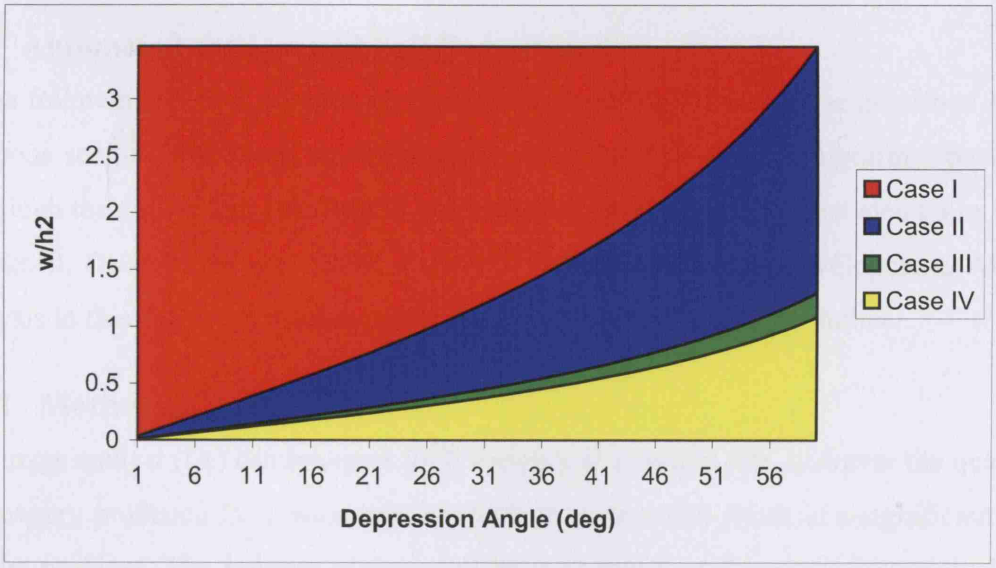

Figure 26: Graph showing the division between classes with respect to grazing angle for an apex roofed building. The y-axis is w/h_2 and $h_1 = h_2/1.6$ in this particular case.

4.5 Automated shadow and building extraction

In the following section, we present results of automating the technique described in the previous section. The work was performed using the SMARTbox, algorithm package. Although the author was involved in its development, much credit must also go to Dave Blacknell, Dave Pedlar and David Carrington of QinetiQ for its development. All the analysis in this section using this package was solely the work of the author.

4.5.1 Motivation

An image analyst (IA) can interpret SAR imagery at a certain rate, however the quantity of imagery produced from wide area surveillance assets will result in a significant data deluge problem. The volume of data will be such that it will become impractical and perhaps impossible for a human operator to provide a full analysis of all the yielded imagery. In order to address this shortfall, algorithms and software are being written and developed to allow the image analyst to perform the interpretation task in a timely manner.

4.5.2 Scope

Here we apply techniques and software developed for assisted target recognition (ATR) to urban SAR imagery in an attempt to automatically extract buildings from urban SAR imagery. We will then employ the techniques presented previously to estimate their dimensions. We shall describe a possible framework for assisted feature extraction from SAR imagery of urban areas. We show outputs from the various stages, including detection, clustering, discrimination and feature extraction. The final stage of the process, building classification, is not addressed. The procedure utilises the SMARTbox (SAR Machine Aided Recognition Toolbox) software environment to perform the target pre-screening [61, 62].

4.5.3 SMARTbox pre-screening

The initial stages of the ATR chain consist of detection, clustering and discrimination algorithms. These are collectively termed as pre-screening algorithms. A sample input image within the SMARTbox environment is shown in Figure 27.

The pre-screening stage begins with a single pixel adaptive CFAR detector. This algorithm passes a test window over the SAR image which identifies anomalously bright pixels. These pixels are then declared as detections (shown in blue in Figure 28) and passed to the clustering stage. The clustering stage identifies which of these single

pixel detections are likely to belong to the same extended target. A unique identification number is then assigned to each cluster of detections. Following the identification of all the clusters, a rectangular target chip containing each cluster is extracted from the original input SAR image. These chips are then passed to the final pre-screening stage. Here a discrimination algorithm performs a coarse classification between man-made objects and clutter discretes such as trees and hedges. The discrimination decision is based upon physical aspects of the cluster such as size, shape and power measures.

The output of the pre-screening stage is a number of target chips. Within the SMARTbox software environment, the discriminated targets are indicated by red crosses superimposed upon the SAR image, as shown in Figure 29. The operator may then select one of these target chips to be passed to the subsequent stage of the ATR chain.

4.5.4 Delineation

The next stage of the ATR chain involves the extraction of the target and possibly its shadow from the surrounding clutter. Here our targets are buildings and the shadow information can provide an estimate of their heights. Two such delineation processes: 'rattling rectangles' and a region based active contour method were considered in this study.

Rattling rectangles

The rattling rectangle algorithm assumes that the object to be delineated (in this case either the building or the shadow) is rectangular [61]. The algorithm then uses a simulated annealing approach to maximise the statistical difference between the pixels enclosed by the rectangle and the surrounding clutter. Five parameters explicitly describing the rectangle are varied: length, width, angle and the two offset values that describe its centre point. The parameters are varied dependent on a predetermined cooling temperature and constraints upon their maxima and minima. After a specified number of iterations, the algorithm outputs five optimised parameters.

Figure 30(a) shows a screen shot from the rattling rectangles algorithm as applied to a building within the urban scene. The latest five iterations are shown in green and the current best fit is shown in magenta. Figure 30(b) also shows the final output overlaid on the original image when applied to the building (cyan) and the radar shadow (red).

Region based active contour method

The statistical snake (or region based active contour) approach, instead of using a rectangle, grows a region bounded by a 'snake' consisting of point nodes which are joined together to form a polygon [62]. The algorithm attempts to minimise the length of the snake's perimeter whilst simultaneously maximising the probability that the two regions (bounded and unbounded) are from different negative exponential distributions. The user can specify the relative weighting between these two constraints and bias the algorithm towards a specified length to width ratio. The number of iterations and perimeter nodes may also be varied. Figure 31(a) shows a screenshot of the algorithm and output image.

For the purposes of this study, we are concerned solely with the lengths of buildings and their shadows and will use the rattling rectangle algorithm. However, for more complicated urban structures and applications where the shape of the delineated region is more important, such as vehicles, the statistical snake algorithm has proved to be the preferred technique and is currently implemented within the SMARTbox framework.

4.5.5 Experimental results

The rattling rectangle delineation algorithm was applied to one of the building chips discriminated by the SMARTbox pre-screening algorithms. The building was part of the squinted village data set described previously. Image chips were extracted from a range of aspect angles (a full 360° image set could have been obtained were it not for air traffic restriction around the target area).

The building in question was a medium size house with a gabled roof of length 10.3m and width 9.5m. Its maximum height (the height of the roof apex above the ground), h_2 = 11.0m, and the height of the roofs lowest point, h_1 = 7.0m.

Extracted imagery from each aspect angle was then used as an input to the rattling rectangle delineator, as shown in Figure 30. The length of the building return in the range direction, X, and the shadow length, Y, can then be used to calculate the two heights h_1 and h_2, at a given imaging grazing angle. Over certain imaging bearings one is able to calculate h_1 from the building extent, X. Using data from the remaining angles, one may calculate h_2. Figure 32 and Figure 33 show the extracted values of X and Y and the calculated heights h_1 and h_2 as a function of aspect angle.

As one would expect, the lengths of the building returns are distributed into two sets. The first set, when the building is imaged from the side and only half the roof is visible,

show building returns of between 3-7m. The other set occurs when the building is imaged end on and the returns are longer (between 4-14m) since the complete building extent is visible. The lengths of the radar shadows are independent of this effect and values range from 15-30m.

From Figure 33, we see that the apex roof model calculates, h_1, to be around 4m higher than its actual value of 7.0m. This may be due to the small length of X or multipath effects that occur between the building's leading wall and the ground. Such effects would increase the size of X thus overestimating h_1.

The calculations of h_2 are more accurate with $h_2 = 11 \pm 3$m. This calculation is dependent only upon shadow lengths, which are longer than X and hence will have a smaller relative error.

Figure 27: SMARTbox screenshot of original SAR image.

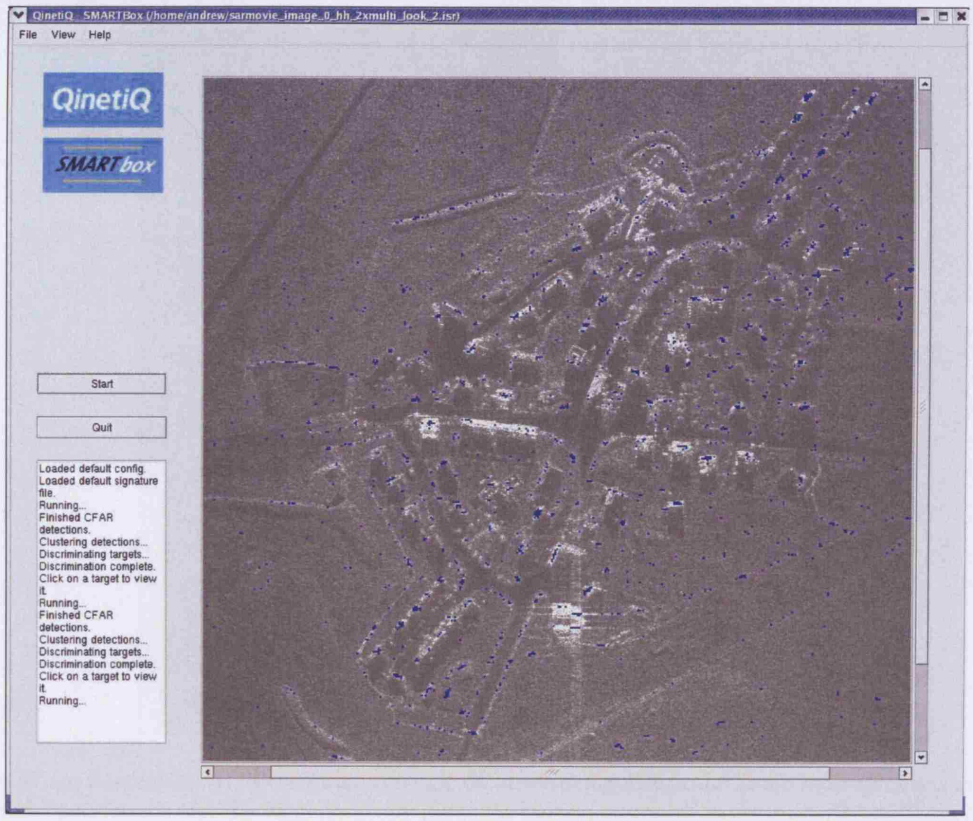

Figure 28: SMARTbox screenshot of detected pixels (shown in blue).

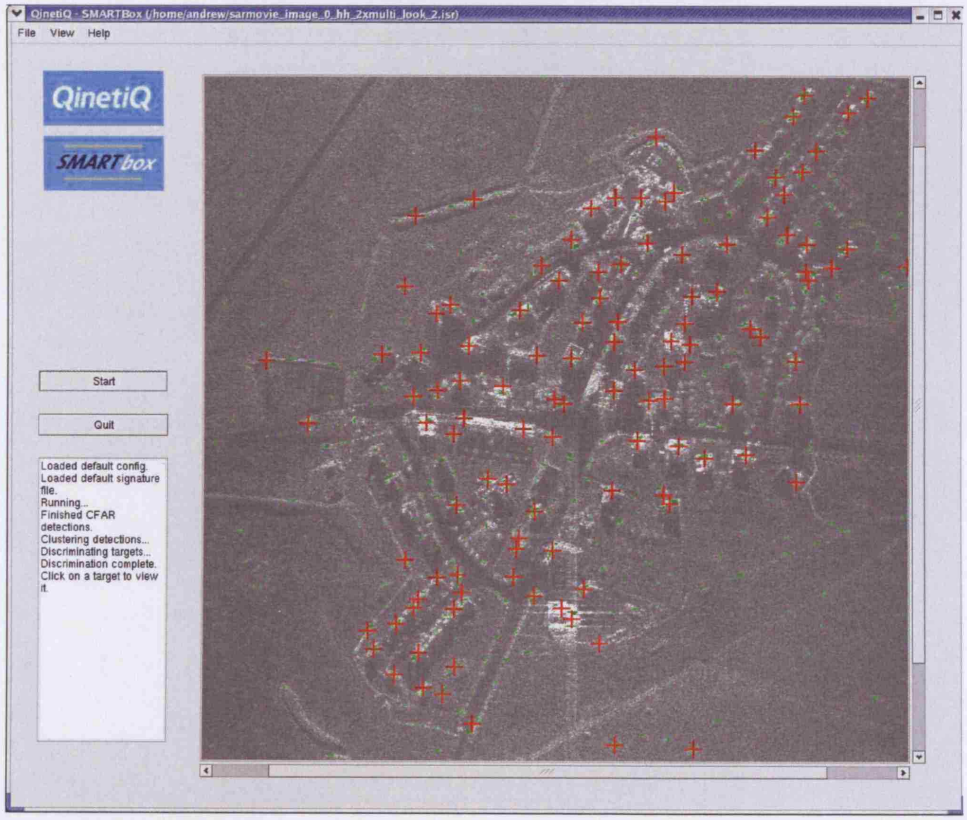

Figure 29: SMARTbox screenshot showing discriminated building (shown as +).

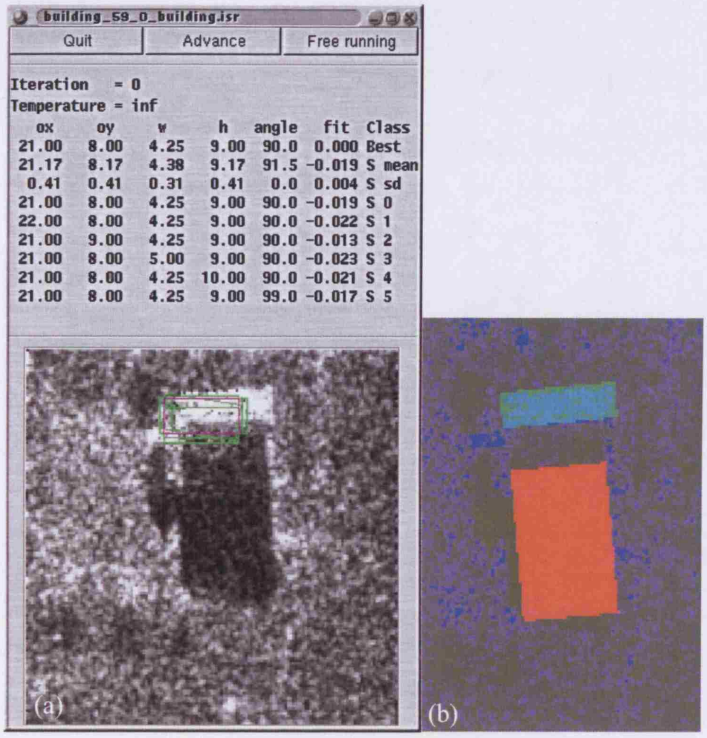

Figure 30: (a) Screenshot of the rattling rectangle delineation algorithm, the green rectangles are some of the previous iterations and the magenta rectangle is the current optimum fit (b) outputted building (cyan) and shadow regions (red).

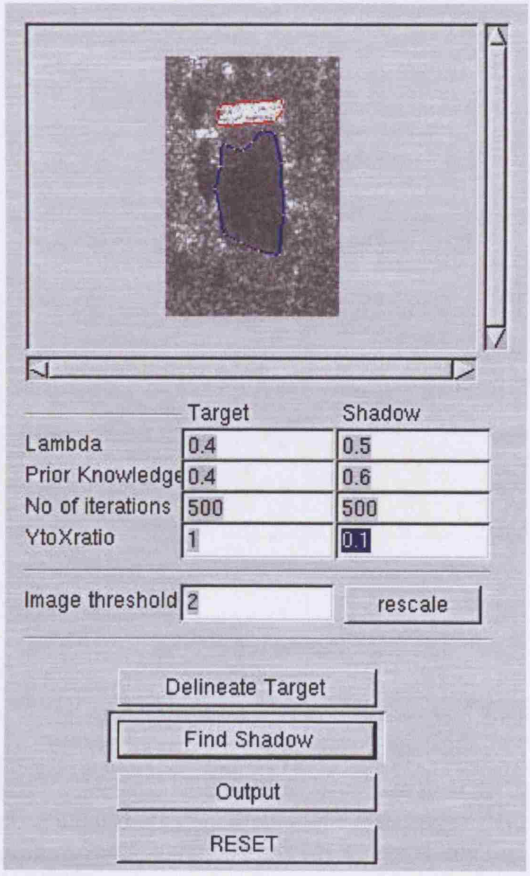

Figure 31: Screenshot of the region based active contour algorithm (outputted building (cyan) and shadow regions (red)).

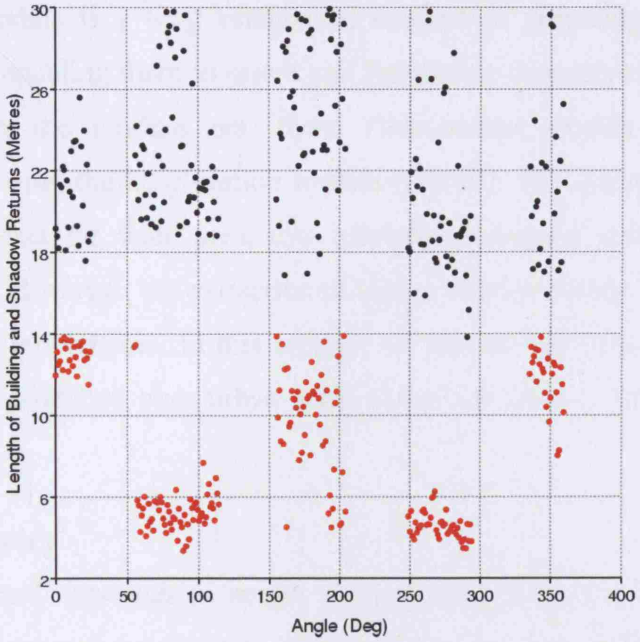

Figure 32: Graph showing the output from the rattling rectangle delineation as a function of imaging bearing. The length of the building return (X) is shown in red and the shadow length (Y) is shown in black.

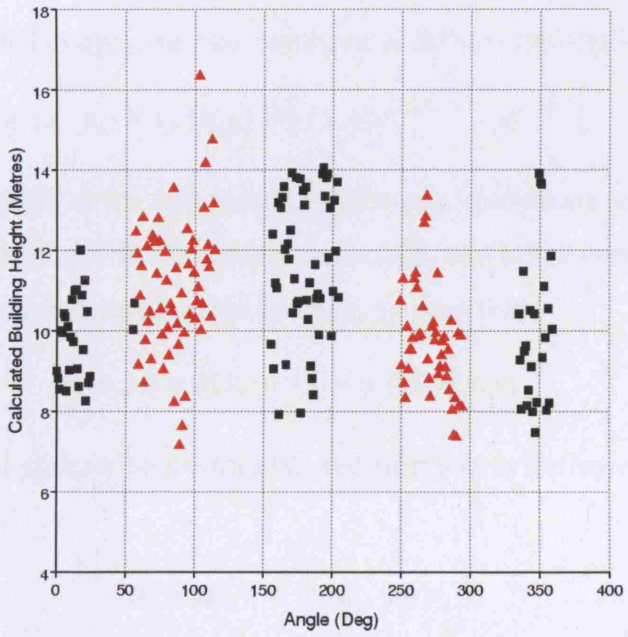

Figure 33: Graph showing the calculated heights as a function of imaging bearing. The black squares indicate h_2 calculated assuming a flat roofed building with a case I geometry, the red triangles indicating h_1 calculated under the assumption that the building has a gabled roof and the geometry is case II. Bearings of 057-147° and 237-327° correspond to flat roof case I, 147-237° and 327-057° correspond to apex case II.

4.6 DEM production

The building of models is a long established method of preparing combatants for military operations, enabling them to orient and familiarise themselves with areas prior to engagements. In the modern era, these visualisation models are virtual 3D environments built using digital elevation models (DEMs). The use of radar to obtain topological height data for wide area, low resolution mapping applications is well understood [13, 14]. However, the extraction of high resolution terrain information over urban areas is more problematic. In this section, we present methods and examples of how DEMs can be produced over urban areas using SAR and some of the inherent limitations.

4.6.1 Interferometry

The most widely used approach to height finding using synthetic aperture radar is interferometry. This process requires two images of a scene to be obtained from sensors separated by a small difference in grazing angle. This can be achieved in two ways. One method is to fly two separate imaging legs at slightly different altitudes (dual-pass interferometry) [63]. Alternatively, one may have a single platform with one transmit antenna and two vertically separated receive antennas, the data may then be collected simultaneously (single-pass interferometry).

From (71) two collected images, may be expressed as the two convolutions [2]

$$g_i(x_i, y_i) = s_{A_i}(x, y) \otimes \left[r(x, y) e^{-j\beta_i Y_{0i} h(x,y)} e^{-jyY_{0i}} \right], \tag{82}$$

where i=1, 2 correspond to the two independent image collections. x and y are cross-range and range co-ordinates in the scene space which, due to the terrain height $h(x, y)$, are translated in the reconstructed image space (x_i, y_i) such that

$$x_i = x + \alpha_i h(x, y) \quad y_i = y + \beta_i h(x, y). \tag{83}$$

The quantities α_i and β_i describe the translational shift due to the layover effect and are given by

$$\begin{aligned} \alpha_i &= \tan\eta_i = \tan\theta_{gi} \tan\psi_i \\ \beta_i &= \tan\psi_i \end{aligned} . \tag{84}$$

where ψ is the angle between the slant plane and ground plane in cross range, y is the angle between these planes in the range direction (grazing angle) and θ_g is the squint

angle projected onto the ground plane (Figure 34(a)). Note that the direction of layover is always perpendicular to the velocity vector of the sensor.

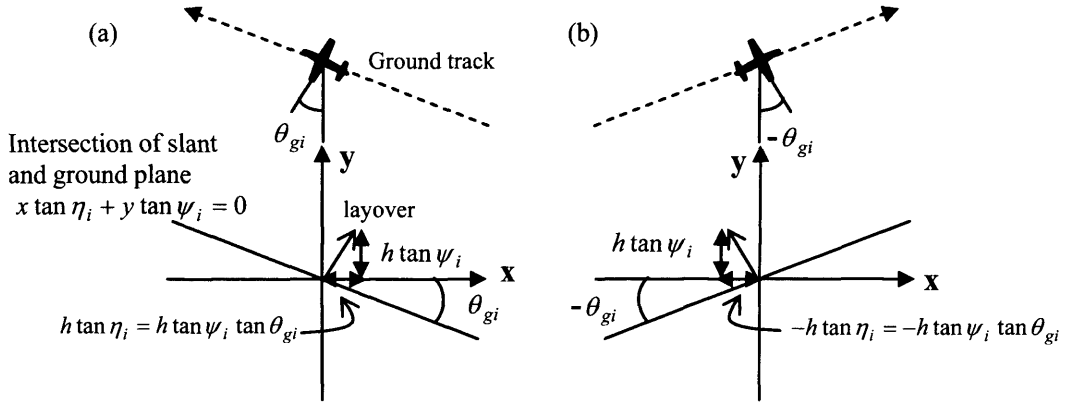

Figure 34: (a) Layover in the ground plane, from a scatterer located at the origin with height, h. (b) Corresponding opposite cross track stereo collection geometry [2, 16].

$s_{A_i}(x,y)$ are the sinc impulse response functions obtained from the inverse Fourier transform of the two synthetic aperture regions A_i. Or more explicitly,

$$s_{A_i}(x,y) = \Delta X_i \Delta Y_i \operatorname{sinc}\left[\frac{x\Delta X_i}{2\pi}\right]\operatorname{sinc}\left[\frac{y\Delta Y_i}{2\pi}\right], \tag{85}$$

where the aperture angle, $\Delta\theta_i$, and bandwidth, B_i, are projected on the ground plane in the Fourier domain over a region $\Delta X_i = \frac{4\pi}{\lambda_i}\Delta\theta_i$ and $\Delta Y_i = \frac{2}{\lambda_i c}\cos\psi_i(2\pi B_i)$ with a baseband offset of $Y_{0i} = \frac{4\pi}{\lambda_i}\cos\psi_i$. The complex reflectivity of the scene is $r(x, y)$.

The process of terrain height extraction begins by demodulating both images to a common baseband, Y_0. Then, assuming the small grazing angle difference, β_1-β_2, varies little over the collection time and that $h(x, y)$ describes a relatively smoothly varying terrain, if we define [2]

$$r_{A_i}(x_i, y_i) \equiv s_{A_i}(x,y) \otimes \left[r(x,y)e^{-j\beta_1 Y_0 h(x,y)}e^{-jyY_0}\right], \tag{86}$$

we then obtain

$$\begin{aligned} g_1(x_1, y_1) &= r_{A_1}(x,y) \\ g_2(x_2, y_2) &= r_{A_2}(x,y)e^{j(\beta_1-\beta_2)Y_0 h(x,y)} \end{aligned}. \tag{87}$$

For a coherent pair collection we must take the region where the apertures A_1 and A_2 overlap in the Fourier domain. Registration of the second image to the reference image,

such that the co-ordinates (x_1, y_1) and (x_2, y_2) coincide, then leaves a phase difference between the two images of

$$\Delta\Psi = (\beta_1 - \beta_2) Y_0 h(x, y). \tag{88}$$

Hence calculating the phase shift between the two images, given that the difference between the grazing angles is known, allows the terrain height, *h(x, y)*, to be extracted.

4.6.2 Limitations of urban interferometry

The 2π ambiguity in phase requires the interferometric height mapping process to contain some form of phase unwrapping. To function correctly, such algorithms require a smoothly varying phase response over the imaged area. Gently undulating terrain satisfies this criterion, however, urban areas contain buildings that produce sharp discontinuities in terrain height and hence introduce correspondingly sharp discontinuities in phase. Invariably, phase unwrapping algorithms cannot cope with such areas and the DEMs produced exhibit discontinuities in height. Moreover, if the phase unwrapping algorithm fails at one point, all successive height measurements will be offset by the resultant error in height.

Problems due to shadowing are also prevalent when attempting to extract height information [32, 64]. Where buildings are closely packed, occultation effects prevent height estimation from obscured buildings. In addition, the extraction of height information in regions of shadow (or low radar cross-sections) produces large height errors resulting from phase noise as coherency between the two images is lost [32].

Layover effects also hinder the extraction of height information. For the DEM to correctly describe the height of buildings within an urban scene, only returns exclusively from roof scattering will produce unambiguous height measurements. With increasing grazing angle, we observe the reduction in size of regions of unambiguous height measurements. For a flat roof of height h, if $\psi < \tan^{-1}\left(w/h\right)$, where w is the extent of the building on the ground plane in the direction of layover, the unambiguous height region (Figure 19), is given by

$$UA = w\cos\psi - h\sin\psi. \tag{89}$$

This region is bounded at near range by scattering between the ground and the leading wall and at far range by the end point of the roof. In the case where $\psi > \tan^{-1}\left(w/h\right)$, all

pixels containing scattering from the building roof also contain elements from ground-wall and ground-only interactions (Figure 20). Thus no area satisfies our earlier definition of an unambiguous height region. Under such conditions one may make the assumption that returns from ground-wall and ground-only are weak compared to the returns from the roof, then the phase of the resultant vector is dominated by the phase of the roof scatterers. Under this assumption the height information is also dominated by the roof return and we may define a region of partially ambiguous (PA) height information (Figure 20),

$$PA = w\cos\psi \,. \tag{90}$$

These effects are greater still in areas with apex roofed buildings where regions of unambiguous height are smaller. For apex roofs we have four distinct cases, I, II, III and IV (Figure 21 to Figure 24). For two of the cases, I and III, we are able to find regions of unambiguous height information, however the remaining two cases contain no such areas, only partially ambiguous regions are present under certain conditions. Table 2 gives the extent of the unambiguous and partially unambiguous regions for the four cases.

Case	Unambiguous Region	Partially Unambiguous Region
I	$\frac{w}{2}\cos\psi - h_2 \sin\psi$	all of building return, X
II	None	$\frac{w}{2}\cos\psi - (h_2 - h_1)\sin\psi$
III	$w\cos\psi - h_1 \sin\psi$	all of building return, X
IV	None	$\frac{w}{2}\cos\psi$

Table 5: Extent of unambiguous and partially unambiguous regions for building height in formation from InSAR imagery.

Additionally, multipath scattering which is also commonplace in SAR imagery of urban areas, may also lead to errors in height measurements using interferometric sensors.

Despite the problems discussed above, it is possible to extract height information from urban areas. The following section shows how information from a DEM produced by an interferometric SAR can be used to measure build heights.

4.6.3 Example of urban interferometry

Airborne interferometric data of the urban village previously shown was collected with the ESR aircraft. The radar was operated at X-band in *VV* polarisation. The ground truth, including photographs and architectural drawings enabled a comparison between the measured and actual building dimensions. The small residential house and barn, as shown Figure 16(a) and (b), are used to illustrate how the collected data can be used to extract building height information. The interferometric height profiles from cross-sections through the two are shown in Figure 35(a) and (b).

(a)

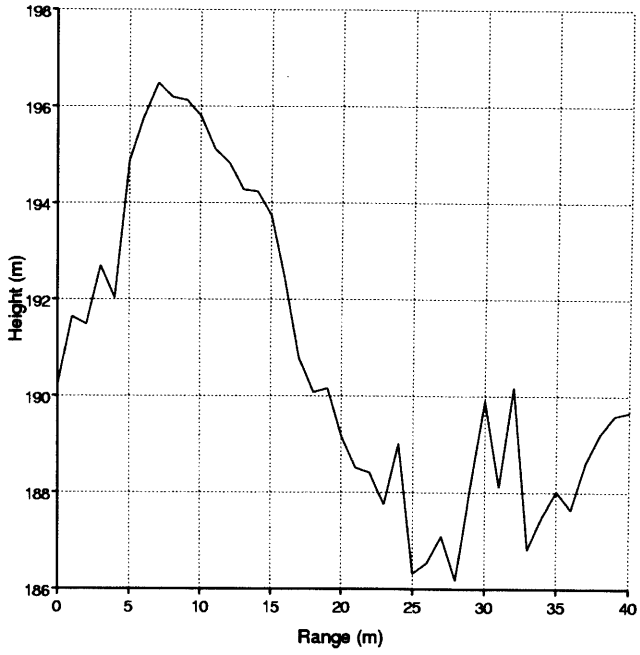

(b)

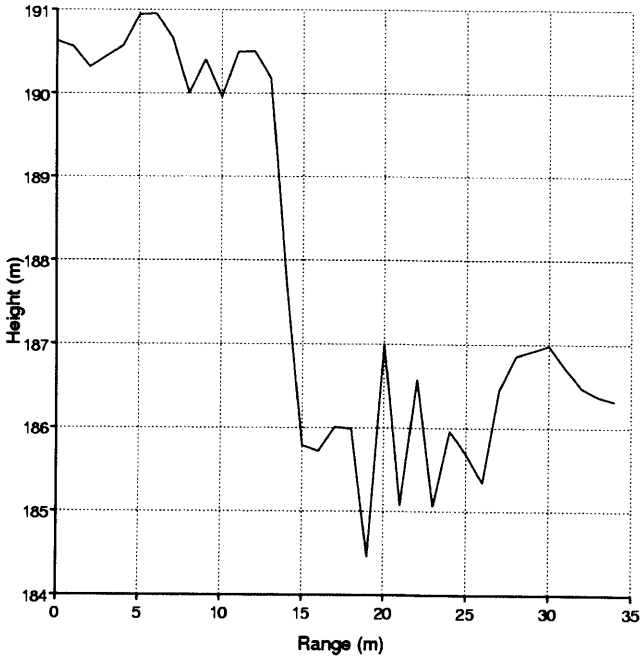

Figure 35: (a) Interferometric height profile of a cross-section through the barn, (b) Interferometric height profile of a cross-section through the small house.

Analysis of the height profile of the barn Figure 35(a) shows a possible area of unambiguous height measurement. From the imaging geometry and architectural drawings this areas is predicted to be ~2.4m in length. The measurement of height above the ground in this region gives a building height of approximately 8.5m compared with the actual height of 9.4m. However, the smaller house Figure 35(b) does not have an area of unambiguous height at this particular imaging geometry. This is visible in the height profile where we observe that the building height above the ground is only 5.0m, far smaller than the actual height of 8.81m.

The task of damage assessment is of obvious military significance. Figure 36(a) shows an optical image of a section of the village, from which one can clearly see that the house second from the left on the lower row has been reduced to rubble. Figure 36(c) shows the height information calculated over the cross section of this row of housing. Taking the reference or ground height to be approximately 184m, we are able to see five houses with heights of around 9m. However, the damaged house has a smaller height of only a few metres above the ground level.

In this example, the identification of the damaged house is made by comparison with the surrounding houses. This approach is therefore limited to areas with homogeneous buildings types. However, such a constraint is avoided if more than one imaging sortie is made over discrete time periods. With such temporally separated images, one could apply change detection techniques to obtain either damage assessment or information on building construction.

Figure 36: (a) Optical photograph of street with damaged building (second from left), (b) Corresponding spotlight SAR image, (c) height profile from cross-section shown in (b).

4.6.4 Stereography

Another technique for the extraction of terrain height, $h(x, y)$, from SAR collections is stereography. Such approaches require that the two images $f_1(x_1, y_1)$ and $f_2(x_2, y_2)$ are obtained from different imaging geometries, thus producing layover effects in differing directions. As in optical stereography, the parallax between the two images may then be used to calculate terrain height. Unlike interferometry, the stereo pair need not be obtained from similar viewing geometries. Indeed imaging paths that differ considerably can often yield better height information.

The approach below links Jakowatz's [2] treatment of interferometry and coherent stereo by generalising the later for non-coherent stereo. The two images that form the stereo pair can be described by

$$\begin{aligned} f_1(x_1, y_1) &= s_{A_1}(x, y) \otimes \left[r(x, y) e^{-j\beta_1 Y_{01} h(x,y)} e^{-jyY_{01}} \right] \\ f_2(x_2, y_2) &= s_{A_2}(x', y') \otimes \left[r(x', y') e^{-j\beta_2 Y_{02} h(x',y')} e^{-jy'Y_{02}} \right] \end{aligned} \quad (91)$$

noting that, since the geometry of collections are no longer similar, the cross range and range axis of the first image (x, y) do not coincide with those of the second (x', y'), see Figure 37. The layover effect creates the translations

$$\begin{aligned} x_1 &= x + \alpha_1 h(x, y) \quad y_1 = y + \beta_1 h(x, y) \\ x_2 &= x' + \alpha_2 h(x', y') \quad y_2 = y' + \beta_2 h(x', y') \end{aligned} \quad (92)$$

We may register the two images such that the origins of their axis (x, y) and (x', y') coincide but with a rotational translation due to the angular separation of ground plane imaging angles, ϕ. The difference in apparent position between the two images is then given by

$$\begin{aligned} \Delta x &= x_2 - x_1 = (\alpha_2 \cos\phi + \beta_2 \sin\phi - \alpha_1) h(x, y) \\ \Delta y &= y_2 - y_1 = (-\alpha_2 \sin\phi + \beta_2 \cos\phi - \beta_1) h(x, y) \end{aligned} \quad (93)$$

Since $a_i = \tan\eta_i = \tan\psi_i \tan\theta_{gi}$ and $\beta_i = \tan\psi_i$, if the grazing angles, ψ_i, and the ground plane squint angles, θ_{gi}, are known, a measurement of Δx and Δy allows the extraction of terrain height $h(x, y)$.

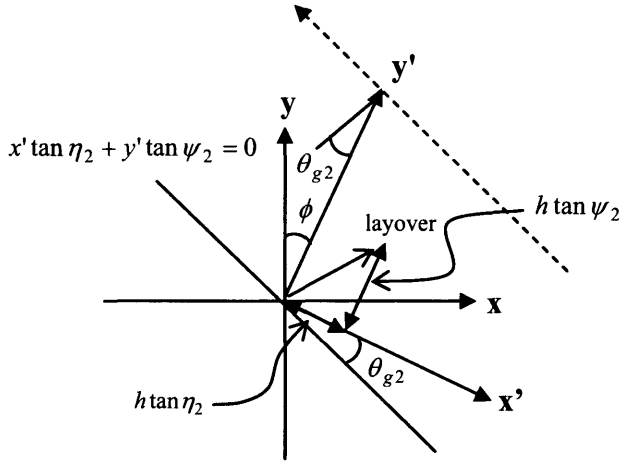

Figure 37: Layover in the second image of the stereo pair (scatterer located at origin with height, h)

From the above we see that, in principle, SAR stereography can be performed from a range of geometries providing the data is collected from two distinct slant planes:

Same side parallel pass stereo [15] with ϕ=0°, leads to

$$\begin{aligned} \Delta x &= (\alpha_2 - \alpha_1)h(x,y) \\ \Delta y &= (\beta_2 - \beta_1)h(x,y) \end{aligned} \quad . \tag{94}$$

Note that if $\psi_1=\psi_2$ then $\Delta x=\Delta y=0$ and no height information can be extracted. This means therefore, that single pass SAR stereo from a straight and level imaging leg is not possible (however, single pass stereo collections are possible from curved flight paths). One example of same side parallel pass stereo allows data to be collected from the same azimuth look angle, with a separation only in grazing angle. This can be advantageous to the registration process when imaging objects, such as buildings within an urban scene, whose scattering responses often vary more with azimuth then grazing angle.

Opposite side stereo [15] (from broadside, θ_{gi}=0°) with, ϕ=180° gives

$$\begin{aligned} \Delta x &= -(\alpha_2 + \alpha_1)h(x,y) \\ \Delta y &= -(\beta_2 + \beta_1)h(x,y) \end{aligned} \quad . \tag{95}$$

Although this collection geometry produces the largest measurable difference in layover, image registration is problematic since very few objects have similar scattering responses when imaged from opposite sides. Moreover, problems due to radar shadowing particularly in urban areas, render this approach unsuitable.

The crossing-track collection geometry and subsequent coherent SAR stereo processing proposed and demonstrated in [16, 37], is potentially the most powerful technique for

the extraction of DEMs over urban areas. Data is collected such that the centres of both synthetic apertures coincide. However, the directions of motion of the two platforms are not identical and therefore their slant planes differ, thus producing layover in different directions (see Figure 34(b)). Such a geometry has ϕ=0° and $\beta_1=\beta_2$ (as $\psi_1=\psi_2=\psi$), therefore

$$\begin{aligned}\Delta x &= x_2 - x_1 = (\alpha_2 - \alpha_1)h(x,y) = (\tan\theta_{g2} - \tan\theta_{g1})\tan\psi \cdot h(x,y) \\ \Delta y &= y_2 - y_1 = 0\end{aligned} \quad . \tag{96}$$

This geometry provides two coherent data collections, thus allowing registration of the two images using both intensity and phase. The ability to perform phase correlations allows a more accurate determination of Δx and hence the terrain height can too be found to a greater accuracy, as demonstrated in [16, 37].

4.6.5 SAR stereography over urban areas

In addition to the greater degree of collection flexibility, unlike interferometry, stereography does not require phase unwrapping and hence does not suffer from problems resulting from building height discontinuities common over urban areas. Indeed, the layover problems associated with interferometry discussed previously are advantageous when using stereographic techniques over urban errors.

Furthermore, for coherent cross-track stereography, since the imaging angle is the same for both collections, the registration task for objects, such as buildings, whose scattering response various considerably with imaging angle is made less problematic. Indeed, scatterers on the ground plane with zero or negligible height will appear identical in each image. However, areas of high relief terrain are difficult to register. Problems due to multipath and occultation are still prevalent and remain fundamental obstacles.

Unfortunately, due to airspace restrictions, it was not possible to fly cross-tracks over the area of interest.

5 Urban SAR Exploitation

In addition to the extraction of building height data, SAR offers the opportunity to provide an image analyst with additional information regarding the physical structure and nature of hard targets in urban areas. In this chapter, we explore various techniques to assist the analyst when working with SAR imagery of urban areas. In particular, we discuss, and show examples of, methods that look beyond the traditional SAR 'image product' and exploit additional information contained within radar data. These approaches generally exploit not only the intensity but also the phase characteristics of the SAR data. We illustrate these techniques using the experimental airborne SAR imagery discussed in the previous chapter.

Firstly, we consider the development of those FOPEN matched filter techniques described in section 3.2 to X-band urban SAR data in an attempt to extract the shape of objects within a scene. We then consider how the synthetic aperture can be split into smaller sub-apertures in order to investigate both the structure and motion of objects in urban areas. In contrast to those studies described in section 3.2, we consider the exploitation of squinted SAR and its impact upon the scattering characteristics of multipath. We conclude by describing the creation and usage of a urban SAR simulation software tool.

5.1 Scattering primitives

5.1.1 Introduction

The ability to assign scattering events to particular physical structures within a SAR scene will potentially aid the image interpretation task. As discussed previously, SAR images of urban areas often contain complex, multiple bounce scattering phenomena. The traditional method of SAR processing assumes that all returns can be best described as point like scatterers. However, this may no longer be the optimal processing approach for urban areas. Here we present a post processing technique that attempts to address this shortfall.

5.1.2 SAR Image Formation

As we saw in our chapter 2, spotlight SAR images are formed by the collection of data over a finite frequency bandwidth and over a range of azimuth angles. Recall that the collected data in the Fourier domain is often projected onto the ground plane and resampled onto a uniform Cartesian grid by the polar format process. As we showed in section 2.3, this region of support can be described by a rectangular region in X-Y plane

of width $\Delta X \sim \frac{4\pi}{\lambda}\Delta\theta$ and $\Delta Y \sim \frac{2\cos\psi}{c}(2\pi B_e)$ which is offset from the origin by $Y_0 = \frac{4\pi}{\lambda}\cos\psi$. The *X*-*Y* plane, describes the orthogonal components, azimuth and range, in the Fourier (or *k*-space) domain. Following the appropriate corrections for platform motion, the SAR image product is produced by a Fast Fourier transform (FFT) of data in both the *X* and *Y* directions.

5.1.3 Feature motivated processing

The conventional SAR processing technique described above relies upon the assumption that the object to be resolved is a point scatterer. This implicitly requires the target scattering response to be uniform in the region of support (ΔX x ΔY), which defines the radar bandwidth and Doppler bandwidth needed to achieve the desired image resolution.

This assumption is invalid for many of the types of complex scattering mechanisms found in urban SAR data. Such effects as multiple bounce, flat plate scattering and edge diffraction all produce effects that deviate from this ideal point scatterer behaviour. The motivation behind this approach is to investigate whether one can use known responses of various scatterer types or mechanisms to post process SAR imagery. It is hoped that such a methodology will identify the physical differences between certain structures common to urban environments.

5.1.4 Frequency Dependency

Previous research has been undertaken into techniques to extract scatterer types from SAR imagery using their characteristic frequency response. The amplitude response with respect to frequency of a particular scatterer is often modelled by the function, Y^{α}, where $\alpha \in \{-1, -½, 0, ½, 1\}$ [41].

Each scatterer type is assigned another parameter *L* which is associated with its spatial extent, localised scatterers having $L = 0$ with distributed scatters having $L > 0$. Maximum likelihood estimators are then designed to provide estimates of these two parameters and thereby estimate the nature of scattering centres within a SAR scene. A table showing values of these parameters for several canonical scatters is shown below [41].

Scatterer	α	L
Dihedral	1	$L>0$
Trihedral	1	$L=0$
Cylinder	½	$L>0$
Sphere (or point scatterer)	0	$L=0$
Edge Broadside	0	$L>0$
Edge Diffraction	-½	$L>0$
Corner Diffraction	-1	$L=0$

Table 6: α and L parameters for canonical scatterers.

The model we employ, based upon the above, assumes a target scattering response in the frequency domain, $H(\tilde{Y})$, given by

$$H(\tilde{Y}) = (k_y \tilde{Y} + \tilde{Y}_0)^{\alpha} \tag{97}$$

for $0 \le \tilde{Y} \le Y_s$, where $\tilde{Y} = Y - Y_0 - {}^{Y_s}\!/_2$ and Y_s is the sampling frequency. k_y is a constant that can be varied to change the form of (97) for a particular scatterer. The response is normalised for all values of α, by choosing $\tilde{Y}_0$ such that $H(Y_s/2) = 1$, or explicitly $\tilde{Y}_0 = 1 - (k_y Y_s / 2)$. Throughout, we assume the support region is fully sampled (i.e. $Y_s > \Delta Y$).

5.1.5 Azimuth Dependency

As described earlier, in traditional SAR processing azimuth compression relies upon the target exhibiting point-like scattering behaviour. As a result, in the Doppler frequency domain, X, the target response is assumed uniform over the entire Doppler bandwidth, ΔX. Here we attempt to consider targets where this simplification is invalid. We model their responses as sinc functions of variable widths described by the function

$$H(X) = \frac{\sin(k_x X)}{k_x X} \tag{98}$$

for $-{}^{X_s}\!/_2 \le X \le {}^{X_s}\!/_2$, where X_s is the Doppler sampling width. $k_x = \dfrac{0.88\pi}{\left({}^{X_{3dB}}\!/_{\Delta X}\right)}$

such that the width of each sinc function is defined by, X_{3dB}, in units of the Doppler bandwidth.

5.1.6 Methodology

Conventionally, the SAR image product, $I(x, y)$, is obtained by an FFT of the received resampled signal, $s(X,\tilde{Y})$. Additionally, a weighting function, $b(X,\tilde{Y})$, designed to achieve sidelobe reduction in the final image, is also often applied. The final image is then

$$I(x,y) = FFT_{X,\tilde{Y}}\left[s(X,\tilde{Y})b(X,\tilde{Y})\right]. \tag{99}$$

We attempt to use the scattering models described above to generalise this procedure for non-point like targets. To maximise the response of targets whose frequency and Doppler frequency responses are given by (97) and (98), we form a new image

$$I_c(x,y) = FFT_{X,\tilde{Y}}\left[\frac{s(X,\tilde{Y})b(X,\tilde{Y})}{H_{\alpha,X_{3dB}}(X,\tilde{Y})}\right]. \tag{100}$$

where $H_{\alpha,X_{3dB}}(X,\tilde{Y})$ is a two-dimensional weighting function describing both (97) and (98) and dependent on the two parameters α and X_{3dB}. The linearity of (99) and (100) allows us to apply this weighting post processing, hence we obtain

$$I_c(x,y) = FFT_{X,\tilde{Y}}\left[\frac{IFFT_{x,y}[I(x,y)]}{H_{\alpha,X_{3dB}}(X,\tilde{Y})}\right]. \tag{101}$$

where *IFFT* denotes an inverse fast Fourier transform.

5.1.7 Results

The same X-band spotlight ESR imagery described previously was used for this study. The bandwidth of the system was 450MHz achieving a range resolution of 0.4m and an aperture of approximately 2° was synthesised to achieve the same resolution in the azimuth direction. Experiments were performed upon the squinted image set used throughout this study. Sample images are shown below showing the effects of the frequency, azimuth and combined filters.

Frequency filtering

Frequency filters shown in Figure 38 were produced for α = -1, -½, 0, ½, and 1, corresponding to the scatterer types described in Table 6.

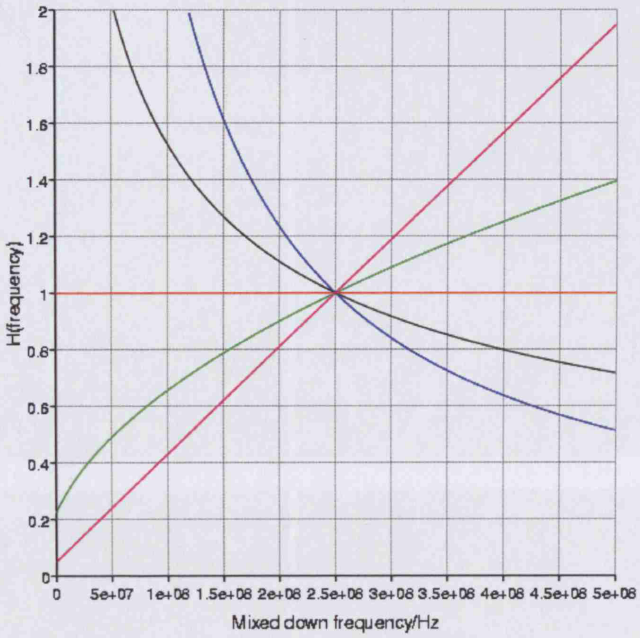

Figure 38: Frequency filters at baseband (α = -1 blue, α = -½ black, α = 0 red, α = ½ green and α = 1 magenta).

The filter constant, k_y, was chosen such that the filters with $\alpha \neq 0$ differed as much as possible to the form of frequency response assumed for point like targets (under the constraint that $H(\widetilde{Y}) > 0$ for $0 \leq \widetilde{Y} \leq Y_s$). The physical significance of k_y was not investigated.

Examples of the application of these filters on the squinted village imagery are shown in Figure 39(a), (b), (c) and (d) with imaging bearings of 164, 166, 268 and 270° respectively. This RGB composite image has a red channel showing the result of applying the α = -1 filter and the green and blue the α = 0 and α = 1 respectively. Here we see that certain scatterers, particularly on the building roof have brighter responses in the red and blue channels, indicating that the scattering is not point-like. However, considering the pairs of images are formed over successive apertures we see how this response is highly dependent on aspect angle. Additionally, the majority of the image appears to be white, and therefore responses to these filters are very similar.

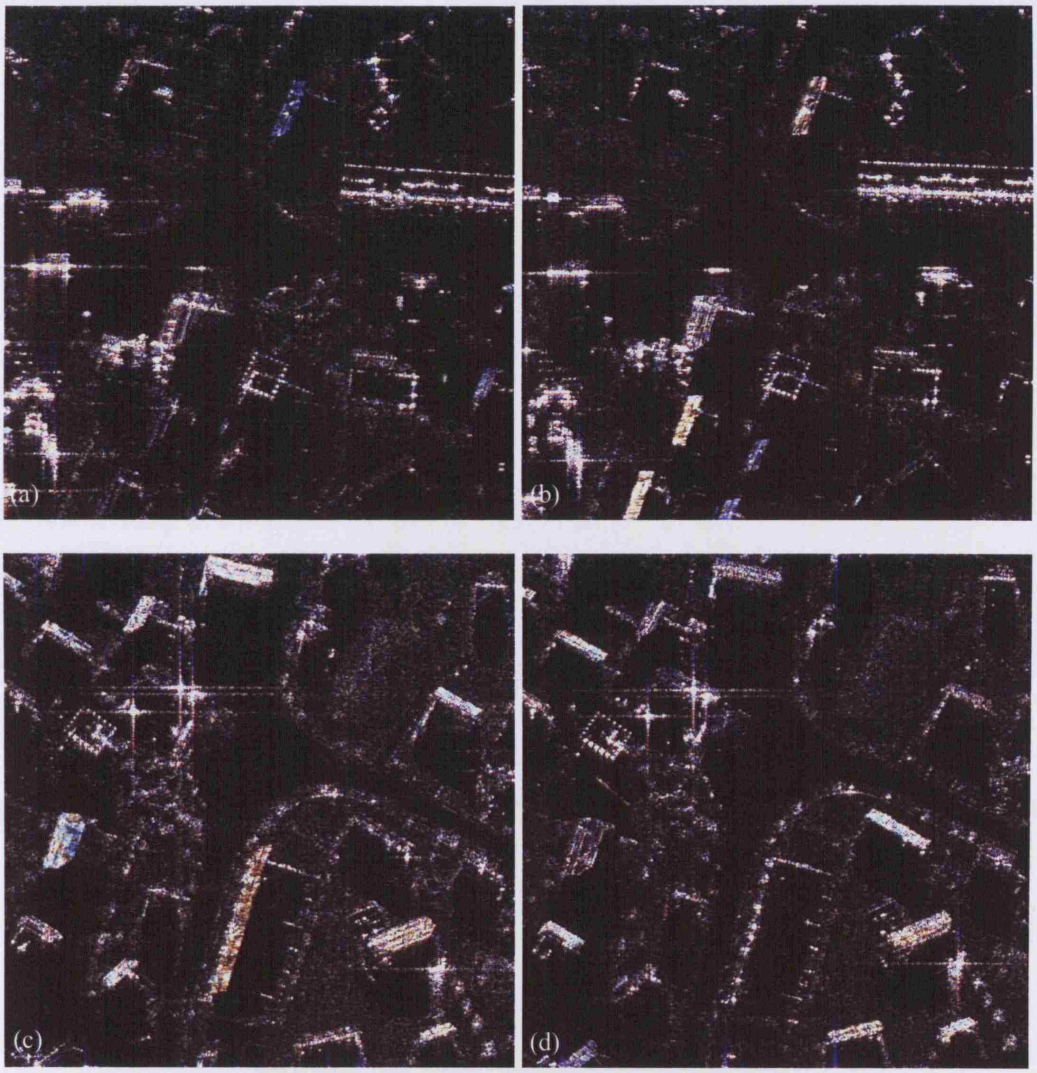

Figure 39: Frequency filtered images (red α=-1, green α=0 and blue α=1). Imaging bearings (a) 164°, (b) 166°, (c) 268° and (d) 270°.

Azimuth filtering

Azimuth filtering was performed upon the same image set. An example azimuth filtered image is shown in Figure 41 for the azimuth filters shown in Figure 40 (widths, X_{3dB}= 0.1, 0.5 and 2 are shown in red, green and blue respectively). Here we observe similar effects to the frequency filtering with most of the image appearing white and thus the effects of the three filters have produced little differences in the final image.

Closer analysis shows the narrower filters, X_{3dB} = 0.1 and 0.5, produce a smearing, in the azimuth direction, of some of the brightest scatterers. This occurs since, for point-like scatterers whose responses are constant over the Doppler range of interest, we have effectively reduced the Doppler bandwidth and hence reduced the azimuth resolution of the final image.

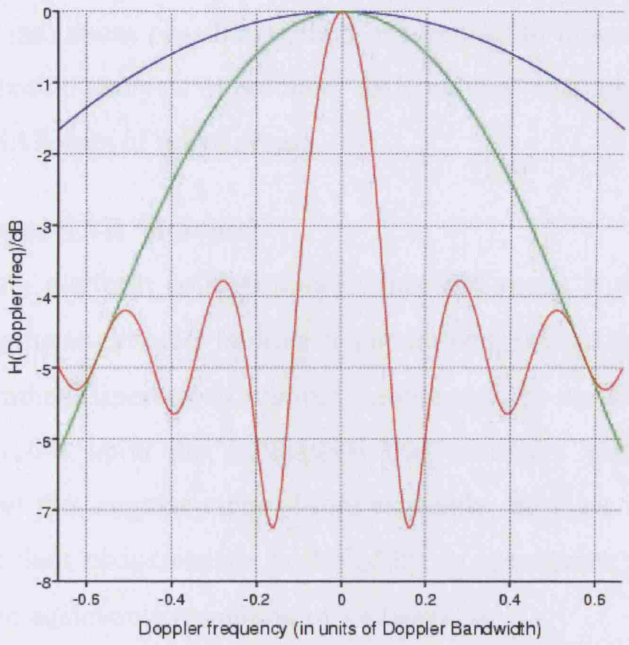

Figure 40: Azimuth filters as a function of Doppler frequency in units of Doppler bandwidth ($X_{3dB} = 2$ in blue, $X_{3dB} = 0.5$ in green and $X_{3dB} = 0.1$ in red).

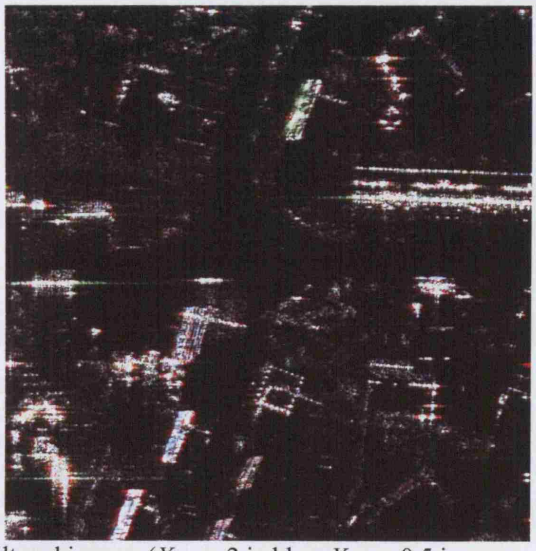

Figure 41: Azimuth filtered images ($X_{3dB} = 2$ in blue, $X_{3dB} = 0.5$ in green and $X_{3dB} = 0.1$ in red).

5.2 Sub-aperture movies

So far we have looked at techniques which utilize the complete Doppler bandwidth to form images at the maximum possible azimuth resolution. In this section we use sub-aperture image formation analysis to produce 'SAR movies' that are shown to assist in the exploitation of SAR data of urban areas.

5.2.1 Generation of SAR 'movies'

As the SAR imaging platform collects data in spotlight mode it records information over a range of imaging angles, $\Delta\theta$. In order to obtain the full cross-track resolution, the full extent of the synthetic aperture is azimuth compressed. As we discussed previously the SAR process relies upon the assumption that scatterers within the scene are persistent throughout this angular range. More explicitly, they are required to appear point-like such that their phase can be modelled by an appropriate quadratic function (14), thus allowing an achievable resolution of $\lambda/(2\Delta\theta)$ (27).

Where scatterers are not persistent during the aperture formation (because of variations in reflectivity, $r(x, y)$, over $\Delta\theta$) then the resulting image can be thought of as a weighted sum of the responses from each constituent imaging angle. The non-point like response is no longer correctly matched filtered by a quadratic reference phase function and information is lost. In which case, it can be beneficial to split the aperture into smaller 'sub-apertures', over which the scattering response varies less. Obviously, this is at the expense of image azimuth resolution, yet it frequently allows a better understanding of the imaged scene to be obtained. The selection of data for each sub-aperture can be overlapped to preserve more of the original azimuth resolution. These sub-apertures can then be animated in sequences frame by frame to produce SAR 'movies'.

Throughout this study, we have expressed the desire to exploit phase information, and implicitly in production of SAR movies, we are doing just that. If a SAR image is formed over the full extent of the synthetic aperture, then, providing we have preserved image phase, the image may be inverse Fourier transformed into the Doppler frequency domain (X, Y) and split into sub-apertures. We are therefore able to produce SAR movies with appropriate post processing of the complex image product.

5.2.2 Urban SAR movies

The imaging of buildings from a number of aspect angles, potentially allows one to use the variation of reflectivity, $r(x, y)$, with respect to aspect angle to extract information

about its structure. Upon analysis of SAR movies of urban areas, one is immediately struck by the magnitude and frequency of the variation of building returns with respect to aspect angle. This is particularly true for building roofs.

Figure 42(a-h) show individual frames of a SAR movie, each sub-aperture is formed over an angle of ~2°, with approximately 4° separating the centres of each aperture. The first four sub-apertures (Figure 42(a-d)) are collected from a track bearing of 180°. The remaining frames view the scene from the opposite direction with a track bearing of 0°. The sequence illustrates how rapidly the urban radar returns vary with aspect angle. The building roof in the centre of the image gives very strong returns in certain sub-apertures but between these, is no brighter than the surrounding grass.

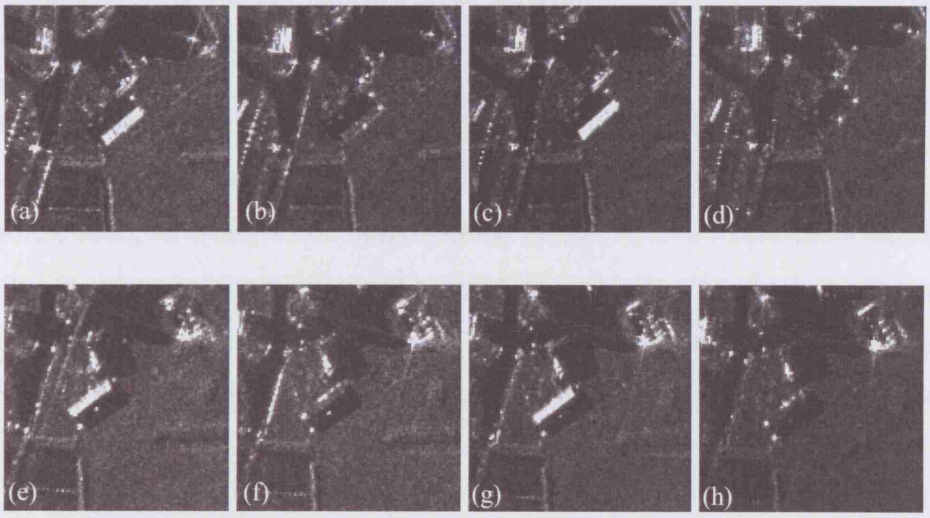

Figure 42: (a) to (d) Spotlight images showing a flashing building with aperture centre to scene bearings of 253°, 258°, 262° and 266°. (e) to (h) The same building with aperture centre to scene bearings of 75°, 79°, 83° and 87°.

The cause of this effect is the periodic nature of the roof tiles on the building. Assuming the mechanism to be Bragg scattering, then for a repeating structure of characteristic length, d, the nth maximum occurs when

$$2d\cos\Phi_n = n\lambda\,. \tag{102}$$

where the angle, Φ_n, is shown in Figure 43. The characteristic length can then be calculated given the angle between two consecutive maxima,

$$d = \frac{\lambda}{2\left(\cos\Phi_n - \cos\Phi_{n-1}\right)}. \tag{103}$$

For the images in Figure 42, one obtains a characteristic length of 10cm. This length is of the same order as the repeating roof tile structure visible in the photograph shown in Figure 43(b).

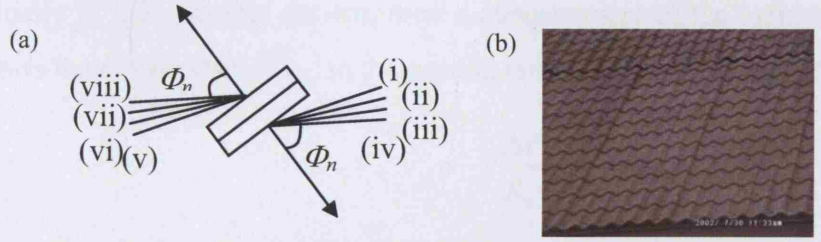

Figure 43: (a) Diagram showing the angles Φ_n between the building normal and each sub-aperture centre (i-viii) (b) Photograph showing the roof structure of building.

5.2.3 Moving targets in urban scenes

In addition to scatterers whose responses vary with imaging angle over the formation of a complete aperture, the formation of SAR movies also assists in identifying and interpreting objects whose signatures exhibit temporal variations during the collection period. An example of which is moving targets.

In Figure 44(a) the black diamond indicates the position of a stationary vehicle located on a road. As the time sequence continues (Figure 44(b)-(f)) the vehicle begins to drive north on the road, In doing so its range motion causes its radar signature (indicated by the black square) to be displaced in the azimuth direction [1]. The blurring is a result of the component of velocity in the azimuth direction and periods of acceleration and deceleration. As the vehicle stops, its radar signature returns to the road slightly above its initial position, Figure 44(f).

The azimuth displacement is best understood by consideration of the role that Doppler frequency plays in SAR image formation. As we saw in equation (20), when a SAR sensor illuminates a scene, the platform motion creates an instantaneous Doppler frequency that varies linearly with time. For broadside collections, during the aperture formation period, this frequency changes from positive to negative values (for squinted collections an offset shown in the first term in (20) is present, but does not effect the discussion here). The SAR process locates targets in azimuth with zero instantaneous Doppler frequency. However, targets which are moving towards the sensor have an additional Doppler frequency due to their line of sight velocity, v_{los}. It can be shown that, following azimuth compression, such moving targets are displaced in azimuth by [1]

$$\Delta x = \frac{R_0 v_{los} \cos\theta_s}{v}. \tag{104}$$

Where θ_s is slant plane squint angle and v is the velocity of the platform. Given that the velocity of the sensor is known, then a measurement of the azimuth displacement, Δx, allows the component of v_{los} in the ground range, v_y, to be calculated as

$$v_y \approx -v\frac{\Delta x}{R_0}\frac{\cos\theta_s}{\cos^2\psi}. \tag{105}$$

Any target motion in the cross range direction results in an instantaneous Doppler response with an azimuth chirp rate no longer given by equation (20) and hence following azimuth compression, the target is no longer correctly focused (measurement of the target's smear length in the SAR image can allow an estimate of the cross range velocity to be made [1]). Accelerating targets produce non-linear instantaneous Doppler responses and are also defocused in the resultant image.

In this case, measurement of Δx suggests that the vehicle's velocity along the ground towards the radar is a maximum of 3.5km/h. This is consistent with the average speed of ~2km/h (since the vehicle moves in range approximately 13.6m in 26 seconds). At this point, we note that in the full aperture scene, since the target changes velocity, it would appear smeared in the azimuth direction and would not be identifiable as a vehicle.

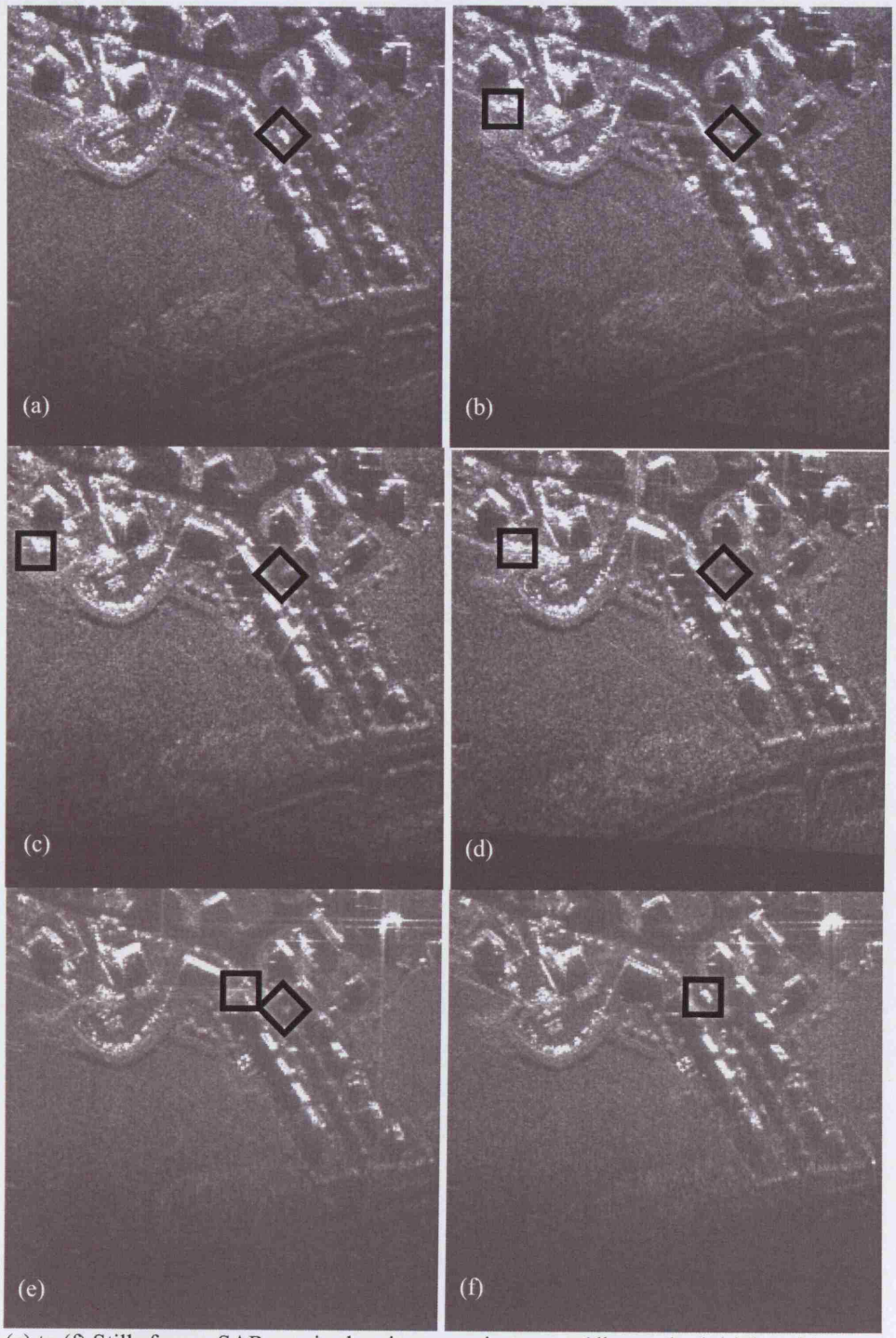

Figure 44: (a) to (f) Stills from a SAR movie showing a moving target (diamond = initial position, square = position in each image).

In certain cases such as this, the production of sub-aperture movies allows one to observe moving targets within the SAR image without the further processing which is required for techniques such as Single Phase Centre Detection [65]. However, if the target was not moving predominately in the range direction, the target return (even in each sub-aperture) would appear smeared. In this case, one needs to apply a quadratic

phase shift to the data in Fourier domain (X, Y) to account for any cross-track motion. The author has investigated such techniques but unfortunately, such data cannot be presentation in this document.

5.3 Layer, shadow and multipath directions in SAR imagery

5.3.1 Introduction

As discussed previously, layer, shadow and multipath are commonplace in SAR imagery. In exploiting SAR imagery of urban areas, the ability of analysts to categorise responses as one of these phenomena is often critical to the identification of the objects that cause such responses. In order to do so, it is vital that the direction of such scattering events can be predicated given a certain imaging geometry, both in the slant and ground planes. This is trivial for broadside collections where layover, shadow and multipath all occur along the slant and ground range axes, $\hat{y}$, and, $\bar{y}$, but for squinted SAR collections this is not the case. In this section, we present the approach described in [2] for the prediction of layover and shadow angles but the author also provides a treatment of multipath that predicts the direction that multipath will follow in SAR imagery.

5.3.2 Coordinate definitions

As shown in chapter 2, the two planes that conventionally define the SAR collection and processing geometries are the slant plane and ground plane, as shown in Figure 45. Herein we follow the convention in [2] and denote the ground plane axes as $(\bar{\mathbf{x}},\bar{\mathbf{y}},\bar{\mathbf{z}})$ and the slant plane axes by $(\hat{\mathbf{x}},\hat{\mathbf{y}},\hat{\mathbf{z}})$. The two sets of axes are co-incidental at their origins, which are positioned at the ground reference point (GRP) and are assumed to be at the centre of the illuminated spotlight scene. The ground plane is chosen by appropriate choice of the ground plane normal $\bar{\mathbf{z}}$. The axes $\bar{\mathbf{y}}$ and $\hat{\mathbf{y}}$ are in the directions of ground range and slant range and the axes $\bar{\mathbf{x}}$ and $\hat{\mathbf{x}}$ represent the cross-range directions in the corresponding planes.

The slant plane normal is $\hat{\mathbf{z}}$ and is defined by two vectors that lie on the slant plane, $\mathbf{R}_i$ and $\mathbf{R}_j$,

$$\hat{\mathbf{z}} = \pm \frac{\mathbf{R}_i \times \mathbf{R}_j}{\left|\mathbf{R}_i \times \mathbf{R}_j\right|}. \tag{106}$$

with the sign chosen such that it has a component along the direction of $\bar{\mathbf{z}}$ (such that $\hat{\mathbf{z}} \cdot \bar{\mathbf{z}} > 0$). In practice, $\mathbf{R}_i$ and $\mathbf{R}_j$ are often chosen to coincide with the GRP to sensor positions at 20% and 80% of the way through the synthetic aperture. $\hat{\mathbf{y}}$ is the unit vector defined by the vector, $\mathbf{R}_{mid}$, which joins the GRP to the position of the SAR sensor at the aperture centre, with

$$\hat{\mathbf{y}} = \frac{\mathbf{R}_{mid}}{|\mathbf{R}_{mid}|}. \tag{107}$$

Hence the third axes, $\hat{\mathbf{x}}$, is defined by the relation

$$\hat{\mathbf{x}} = \hat{\mathbf{y}} \times \hat{\mathbf{z}}. \tag{108}$$

$\overline{\mathbf{y}}$ is the normalised projection of the unit vector $\hat{\mathbf{y}}$ onto the ground plane

$$\overline{\mathbf{y}} = \frac{\hat{\mathbf{y}} - (\hat{\mathbf{y}} \cdot \overline{\mathbf{z}})\overline{\mathbf{z}}}{|\hat{\mathbf{y}} - (\hat{\mathbf{y}} \cdot \overline{\mathbf{z}})\overline{\mathbf{z}}|}, \tag{109}$$

thus defining $\overline{\mathbf{x}}$ as

$$\overline{\mathbf{x}} = \overline{\mathbf{y}} \times \overline{\mathbf{z}}. \tag{110}$$

The choice of the ground and slant planes in turn defines three fundamental angles; φ, ψ, and ζ which are known as the tilt, grazing and slope angles respectively as shown in Figure 45 [2] and are defined below;

$$\cos\varphi = \hat{\mathbf{x}} \cdot \overline{\mathbf{x}}, \tag{111}$$

$$\cos\psi = \hat{\mathbf{y}} \cdot \overline{\mathbf{y}}, \tag{112}$$

$$\cos\zeta = \hat{\mathbf{z}} \cdot \overline{\mathbf{z}}. \tag{113}$$

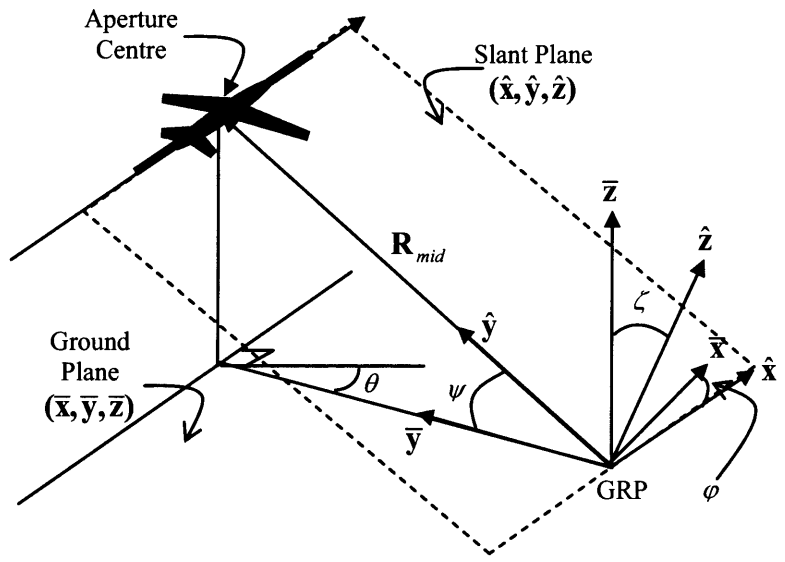

Figure 45: Definitions of slant and ground planes and the fundamental angles; φ, ψ, and ζ.

When calculating the directions of shadows, layover and multipath, it is also instructive to introduce the angle, η, which is the angle between the slant plane and the ground plane in the direction of the $\overline{\mathbf{x}}$ axes (see Figure 12, Chapter 2).

Two vectors that lie on the slant plane may be written in terms of ground plane co-ordinate system $(\bar{\mathbf{x}},\bar{\mathbf{y}},\bar{\mathbf{z}})$ as

$$\mathbf{v}_1 = \bar{\mathbf{x}} + \tan\eta\bar{\mathbf{z}} \tag{114}$$

$$\mathbf{v}_2 = \bar{\mathbf{y}} + \tan\psi\bar{\mathbf{z}}. \tag{115}$$

The slant plane normal can then be described by

$$\hat{\mathbf{z}} = \frac{\mathbf{v}_1 \times \mathbf{v}_2}{|\mathbf{v}_1 \times \mathbf{v}_2|} = -\tan\eta\bar{\mathbf{x}} - \tan\psi\bar{\mathbf{y}} + \bar{\mathbf{z}}, \tag{116}$$

which, with $\tan\eta = \alpha$, $\tan\psi = \beta$ and $\gamma = \frac{1}{|\mathbf{v}_1 \times \mathbf{v}_2|} = \frac{1}{\sqrt{\tan\eta^2 + \tan\psi^2 + 1}} = \cos\varsigma$ can be rewritten as

$$\hat{\mathbf{z}} = \gamma(-\alpha\bar{\mathbf{x}} - \beta\bar{\mathbf{y}} + \bar{\mathbf{z}}). \tag{117}$$

Additionally, from see Figure 12 (Chapter 2),

$$\hat{\mathbf{y}} = \cos\psi\bar{\mathbf{y}} + \sin\psi\bar{\mathbf{z}}, \tag{118}$$

so that from (110)

$$\hat{\mathbf{x}} = \gamma[(\cos\psi + \beta\sin\psi)\bar{\mathbf{x}} - \alpha\sin\psi\bar{\mathbf{y}} + \alpha\cos\psi\bar{\mathbf{z}}]. \tag{119}$$

5.3.3 Layover

As we showed earlier in chapter 2, equation (72), objects above the ground plane will appear translated in a SAR image due to the layover effect. This effect may also be described by the projection of a target of height, *h*, in the direction $\bar{\mathbf{z}}$ onto the slant plane given by (Figure 46(a))

$$\hat{\mathbf{p}} = h[\bar{\mathbf{z}} - (\hat{\mathbf{z}} \cdot \bar{\mathbf{z}})]\hat{\mathbf{z}}. \tag{120}$$

For some value of *k*, the target will also project in the same direction onto the ground plane (Figure 46(b))

$$\bar{\mathbf{p}} = h[\bar{\mathbf{z}} - k\hat{\mathbf{z}}] \tag{121}$$

$$\frac{1}{h}\bar{\mathbf{p}} \cdot \bar{\mathbf{z}} = \bar{\mathbf{z}} \cdot \bar{\mathbf{z}} - k\hat{\mathbf{z}} \cdot \bar{\mathbf{z}}$$

$$0 = 1 - k\hat{\mathbf{z}} \cdot \bar{\mathbf{z}}$$

$$k = \frac{1}{\hat{\mathbf{z}} \cdot \bar{\mathbf{z}}}$$

$$\Rightarrow \bar{\mathbf{p}} = h\left(\bar{\mathbf{z}} - \frac{\hat{\mathbf{z}}}{\hat{\mathbf{z}} \cdot \bar{\mathbf{z}}}\right). \tag{122}$$

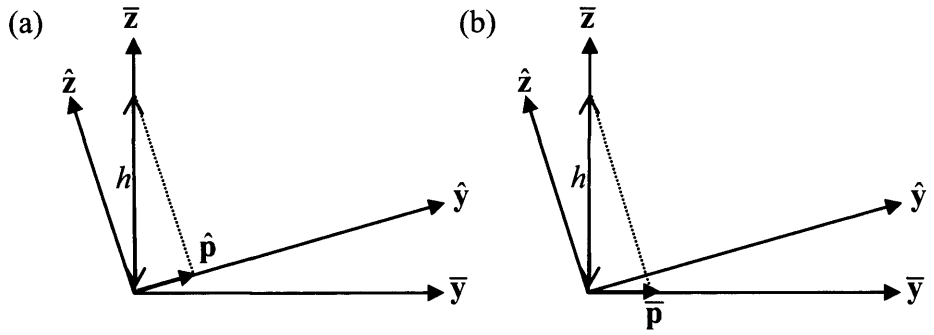

Figure 46: Target of height h projected onto (a) slant plane, (b) ground plane.

Using (117) to (119), (120) and (122) can be decomposed into range and cross-range components in the slant and ground planes. The results are summarised in

Table 7.

	Slant plane	Ground Plane
Cross-range(x)	$h\gamma\alpha\cos\psi = h\cos\varsigma\tan\eta\cos\psi$	$h\alpha = h\tan\eta$
Range(y)	$h\sin\psi$	$h\beta = h\tan\psi$
Magnitude	$h\sin\varsigma$	$h\tan\varsigma$

Table 7: Extent of layover in cross-range and range directions for slant and ground plane imagery of an object of height, h.

5.3.4 Shadowing

An object of height h may also cast a shadow from the top of the object onto the ground plane in the direction of imaging, $-\hat{\mathbf{y}}$. From Figure 47, for some value of k'

$$\bar{\mathbf{s}} = h[\bar{\mathbf{z}} - k'\hat{\mathbf{y}}] \tag{123}$$

$$\bar{\mathbf{s}} \cdot \bar{\mathbf{z}} = h\bar{\mathbf{z}} \cdot \bar{\mathbf{z}} - hk'\hat{\mathbf{y}} \cdot \bar{\mathbf{z}}$$

$$k' = \frac{1}{\hat{\mathbf{y}} \cdot \bar{\mathbf{z}}}$$

$$\Rightarrow \bar{\mathbf{s}} = h\left[\bar{\mathbf{z}} - \frac{\hat{\mathbf{y}}}{\hat{\mathbf{y}}.\bar{\mathbf{z}}}\right]. \tag{124}$$

In the slant plane, for some value of k'', from Figure 47, we have

$$\hat{\mathbf{s}} = \bar{\mathbf{s}} - k''\hat{\mathbf{z}} \tag{125}$$

$$\hat{\mathbf{s}} \cdot \hat{\mathbf{z}} = \bar{\mathbf{s}} \cdot \hat{\mathbf{z}} - k''\hat{\mathbf{z}} \cdot \hat{\mathbf{z}},$$

$$k'' = \bar{\mathbf{s}} \cdot \hat{\mathbf{z}}$$

$$\Rightarrow \hat{\mathbf{s}} = \bar{\mathbf{s}} - (\bar{\mathbf{s}} \cdot \hat{\mathbf{z}})\hat{\mathbf{z}}. \tag{126}$$

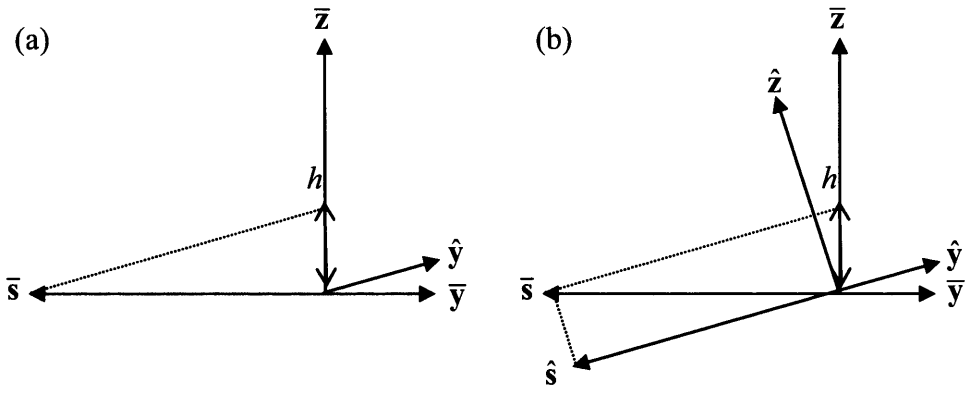

Figure 47: Target of height h casting a shadow vector, $\bar{\mathbf{s}}$, in the ground plane (a) and, $\hat{\mathbf{s}}$, in the slant plane (b).

Using (12) to (14), (19) and (21) can be decomposed into range and cross-range components in both the slant and ground plane. These results are summarised in Table 8.

	Slant plane	Ground Plane
Cross-range(x)	$h\tan\eta\cos\psi$	0
Range(y)	$-h\cos\psi/\tan\psi$	$-h/\tan\psi$
Magnitude	$h\sqrt{\cos^2\psi\cos^2\varsigma}$	$h/\tan\psi$

Table 8: Shadow extent in cross-range and range directions for slant and ground plane imagery of an object of height, h.

5.3.5 Multipath

Multipath effects occur when either the transmitted or received radar signal is scattered from more than one object or surface. Common instances of multipath often occur when cavities are illuminated in SAR images (such as engine ducts, vents, or opening in buildings). Typically, the resultant multipath signatures can be classified as either discrete or diffuse. Discrete signatures appear like bright point-light responses and may be modelled by appropriate EM prediction algorithms. Diffuse signatures appear like a random 'cloud' of lower intensity responses and are often formed by processes that are difficult to model.

A multipath response can be thought of a time delayed return. Here we introduce the vector $\hat{\mathbf{m}}$ to model this multipath in the slant plane. We define $\hat{\mathbf{m}}$ such that it is in the direction, $-\hat{\mathbf{y}}$, and has a length, $m = |\hat{\mathbf{m}}|$ (which is the slant plane path length related to the time delay). We also introduce the vector $\overline{\mathbf{m}}$ in the ground plane, that when projected onto the slant plane, produces an equivalent path length delay as $\hat{\mathbf{m}}$. Without loss of generality we may express $\overline{\mathbf{m}}$ as

$$\overline{\mathbf{m}} = (\overline{\mathbf{m}}\cdot\overline{\mathbf{x}})\overline{\mathbf{x}} + (\overline{\mathbf{m}}\cdot\overline{\mathbf{y}})\overline{\mathbf{y}}\,. \tag{127}$$

We may then project this vector onto our slant plane

$$\begin{aligned}\hat{\mathbf{m}} &= \overline{\mathbf{m}} - (\overline{\mathbf{m}}\cdot\hat{\mathbf{z}})\hat{\mathbf{z}} \\ &= (\overline{\mathbf{m}}\cdot\overline{\mathbf{x}})\overline{\mathbf{x}} + (\overline{\mathbf{m}}\cdot\overline{\mathbf{y}})\overline{\mathbf{y}} - (\overline{\mathbf{m}}\cdot\overline{\mathbf{x}})(\overline{\mathbf{x}}\cdot\hat{\mathbf{z}})\hat{\mathbf{z}} - (\overline{\mathbf{m}}\cdot\overline{\mathbf{y}})(\overline{\mathbf{y}}\cdot\hat{\mathbf{z}})\hat{\mathbf{z}}\,.\end{aligned} \tag{128}$$

From our earlier definition of $\hat{\mathbf{m}}$ we insist that

$$\hat{\mathbf{m}}\cdot\hat{\mathbf{x}} = (\overline{\mathbf{m}}\cdot\overline{\mathbf{x}})(\overline{\mathbf{x}}\cdot\hat{\mathbf{x}}) + (\overline{\mathbf{m}}\cdot\overline{\mathbf{y}})(\overline{\mathbf{y}}\cdot\hat{\mathbf{x}}) = 0 \tag{129}$$

$$\hat{\mathbf{m}}\cdot\hat{\mathbf{y}} = (\overline{\mathbf{m}}\cdot\overline{\mathbf{x}})(\overline{\mathbf{x}}\cdot\hat{\mathbf{y}}) + (\overline{\mathbf{m}}\cdot\overline{\mathbf{y}})(\overline{\mathbf{y}}\cdot\hat{\mathbf{y}}) = -m\,. \tag{130}$$

Then from (129) and using (118)

$$\hat{\mathbf{m}} \cdot \hat{\mathbf{y}} = (\overline{\mathbf{m}} \cdot \overline{\mathbf{y}})(\overline{\mathbf{y}} \cdot \hat{\mathbf{y}})$$
$$\Rightarrow \overline{\mathbf{m}} \cdot \overline{\mathbf{y}} = \frac{\hat{\mathbf{m}} \cdot \hat{\mathbf{y}}}{\overline{\mathbf{y}} \cdot \hat{\mathbf{y}}} = \frac{-m}{\cos\psi} \cdot \tag{131}$$

Similarly, from (129) and using (119)

$$\overline{\mathbf{m}} \cdot \overline{\mathbf{x}} = -\frac{(\overline{\mathbf{m}} \cdot \overline{\mathbf{y}})(\overline{\mathbf{y}} \cdot \hat{\mathbf{x}})}{\overline{\mathbf{x}} \cdot \hat{\mathbf{x}}} = -\frac{m}{\cos\psi}\frac{\gamma\alpha\sin\psi}{\cos\varphi} \tag{132}$$

and since $\gamma = \cos\varsigma = \dfrac{\sin\varphi}{\tan\eta}$ and $\alpha = \tan\eta$

$$\overline{\mathbf{m}} \cdot \overline{\mathbf{x}} = -m\tan\varphi\tan\psi = -m\tan\theta\sin\psi\tan\psi \tag{133}$$

5.3.6 Summary and output

The directions and extent of the layover, shadow and multipath vectors are summarised in Figure 48. Predicted multipath directions have been confirmed by comparison with real SAR imagery, but unfortunately, such data cannot be presented in this document.

The output of this study is a java software tool written by the author and currently used by image analysts that regrettably cannot be presented in this document. However, a brief description of its functionality is included here.

The tool reads in raw radar data from various sources, reads in the metadata and provides graphical outputs of radar parameters, collection information and the exploitation information derived above. It allows the analyst to calculate layover and shadow extent and their direction for a given object height. Alternatively, it permits the height to be calculated by measurement of the shadow or layover return. Additionally, the angle of the multipath relative to the shadow is also displayed. It provides the user with this information for full azimuth resolution imagery but also allows the user to specify sub-apertures (users may control the number of frames and percentage of full aperture used) and outputs the equivalent information for each frame. This information is then animated, to enable analysts to compare the motion of any observed scattering phenomenology in the sub-aperture movie with the predicted information in order to aid the identification of objects within the imaged scene.

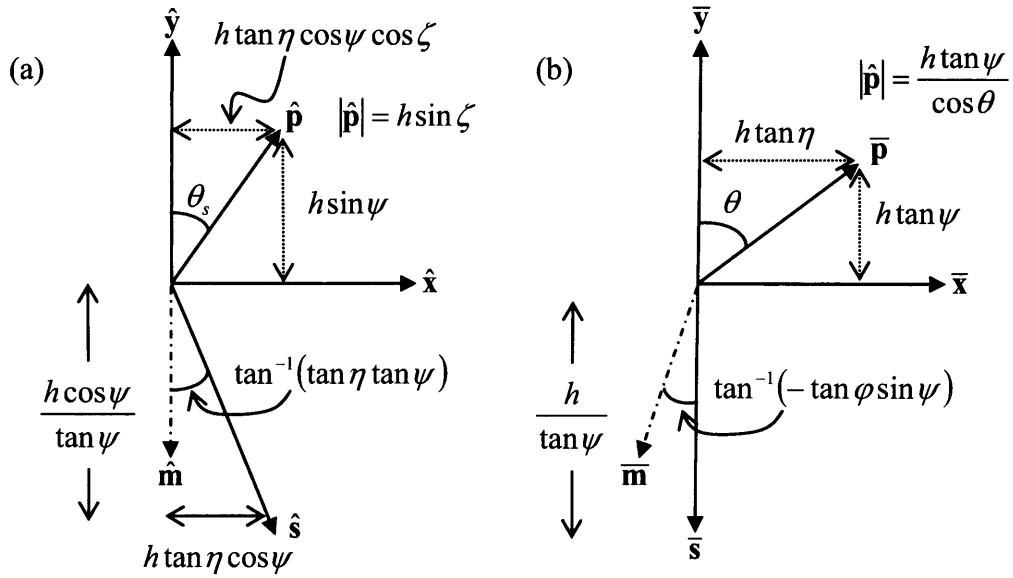

Figure 48: Summary of layover, shadow and multipath vectors for slant (a) and ground planes (b).

5.4 Urban shadow simulation

5.4.1 Motivation

Previously, we have shown how shadowing effects can be advantageous when attempting to extract height information, additionally, the classification stage of an assisted target recognition (ATR) process benefits from target shape and height information that the shadow can provide [62]. However, in general the presence of shadowing in urban images is detrimental to the image interpretation task. A scatterer that is obscured during part of the synthetic aperture formation may not be fully resolved in the azimuth direction. The degree to which its resolution is coarsened is proportional to the fraction of the aperture that is obscured. Moreover, if a scatterer remains obscured throughout the image formation process then it will not be visible in the SAR image. This could result in a possible target remaining undetected or the loss of potential surveillance information.

The following section attempts to quantify the relative impact of this effect for different radar operating modes. The approach used was to develop shadowing and layover prediction algorithms and analyse the resultant outputs. The goal of the simulation algorithms is not to predict the signatures of the particular buildings but to accurately simulate the layover and shadows cast by each building.

5.4.2 Model generation

The simulation procedure begins with the generation of a two dimensional array of complex numbers $x_{i,j}$ that represents the position and height of buildings on the ground plane of a particular scene. The indices, i and j, correspond to the ground range spatial co-ordinates of each pixel. The real part of $x_{i,j}$ is set to 2 if the pixel is part of a building and 1 if it is part of the ground return (i.e. $Re[x_{i,j}] \in \{1, 2\}$). The height of each pixel in metres above the ground level is given by the imaginary part of $x_{i,j}$, $Im[x_{i,j}]= h$. Pixels forming the ground return are set to zero height. For simplicity, each building is assumed to have a flat roof and the ground is assumed to be a horizontal plane. The type of buildings and their arrangement within each scene can be generated randomly or as specified by the user. An example input file is shown below.

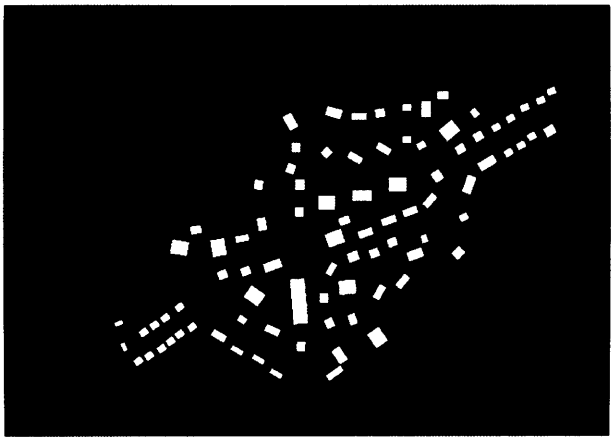

Figure 49: Building model of village (buildings modelled as flat roofed rectangular structures, dimensions and positions obtained from architectural drawings)

5.4.3 Shadow and layover simulation

The next stage of the procedure involves the production of an image containing the simulated shadows and foreshortened buildings. The user specifies the imaging geometry in terms of the imaging leg bearing, ϕ_{leg}, ground plane squint angle, θ, and grazing angle, ψ. From Figure 50, the imaging bearing $\phi_{imaging}=\phi_{leg}+90-\theta$.

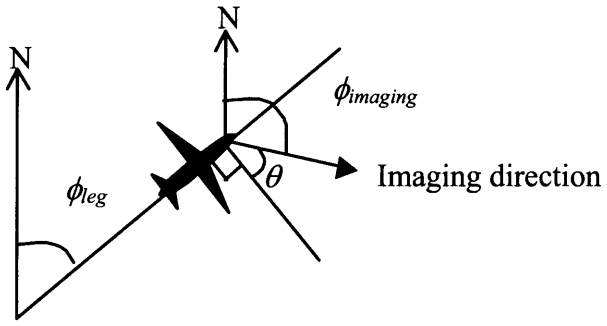

Figure 50: Definition of imaging geometry for shadow and layover simulation.

The input building model is then rotated so that the imaging direction is from the top of the image to the bottom. The rotated model is then interpolated into slant range co-ordinates. Each pixel with a non-zero height is shifted as described to account for the layover as described in equation (122). Correspondingly, shadowing information is then computed using equation (124).

For the purposes of this study, we assume that all buildings are flat roofed case 1, as defined previously. Pixels which are in shadow are assigned a zero real component. Hence we produce an image where buildings have $Re[x_{i,j}] = 2$, the ground plane has $Re[x_{i,j}] = 1$ and shadows have $Re[x_{i,j}]=0$. An example output of the simulation is shown in Figure 52. The simulation input was the village model shown in Figure 49 and the

grazing angle used was 28°. A real SAR image at this same viewing geometry is shown as comparison.

Before any building pixel is shadowed, a calculation is performed to establish whether its height is great enough to allow it to be seen above the shadow, if it can be seen its real component remains equal to 2. An example of a down range building and its own shadow becoming visible within another buildings shadow is illustrated in Figure 51. At this point we recall, as stated previously, that we are not concerned with the modelling of the building's radar signature, merely the layover and shadowing effects. We consider only uniform scattering from the buildings roofs, and do not address effects such as multipath.

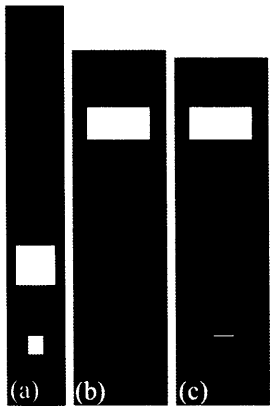

Figure 51: (a) Building model, (b) slant plane shadow and foreshortening prediction produced at a shallow grazing angle showing the smaller building obscured by the shadow cast by the larger structure, (c) slant plane image formed at slightly larger grazing angle allowing a section of the smaller building and its resultant shadow to be seen.

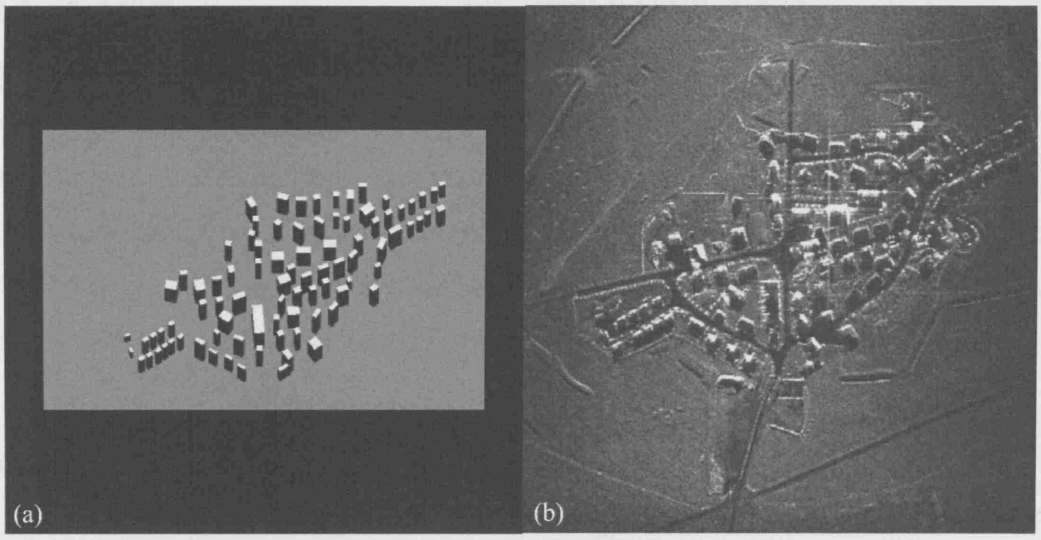

Figure 52: (a) Simulated shadow and layover areas of the village from the input model shown in Figure 49(grazing angle = 28°). (b) Real SAR image from the same imaging geometry.

5.4.4 Aperture formation

As we showed in chapter 2, the formation of a spotlight SAR image at a wavelength of, λ, at an azimuth resolution of, ρ, requires the scene to be illuminated over the angular range defined by equation (25)

$$\Delta\theta = \lambda/2\rho . \tag{134}$$

Hence, the actual shadow cast by an object in a SAR image will be a combination of the shadows cast from all angles used to form the aperture. In the final image, shadows will appear 'fan' like as shown in Figure 53. The resolution to which these shadow pixels may be resolved (in the azimuth direction) is proportional to the angular aperture over which they have been obscured. Pixels that are obscured throughout the aperture will not be visible in the final image.

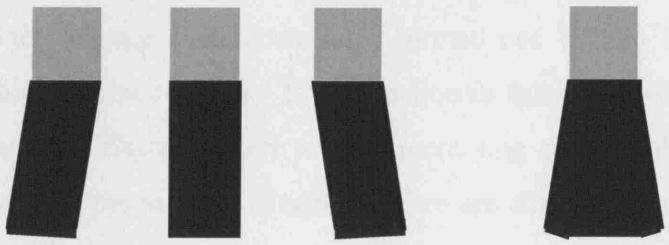

Figure 53: Shadows cast from the start, centre and end of the aperture combine to produce a fan like shadow in the final image.

5.4.5 Analysis

For a given input model and imaging geometry the areas of building, ground and shadows are calculated using the method above. This is repeated over the range of aspect angles needed to form the required aperture. The real components of these outputs (0=shadow, 1=ground and 2=building) are then multiplied on a pixel by pixel basis and clipped between 0 and 1. Therefore, all nonzero pixels are visible to the radar throughout the aperture and are thus fully resolvable.

The objective of the following analysis is to quantify the relative proportion of pixels within a given scene that may be fully resolved for various operating parameters. The results are presented as a cumulative statistic, where the percentage of resolvable pixels are calculated from imaging collections over an increasing number of aspect angles.

Here, the simulations were produced using only a limited number of models and hence the absolute percentage of fully resolvable pixels is somewhat arbitrary. Conclusions are only possible by a comparison between performances of different radar operational modes only. A future study should use randomly produced models to provide a Monte Carlo simulation estimate of these absolute levels.

5.4.6 Shadow variation with imaging geometry

The graph shown in Figure 56 shows the cumulative percentage of fully resolvable pixels verses aspect angle coverage for the simulated village scene (Figure 49) processed to 0.4m azimuth resolution at X-band from radar grazing angles of 28 and 5°. A 28° grazing angle corresponds to spaceborne or UAV type imaging geometry and 5° is a grazing angle typical of an airborne long standoff surveillance asset.

As one would expect, since shadow lengths are increased at lower grazing angles, the percentage of fully resolvable pixels is less at 5° than 28°. This effect is most marked for smaller angular coverage (where we have formed one or two images). For this particular scene this corresponds to a ~20% reduction in fully resolvable pixels. As we form more images at different aspect angles, increasing our angular coverage, the difference becomes less pronounced. Eventually, we are able to image the majority of pixels at both grazing angles as coverage approaches 90°.

5.4.7 Shadow variation with radar mode

Another factor that will influence the percentage of fully resolvable pixels is the resolution and the centre frequency at which the radar is operated. From (134), the finer

the azimuth resolution the wider the required angular aperture. Additionally, again from (134), when operating at low frequencies the angular aperture is further widened. For example, at UHF frequencies, to achieve an azimuth resolution of 0.5m, an angular aperture of 50° is required.

The graph shown in Figure 57 illustrates both these effects. From Figure 57 we see that as we image at finer resolutions the percentage of pixels we are able to fully resolve decreases. One should not interpret this result as suggesting that imaging should be performed at coarser resolutions over urban areas since those pixels that are not fully resolved, at 10cm resolution for example, may be resolvable at a lower resolution. Instead, it suggests that operating with very long apertures over urban areas may not result in fine resolution over all of the area under surveillance. Consequently, bandwidth interpolation approaches, such as those discussed in [23], should be employed.

However, the relationship with operational frequency is more straightforward. From in Figure 57 we see a reduction of ~30% in the percentage of fully resolvable pixels when we move from X-band to UHF.

5.4.8 Bistatic imaging

An area of current interest in both radar design and image exploitation is the use of bistatic SAR imaging systems [18, 19 and 20]. Bistatic radar systems are able to transmit on one platform and receive on another. This capability reduces the system's vulnerability to jamming and other countermeasures. For example, high value assets such as long standoff radars may transmit whilst remaining at a long standoff whilst a smaller value platform, such as UAV, may act as a receiver at a much closer range.

Conventionally, the angle between the two vectors describing the direction of the target from each platform is termed the bistatic angle, ϕ_b, as shown in Figure 54.

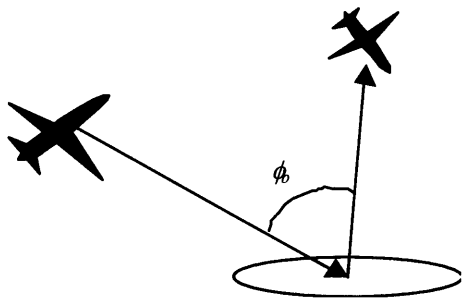

Figure 54: Bistatic imaging geometry.

During such an imaging process objects will cast two shadows caused by occultation on both the transmit path and the receive path. By combining the results of the shadowing prediction algorithms for both these paths one may produce a prediction of the shadowing characteristics for the bistatic SAR imaging process. An example bistatic prediction is shown in Figure 55. The corresponding graph showing cumulative percentage of fully resolvable pixels verses aspect angle coverage is shown in Figure 58. Over this particular area, we see how the double shadowing has reduced the area which can be fully resolved by approximately 10%. We also note that for the bistatic image even when the angular coverage reaches 90° we still have areas that cannot be resolved.

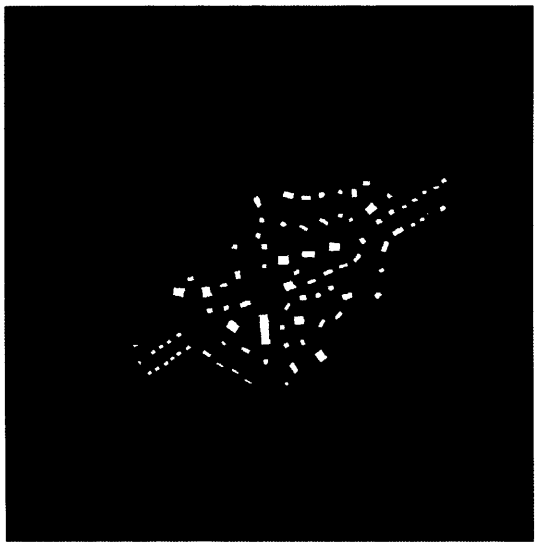

Figure 55: Bistatic shadow prediction using the village model with a bistatic angle of 67° and a 9° grazing angle

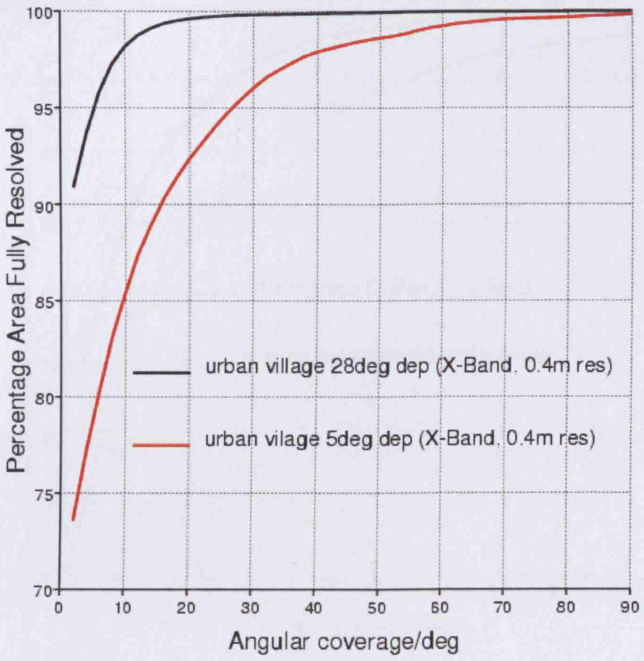

Figure 56: Graph showing the cumulative percentage of resolvable pixels verses aspect angle coverage for the simulated village scene (Figure 49) processed to 0.4m azimuth resolution at X-band from radar grazing angles of 28 and 5°.

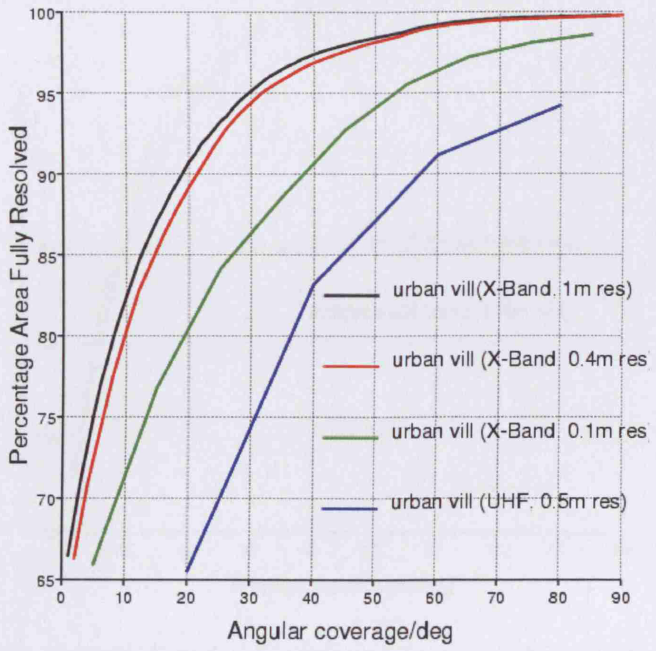

Figure 57: Graph showing variation of resolvable pixels verses aspect angle coverage for various radar operating modes.

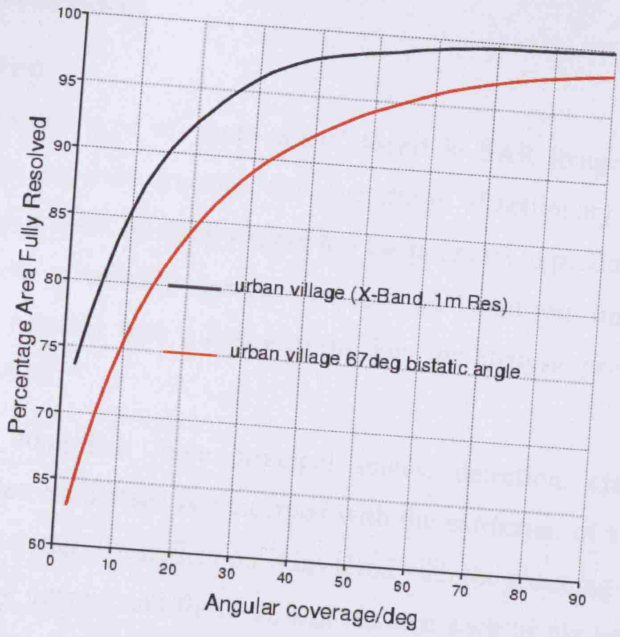

Figure 58: Graph showing variation of resolvable pixels verses aspect angle coverage for monostatic and bistatic X-band imaging (with an azimuth resolution of 0.4m).

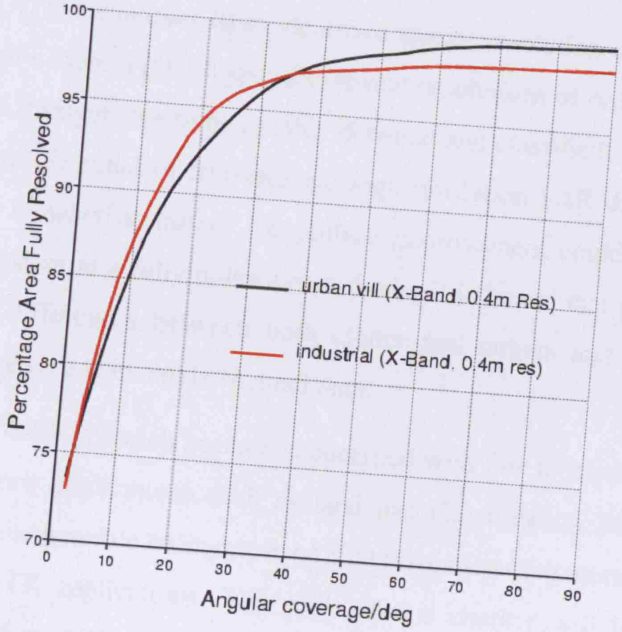

Figure 59: Graph showing variation of resolvable pixels verses aspect angle coverage when imaging the village scene and an industrial area based upon the Malvern site.

6 Polarimetric ATR

6.1 Introduction

In this chapter, another type of 'hard target' found in SAR imagery is considered. Instead of buildings and infrastructure, the recognition of stationary vehicles in SAR images is addressed. A SAR imaging system has the potential to produce large amounts of data hence from a military perspective the workload on image analysts is considerable. This, together with a desire to quicken the analysis process, has driven much research into ATR.

Target recognition comprises three principal stages; detection, classification and identification. The detection stage is concerned with the extraction of a possible target from its surrounding clutter. Classification is involved with the grouping of these targets into those of military interest and those of less concern such as civilian buildings or trees. The identification stage takes these targets, usually vehicles, and categorises them into various classes such as tanks or armoured personnel carriers.

Past studies into ATR techniques have identified spatial resolution as being critical in the success of such a system [66]. Typically, spatial resolutions of order half a meter or better are required if targets are to be reliably detected and classified. Given the current military exploitation potential of conventional high resolution SAR data, an important question exists as to whether further recognition improvement could be obtained by operating such a system in a fully polarimetric mode. It is hoped that polarimetry may highlight physical differences between both clutter and targets and different target classes to a greater degree than single channel data.

As discussed in 3.3 much research has been concerned with low to medium resolutions for civilian geoscience applications such as land use classification [48]. This study attempts to examine the possible military use of high resolution (sub metre) polarimetric SAR imagery for ATR applications. This bulk of this chapter will investigate the classification stage of an ATR system, in particular the analysis of the statistical and physical properties of polarimetric target signatures.

The radar used for this study was the MIDAS system owned and operated by Racal Defence Electronics in Wells. The system was operated at I-band and provided range and azimuth resolutions of up to10cm.

6.2 Calibration of ISAR imagery

6.2.1 ISAR

In order to analyse the statistical properties and test recognition algorithms a sizeable image set is required over a representative range of aspect and grazing angles. To gather such a data set with an airborne SAR system would prove practically infeasible, however using ISAR turntable imaging techniques, an appropriate sample set of images may be obtained.

Turntable inverse synthetic aperture radar (ISAR) provides a controlled environment in which to investigate the polarimetric signatures of vehicles over a wide range of different viewing geometries, shown in Figure 60. Unlike traditional SAR, ISAR uses movement of the target rather than the platform to produce the required Doppler bandwidth to achieve fine azimuth resolutions of up to 10cm [67]. The limitation of turntable data is that the target is not imaged within a clutter context. It is therefore imperative that the 'clean' signatures of ISAR targets are properly combined with research based on data collected from targets within realistic clutter backgrounds.

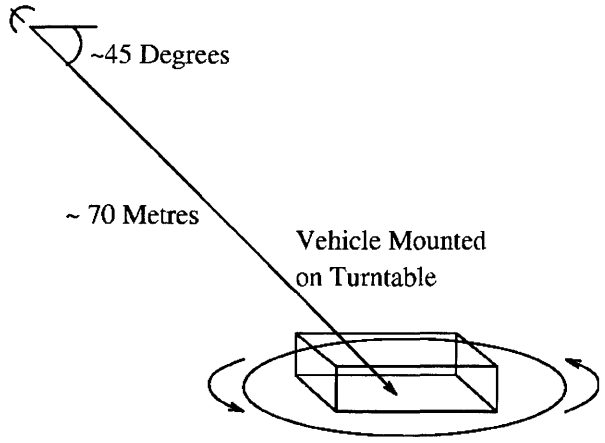

Figure 60: ISAR imaging set up

6.2.2 Motivation

In order to fully exploit polarimetric radar data it is essential that an accurate polarimetric calibration be performed. In addition to magnitude, it is vital that the relative phase of each channel may be accurately calibrated. This involves compensating for mismatches in amplitude and phase between the polarimetric channels. In practical terms, such a calibration procedure should be short enough to be undertaken before subsequent vehicle imaging, robust and repeatable. Yet it must also provide all the necessary information required to perform a fully polarimetric calibration of the given radar system. Since no calibration models or procedures were

applicable to the MIDAS data, the derivation of a generalised distortion model and novel calibration method was a vital component of this study. The approach is described in this section.

6.2.3 Calibration model

Every polarimetric radar system will contain distortions due to imbalances and cross-talks between different polarimetric channels on both transmit and receive. These may be characterised by the following distortion model.

On transmit, both H and V channels will have associated gains, G_H^T and G_V^T, together with cross-talks, g_H^T and g_V^T (these gains and cross-talks are complex quantities, representing both magnitude and phase imperfections within the system). The scattered field, $\mathbf{E_s}$, may then be modelled as,

$$\mathbf{E}_s = \begin{bmatrix} E_{HH}^S & E_{VH}^S \\ E_{HV}^S & E_{VV}^S \end{bmatrix} = c' e^{i\phi} G_H^T \begin{bmatrix} S_{HH} & S_{VH} \\ S_{HV} & S_{VV} \end{bmatrix} \begin{bmatrix} 1 & \gamma_H^T \\ \gamma_V^T & \Gamma_V^T \end{bmatrix}, \tag{135}$$

where c' is a constant for fixed range and ϕ is the phase of the point target. $\mathbf{S} = \begin{bmatrix} S_{HH} & S_{VH} \\ S_{HV} & S_{VV} \end{bmatrix}$ is the target's Sinclair scattering matrix as shown in equation (28) in the coordinate systems of the transmit-receive antenna. The Greek symbols are the corresponding Roman symbols normalised to G_H^T, e.g.

$$\gamma_V^T = g_V^T / G_H^T \text{ and } \Gamma_V^T = G_V^T / G_H^T. \tag{136}$$

The distortions present on receive are often modelled as

$$\mathbf{E}_r = G_H^R \begin{bmatrix} 1 & \gamma_V^R \\ \gamma_H^R & \Gamma_V^R \end{bmatrix} \mathbf{E}_s = c' e^{i\phi} G_H^T G_H^R \begin{bmatrix} 1 & \gamma_V^R \\ \gamma_H^R & \Gamma_V^R \end{bmatrix} \begin{bmatrix} S_{HH} & S_{VH} \\ S_{HV} & S_{VV} \end{bmatrix} \begin{bmatrix} 1 & \gamma_H^T \\ \gamma_V^T & \Gamma_V^T \end{bmatrix}, \tag{137}$$

where the superscript R denotes receive, for example, Γ_V^R, denotes the normalised gain when a signal is received in the V channel [10].

However this is only valid if, for example, the gain on receive VV, Γ_{VV}^R, is equal to the gain on receive HV, Γ_{HV}^R, and similarly for the cross-talk, $\gamma_{VV}^R = \gamma_{HV}^R$. The general requirement is that

$$\Gamma_{HH}^R = \Gamma_{VH}^R \equiv \Gamma_H^R, \Gamma_{VV}^R = \Gamma_{HV}^R \equiv \Gamma_V^R, \gamma_{HH}^R = \gamma_{VH}^R \equiv \gamma_H^R, \gamma_{VV}^R = \gamma_{HV}^R \equiv \gamma_V^R. \tag{138}$$

Unfortunately however, this is not the case within the MIDAS system. The receive path for *HH* is not the same as *VH* and likewise for *VV* and *HV*. This difference arises as the receive co-channels follow one path and the cross-channels another (this design allows the co and cross channels to be attenuated separately).

6.2.4 A new distortion model.

This aspect of the MIDAS design and indeed the design of other widely used radar systems made the development of a new, more general, distortion model vital to the success of this study. The following model is introduced to account for the shortcomings of the above distortion model.

In order to model all the imbalances and cross-talks in this case, it is convenient to transform $\mathbf{E_s}$, the scattered wave's 2x2 matrix, to its four vector form. Hence the operator, **V**, is introduced and defined by

$$\begin{bmatrix} E_{HH}^S \\ E_{HV}^S \\ E_{VH}^S \\ E_{VV}^S \end{bmatrix} = \mathbf{V} \begin{bmatrix} E_{HH}^S & E_{VH}^S \\ E_{HV}^S & E_{VV}^S \end{bmatrix}. \tag{139}$$

The distortions on receive may then be modelled using the 4x4 matrix operator below

$$\mathbf{E_r} = G_{HH}^R \begin{bmatrix} 1 & \gamma_{HV}^R & 0 & 0 \\ \gamma_{HH}^R & \Gamma_{HV}^R & 0 & 0 \\ 0 & 0 & \Gamma_{VH}^R & \gamma_{VV}^R \\ 0 & 0 & \gamma_{VH}^R & \Gamma_{VV}^R \end{bmatrix} \mathbf{V}\mathbf{E_S}, \tag{140}$$

where the elements are now normalised with respect to the gain of the *HH* channel. The distortion matrices for transmit and receive may be approximated in the combined form

$$\begin{aligned} \mathbf{E_r} &= c' e^{i\phi} G_H^T G_{HH}^R \begin{bmatrix} 1 & \gamma_{HV}^R & \gamma_V^T & 0 \\ \gamma_{HH}^R & \Gamma_{HV}^R & 0 & \gamma_V^T \Gamma_{HV}^R \\ \gamma_H^T \Gamma_{VH}^R & 0 & \Gamma_V^T \Gamma_{VH}^R & \gamma_{VV}^R \Gamma_V^T \\ 0 & \gamma_H^T \Gamma_{VV}^R & \gamma_{VH}^R \Gamma_V^T & \Gamma_V^T \Gamma_{VV}^R \end{bmatrix} \begin{bmatrix} S_{HH} \\ S_{HV} \\ S_{VH} \\ S_{VV} \end{bmatrix}, \\ &\equiv c e^{i\phi} \begin{bmatrix} 1 & \sigma_3 & \sigma_2 & 0 \\ \sigma_4 & f_2 & 0 & \sigma_2 f_2 \\ \sigma_1 f_3 & 0 & f_1 f_3 & \sigma_5 f_1 \\ 0 & \sigma_1 f_4 & \sigma_6 f_1 & f_1 f_4 \end{bmatrix} \begin{bmatrix} S_{HH} \\ S_{HV} \\ S_{VH} \\ S_{VV} \end{bmatrix} \end{aligned} \tag{141}$$

to first order in cross-talk magnitude. Where f_i are the channel imbalances and σ_i the cross-talk elements and $c = c' G_H^T G_{HH}^R$.

6.2.5 Calibration using a static dihedral

Polarimetric Calibration is often performed by imaging a flat plate reflector together with a dihedral reflector whose seam angle is set to a nominal 45°. The Sinclair scattering matrix for a flat plate and a dihedral with a seam angle, θ, is given by [10]

$$\mathbf{S}_{fp} = c_{fp}\begin{bmatrix} 1 & 0 \\ 0 & 1 \end{bmatrix} \qquad \mathbf{S}_{di} = c_{di}\begin{bmatrix} \cos 2\theta & \sin 2\theta \\ \sin 2\theta & -\cos 2\theta \end{bmatrix}. \tag{142}$$

Using the flat plate an estimate of the cross-polar isolation may be obtained, defined as the power ratio of the cross-channel to the co-channel. If the isolation is sufficiently small (<-25dB) the cross-talk may be assumed negligible and it is possible to calibrate the two co-channels relative to one another through calculation of the product, $f_1 f_4$. From the dihedral, relative calibration of the two cross channels may also be achieved. For a dihedral at 45° the return from the co-channels is only due to the cross-talk, making cross to co-channel calibration impossible within this set up.

Calibration of all the relative channel imbalances is only possible if there is received power in all four channels. This is best achieved with a seam angle of 22.5° when a perfect system receives equal power in all four channels. In order to find $ce^{i\phi}, f_2, f_1 f_3$ and $f_1 f_4$ the cross-talk must be assumed negligible and an accurate measurement of the dihedral seam angle relative to the polarisation basis must be obtained. These two requirements produce a significant error in the calculation of the channel imbalances. Given an angular error of δ, using (141) and (142) and expanding for small δ, the relative error in $|f_2|$, is given by

$$\Delta |f_2| = \frac{|f_2(\theta = 22.5 + \delta)|}{|f_2(\theta = 22.5)|} \approx 4\delta - (\sigma_2 + \sigma_3)(1 + 4\delta) + \frac{\sigma_4 + \sigma_2 f_2}{f_2}, \tag{143}$$

to first order in both δ and cross-talk. The quantities $|\sigma_2 + \sigma_3|^2$ and $\left|\frac{\sigma_4 + \sigma_2 f_2}{f_2}\right|^2$ are the co-polar and cross-polar isolation found when the dihedral seam angle is set to 45° and 0°. These are typically of the order of -25dB. Taking a root mean squared estimate the percentage errors are shown in Table 9.

$\Delta\lvert f_2\rvert$	δ(degree)
12%	0.5
16%	1
23%	2

Table 9: Channel imbalance RMS errors from static dihedral calibration.

From the symmetry of the dihedral's scattering matrix at θ = 22.5°, the errors in magnitude of $f_1 f_3$ and $f_1 f_4$ are also of the same order. Actual errors will be greater due to boresight misalignment. Data from Table 9 shows that, even if the seam angle is found to a reasonable accuracy and cross-talk is minimal, errors in determining channel imbalances are significant.

6.2.6 Calibration using a rotating dihedral

A different approach is to image a motor driven dihedral (shown in Figure 61) whose seam angle is constantly rotated over 360° [44]. This method allows the channel imbalances to be determined more accurately and efficiently by removing the θ dependency and the need to assume negligible cross-talk. A similar approach is described in [45] for the case of a reciprocal radar system.

This technique was investigated during a Polarimetric Calibration Trial at the Wells Quarry Facility in December 1998 [68]. Where a rotating dihedral was imaged using the MIDAS system operated at I-band (10GHz). Grazing angles of between 41 and 50° at a range of approximately 70metres were chosen to reproduce the geometries of the Wells Polarimetric Vehicle Imaging Trial, June 1998 [69], shown in Figure 62. Two speeds of seam angle rotation, 10 and 18°/s, were imaged over periods of three complete revolutions. A method of accurately boresighting the dihedral was developed. The dihedral was swept in elevation and azimuth and through appropriate maximisation and minimisation of the returns in the four channels the boresight position was found. This was supplemented with the use of a telescopic sight housed within the dihedral seam.

Figure 61: Photograph of the rotating dihedral

Figure 62: Photograph of the imaging geometry

6.2.7 Calculation of distortion elements

Figure 63 shows example data from the Calibration Trial. The graph clearly shows the characteristic $\cos^2 2\theta$ and $\sin^2 2\theta$ power variation with respect to seam angle as expected from the form of the dihedral's Sinclair scattering matrix (142). From the maxima and minima a period of rotation may be extracted.

Upon performing the following sine and cosine transforms as defined below.

$$\in_C^{ij} = \frac{4}{\pi}\int_0^{\pi/2} E_{ij}\cos 2\theta d\theta \quad \text{and} \quad \in_S^{ij} = \frac{4}{\pi}\int_0^{\pi/2} E_{ij}\sin 2\theta d\theta\,, \tag{144}$$

where $i, j \in \{\mathrm{H}, \mathrm{V}\}$. The following quantities may be evaluated,

$$\begin{aligned} \in_C^{HH} &= ce^{i\phi} & \in_S^{HH} &= ce^{i\phi}(\sigma_2+\sigma_3) \\ \in_C^{HV} &= ce^{i\phi}(\sigma_4-\sigma_2 f_2) & \in_S^{HV} &= ce^{i\phi} f_2 \\ \in_C^{VH} &= ce^{i\phi}(\sigma_1 f_3-\sigma_5 f_1) & \in_S^{VH} &= ce^{i\phi} f_1 f_3 \\ \in_C^{VV} &= -ce^{i\phi} f_1 f_4 & \in_S^{VV} &= ce^{i\phi}(\sigma_1 f_4+\sigma_6 f_1). \end{aligned}, \tag{145}$$

where σ_i and f_i, are elements of the distortion matrix.

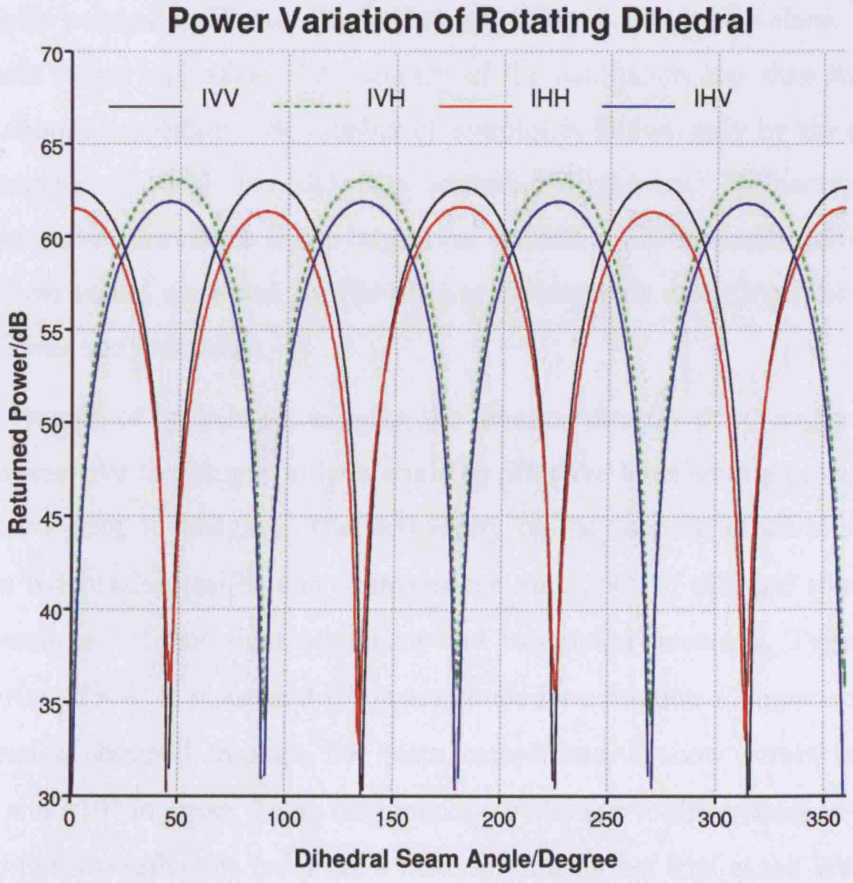

Figure 63: Power variation of a rotating dihedral

It is now possible to calibrate out channel imbalances simultaneously in all four of the polarimetric channels (i.e. the quantities $ce^{i\phi}, f_2, f_1f_3$ and f_1f_4 may all be determined over the period of 90°). For example, from the data in Figure 63 this process gives f_2 = 1.05e1.50i, f_1f_3 = 1.20e0.89i and f_1f_4 = 1.17e-0.75i. These measurements, unlike in the case of a static dihedral target, are independent of cross-talk, whose magnitude may also be estimated simultaneously from $\in_S^{HH}, \in_C^{HV}, \in_C^{VH}$ and $\in_S^{VV}$. Assuming the channel imbalances to be of the order of unity, an average root mean squared estimate of the cross-talk power may be calculated from,

$$\begin{aligned}
&\frac{1}{8\left|\in_C^{HH}\right|}\left(\left|\in_S^{HH}\right|^2+\left|\in_C^{HV}\right|^2+\left|\in_C^{VH}\right|^2+\left|\in_S^{VV}\right|^2\right)\\
&\approx\frac{1}{8}\left(\left|\sigma_2+\sigma_3\right|^2+\left|\sigma_4-\sigma_2\right|^2+\left|\sigma_1-\sigma_5\right|^2+\left|\sigma_1+\sigma_6\right|^2\right),\\
&\approx\frac{1}{8}\left(2\left|\sigma_1\right|^2+2\left|\sigma_2\right|^2+\left|\sigma_3\right|^2+\left|\sigma_4\right|^2+\left|\sigma_5\right|^2+\left|\sigma_6\right|^2\right)\\
&=\text{average r.m.s. cross - talk power.}
\end{aligned} \tag{146}$$

For the illustrated data set this gives a cross-talk power of approximately –31dB

As the above method performs the calibration using a series of values, individual measurement errors will affect the accuracy of the calibration less than in the static dihedral calibration method. The number of samples is limited only by the dwell time on the rotating dihedral and the data sampling frequency. Furthermore, as all measurements are taken for a single target, the method is automatically self-consistent in terms of the values measured for flat-plate or diplane type scattering. The method is robust, efficient and repeatable.

A possible source of error is not imaging the dihedral directly at boresight. Since the dihedral is sensitive to changes in look angle an effective boresighting procedure must be performed prior to imaging. The periodicity of the rotating dihedral's signature yields four independent calibration estimates for each 360° of dihedral rotation. This allows assessment of boresight alignment and calibration accuracy. Typical results indicate errors of < 4° in phase and 1% in amplitude for a rotation. Comparison with the co-polar ratios obtained through flat plate measurements show errors of ~2% in amplitude and <10° in phase. These differences may be due to differences in the spatial position of the two reflectors (of order 4 meters). In a further trial at the Wells facility during December 1999 [70] this effect was investigated. The rotating dihedral was imaged at the near and far range of the beam and the calculated channel imbalances

were compared to those from a dihedral positioned at the centre of the turntable. It was found that the near beam channel imbalance differences were approximately 5-10% in amplitude and <12° in phase, far beam results show differences of 10-20% in amplitude and <8° in phase. These suggest that the calibration parameters do vary somewhat at the beam extremities and although this should be noted it is not thought to be problem in calibrating turntable imagery where the region of interest is well contained within the beam centre.

Also investigated at the same trial were off-boresight errors. Dihedrals were imaged at boresight and then imaged at 1 and 2° away from this position. Results showed that even up to 2° from boresight channel imbalances were correct to within 5% in amplitude and 8° in phase. Although imbalances were found to be fairly robust cross-talk values were greatly overestimated. This is because channels imbalances are found using sine and cosine filters which extract only the sinusoidal behaviour and cross-talks manifest themselves as deviations from these functions. An example of the power variation of a rotating dihedral imaged at 2° from boresight is shown in Figure 64 below.

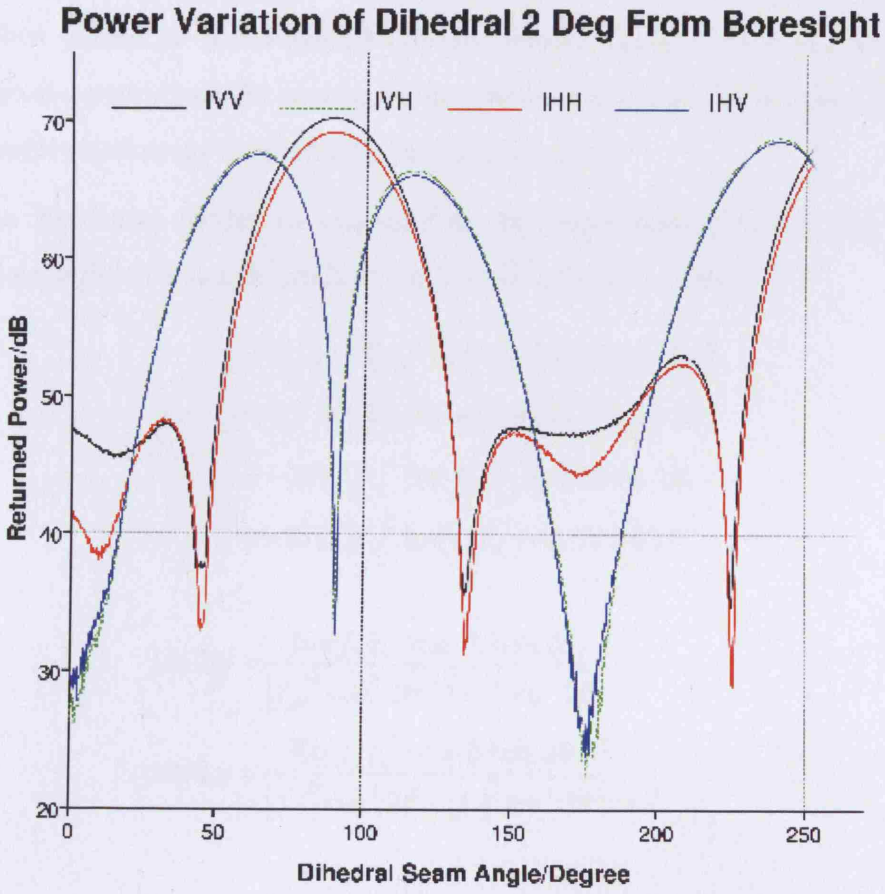

Figure 64: Power variation of a rotating dihedral 2° from boresight position

6.2.8 Poincaré sphere representation of the calibration procedure

Electromagnetic waves are often represented on a Poincaré sphere [9]. A monochromatic wave of the form (E_H, E_V) has the three independent Stokes parameters Q, U and V which form Cartesian co-ordinates of a sphere of radius I_0. Where

$$\begin{aligned} I_0 &= |E_V|^2 + |E_H|^2 = Q^2 + U^2 + V^2 \\ Q &= |E_V|^2 - |E_H|^2 = I_0 \cos 2\psi \cos 2\chi \\ U &= 2\,\mathrm{Re}(E_V E_H{}^*) = I_0 \sin 2\psi \cos 2\chi \\ V &= 2\,\mathrm{Im}(E_V E_H{}^*) = I_0 \sin 2\chi \end{aligned} \quad . \tag{147}$$

The two quantities ψ and χ are often referred to as the rotation and ellipticity angles.

For transmit V polarisation, i.e. an incident wave of (0, $E_0 e^{i\phi}$), a perfect system will return radiation from a rotating dihedral with the following Stokes vectors

$$\begin{aligned} I_0 &= E_0{}^2 \\ Q &= E_0{}^2(\cos^2 2\theta - \sin^2 2\theta) \\ U &= -2E_0{}^2 \cos 2\theta \sin 2\theta \\ V &= 0 \\ \therefore \psi &= -2\theta \text{ and } \chi = 0. \end{aligned} \quad . \tag{148}$$

Hence when plotted on a normalised Poincaré sphere, (Q/I_0, U/I_0, V/I_0), the rotating dihedral plots a path along the equator of the sphere, orbiting the sphere once every 90° of seam angle rotation (as shown by the red line Figure 65).

Using the distortion model to characterise the imperfections within the system, assuming negligible cross-talk, leads to the following Stokes vectors

$$\begin{aligned} I_0 &= E_0{}^2 |f_1|^2 \left(|f_4|^2 \cos^2 2\theta + |f_3|^2 \sin^2 2\theta \right) \\ Q &= E_0{}^2 |f_1|^2 \left(|f_4|^2 \cos^2 2\theta - |f_3|^2 \sin^2 2\theta \right) \\ U &= -2E_0{}^2 |f_1|^2 \,\mathrm{Re}(f_3 f_4{}^*) \cos 2\theta \sin 2\theta \\ V &= -2E_0{}^2 |f_1|^2 \,\mathrm{Im}(f_3 f_4{}^*) \cos 2\theta \sin 2\theta \end{aligned} \quad . \tag{149}$$

$$\tan 2\psi = \frac{\mathrm{Im}(f_3 f_4{}^*) \cos 2\theta \sin 2\theta}{|f_4|^2 \cos^2 2\theta + |f_3|^2 \sin^2 2\theta}$$

$$\sin 2\chi = \frac{\mathrm{Re}(f_3 f_4{}^*) \cos 2\theta \sin 2\theta}{|f_4|^2 \cos^2 2\theta - |f_3|^2 \sin^2 2\theta}.$$

So when plotted on a normalised Poincaré sphere, the channel imbalances skew the path of the rotating dihedral so that it no longer traces the path of the equator. The rotation and ellipticity angles are determined by the imaginary and real parts of the product, $f_3 f_4$.

Figure 65 shows 360° of rotation of the uncalibrated data. Clearly the dihedral's orbit around the Poincaré sphere is skewed compared to the perfect system (shown in red) by the distortions within the system. Note how a non-zero phase of the channel imbalances skews the orbit considerably. Figure 66 shows how, after calculation of f_2, $f_3 f_4$ and $f_1 f_4$, appropriate calibration may be performed to map the real data onto the equator of the Poincaré sphere.

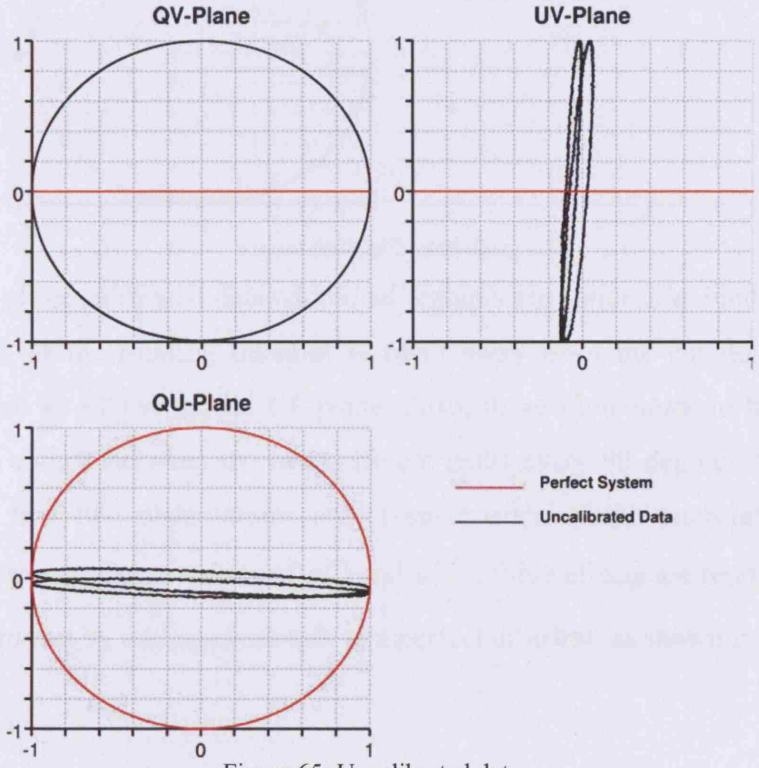

Figure 65: Uncalibrated data.

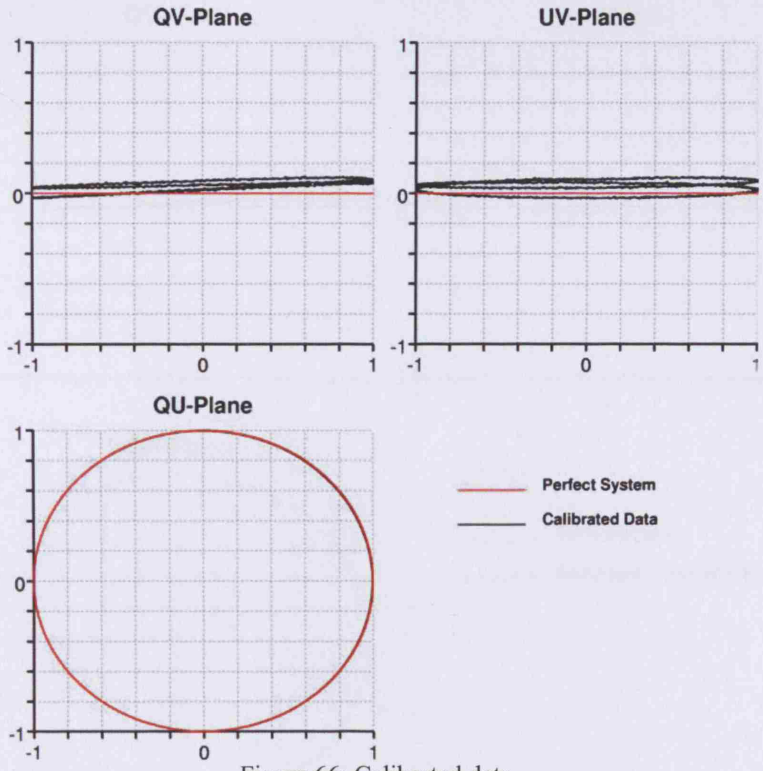

Figure 66: Calibrated data.

From the plot of the calibrated data additional features are noticeable. Firstly, in the *QV*-plane the path of the rotating dihedral is tilted away from the equator slightly and appears to form an ellipse in the *UV*-plane. Also, these plots seem to have a double period, with a switch between the two different paths every 90 degrees of seam angle rotation. The first two observations are characteristics of the cross-talk within the system. Using the measured values of $\in_C^{VH}$ and $\in_C^{VH}$, these effects are reproduced within the distortion model by adding cross-talk to a perfect dihedral, as shown in Figure 67.

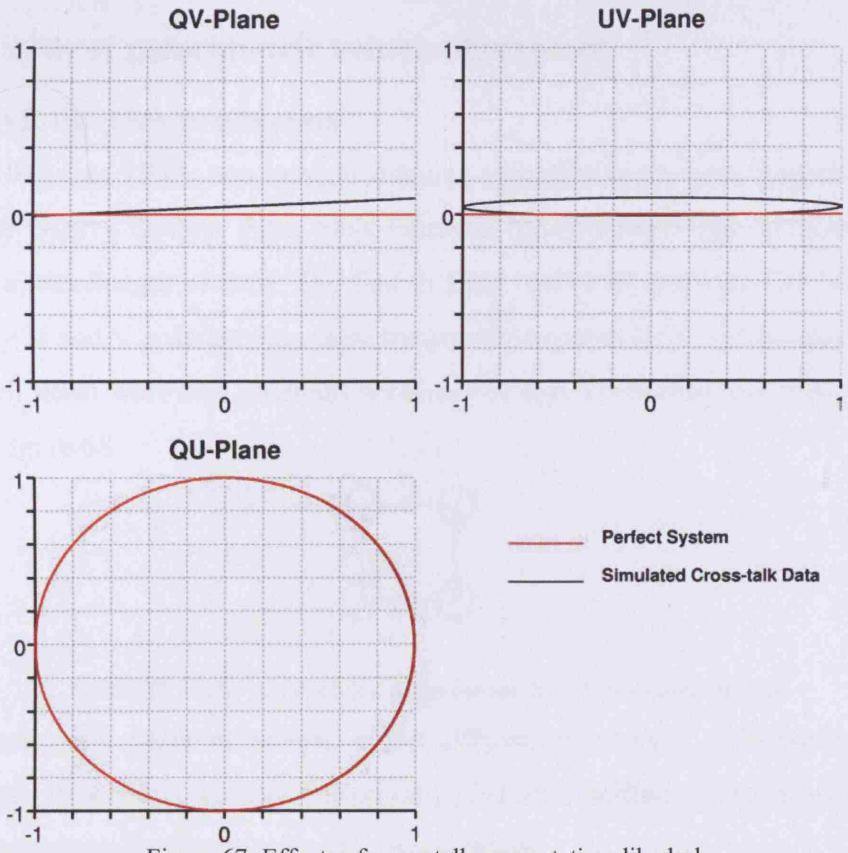

Figure 67: Effects of cross-talk on a rotating dihedral

Unfortunately, without making assumptions about a target's scattering matrix, these cross-talks cannot be removed on real data. However, with cross-talk powers found to be of the order of –30dB, the effects will be minimal. The double period effect however is not explained within this model. Possible explanations include effects due to small boresighting errors or physical imperfections in dihedral production.

6.3 Analysis of polarimetric vehicle signatures

6.3.1 ISAR imagery production

Between 1998 and 1999, two vehicle imaging turntable trials were undertaken at the RDE Wells Quarry facility. Both trials used the MIDAS radar system operating at I-band with a wavelength of 3cm. The first in June 1998 [69] employed a radar head set up whereby H and V polarisations were transmitted separately from two upper antennas and beneath these were two antennas receiving H and V polarisations respectively, as shown in Figure 68.

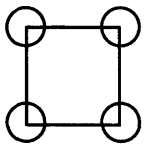

Figure 68: Radar head configuration during June 1998 turntable trial

Unfortunately, this produces relative phase differences between polarimetric channels that are range dependent. For this reason only channel amplitudes were analysed and no coherent decomposition techniques were investigated.

The trial produced a data set containing 8 vehicles; two Main Battle Tanks (MBTs), three Armoured Personnel Vehicles (APVs) and two lorries. All vehicles were processed over an entire period of rotation at 1° intervals and in order to aid analysis vehicle images were rotated about the centre of the turntable such that the turntable becomes the stationary frame of reference. Images were polarimetrically calibrated using a static dihedral and a flat plate (the rotating dihedral method described previously was developed following this trial). Individual channels were range registered by use of a down range corner reflector. Each vehicle was processed at up to 10cm range and azimuth resolutions and oversampled to half a resolution cell. Grazing angles simulating spaceborne geometries were chosen, the data processed was from 41° although additional data was recorded at between 41 and 60° grazing angles. A discussion of the variation of polarimetric intensity with respect to aspect angle is included in section 6.3.2.

The second turntable trial was undertaken during December 1999 [70] using the same MIDAS system but with a different radar head configuration. This time all polarimetric channels were transmitted and received by the same two antennas, shown in Figure 69.

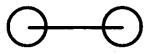

Figure 69: Radar head configuration during December 1999 turntable trial

The transmit and receive antennas are polarimetrically agile (PAG) and switch to give the following sequence; *VV*, *HV*, *VH*, *HH*. This system does not have the same range dependent polarimetric phase differences and so allows the use of coherent decomposition. During this trial nine vehicles were imaged each day, over a period of six days. Eight APVs were imaged together with one MBT. The rotating dihedral calibration process was performed enabling the production of a more accurately calibrated data set. Again all channels were range registered and each vehicle was processed to up to 10cm range and azimuth resolutions and oversampled to half a resolution cell.

6.3.2 Analysis of June 1998 turntable data

This initial analysis uses imagery of a MBT viewed at 41° grazing angle obtained from the June 1998 trial previously discussed, calibrated and processed at 20cm resolution. For the reasons described above only amplitude data was analysed. The objective of the analysis was to investigate the differences in behaviour of the polarimetric channels as the vehicle aspect angle changes through an entire revolution.

The intensity in any particular polarimetric channel may be averaged over the pixels containing returns from the vehicle for all of the 360 aspect angles. The mean pixel intensities over a 360° rotation are shown in Figure 70. Note the mean dB intensities have no absolute calibration and that the 0° reference is the angle where the tank is viewed head on by the radar, i.e. looking straight down the barrel. For a more concise graphically representation only one cross-channel (*HV*) is shown.

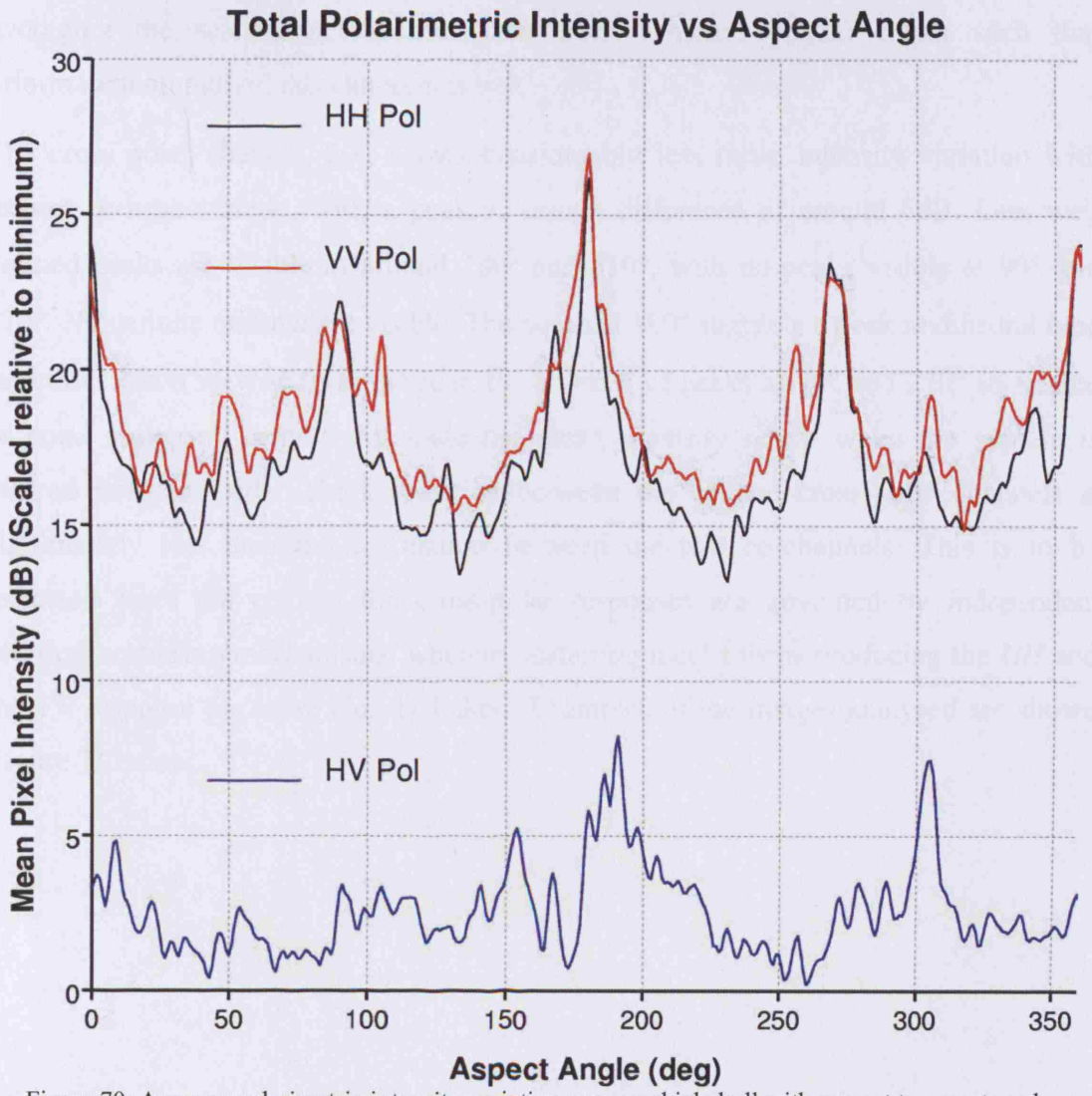

Figure 70: Average polarimetric intensity variation over a vehicle hull with respect to aspect angle

One feature immediately noticeable is the intensity difference between the co-polar and cross-polar channels, co-polar scattering being far the most dominant scattering mechanism with returns of the order of 15dB greater than the cross-polar channel. Also visible are the sharp peaks in intensity in the co-polar channels at 0°, 90°, 180° and 270°. The peaks at 0° and 180° are the largest, approximately 13dB greater than the minima at odd multiples of 45°. This shows that the vehicle appears brightest in the co-polar channels when viewed head on or directly from the rear or the side. At these viewing geometries the vehicle presents the most flat plate type structures to the boresight of the antenna head, thus maximising the co-channel return. Also noticeable is the degree of correlation between the *HH* and the *VV* channels, suggesting that when averaging pixels over the complete vehicle, only limited additional information is gained through the utilisation of both the *HH* and the *VV* channels. This is caused by

averaging the scattering responses over each vehicle's spatial extent such that information on individual scatterers is lost.

The cross polar channel, *HV*, shows considerably less mean intensity variation with respect to aspect angle, with a peak to trough difference of around 6dB. Less well defined peaks are visible at around 180° and 310°, with no peaks visible at 90° and 270°. No definite minima are visible. The peaks at 180° suggests a peak in dihedral type structures when viewed from the rear, the absence of peaks at 90° and 270° show that co-polar scattering centres dominate the mean intensity return when the vehicle is viewed from the side. The correlation between the co and cross-polar channels is significantly less than the correlation between the two co-channels. This is to be expected since the co and the cross-polar responses are governed by independent physical scattering mechanisms, whereas scattering mechanisms producing the *HH* and the *VV* response are more closely linked. Examples of the images analysed are shown Figure 71 below.

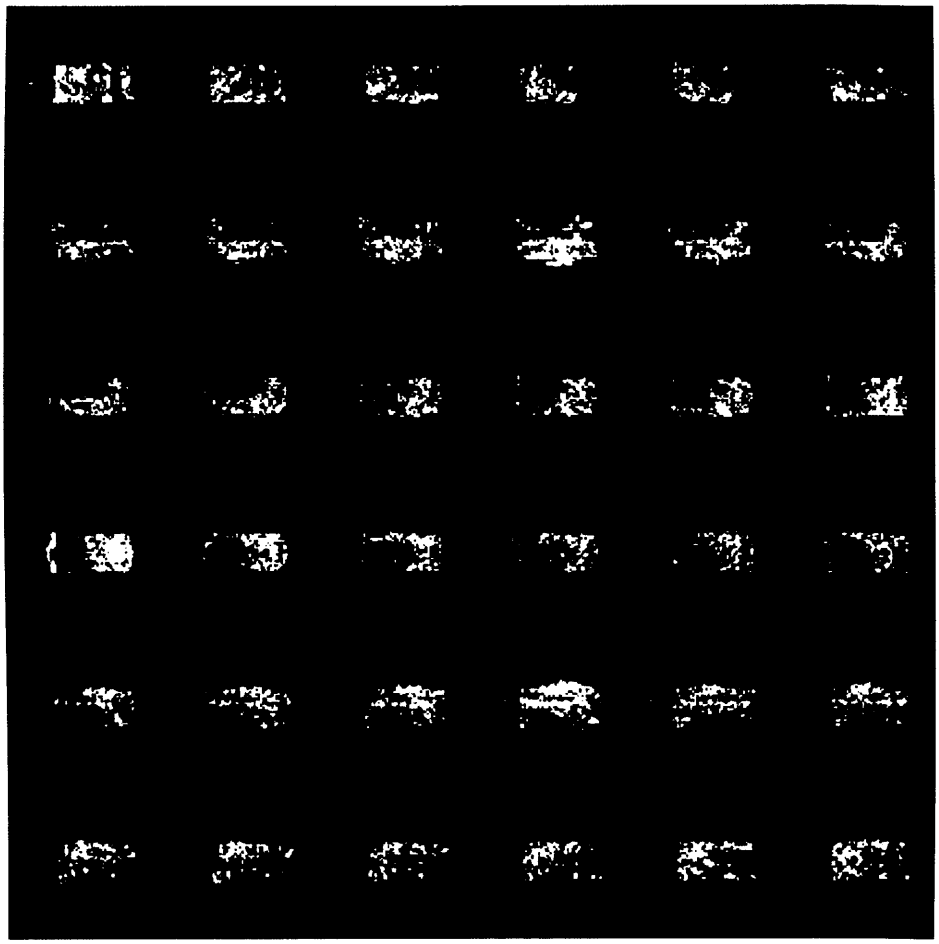

Figure 71: Changes in the *HH* polarimetric intensity at 10° intervals over a complete revolution (MBT Imaged at 41° grazing processed at 20cm range and azimuth resolution)

6.3.3 Analysis of December 1999 turntable data

The radar configuration in the December trial allowed the formation of coherent combinations of polarimetric channels. The question of signature stability with respect to aspect angle was again addressed. As was highlighted in the previous section vehicle signatures vary considerably with aspect angle, Figure 71 shows how different vehicles appear with only a 10° change in aspect angle. Using the December, data the question was posed as to whether one could identify any polarimetrically stable areas of a vehicle over a certain range of angles. A method using a variation of Cloude's polarimetric entropy technique [11, 48, 49], discussed previously, was employed to attempt to answer this question. The imagery used contained a MBT in travelling configuration imaged at 20cm resolution with a pixel spacing of 10cm from a grazing angle of 35°. Channel imbalances were calibrated using a rotating dihedral and crosstalk values were less then –30dB.

For each image pixel position one may calculate an average covariance matrix [9] over a certain range of angles

$$C = \begin{bmatrix} \langle |HH|^2 \rangle_\theta & \langle HHHV^* \rangle_\theta & \langle HHVV^* \rangle_\theta \\ \langle HVHH^* \rangle_\theta & \langle |HV|^2 \rangle_\theta & \langle HVVV^* \rangle_\theta \\ \langle VVHH^* \rangle_\theta & \langle VVHV^* \rangle_\theta & \langle |VV|^2 \rangle_\theta \end{bmatrix}, \tag{150}$$

where the $<>_\theta$ denotes an average over an angle θ. Since the ISAR imaging process uses a spread of angles in order to obtain such fine azimuth resolutions angular sections of images will be artificially correlated. The angle required to produce an azimuth resolution of ρ_r is given by

$$\Delta\theta = \frac{\lambda}{2\rho_r}. \tag{151}$$

So to form our images at 20cm with a wavelength of 3cm we have used 4.3° of rotation. Hence, to avoid producing artificially high correlations we generate the covariance matrix from images with an angular spacing of 5°. The choice of how many angles to average over is less constrained, here we arbitrarily chose 12 images chosen covering a range from –30 to 25° in aspect angle for illustrative purposes Again we nominally define vehicle boresight to be 0°.

Since the matrix is Hermitian it may be diagonalised with real eigenvalues μ_i and orthogonal eigenvectors U_i,

$$C = [U_3] \begin{bmatrix} \mu_1 & 0 & 0 \\ 0 & \mu_2 & 0 \\ 0 & 0 & \mu_3 \end{bmatrix} [U_3]^{*T}, \tag{152}$$

where

$$[U_3] = \begin{bmatrix} \cos\alpha_1 & \cos\alpha_2 & \cos\alpha_3 \\ \sin\alpha_1 \cos\beta_1 e^{i\delta_1} & \sin\alpha_2 \cos\beta_2 e^{i\delta_2} & \sin\alpha_3 \cos\beta_3 e^{i\delta_3} \\ \sin\alpha_1 \sin\beta_1 e^{i\gamma_1} & \sin\alpha_2 \sin\beta_2 e^{i\gamma_2} & \sin\alpha_3 \sin\beta_3 e^{i\gamma_3} \end{bmatrix}. \tag{153}$$

One may use polarimetric entropy as a measure of the polarimetric variation over the specified range of angles. This measure, introduced by Cloude, has been applied previously to clutter data on spatially averaged coherency matrices. Here we are concerned with how polarimetric properties change with aspect angle so we form an angular average. In the case of high resolution vehicle data, spatially averaging is not

appropriate since, unlike clutter, vehicle returns at high resolutions are spatial inhomogeneous.

Entropy, H, is defined as the logarithmic sum of the normalised eigenvalues, μ_i,

$$H = -\sum_{i=1}^{3} P_i \log_3 P_i, \quad P_i = \frac{\mu_i}{\sum_{i=1}^{3} \mu_i}. \tag{154}$$

By definition, entropy values vary between zero and one. Areas where H tends to zero are polarimetrically stable over the given angular range and are dominated by one primary scattering mechanism. Areas where the entropy approaches unity contain much polarimetric variation over the angular section. In the limit where H=1 the region is completely depolarising such as the return from a randomly orientated cloud of anisotropic particles.

One may now produce an entropy map using the calculated average covariance over the angular section from –30 to 25°, using images spaced by 5°. ISAR sample images in *HH* polarisation from within this angular section are included for reference (see Figure 72). The entropy map shown in Figure 73 is plotted as (1-H) so that bright areas of the image are polarimetrically stable.

Figure 72: ISAR Images (*HH*) of an MBT in travelling configuration imaged at –30°, -8° and 25° from boresight

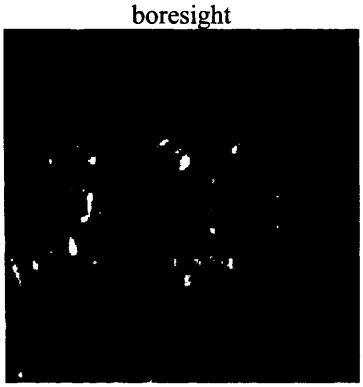

Figure 73: (1-*H*) Entropy map from –30° to 25° (bright areas have low entropy)

From Figure 73 we can see that there are definite regions of stability on the vehicles hull. Areas along the edges of the vehicle seem to be generally stable. Also clearly visible as stable regions are the front left hand corner of the tank, the front grill and the area on the right of the turret. These are the sort of features that may well be of use to an imaged analyst in identifying a vehicle type. Building such features into an automated classifier is a much harder task, requiring the generation of a single statistical variable characterising the spatial distribution of these features.

The next obvious question is whether we can identify the scattering mechanisms that produce these stable areas, this helps to interpret the underlying physical structures within the image. Again applying Cloude's land-use classification theorems to our vehicle analysis we use the alpha parameter as a polarimetric descriptor. Alpha is a weighted mean of the three eigenvector's rotation angles,

$$\alpha = \sum_{i=1}^{3} P_i \alpha_i \,. \tag{155}$$

where α_i is defined from the eigenvector u_i,

$$u_i = \begin{bmatrix} \cos\alpha_i \\ \sin\alpha_i \cos\beta_i e^{i\delta_i} \\ \sin\alpha_i \sin\beta_i e^{i\gamma_i} \end{bmatrix}. \tag{156}$$

Alpha is an angle between 0° and 90°. It can be shown that alpha tends to 0° for sphere or single bounce type scattering and approaches 90° for dihedral or double bounce type scattering [48]. We may now produce an alpha map as in Figure 74, where green areas correspond to stable sphere type scatterers and red areas stable diplane scatterers.

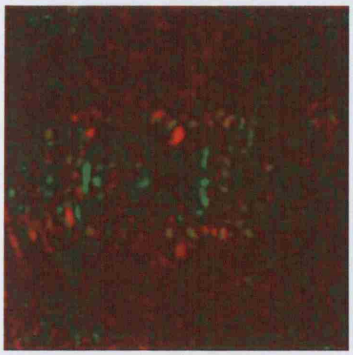

Figure 74: Alpha map of a MBT, green areas are stable sphere type scatterers, red areas are stable diplane type scatterers

We observe that the front grill has a strong single bounce return together with the flat areas of the hull behind the turret area. On the right of the turret is a prominent diplane scatter, perhaps from the side of the turret and the commander's hatch. This may also be shown when the small group of pixels over the angle range –30° to 25 in this spatial region are plotted on a Poincaré sphere, as in Figure 75 and Figure 76. The pixels over the range of aspect angles from this stable region are clustered away from the area (Q=1, U=0, V=0), which is sphere type scattering and are the result of some other double bounce type scattering process.

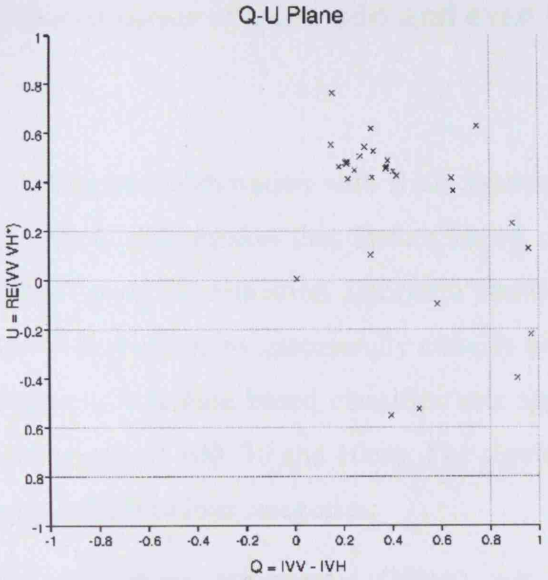

Figure 75: Projection on the *Q-U* plane of the pixels in the stable diplane region

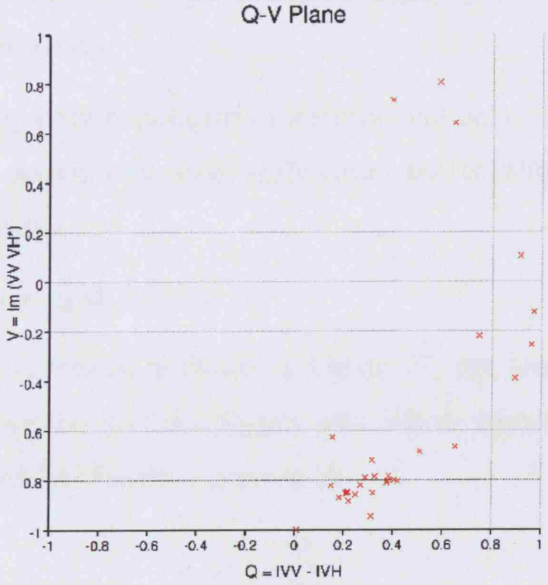

Figure 76: Projection on the *Q-V* plane of the pixels in the stable diplane region

6.4 The stability of the number of pure odd and even bounce scatterers

6.4.1 Introduction

A previous study by the author in collaboration with BAE Systems has suggested that polarimetric features do contain information that feature based classifiers can utilise [71]. In this study a feature based classification algorithm showed that using simple polarimetric features alone it is possible to successfully classify military vehicles from high resolution ISAR imagery. A feature based classifier was applied to polarimetric ISAR turntable data at resolutions of 100, 30 and 10cm. The algorithm was run using a large number of features grouped into four categories:

- Features using only shape information (Mask), e.g. area, width, fractal dimension
- Features derived from single channel imagery (*HH*), e.g. power, variance and texture measures
- Features using only polarimetric measures (Pol only), e.g. between channel correlations, polarimetric phase differences, power ratios and decomposition derived measures
- The set containing all features

A graph summarising the results is shown in Figure 77, the four lines represent the classification performance for the four feature sets. Where kappa, which weights the results compared to a random classifier, is given by

$$\kappa = \frac{P_0 - P_e}{1 - P_e}, \tag{157}$$

where P_0 are the proportion of correctly classified samples and P_e the proportion that may be expected due to chance. Thus a perfect classifier would have kappa equal to one and a random classifier have zero kappa. From Figure 77 we can see that the resolution is more critical to the performance level of the polarimetric features than other non-polarimetric feature types, with robust classification only possible using imagery of 10cm or better resolution. To investigate the behaviour of these polarimetric features in more depth, here we investigate two features more thoroughly. For the relative simplicity of their physical interpretation, the percentage of pure odd and even bounce measures were the two features chosen.

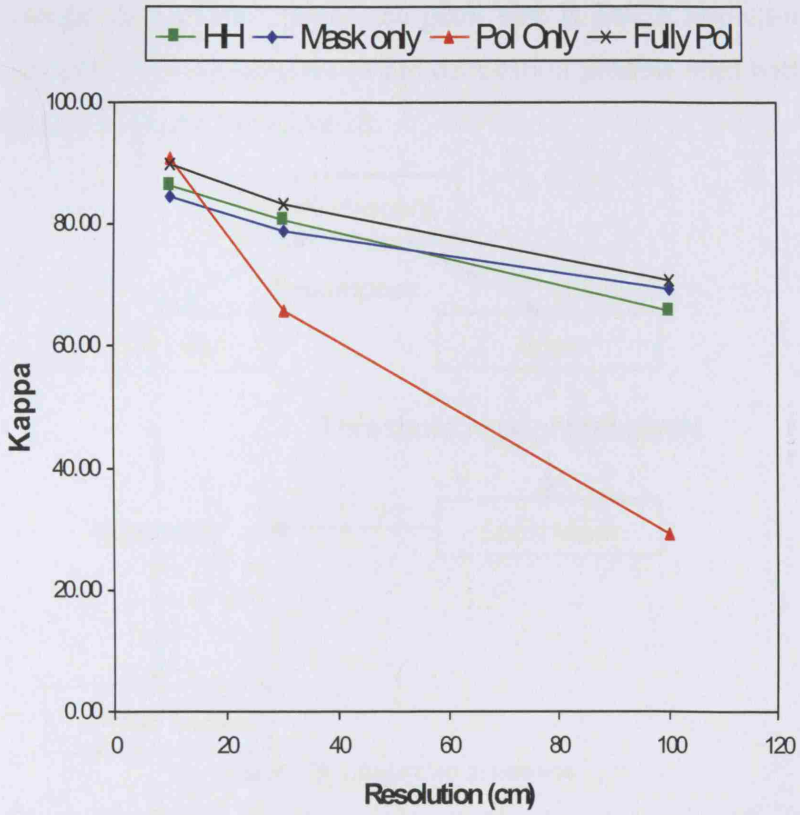

Figure 77: Summary of classification performance versus resolution [71]

6.4.2 Odd/even bounce

The odd/even bounce scattering decomposition is defined as follows [50]

$$\text{odd bounce} = \frac{\left|E_{HH} + E_{VV}\right|^2}{2}$$
$$\text{even bounce} = \frac{\left|E_{HH} - E_{VV}\right|^2}{2} - 2\left|E_{HV}\right|^2 \tag{158}$$

Hence upon decomposition each image pixel has an odd and even bounce component. Here we define a pixel to be pure odd bounce if the intensity of the odd component is greater than 75% of its total intensity and likewise for pure even bounce pixels.

6.4.3 Analysis

The motivation behind the analysis was to mimic some of the stages in a typical ATR system as described in section 6.1. The ISAR Imagery was decomposed into odd, even bounce and span channels. The span channel $(=|HH|^2+|HV|^2+|VH|^2+|VV|^2)$ was thresholded to determine the N brightest pixels and this binary mask was than used to create the image chips for the odd and even bounce channel. The value of N used was varied with resolution so that equal target areas could be compared at different resolutions. N = 36, 400, and 3600 pixels for 100, 30 and 10cm resolutions respectively

giving an on-target area of $9m^2$ (since the pixel size is half a resolution cell). This process was designed to be analogous to the delineation process used within a feature based classifier and is shown in Figure 78.

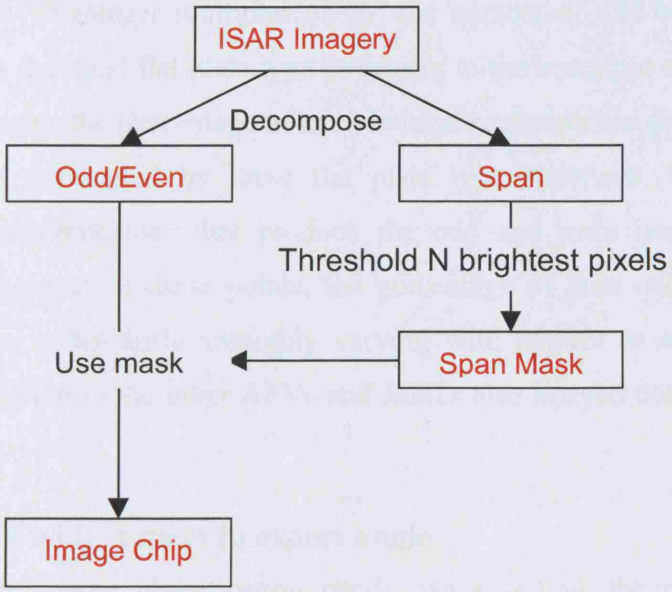

Figure 78: Image chip generation

At every 1° of rotation the image chips were analysed to determine the percentage of pure odd or even bounce pixels compared with the total number of on-target pixels (i.e. the number of non-zero pixels of the target mask. Figure 79 shows the percentage of pure odd and even bounce scatterers over an AFV versus vehicle aspect angle when processed to 10cm resolution.

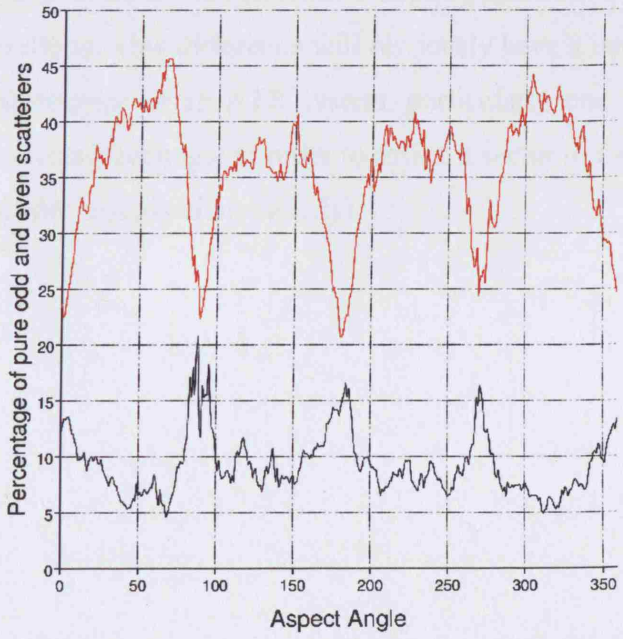

Figure 79: Percentage of odd and even bounce scatterers for an AFV as a function of aspect angle at 10cm resolution (black = odd bounce, red = even)

Note that at this particular geometry the percentage of even bounce scatterers is considerable greater than the pure odd bounce. This high proportion of even bounce scatterers is a characteristic of man-made objects such as vehicles or urban areas. One can also see that at integer multiples of 90° the number of odd bounces peak as the vehicle presents the most flat plate type structures to the boresight of the antenna head. Also at these angles the percentage of even bounce scatterers has definite local minima as scattering is dominated by these flat plate type structures. This illustrates the differing physical processes that produce the odd and even bounce radar returns. Besides the behaviour at these points, the percentage of pure odd and even bounce scatterers seems to be fairly smoothly varying with respect to aspect angle. These features are common to the other AFVs and MBTs also imaged during the Wells 1999 turntable trial.

6.4.4 Stability with respect to aspect angle

From the feature based classification results we saw how the performance of the polarimetric features increased more dramatically with finer resolutions than the other available feature sets (Figure 77). This can be partly explained by Figure 80, which shows how resolution affects the percentage of even bounces over a complete turntable rotation. At 10cm resolution, we see a smoothly varying curve with respect to aspect angle but at 30cm resolution, the function varies far more rapidly. Hence when comparing the number of even bounce scatterers in two images of the same vehicle, they will appear far less alike if viewed from a slightly different aspect angles when imaged at lower resolutions. This difference will obviously have a detrimental effect on the classification performance of an ATR system, particularly one which requires an estimation of the vehicles aspect angle in order to assign a sector to the test data (as with the feature based classifier discussed previously).

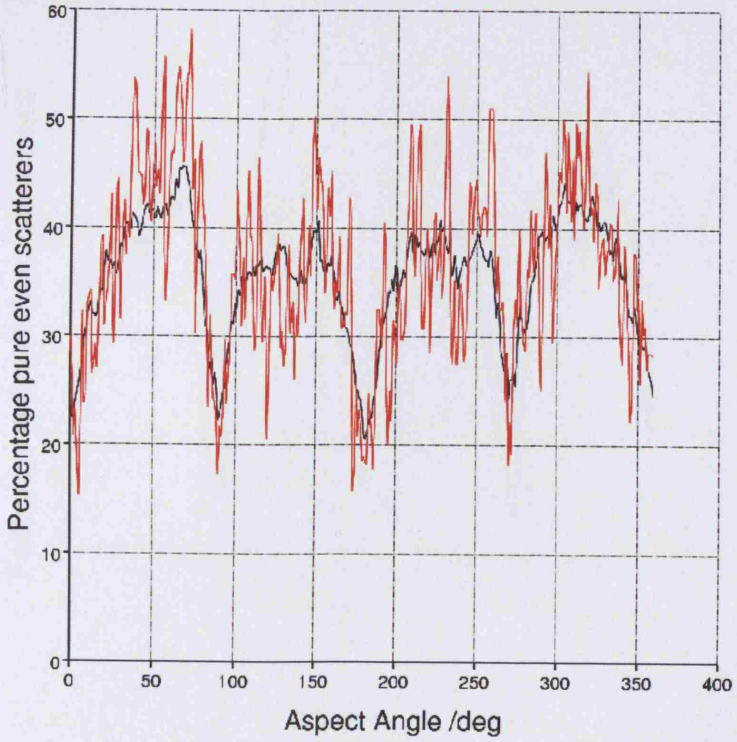

Figure 80: Percentage of even bounce scatterers for AFV #1 as a function of aspect angle (black = 10cm resolution, red = 30cm)

The origins for the more rapidly varying response with respect to aspect angle at coarser resolutions are twofold. Firstly, since we have normalised the mask to vehicle area, at coarser resolutions we have less pixels on the target so our percentage estimate is obtained from a smaller sample size. Additionally, as discussed previously, at finer resolutions we are able to isolate individual scatterers that have more stable polarimetric responses than at coarse resolutions where cells contain multiple scatterers. Furthermore, at the finest resolutions images are processed using data from larger collection angles ($\Delta\theta$) and hence will be correlated over wider angles. The plot of the 10cm resolution data is analogous to the result of applying a low pass filter to the 30cm resolution data.

6.4.5 Temporal and within class stability

Similar graphs to Figure 79 and Figure 80 can also be produced for different vehicle classes imaged at differing time periods. Figure 81 shows the percentage of even bounce scatterers versus aspect angle for 10cm imagery of four different AFVs (AFV1-4), a MBT and AFV1 imaged three days after the first image collection.

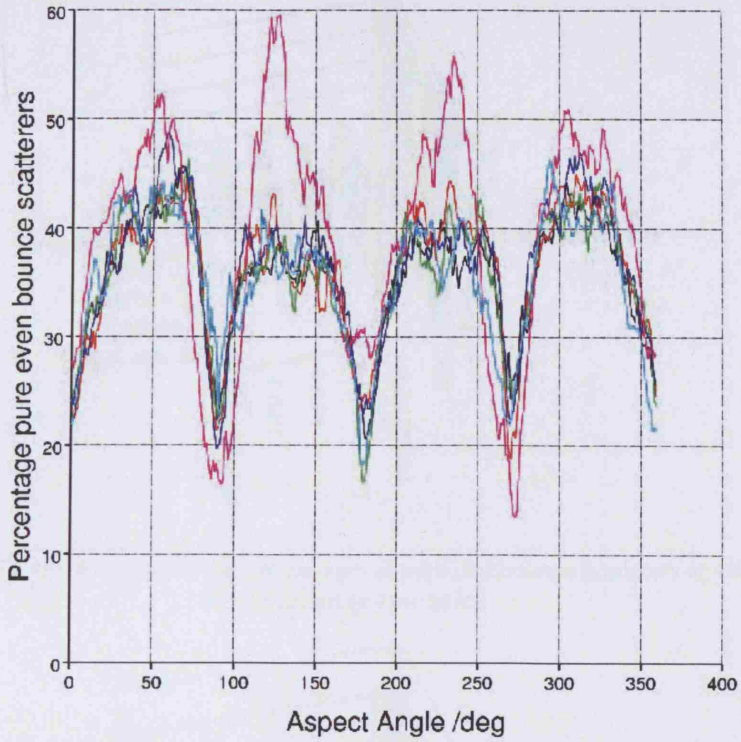

Figure 81: Percentage of pure even bounce scatterers for different vehicle images (10cm resolution), black=AFV1, red=AFV2, green=AFV3, blue=AFV4, magenta=MBT, cyan=AFV1 (day2)

From Figure 81 one immediately sees a high degree of correlation between the curves obtained from the AFV images compared to the curve for the MBT. This suggests that the feature may well be of use to discriminate between the two vehicles.

To examine this in more detail here we compute the RMS difference between pairs of these curves. In this case the mean is performed over one complete revolution. Figure 82, Figure 83 and Figure 84 show RMS differences obtained between four vehicles of the same class (AFVs #1-4) and for one vehicle of a differing class (MBT). Additional RMS differences are shown as calculated from images of AFV #1 collected over it's next turntable revolution (rev2 AFV 1) and imaged three days later after having been driven on and off the turntable (day2 AFV 1). The three figures show the RMS differences over the resolutions 10, 30 and 100cm. The height of the columns is the RMS difference between the pairs of vehicles on the x and y-axis.

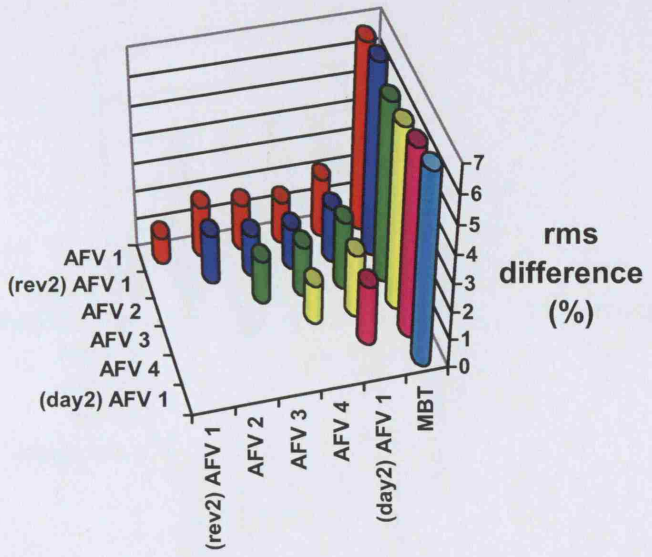

Figure 82: RMS differences between the percentages of pure odd bounce scatterers at 10cm resolution over a complete revolution

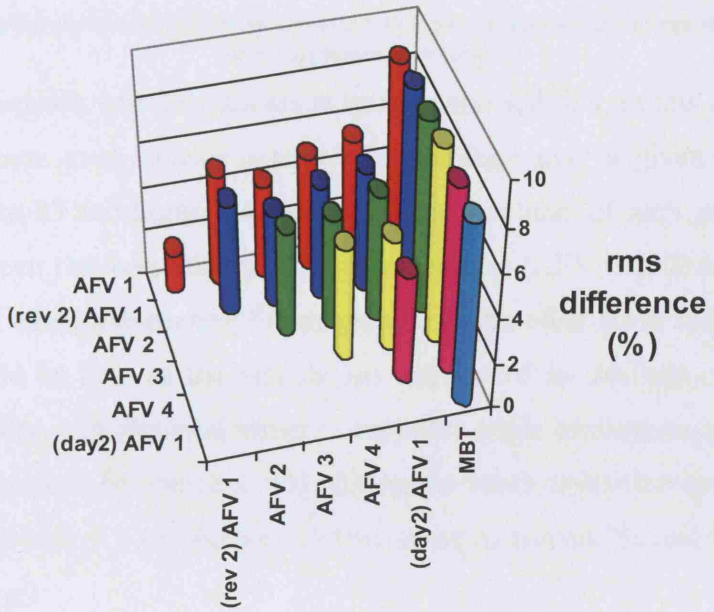

Figure 83: RMS differences between the percentages of pure odd bounce scatterers at 30cm resolution over a complete revolution

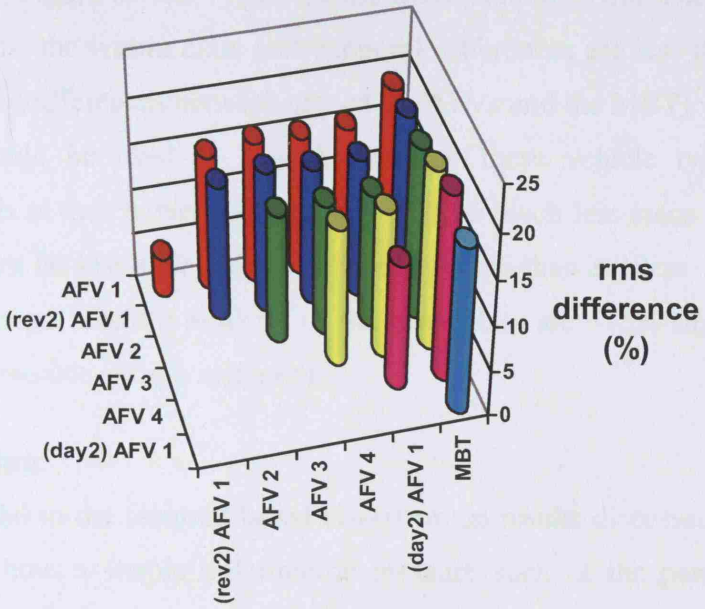

Figure 84: RMS differences between the percentages of pure odd bounce scatterers at 100cm resolution over a complete revolution

An important question with any feature is its temporal stability, in this case whether the percentage of pure even bounce scatterers is constant over a given time period. In Figure 82, Figure 83 and Figure 84 the top left hand column of each graph is the RMS difference between two revolutions of the same vehicle (AFV #1). This can be thought of as a baseline when interpreting the magnitude of the other RMS values. Ideally this difference should be zero as the vehicle has not moved its position on the turntable. However in reality, experimental errors in turntable angle measurement and radar drift cause this difference to be non-zero. This difference was found to be less than 1% of the total number of pixels at a resolution of 10cm, rising to around 2% and 4% at 30cm and 100cm respectively.

Comparing these values with the differences when AFV #1 is imaged over two revolutions on different days shows how rapidly the feature decorrelates with time. This is to be expected as the vehicle's position upon the turntable has now been changed. Differences now are 2%, 5.5% and 15.5% for 10, 30 and 100cm resolutions. At the finest resolution this seems small but, as with all three resolutions, the difference between the same vehicle imaged on two different days is greater than the differences between vehicles of the same class (i.e. between AFVs #1-4). Since this feature is less stable from day to day than between vehicles of the same class, it suggests that it is not robust enough to be used to identify particular vehicles within a class. The same trends are also found in the even bounce channel data.

From Figure 82, Figure 83 and Figure 84 the MBT column is consistently the highest. At all resolutions, the within class and temporal differences are less than the between class differences (differences between any of the AFVs and the MBT). This shows how the measure could be used to classify between these vehicle types. However, confidence levels at the coarser resolutions would be much less since the peaks of the MBT columns are far less well defined at 30 and 100cm than at 10cm. In fact at 100cm the RMS differences between vehicles of the same class are ~15% suggesting that the measure is only reliable at high resolutions.

6.4.6 Discussion

Viewed in parallel to the featured based classification results discussed previously, the analysis shows how a simple polarimetric measure such as the percentage of even bounces within a vehicle chip could be used to discriminate between vehicle classes at fine resolutions. The feature is shown to be stable both within class and from day to day. The decrease in feature stability as resolution is degraded corresponds to the drop in classification performance found at coarser resolutions when the polarimetric features were used within the feature based classifier. As within class stability is greater than the day-to-day stability, it suggests that such a simple measure is not sensitive enough to identify individual vehicles within a vehicle class.

6.5 Spatial stability of polarimetric decompositions

6.5.1 Introduction

In the previous section, whilst investigating the stability of the number of pure odd and even bounce scatterers, we disregarded information on their spatial distribution. It seems probable that this spatial distribution could provide additional information of use within a target classification algorithm. To utilise this information one must first establish some measure of the target pixels' spatial distribution. This is a non-trivial task and to begin this section we concern ourselves with the task of finding a measure robust enough to enable direct comparisons between different vehicle images to be made. This is required since in order to use such information, as with the number of odd/even bounces, we must first establish whether this spatial distribution is stable.

Additionally, unlike with the previous analysis, one is able to make a direct comparison between the stability of a single polarimetric channel and the stability of a decomposed channel such as the odd or even bounce. This goes some way to addressing the fundamental question as to whether there is any additional useful information in the polarimetric channels.

6.5.2 Power spectral density

In examining the spatial distribution of an image a generic approach is to investigate the statistics of pairs of pixels. Such techniques generate measures called second order statistics. This approach is greatly simplified if the image process is assumed to be stationary. Stationarity assumes that if each pixel is generated from some stochastic process, then the joint probability distribution of a pair of pixels is dependant solely on their separation, not their absolute positions [72]. The SAR image formation process allows such an assumption to be made.

The autocorrelation function is a second order statistical measure that measures the rate of dependency between pairs of image pixels as a function of their separation. For a square NxN image containing complex pixel values, $x(i, j)$, the autocorrelation function, $R(k, l)$, is defined as the normalised autocovariance function, $C(k, l)$, where

$$C(k,l) = \frac{1}{(N-|k|)(N-|l|)} \sum_{i=0}^{N-|k|} \sum_{j=0}^{N-|l|} x(i,j)x^*(i+k, j+l), \tag{159}$$

$$R(k,l) = {C(k,l)}/{C(0,0)}, \tag{160}$$

such that $R(0, 0) = 1$, $R(k, l) = R^*(-k, -l)$ and $|R(k, 1)| \leq 1$. $C(k, l)$ and $R(k, l)$ are defined over the region $\{|k| < N; |l| < N\}$. The power spectral density (PSD) function, $\phi(\omega_k, \omega_l)$, may then by defined as the discrete Fourier transform of the autocorrelation function [73],

$$\phi(\omega_k, \omega_l) = \sum_{l=-(N-1)}^{N-1} \sum_{k=-(N-1)}^{N-1} R(k,l) e^{-i(\omega_k k + \omega_l l)} . \tag{161}$$

The PSD measures the spectral content of the image, it gives the energy distribution over the spatial frequencies ω_k and ω_l. Effectively $\phi(\omega_k, \omega_l) d\omega_k \, d\omega_l$ is the signal power over the infinitesimal region $(\omega_k \pm d\omega_k /2, \omega_l \pm d\omega_l /2)$. From equation (161) the PSD may be more efficiently computed in the form

$$\phi(\omega_k, \omega_l) = \frac{1}{\sum_{i=0}^{N_{ZP}} \sum_{j=0}^{N_{ZP}} |x(i,j)|^2} \left| \sum_{i=0}^{N_{ZP}} \sum_{j=0}^{N_{ZP}} x(i,j) e^{-i(\omega_k i + \omega_l j))} \right|^2 , \tag{162}$$

which is simply the modulus squared of the discrete Fourier transform of the original image with the appropriate normalisation factor [73]. The DFT requires the original image to be zeropadded to N_{ZP} such that $N_{ZP} > 2N$. Usually, to decrease computational time, N_{ZP} is set to the next power of 2.

The PSD provides a measure of the spatial distribution of pixels within an image. The measure is independent of linear translations in absolute pixel position. This property makes it ideal for comparing image chips of different vehicles over many days. Since vehicles are unlikely to be in the same position on the turntable, pixel to pixel comparisons are inappropriate especially at fine resolutions. However, in this form the PSD is still vulnerable to rotational errors in vehicle position, hence we transform (162) to polar coordinates and average in θ.

$$\phi(\omega_r) = \frac{1}{2\pi} \int_{-\pi}^{\pi} \phi(\omega_r, \omega_\theta) d\theta , \tag{163}$$

The radial PSD, $\phi(\omega_r)$, is invariant to linear and rotational vehicle alignment errors unlike cross-correlation techniques which are only invariant to linear translations. We shall use this measure to investigate the stabilities outlined in the previous sections.

6.5.3 Analysis

The radial PSD (equation (163)) was used as a measure of spatial distribution for the same vehicles studied in section 6.4, namely four AFVs and one MBT. Recall that one AFV was imaged during the subsequent turntable revolution and imaged again three days later. Images were analysed at two resolutions, 10 and 30cm, over a complete turntable revolution. The stabilities of images from the two polarimetric intensity channels, $|HH|^2$ and $|HV|^2$, and two odd and even bounce decomposed channels, were investigated.

Initially the images were masked using the technique described in section 6.4.3 and their radial power spectral densities were calculated at one degree intervals over a complete turntable revolution from equations (162) and (163). A typical PSD, at just one angle (0° i.e. boresight), is shown in Figure 85.

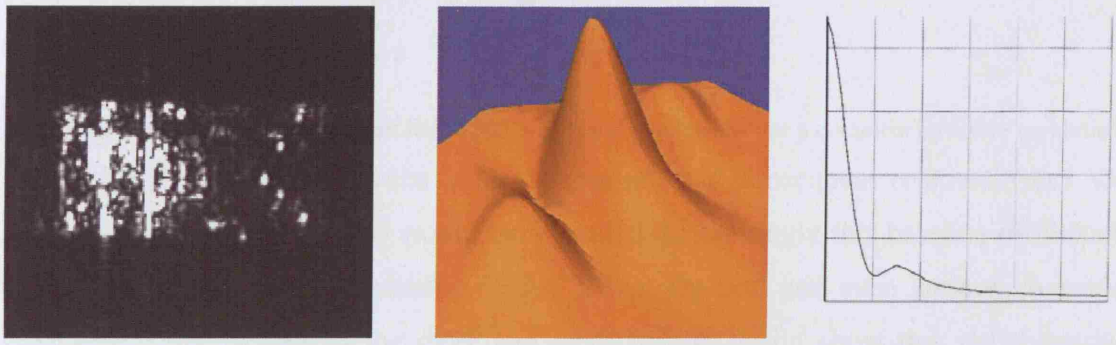

Figure 85: Left: Masked ISAR odd bounce image of AFV#1 at 10cm resolution, Centre: PSD of masked image, Right: Radial component of PSD.

Spatial distributions of different images are then compared by computing the RMS differences between the two sets of 360 radial PSDs obtained at each aspect angle. RMS differences between the calculated radial PSD are then averaged over one rotation for pairs of images.

6.5.4 Discussion of results

RMS differences for odd, even, $|HV|^2$ and $|HH|^2$ channel images processed to 10cm resolution were calculated. Figure 86 below provides a summary of those results with the height of the columns being the RMS difference between pairs of vehicles on the x and y-axis. The rev1 vs. rev2 column shows the RMS differences for AFV #1 imaged on successive revolutions and the day1 vs. day2 column shows the RMS differences for AFV #1 imaged on day1 and again on three days later. AFV X vs. AFV Y shows the average RMS difference between the different AFVs on the same day and AFV vs.

MBT shows the average RMS difference between each AFV and the MBT again only on the same day. These values are calculated for four data channels; odd, even, *HH* and *HV*.

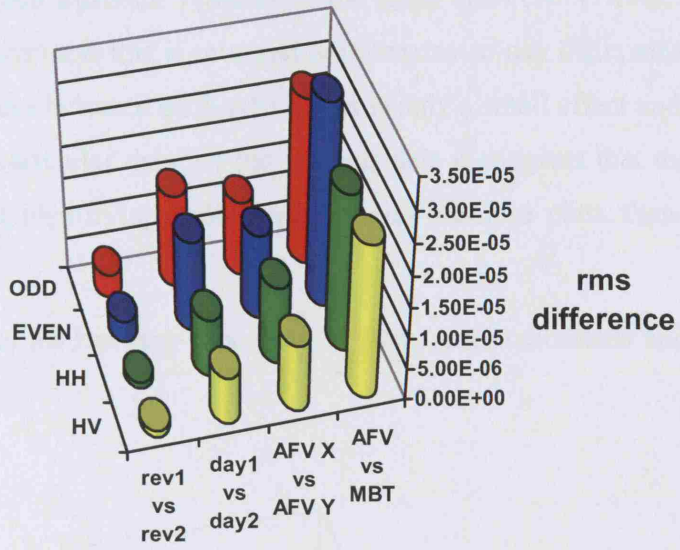

Figure 86: RMS differences between radial PSDs at 10cm resolution over a complete turntable revolution

The baseline difference between vehicles imaged over subsequent rotations (rev1 vs. rev2) is by far the smallest as would be expected. Interestingly this baseline difference is smaller for the single channels (~$1x10^{-6}$) than the odd and even bounce channels (~$3.5x10^{-6}$). The results in the day1 and day2 column again show that radial spatial statistics are temporally more stable for the single channels. The *HV* and *HH* intensity channels have RMS differences of ~$8x10^{-6}$ compared with values of ~$1.5x10^{-5}$ for the decomposed channels. The rapid temporal decorrelation time for the decomposed channels may be due to a sharp decorrelation in phase, the single channel intensity spatial distribution being independent of phase and thus more robust.

All four measures discriminate well between the AFV and the MBT with RMS differences of the AFV against the MBT higher than the values between the different images of the AFVs. The single channels and the decomposed channels both show similar magnitudes for the differences between the AFVs (AFV *X* vs. AFV *Y*), of the order of 1.2-1.3$x10^{-5}$, the *HV* channel has marginally smaller values (1.07$x10^{-5}$). The RMS differences of the AFV with the MBT show that although all channels seem to be able to discriminate between the AFV and the MBT the decompositions do this slightly better with larger RMS values in the AFV vs. MBT column.

There is another observable in the RMS differences between the single and decomposed channels that may affect their ability to distinguish between vehicles of the same class. We see that for the odd and even bounce channels the RMS differences between vehicles imaged over different days (day1 vs. day2) is slightly larger than the differences between different vehicles of the same class (AFV *X* vs. AFV *Y*). For the single intensity channels this is reversed with the day-to-day differences marginally less than the differences between each AFV. This is only a small effect and may well be just peculiar to this particular data set but if repeatable it suggests that the single channels may be better at identifying individual vehicles within a class than the decomposed channels.

Analogous results for imagery processed to 30cm were calculated and are summarised below.

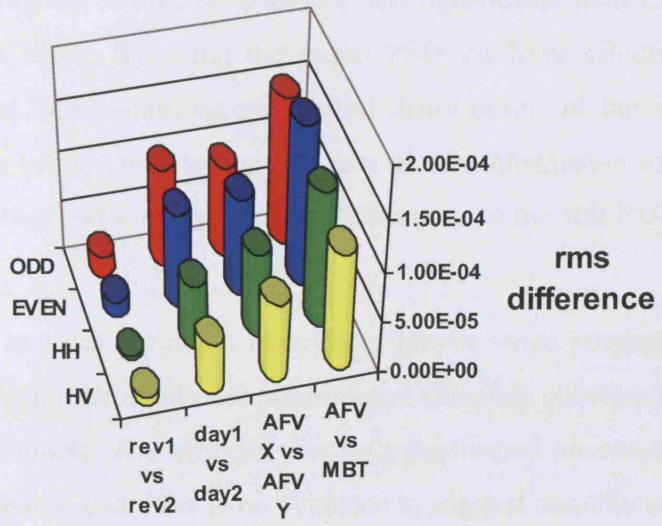

Figure 87: RMS differences between radial PSDs at 30cm resolution over a complete turntable revolution

The same trends discussed previously for the 10cm data are again present. The AFV RMS differences in the radial PSD are least when the same vehicle is imaged over subsequent turntable revolutions. Again day to day temporal differences are smaller for the single channels, but so too are the differences between the AFV and the MBT classes. All the columns in Figure 87 show RMS differences larger at this coarser 30cm resolution than in the 10cm case shown in Figure 86. The separability between the AFV and the MBT is less well defined at the coarser resolution. This is shown by the less pronounced peaks of the RMS differences in the AFV vs. MBT column in Figure 87 than in Figure 86.

6.5.5 Discussion

As a measure of the spatial distribution of an image the radial PSD generally seems to perform reasonably well in distinguishing between the AFV and the MBT. The RMS differences between subsequent revolutions are also encouragingly small yet the day-to-day differences, particularly for the polarimetric decompositions, are significantly larger. However, as the single channels have smaller day-to-day differences than within class differences, the radial PSD is a robust measure. This result shows it is possible to extract the underlying differences in spatial distribution of the vehicle pixels from the errors in vehicle positioning upon the turntable. This is of vital importance to any classification feature.

In comparing the information content of the single and decomposed channels there seem to be only slight differences between the two. As stated above the single channel intensities have the important property of producing smaller day-to-day differences than within class differences. Yet the polarimetric decompositions distinguish better between the AFV and the MBT. By using the radial PSD we have effectively discarded all angular dependant information on the spatial distributions of the imagery. Although robust to errors in vehicle positioning this loss of this information may be too much of an oversimplification and a study into the differences in the full PSD could be an area for further study.

It is not possible to infer too much from these results when attempting to address the question as to whether the additional polarimetric channels contained more information than the single channels. The analysis was only performed on one decomposition; the odd-even bounce basis, and there is no evidence to suggest that this is the optimum way to combine the polarimetric channels for vehicle classification. Also since we have used the span image to mask the single channel image chips means that the single channels contain additional polarimetric information. This was done to mimic the processing chain used in the featured based classification algorithm but to provide a clearer comparison between the polarimetric and single channels the analysis was repeated on unmasked imagery.

6.5.6 Analysis of unmasked imagery

In order to eliminate the effects of the masking process on the power spectral densities some of the previous analysis was performed again on the unmasked odd, even, *HH* and *HV* intensity channels. A smaller scale investigation was performed at only 10cm

resolution and only one vehicle of each class was studied. The results are shown in Figure 88 below.

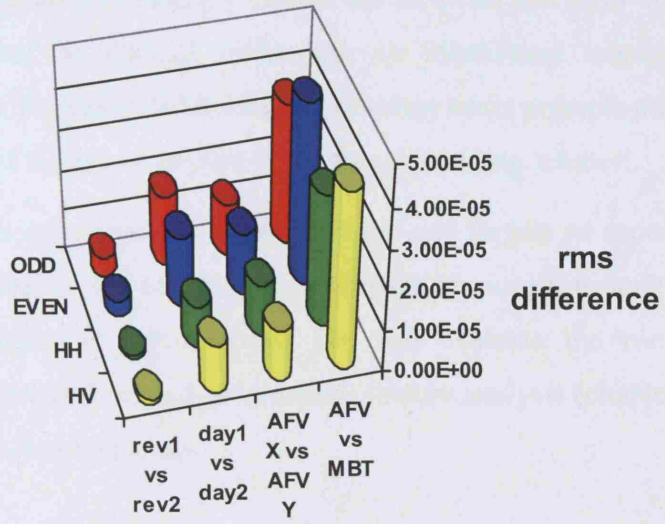

Figure 88: RMS differences between radial PSDs at 10cm resolution over a complete turntable revolution for unmasked imagery

The magnitudes of the unmasked RMS differences are generally slightly larger than those obtained from the masked image chips (Figure 86). This is probably because by not masking the image chip we have not eliminated the surrounding clutter and sidelobe returns. These 'noisy' returns will increase the differences between different images. However the overall trends of Figure 88 seem to be identical to those of Figure 86 described previously, thus suggesting that the polarimetric information content in the span mask is not critical to the form of the radial PSD differences.

7 Targets in Urban Areas

7.1 Overview

Military operations are increasingly carried out in urban and semi-urban environments, such areas present heightened difficulties in identifying targets and minimising collateral damage. However, SAR imagery of urban areas presents particular difficulties in the extraction of targets of interest from the surrounding 'clutter'.

In earlier chapters we have looked at buildings and targets as separate 'hard targets'. Here we apply some of the techniques developed previously to look at the problem of discriminating targets in urban areas. We will evaluate the use of the primitive scattering filter (section 5.1) and polarimetric feature analysis (chapter 6) for the task of detecting vehicles in urban areas.

7.2 Data collection trial

The data on which this study was based was obtained using the jointly owned QinetiQ and Thales Airborne Data Acquisition System (ADAS). The radar was mounted onboard a Squirrel helicopter and flown in June 2003. The urban area imaged was part of a mock village in the north of England. ADAS was operated at X-band with eight 50% overlapping pulses, each with a bandwidth of 500MHz, from 9 to 11.25GHz, thus producing a 2.25GHz effective bandwidth. Fully polarimetric spotlight data was collected over range of aspect angles at nominal grazing angles of 5 and 28°. The purpose of the trial was to obtain wide bandwidth data of military vehicles, decoys and civilian vehicles deployed in as realistic scenarios as possible in urban environments. Photographs of the imaged targets are shown in Figure 89.

No. 1

No. 2

No. 3

No. 4

No. 5

No. 6

No. 7

No. 8

No. 9

No. 10

No. 11

No. 12

No. 13

Figure 89: Photographs of the imaged targets within the mock village.

Ground truth of the mock village was obtained during the trial in the form of GPS data and digital photography. In addition, airborne photographs were also obtained, one example is shown in Figure 90.

Figure 90: Aerial photograph of trials scene.

7.3 SAR processing and calibration

All the spotlight data was processed using QinetiQ's Third Generation SAR Processor. Imagery was produced to a resolution of 0.08m in the range direction and 0.18m in azimuth with a pixel spacing of 0.07m. This study considers imagery obtained from a grazing angle of 28° over squint angles of –5 to 4° relative to boresight.

Three polarimetric channels; *HH*, *VV* and *VH* were processed. Relative polarimetric calibration was performed by imaging a scene containing four dihedral and seven trihedral calibration targets. Calculations were performed to extract the amplitude and phase of the polarimetric channel imbalances. Calibration errors due to cross-talk, (which are commonly less than –25dB with this system) were neglected. The image on the left in Figure 91 shows the return from all three channels (red = $|HH|$, green = $|VV|$ and blue = $|HV|$. On the right of Figure 91 the span ($\sqrt{(|HH|^2+ VV|^2+2|HV|^2)}$) amplitude image is shown. Both images have been averaged to a pixel spacing of 0.21m to enable them to be reproduced in this document.

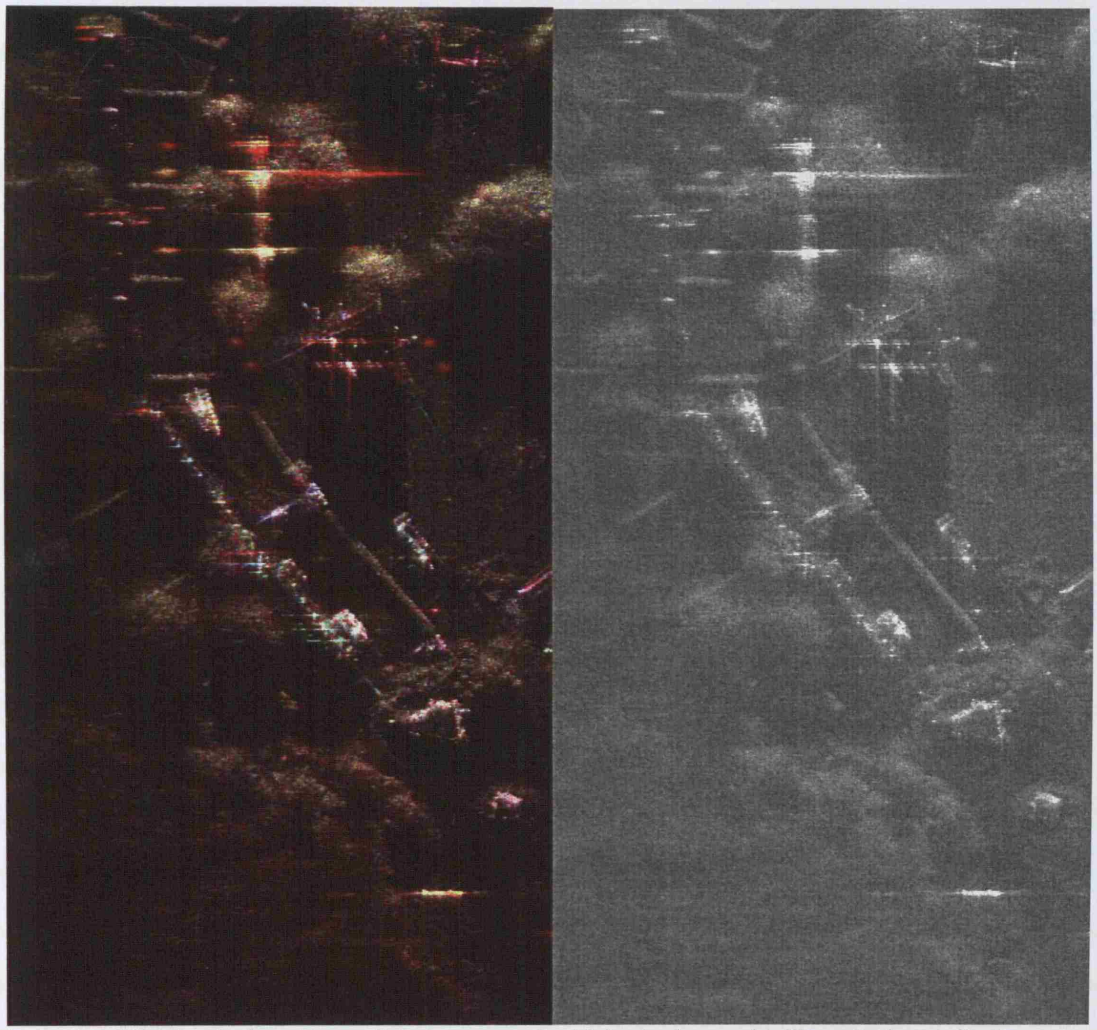

Figure 91: ADAS polarimetric spotlight imagery of vehicles in the mock village. Left; amplitude returns; red = $|HH|$, green = $|VV|$ and blue = $|HV|$. Right; polarimetric span

7.4 Post-processing techniques

Here, two post-processing image exploitation techniques are investigated; coherent polarimetric decompositions and primitive scatterer (or canonical scattering) analysis.

7.4.1 Odd/even bounce decomposition

Figure 92 shows the result of applying the odd/even bounce decomposition (158) to the imagery shown in Figure 91. The amplitude of the odd and even bounce channels are shown in red and green respectively. Pixels that have equal amplitudes in the odd and even channels will therefore appear yellow. From Figure 92 we see that the returns from the tree canopies are predominately odd bounce scattering events, whereas the hard structures within the scene, such as the buildings and targets, exhibit more even bounce scattering behaviour.

The details of vehicles 1, 3, and 9, shown in Figure 93, do not appear to highlight any physical structures upon the target vehicles. Much of the vehicle signature is equally bright in the odd and even channels. This observation suggests that such an approach may not significantly aid in the classification of these targets. However, as we saw earlier in chapter 1 the number and spatial distribution of odd and even bounce events within a target's signature may be used to distinguish between vehicles at fine resolutions (10cm). Therefore, this may suggest that the azimuth resolution of the image is not fine enough to isolate individual scatterers within the vehicles signature, or that the polarimetric calibration is sub-optimal.

Figure 92: Results of the odd/even bounce decomposition; red=odd channel amplitude, green=even channel amplitude. Vehicles 1, 3 and 9 are shown in the blue inserts.

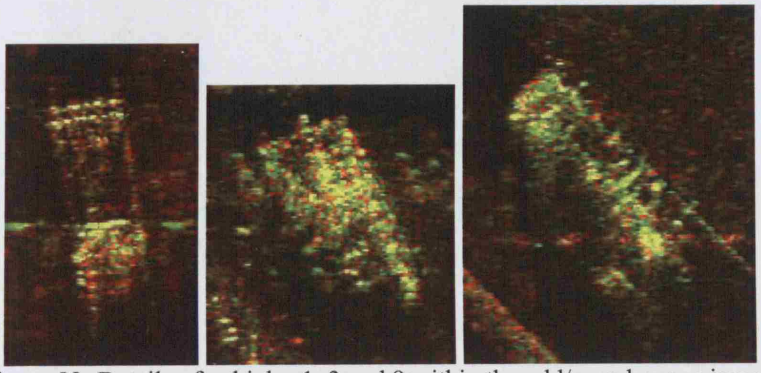

Figure 93: Details of vehicles 1, 3 and 9 within the odd/even bounce image.

7.4.2 Scattering primitives

In chapter 5, using imagery with spatial resolutions of 0.3m, it was shown that the scattering responses of structures in urban environments varied little over the frequency and Doppler bandwidths required to achieve such resolutions. However, here it was hoped that when operating with higher bandwidths and collecting over wider angles, scattering responses would exhibit more dependency on radar and Doppler frequency.

Figure 94 shows the result of applying the frequency filters to the *HH* image of vehicles within the mock village. Three filters were chosen, with alpha values of -1, 0 and 1, shown in red, green and blue in Figure 94. Pixels that have equal intensities after the application of each filter appear white. Figure 94 is predominately white, suggesting that the majority of scatterers have similar responses to the three filters. This is confirmed when the signatures of the vehicles 1, 3 and 9, as shown in Figure 95, are considered. The effect of the alpha = 1 filter appears to smear the image in the range direction, evidenced by the blue areas of the image around the dominant scatterers. This may occur if a point-like scatterer is post-processed with a filter that does not correctly match its frequency response, effectively reducing the available bandwidth and leading to a loss of resolution.

Similar effects are evident when the Doppler filters are applied to the imagery, as shown in Figure 96 and Figure 97. Again the majority of the image is white, since there is little variation in the responses to each filter. The vehicle signatures show similar characteristics. Indeed the effect of the narrowest filters is to degrade image resolution by reducing the available Doppler bandwidth, indicated by the green and blue smearing in the azimuth direction.

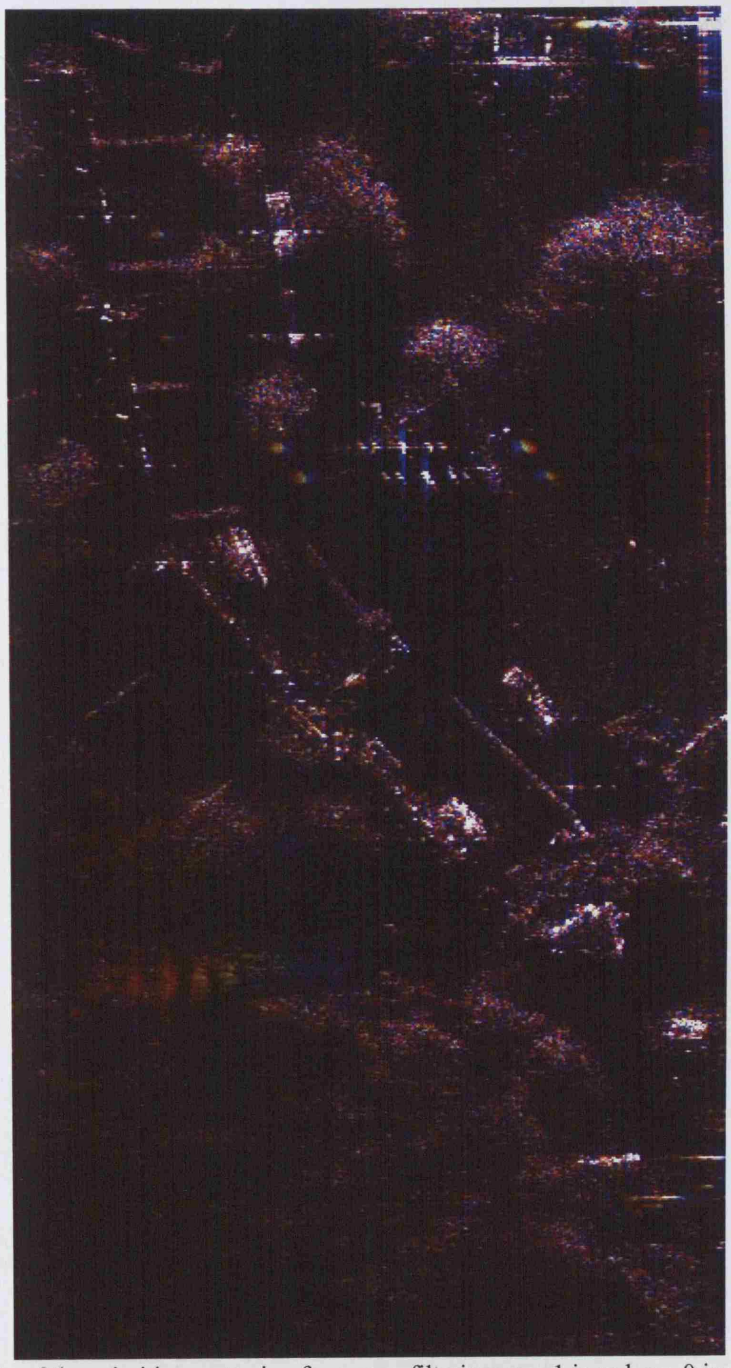

Figure 94: Results of the primitive scattering frequency filtering; α =-1 in red, α =0 in green and α =1 in blue.

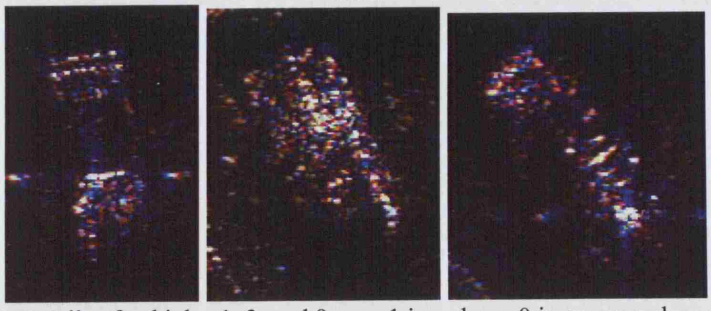

Figure 95: Details of vehicles 1, 3, and 9; α =-1 in red, α =0 in green and α =1 in blue.

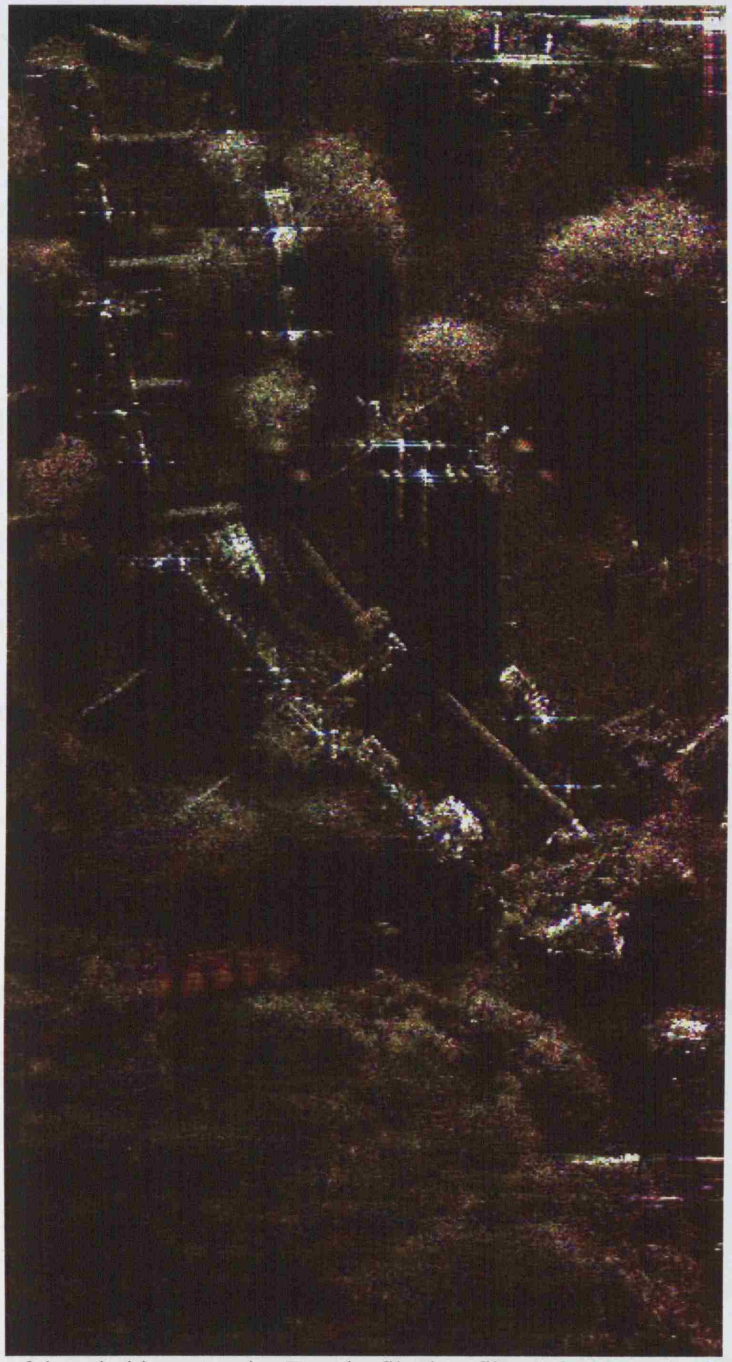

Figure 96: Results of the primitive scattering Doppler filtering; filters of widths of twice, half and a tenth of the Doppler bandwidth are shown in red, green and blue respectively.

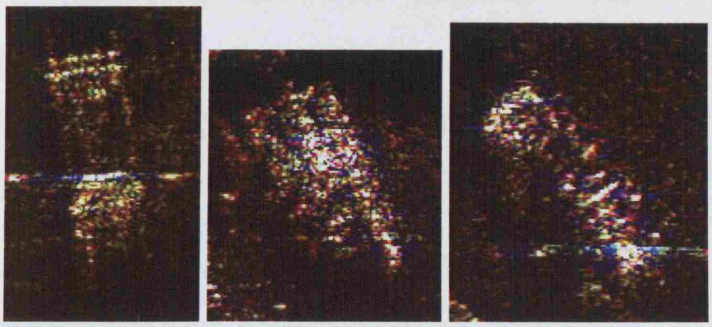

Figure 97: Details of vehicles 1, 3 and 9; filters of widths of twice, half and a tenth of the Doppler bandwidth are shown in red, green and blue respectively.

7.5 Evaluation of post-processing techniques

In order to allow a qualitative comparison of the effects of the post-processing techniques, a correlation based approach was undertaken.

A target chip was extracted from the image containing a target of interest. This target chip was then correlated with the original image using a locally computed mean and standard deviation to ensure a normalised output. The product of this correlation procedure is a correlation map. Each pixel within the correlation map contains a value between –1 and 1, indicating the similarity between the extracted target chip and each area of the image. A correlation value of one occurs when the target chip and particular area of the image are identical, and hence will occur in the position at which the chip was extracted.

The object of this approach is to assess whether various image post-processing techniques are able to increase the differences between a target and its background and therefore assist in task of automatically extracting targets in SAR images of urban scenes. This can be quantitated by calculating the level to which the post-processing filter reduces the correlation between the target chip and the remainder of the scene.

Correlation maps were produced from imagery over nine squint angles from –5 to 4° for the vehicles 1, 3, and 9 for the following images and post-processed images;

Polarimetric Channels and Decompositions;

- *HH*, *VV*, *VV*, Span, Odd, Even and log(*HH*),

Primitive Scatterer filters applied to *HH* image;

- Alpha = -1, Doppler filter width/Doppler bandwidth = 100, 2, 0.5 and 0.1,
- Alpha = 0, Doppler filter width/Doppler bandwidth = 100, 2, 0.5 and 0.1,
- Alpha = 1, Doppler filter width/Doppler bandwidth = 100, 2, 0.5 and 0.1.

From each correlation map, an average cumulative density function over all squint angles was calculated. The results of the polarimetric, log and primitive scattering post-processing techniques for vehicle 9 are shown in Figure 98 to Figure 101. Similar results were obtained for vehicles 1 and 2.

For the results of the polarimetric post-processing techniques shown in Figure 98, we see that, compared to the *HH* imagery, the span imagery produces nearly identical results. However, the odd and even bounce decompositions show a small decrease in the correlation between the target chip and the remaining image. Thus suggesting a minor

improvement in the separability between the two classes after the odd/even bounce decomposition has been performed.

Analysis of the cumulative frequency density functions after the primitive scatterer post-processing has been performed (Figure 99 and Figure 100), show no difference in the correlation between the target and the background. This suggests that neither the frequency nor the Doppler filtering result in any increase in target-background separability.

From Figure 101 we observe that taking the log of the single channel *HH* image appears to increase the similarity between the target chip and its background.

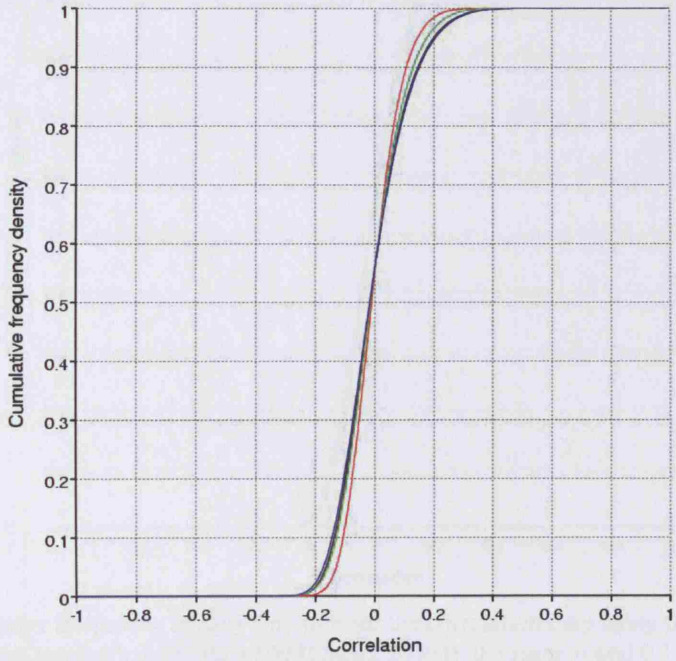

Figure 98: Cumulative frequency density function for the correlation map using the *HH* image (black), odd bounce image (red), even bounce image (green) and span image (blue) for vehicle 9.

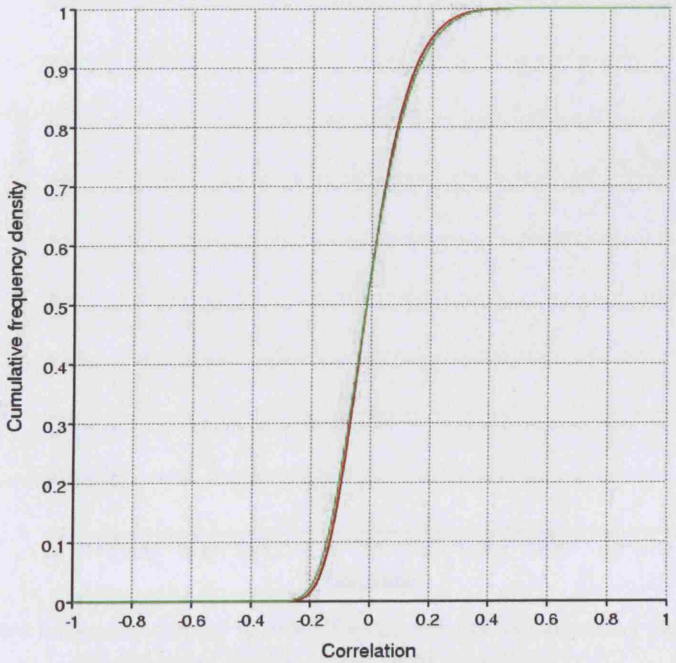

Figure 99: Cumulative frequency density function for the correlation map using the *HH* alpha = -1 image (black), *HH* alpha = 0 image (red) and *HH* alpha = -1 image (green) for vehicle 9.

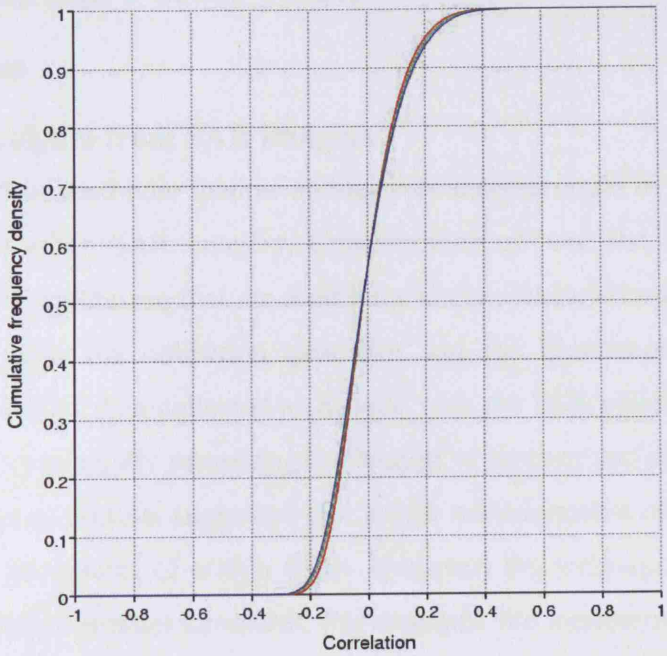

Figure 100: Cumulative frequency density function for the correlation map using the *HH* image and Doppler filters of width/Doppler bandwidth =100 (black), 2 (red), 0.5 (green) and 0.1 (blue) for vehicle 9.

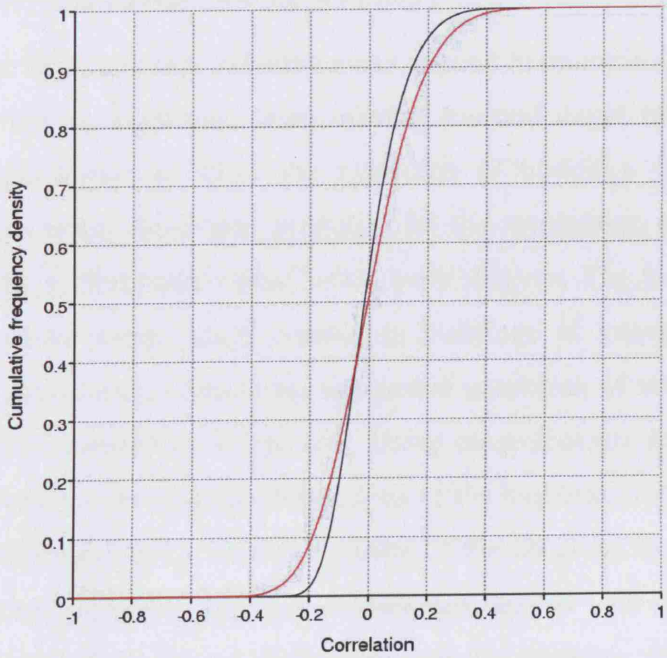

Figure 101: Cumulative frequency density function for the correlation map using the *HH* image (black) and the log of the *HH* image (red) for vehicle 9.

8 Conclusions and Future Work

8.1 Conclusions

8.1.1 Building heights from SAR imagery

In section 4.4, we described how shadow and layover analysis could be used to estimate building heights in urban SAR imagery. Consideration of both flat and apex roofed buildings lead to the conclusion that the scattering can be characterised into six distinct cases, dependent upon the collection geometry and the dimensions of the target building. Using spotlight data collected at X-band with the ESR system, the technique was demonstrated by manually measuring the lengths of layover and shadow regions in the processed imagery. Results suggested that height measurements of larger buildings could be made to accuracies of within 0.3m. However, the technique less accurately measured the heights of smaller structures. For example, the minimum roof height of a small apex roofed residential house was calculated to be 1.3m higher than its actual height. In such cases, the number of pixels comprising the shadow and layover regions is relatively small at the processed resolution of 0.4m.

The shadow/layover approach was automated and applied to multiple squinted spotlight collections. Pre-screening algorithms from existing assisted target recognition (ATR) software were demonstrated to allow the extraction of buildings from urban SAR imagery. These algorithms, developed primarily for the recognition of vehicles, were modified for optimal performance within urban environments. The results of this pre-screening stage enabled image chips containing buildings of interest to be further analysed. Building delineation allowed the automated extraction of both the building's radar signature and in some cases its shadow. Using measurements derived from both the building return and its shadow, the dimensions of the building, including its height, were calculated. Although reliant on the visibility of the shadows in the SAR image, this automated method provided estimates of buildings heights with accuracies of less than 3m. This initial analysis shows encouraging results, however further analysis is required to establish the robustness of the delineation.

In addition, building heights were also extracted using interferometric SAR processing techniques. Analysis of both flat and apex roofed buildings again resulted in the formation of six scattering cases. It was shown that only under certain conditions are unambiguous measurements of roof heights possible. The collection geometries and building dimensions of these cases were described, enabling an estimation of the

position and extent of these regions to be made. Single pass airborne X-band InSAR data allowed building heights to be estimated to accuracies of approximately 1m within these regions. However, where there was lack of unambiguous height information, measured height accuracies were poorer, particularly when small buildings were imaged from steep grazing angles. With this geometry, the unambiguous or partially ambiguous height regions contained very few pixels. Additionally, the analysis of a building's radar signature in spotlight imagery and the corresponding height profile generated from single pass InSAR enabled the detection of areas of structural damage within the urban area.

Both the shadow/layover and InSAR height extraction techniques require varying degrees of *a prior* knowledge in order to establish which of the six classes a target building belongs too. This remains a problem with both techniques and is often over looked in many of studies discussed in section 3.1. Under certain conditions, specific geometries could be chosen to ensure target buildings fall into a known class. For instance, the use of small grazing angles would ensure buildings fell into case I. Alternatively, data from a number of collection angles (or from a bistatic system) could allow the assignment of a target building to a specific case by comparing the signatures in more than one image. In addition, polarimetric information may also be used to determine the location of unambiguous height regions in the radar signatures of buildings. Decompositions, such as those described in section 3.3.2, could be used to differentiate between direct and multiple bounce scattering.

The technique of coherent cross-track stereo (developed by Jakowatz et al) was proposed as potentially particularly useful for DEM production over urban areas since, unlike InSAR, no phase unwrapping is required. We showed how Jakowatz's common treatment of this approach and interferometry is readily extended to describe more generic stereo collection geometries.

8.1.2 Urban SAR exploitation

The complex nature of radar scattering in urban areas was addressed by the development and demonstration of a post processing match filter technique for the extraction of primitive scatterers. Unlike traditional SAR processing, this technique responds to signatures from non-point-like structures such as corners, edges and cylinders. For urban areas, where many such scatterers are present, this approach is particularly relevant. Distinct from many of the approaches discussed in section 3.2, segmentation was not used and hence image resolution was not lost. Imagery was

produced using both frequency and Doppler match filtering. Analysis of the resultant imagery showed phenomena (such as frequency dependent roof scattering) that may be relevant for building characterisation. However, the observable effects were small for systems with relatively narrow fractional frequency and Doppler bandwidths. Azimuth filtering showed that most scattering was point-like over the small angular range (~2°) required to process imagery at a resolution of 0.4m at X-band. Furthermore, a high degree of aspect angle dependency was observed making the interpretation of any such information difficult.

The use of sub-aperture processing to produce SAR movies was described and its application to urban imagery interpretation was addressed specifically. Examples of how SAR movies can allow the structural properties of buildings to be characterised were demonstrated. The particular example described showed how the widths of roof tiles were measured by application of a Bragg scattering model to the SAR movie response of a target building's roof. Additionally, the imaging and subsequent velocity estimation of a moving vehicle was demonstrated. It was noted that velocity estimation in cases where vehicle motion is not predominately in the line of sight direction is not possible using the technique applied here.

Software was developed to produce models of urban areas assuming simple building structures. Algorithms were written to predict the effects of shadowing and layover for various SAR imaging geometries and radar modes. It was shown that the proportion of pixels that may be fully resolved is reduced if long apertures are required for either high resolution or low frequency imaging. Furthermore, bistatic imaging over urban areas may produce additional difficulties in image interpretation due to the presence of two shadows. The impact of shadowing was shown to be greatest when operating at low grazing angles, typical to airborne long range surveillance aircraft. This study suggests the need for sensor deployment studies to investigate how multi-static systems may provide best coverage for urban scenes. The software written is also useful for planning collection campaigns against specific targets, to ensure that they will be resolvable in the processed imagery.

The direction of multipath returns in squinted SAR images has been characterised and compared with collected imagery (unfortunately the data cannot be presented in this document). The direction of multipath returns was found as a function of grazing and squint angles (equations (131) and (132)). At large grazing and squint angles the angle between the multipath and shadow returns is greatest. It is suggested that the angular

change in multipath angle within a spotlight SAR collection could be used to identify multipath returns in SAR imagery. Software has been written to provide graphical outputs of radar parameters, collection information and exploitation information (such as layover, shadowing and multipath characteristics) for spotlight SAR images and SAR movies.

8.1.3 Polarimetric ATR

The polarimetric calibration of ISAR imagery was addressed in depth. A distortion model was derived that is more general than the models described in [10] and is therefore applicable to a wider range of radar systems. Moreover, unlike similar polarimetric calibration models [44, 45], it is not dependent on assumptions of the form of a target's scattering matrix or the reciprocity of the radar system. A polarimetric calibration method has been successfully developed which uses the radar return from a rotating dihedral to calculate the channel imbalances within the system, enabling a fully polarimetric amplitude and phase calibration to be performed. The procedure is robust to alignment errors and is independent of cross-talk. Unfortunately, the technique is not thought applicable to the calibration of airborne platforms due to issues with dihedral alignment and mechanical stability.

ISAR images from two turntable trials were analysed. The first trial did not allow the polarimetric phase differences to be calibrated and hence only channel amplitudes were examined. Using imagery of a military vehicle, the variation of polarimetric intensity with respect to aspect angle was investigated. When averaged over an entire vehicle, the cross-polar returns were of the order of 15dB below co-polar returns. Characteristic peaks in co-polar intensity at multiples of 90° were found when the largest number of scattering centres were boresighted to the antenna. The correlation between the two co-channels was far greater than the correlations between the co and the cross-channels. This effect occurs as the co and cross-polar responses are generated by independent physical scattering mechanisms, whereas the scattering mechanisms that produce the *HH* and the *VV* channel responses are often more closely linked. However, polarimetric information on individual scatterers was lost when the average intensities of pixels was taken over the spatial extent of the vehicle's signature.

The second trial produced turntable data with correct phase information and the rotating dihedral calibration method was applied to produce a more effectively calibrated image set. In contrast with the previous study, rather than spatially averaging, an attempt to identify polarimetrically stable areas at high resolutions using coherent decomposition

methods was undertaken. Polarimetric entropy techniques were adapted from land-use classification studies in order to find polarimetrically stable areas of a vehicle. The scattering processes that produced these areas were identified using the alpha parameter. The analysis involved the production of an average covariance matrix over a defined number of aspect angles. Such an approach may have biased the results towards the brightest scatterers and further work on normalised signatures was suggested.

In order to investigate the use of polarimetry for SAR target classification the behaviour of two polarimetric features, the percentage of pure odd and even bounces, were studied in depth. The instabilities of these features with respect to aspect angle at coarse resolutions reasserted the requirement for high resolution data if polarimetric information is to be successfully utilised in ATR systems. Even with this relatively simple feature, the differences between a MBT and an AFV were apparent, particularly at the finest resolutions. Although stable from day to day, the features were not sensitive enough to discriminate between individual AFVs of the same class.

The stability of the spatial distribution of scatterers in ISAR imagery was investigated using the radial power spectral density function. The study showed little differences in the stabilities of the single channel and odd/even bounce polarimetric decompositions. Both sets of radial PSDs were able to distinguish between an AFV and a MBT. The polarimetric decompositions were marginally more successful than the single channels at distinguishing between vehicle classes but were less temporally stable. One benefit of the radial PSD is its robustness to errors in vehicle positioning. However, any angularly dependant information is lost in the averaging process. The impact of this information loss on target discrimination performance should be addressed by further studies using the full PSD.

For this study, much of the analysis was performed on one polarimetric measure; the odd/even bounce decomposition. It is probable that there are more efficient ways to combine polarimetric channels for vehicle classification and hence any conclusions presented here are appropriately caveated.

8.1.4 Targets in urban areas

High resolution polarimetric data was obtained using the ADAS sensor to establish whether polarimetric feature analysis and the primitive scatterer filter could be used to assist target discrimination in urban SAR imagery. A qualitative visual assessment showed that the odd and even bounce decompositions separated the man-made structures from the trees and ground returns but did not discriminate between the targets

and the visible building structures. Despite using fractional frequency and Doppler bandwidths that were greater than the ESR data discussed in section 4.3.2, there was little evidence that scatterers responded significantly differently to each filter type.

A quantitative measure of the correlation between target chips and clutter was made for each of the post-processing techniques and results confirmed the visual interpretation. Results suggested small improvements in target from clutter discrimination for the odd and even bounce decompositions but showed no improvement for the scattering primitives matched filter.

8.2 Future Work

8.2.1 Building heights from SAR imagery

The fundamental problem associated with building height extraction using shadow/layover and InSAR techniques is the requirement to assign target buildings to the correct class (section 4.4.3). For the generation of robust and accurate building height measurement this issue needs to be addressed. The various methods that could be investigated include;

- Multiple look angle collections. The properties of a target building's signature and shadow when imaged from a number of aspect and grazing angles may allow it to be automatically placed into one the six categories.
- Single image scattering region identification. Areas of direct and multipath scattering could potentially be discriminated using polarimetric decompositions, SAR movie multipath analysis and primitive scatterer match filtering (with large fractional bandwidths). The extent and position and these areas could be fitted to the models described in section 4.4.3 and a case assigned for each target building.

The automated shadow/layover height extraction method described in section 4.4 was found to be vulnerable to errors in the delineation process. As such, further work should attempt to make this process more robust and allow the delineation of non-rectangular objects. The active contour delineation method was suggested as potentially useful for this task and an extension to this study has addressed this area [1].

Other methods for building height extraction such as stereography [15, 16] and the combined use of both shadow and InSAR data [31, 36] should also be examined.

8.2.2 Urban SAR exploitation

Future work should address how best to exploit information from SAR movies. The radar return from a particular scatterer extracted from a SAR movie may be represented as a time series. The variation of both the amplitude and phase information over time may contain information that can be used to either discriminate or recognise structures in urban scenes. Furthermore, the angular variation of multipath returns (as described in section 5.3.5) could be used to discriminate such signatures from direct scattering. Velocity estimation from SAR movies should be examined for target motion that is not predominately in the line of sight direction. For instance, quadratic phase filters could be used to focus targets with motion in the azimuth direction.

The urban shadow simulation was not able to produce absolute figures regarding the impact of radar mode and collection geometry on the percentage of fully resolvable areas within urban scenes (only relative comparisons could be made). To address this shortfall a Monte Carlo simulation approach could be used to quantify absolute levels in terms of building density and type. Building models may be randomly generated using the current software and the average percentage of fully resolvable pixels could then be calculated over several building scene realisations. Future developments of the software could also be used to aid mission planning. For instance, one may wish to monitor a known area. In which case the shadowing predictions could be used to maximise the resolvable area for a given number of imaging legs by defining optimal imaging geometries. Alternatively, one might wish to assess the benefit of flying additional imaging legs or the impact of denial of airspace on coverage rates. Additionally, the approach could assist future cost benefit studies concerning the deployment of multistatic systems over urban areas (such as netted UAVs). The fully resolved area could be computed as a function of the number of available sensors and their corresponding radar modes.

8.2.3 Polarimetric ATR

The use of ISAR turntable imagery allows access to clean signatures over a range of geometries. However, using ISAR imagery alone could provide misleading results. Therefore, the feature based classification and polarimetric stability analysis performed in section 6.3 should be repeated on full scene SAR data. Vehicles should be viewed from as wide a range of orientation angles as is practically feasible. Nevertheless, there appears little benefit in using these polarimetric features for target classification on imagery with resolutions coarser than 30cm.

The comparison of the spatial statistics of the odd and even bounce channels with the single channels showed only small differences in temporal and between class stabilities. The odd and even bounce decomposition was chosen rather arbitrarily and hence further research should attempt to establish the optimum combination of polarimetric channels for target recognition (Novak [54] has proposed an optimum polarimetric filter for target detection, but little work has address the problem of recognition). A principal component analysis approach could potentially be used to optimise between class separability whilst minimising temporal stability.

8.2.4 Targets in urban areas

Although the frequency and Doppler match filtering approach was applied with limited success to the X-band imagery discussed here, the technique may be more suited to low frequency systems which offer larger fractional bandwidths. The techniques developed in this study were used by subsequent research into the use of UHF SAR for FOPEN target detection and is described in [23]. Furthermore, any future studies may wish to fuse information from both frequency and Doppler analysis with polarimetric approaches.

9 References

1. W. G. Carrara, R. S. Goodman, R. M. Majewski, *Spotlight Synthetic Aperture Radar*, Artech House, 1995.
2. C. V. Jakowatz et al, *Spotlight-Mode Synthetic Aperture Radar: A Signal Processing Approach*, Kluwer, 1996.
3. D. C. Munson et al, 'A Tomographic Formulation of Spotlight-Mode Synthetic Aperture Radar', Proceedings of the IEEE, Volume 71, No. 8, pp917-925, August 1993.
4. P. Lacomme et al. *Air and Spaceborne Radar Systems: An Introduction*, William Andrew Publishing, 2001.
5. G. W. Stimpson, *Introduction to Airborne Radar, Hughes*, 1983.
6. C. A. Wiley, 'Synthetic Aperture Radars – A Paradigm for Technology Evaluation', IEEE Transactions on Aerospace and Electronic Systems, AES-21, pp 440-443, 1985.
7. D. P. Belcher, C J Baker, 'High resolution processing of hybrid strip-map/spotlight mode SAR', IEE Proceedings Radar, Sonar and Navigation, Volume 143, Issue: 6, pp366-374, Dec. 1996.
8. D. Blacknell, 'Statistical target behaviour in SAR images', IEE Proceedings Radar, Sonar and Navigation, Volume 147, Issue: 3, pp143-148, June 1996.
9. H. Mott, *Antennas for Radar and Communication: A Polarimetric Approach*, Wiley, 1992.
10. F. T. Ulaby, C. Elachi, *Radar Polarimetry for Geoscience Applications*, Artech House, 1990.
11. S. Cloude, E. Pottier, 'A Review of Target Decomposition Theorems in Radar Polarimetry', IEEE Trans. on Geoscience and Remote Sensing, Volume 34, No.2, pp498-517, 1996.
12. A. J. Bennett, A. Currie, 'The Use of High Resolution Polarimetric SAR for Automatic Target Recognition', Algorithms for Synthetic Aperture Radar Imagery IX, Orlando, 1-3 April 2002, Proceedings of SPIE, Volume 4727, pp146-153, August 2002.
13. E. Rodriques, J. Martin, 'Theory and Design of Interferometric Synthetic Aperture Radars', Proceedings of the IEEE, 139, No. 2, pp127-159, April 1992.
14. H. A. Zebker, J. Villasenor, S.N. Madsen, 'Topographic Mapping from ERS-1 and Seasat Radar Interferometry', IEEE Proceedings of the International

Geoscience and Remote Sensing Symposium, IGARSS '92, pp387–388, May 1992.

15. M. D. Desai, 'Spotlight mode SAR stereo technique for height computation', IEEE Transactions on Image Processing, Volume 6, Issue 10, pp1400-1411, Oct. 1997.
16. D. A. Yocky, D. E. Wahl and C. V. Jakowatz, 'Terrain Elevation Mapping Results from Airborne Spotlight-Mode Coherent Cross-Track Stereo', IEEE Transactions on Geoscience and Remote Sensing, 42, No. 2, pp301-308, Feb. 2004.
17. A. J. Bennett, D. Blacknell, 'Exploiting the Intensity and Phase Characteristics of Airborne SAR Data Over Urban Areas', Algorithms for Synthetic Aperture Radar Imagery XII, Orlando, 28 March-1 April 2005, Proceedings of SPIE Volume 5808, pp185-195, May 2005.
18. A. M. Horne, G. A Yates, 'Bistatic synthetic aperture radar', IEE Proceedings of Radar 2002, Edinburgh, 15-17 October 2002, pp6-10, Sept. 2002.
19. H. D. Griffiths 'From a different perspective: principles, practice and potential of bistatic radar', Proceedings of the International Radar Conference, Adelaide, Australia, 2003, pp1-7, Sept. 2003.
20. G. A. Yates, et al. 'Bistatic SAR Image Formation', Proceedings of EUSAR 2004, Ulm, 25-27 May 2004, Vol. 2, pp581-584.
21. G. Krieger et al, 'Analysis of multistatic configurations for spaceborne SAR interferometry' IEE Proceedings of Radar, Sonar and Navigation, Volume 150, Issue 3, pp87-96, June 2003.
22. B. Binder et al., 'SAR foliage penetration phenomenology of tropical rain forest and northern U.S. forest', Record of the IEEE International Radar Conference, pp158-163, 8-11 May 1995.
23. M. Magnusson, J. E. S. Fransson, 'Combining CARABAS-II VHF SAR and Landsat TM satellite data for estimation of forest stem volume', IEEE Proceedings of the International Geoscience and Remote Sensing Symposium, IGARSS '04, Volume 4, pp2327 – 2331, Sept. 2004.
24. A. J. Lawson, 'Low frequency algorithms for FOPEN', QINETIQ/S&E/APC/TR032377 (MoD Technical Report), January 2004.
25. D. Barker, 'UWB Radar for hidden Target Detection and Identification', QINETIQ/S&E/APC/CR031943 (MoD Customer Report), November 2003.

26. R .J. Sullivan et al, 'Polarimetric X/L/C-band SAR', IEEE Proceedings of the 1988 National Radar Conference, Michigan, USA, pp9-14, April 1988.
27. K. Schulz et al, 'Elimination of across-track phase components in airborne along-track interferometry data to improve object velocity measurements', IEEE Proceedings of the International Geoscience and Remote Sensing Symposium, IGARSS '03, Volume 7, pp4377-4379, July 2003.
28. Janes Information Group, www.janes.com.
29. P. Gamba, B. Houshmand, 'Three Dimensional Urban Characterisation by IFSAR Measurements', IEEE Proceedings of the International Geoscience and Remote Sensing, IGARSS '99, pp2401-2403, 1999.
30. P Gamba, B. Houshmand, 'Comparison of C- and X-band InSAR Data for 3D Characterisation of an Urban Area', IEEE Aerospace and Electronic Systems Magazine, Vol. 17, Issue 6, pp9-15, June 2002.
31. U. Soergel, K. Schulz, U. Thoennsessen, 'Enhancement of Interferometric SAR Data Using Segmented Intensity Information in Urban Areas', IEEE 2000, pp3216-3218.
32. U. Stiller, U. Soergel and U. Thoennessen, 'Potential and Limits of InSAR data for the reconstruction of buildings', Remote Sensing and Data Fusion over Urban Areas, IEEE/ISPRS Joint Workshop, 8-9 November, 2001, pp64-68.
33. C. Tison, F. Tupin, H. Maitre, 'A Markovian Scheme for Joint Retrieval of Classification and Height Map from Urban Interferometric SAR Images', International Conference on Image Processing, Vol. 1, IEEE, 11-14 Sept. 2005, pp641-644.
34. R. Bolter and F, Leberl, 'Detection and Reconstruction of Buildings from Multiple View Interferometric SAR data', Proc. Geoscience and Remote Sensing Symposium, 24-28 July 2000, Vol. 2, IEEE, 74 -751.
35. R. Bolter, 'Reconstruction of Man-made Objects from High Resolution SAR Images', Proc. Aerospace Conference, Vol. 3, 18-25 March 2000, IEEE, pp287-292.
36. C. Tison, F. Tupin, H. Maitre, 'Retrieval of Building Shapes from Shadows in High Resolution SAR interferometric Images, Proc. of Geoscience and Remote Sensing Symposium', 2004, IEEE, Vol. 3, pp1788-1791.
37. C. Jakowatz, D. Wahl, P. Thompson, 'Three-Dimensional SAR Imaging Using Cross-Track Coherent Stereo Collections', Signals, Systems and Computers, 1997 Conf. Record of 31st Asilomar Conf. Vol. 2, 2-5 Nov 1997, pp1199-1203.

38. U. Soergel, U. Thoennessen and U. Stilla, 'Visibility Analysis of Man-made Objects in SAR Imagery', 2nd GRSS/ISPRS Joint Workshop on Data Fusion and Remote Sensing over Urban Areas, pp120-124, 2002.
39. G. Franceschetti et al, 'SAR Raw Signal Simulation for Urban Structures', IEEE Transactions on Geoscience and Remote Sensing, Vol. 41, No. 9, pp1986-1995, Sept. 2003.
40. D. Garren et al, 'SAR Image Formation Algorithm with Multipath Reflectivity Estimation', IEEE, pp323-326, 2004.
41. M. A. Koets, R. L. Moses, 'Feature Extraction using Attributed Scattering Centre Models on SAR Imagery', Proc. SPIE, Algorithms for Synthetic Aperture Radar Imagery VI, 3721, 5-9 April 1999, pp104-115, August 1999.
42. Y. Akyildiz and R. Moses, 'A Scattering Centre Model for SAR Imagery', SAR Image Analysis, Modelling and Techniques II, Florence 1999, Proc. SPIE Vol. 3869, pp76-85.
43. M. Allen, J. Jauregui and L. Hoff, FOPEN Detection by Direct Use of Simple Scattering Physics, IEEE International Radar Conference, 1995, pp152-157, 1995.
44. H. Schimpf, 'Calibration of a Polarimetric Radar by Means of a Rotating Dihedral', IEEE Second Internationals Workshop on Radar Polarimetry, IRESTE, Nantes, France, pp490-497, September 1992.
45. L. A. Muth, 'Calibration Standards and Uncertainties in Radar Cross Section Measurement', The Record of the 1999 IEEE Radar Conference, 20-22 April 1999, pp326-331.
46. R .A. Cordey, 'On the Accuracy of Crosstalk Calibration of Polarimetric SAR Using Natural Clutter Statistics', IEEE Transactions on Geoscience and Remote Sensing, Vol. 31, No.2, pp447-454, March 1993.
47. D. R. Sheen, A. Freeman, E. Kasischke, 'Phase Calibration of Polarimetric Radar Images', IEEE Transactions on Geoscience and Remote Sensing, Vol. 27, No.6, pp719-731, November 1989.
48. E. Pottier, S. R. Cloude, 'Application of the H/A/α Polarimetric Decomposition Theorem for Land Classification', Wideband Interferometric Sensing and Imaging Polarimetry, Proceedings of SPIE, San Diego, USA, July 1997, pp132-143, Dec 1997.

49. S. R. Cloude, 'Wide Band Radar Inversion Studies Using the Entropy-Alpha Decomposition', Wideband Interferometric Sensing and Imaging Polarimetry, Proceedings of SPIE, San Diego, USA, July 1997, pp118-129, Dec. 1997.
50. C. Jackson, H. Rais, B. Huxtable, 'Polarimetry and its Use in Automatic Target Detection: With Examples from Search and Rescue', Automatic Target Recognition VII, Orlando, April 23-24, 1997, Proceedings of SPIE, 3069, pp204-214, June 1997.
51. E. Krogager, Z. H. Czyz, 'Properties of the Sphere, Diplane, Helix Decomposition', IEEE Third International Workshop on Radar Polarimetry, IRESTE, Nantes, France, March 1995, pp106-114.
52. W. L. Cameron, L. K Leung, 'Identification of Elemental Polarimetric Scatterer Responses in High Resolution SAR and ISAR Signature Measurements', IEEE Second International Workshop on Radar Polarimetry, IRESTE, Nantes, France, September 1992, pp196-212.
53. R. Touzi et al, 'Polarimetric Discriminators for SAR Imagery, IEEE Transactions on Geoscience and Remote Sensing', Vol. 30, No.5, pp973-979, September 1992.
54. L. Novak et al, 'Optimal Processing of Polarimetric SAR Imagery', Lincoln Laboratory Journal, Volume 3, No. 2, 1990, pp273-290, 1990.
55. L Novak et al, 'Performance of High-Resolution SAR Automatic Target Detection Recognition Target Detection System', Lincoln Laboratory Journal, Volume 6, No. 1, 1993, pp11-24, 1993.
56. N. Arini, A. J. Bennett, 'Trials Plan for 2001 RAAT Trial', September 2001.
57. A. P. Blake, A.M. Horne, R. Middleton, 'Geometrically Rigorous SAR Autofocus', Proceedings of the IRS International Radar Symposium, Dresden, 30 September-02 October 2003.
58. N.A. Software Ltd Technical Report /DERA/GRAPE/UG/1, Version 3.0.3, 2002.
59. D. Blacknell, 'Assessment of the Effect of Polarisation on Target Detection for Battlefield Surveillance' QINETIQ/S&E/APC/TR030659 (MoD Technical Report), March 2003.
60. A. J. Bennett, D. Blacknell, 'The Extraction of Building Dimensions from High Resolution SAR Imagery', IEEE Proceedings of Radar 2003, Adelaide, 3-5 September 2003, pp182-187.

61. A. J. Bennett, D. Blacknell, 'Infrastructure Analysis from High Resolution SAR and InSAR Imagery', Remote Sensing and Data Fusion Over Urban Areas, IEEE/ISPRS Joint Workshop, 22-23 May 2003, pp230-235.
62. D. Blacknell, D. Pedlar, 'SAR Target Detection and Aided Target Recognition', QINETIQ/S&E/APC/CR032015 (MoD Customer Report), September 2003.
63. A. L. Gray and P.J. Farris-Manning, 'Repeat-pass interferometry with airborne synthetic aperture radar', IEEE Transactions on Geoscience and Remote Sensing, 31, Issue: 1, pp180–191, Jan. 1993.
64. A. J. Bennett, D. Blacknell, 'The Benefits and Detriments of Radar Shadowing in Urban SAR Imaging', Proceedings of EUSAR 2004, Ulm, 25-27 May 2004, pp419-422.
65. R. Middleton, 'Single Phase Centre Detection Of Moving Targets In SAR', QINETIQ/S&E/APC/TN032646 (MoD Technical Note), December 2003.
66. A. Horne, R. G. White, 'Performance Comparison of Algorithms for Automatic Target Classification', DRA/LS2/CR97058/1.0, (MoD Customer Report), April 1997.
67. S. D. Richards et al, 'An Inverse Polar Format Algorithm for Turntable Spotlight ISAR Imaging Systems Using Stepped Frequency Waveforms', Proceedings of the IEEE Radar Conference, 26-29 April 2004, pp212 – 217.
68. A. Currie, 'Trials Plan for the MIDAS and ADAS Polarimetric Calibration Experiment at Wells, December 1998', DERA/S&P/SNRRR/376/2.0, November 1998.
69. A. Currie, 'Trials Plan for the Polarimetric Turntable Experiment at Wells, June 1998', DERA/S&P/SNRRR/376/01/01/05, May 1998.
70. A. Currie, 'Trials Plan for the Polarimetric and 3-D Turntable Experiment at Wells, December 1999', DERA/S&P/SNRRR/376/01/01/06/2.0, October 1999.
71. A. J. Bennett, 'The Use of High Resolution Polarimetric SAR for Automatic Target Recognition, DERA/S&E/RAD/TR010608 (MoD Customer Report), March 2001.
72. F. van der Heijden, *Image Based Measurement Systems*, Wiley 1994.
73. P. Stoica, R. Moses, *Spectral Analysis*, Prentice Hall, 1997.
74. R. D. Hill, C. Moate, D. Blacknell, 'Urban Scene Analysis from SAR Image Sequences', Proceedings of EUSAR 2006, Dresden, 16-18 May 2006.